Multiscale Fracture Simulations for Composite Materials

Developing a Failure Criterion: Proof of Concept

N. van Hoorn

Master of Science Thesis

TU Delft Delft University of Technology

Aerospace Structures & Computational Mechanics

Multiscale Fracture Simulations for Composite Materials

Developing a Failure Criterion: Proof of Concept

MASTER OF SCIENCE THESIS

For the degree of Master of Science in Aerospace Engineering at Delft University of Technology

N. van Hoorn

January 27, 2016

Faculty of Aerospace Engineering · Delft University of Technology

TU Delft Delft University of Technology

AIRBUS DEFENCE & SPACE

Copyright © Aerospace Structures & Computational Mechanics
All rights reserved.

DELFT UNIVERSITY OF TECHNOLOGY
DEPARTMENT OF
AEROSPACE STRUCTURES & COMPUTATIONAL MECHANICS

The undersigned hereby certify that they have read and recommend to the Faculty of Aerospace Engineering for acceptance a thesis entitled

MULTISCALE FRACTURE SIMULATIONS FOR COMPOSITE MATERIALS

by

N. VAN HOORN

in partial fulfillment of the requirements for the degree of

MASTER OF SCIENCE

Dated: January 27, 2016

Committee chairman:

dr. S. R. Turteltaub, MSc

Committee members:

dr. J. Fatemi, MSc

dr. C. Kassapoglou, MSc

dr. ir. R. C. Alderliesten

Summary

Fracture mechanics has grown to one of the most important disciplines within engineering and is mainly focused on why and how structures fail. The fracture mechanisms in isotropic materials are well understood, but for composite materials the developments are still ongoing. There are several failure and fracture criteria available for composite materials that have been proven to work. In this thesis a completely new simple failure criterion based on the micromechanics of a Uni-Directional (UD) Carbon-Fiber Reinforced Plastic (CFRP) material was developed. The resulting method provided a solid proof of concept. The goal was to incorporate microscopic fracture mechanisms, i.e. microcracks or fiber-matrix debonding, in a macroscopic failure criterion by performing Two-Dimensional (2D) numerical experiments on a Representative Volume Element (RVE) containing multiple fibers. The results of these numerical experiments were correlated into a simple bilinear Traction-Separation Law (TSL) that represents the failure criterion. This failure criterion was implemented on a macroscopic scale such that the response of a single cohesive element is in line with the response of the microscopic RVE.

The numerical experiments were performed in ABAQUS and fracture was simulated by the use of cohesive elements. A fully scripted procedure in PYTHON and MATLAB was developed that allowed for a fast and efficient pre- and post-processing. The ABAQUS input files were generated by first initiating a MATLAB meshing script that ensured a random fiber distribution, random meshing of triangular elements and implemented the cohesive elements. Using PYTHON the remainder of the input file was written, i.e. material properties, Boundary Conditions (BC) and step properties. By scripting this procedure the parameters for the numerical experiments could easily be changed. For the post-processing scripting was used to extract the relevant data from the ABAQUS output files and translate this data into an Effective Traction-Separation Law (ETSL) that describes the fracture mechanism. This ETSL was approximated by a bilinear TSL that has three parameters: an initial slope K, cohesive strength t_u (peak) and fracture energy G_f (area).

The effect of five variables was studied: interface cohesive strength, fiber cohesive strength, interface fracture energy, fiber fracture energy and fiber volume fraction (or fiber diameter for the single fiber simulations). The first four cohesive element properties were studied relative to the matrix cohesive element properties and the material properties were kept constant. Single fiber numerical experiments were performed to test the above method, check mesh convergence and to get a first insight in the effect of the five variables. From these simulations the required mesh density was obtained and the scripts were optimised for the multiple fiber numerical experiments.

Before the multiple fiber numerical experiments could be performed the dimensions of the Microstructural Volume Element (MVE) had to be determined at which point it can be considered representative for the larger structure, i.e. a RVE. For this a convergence study was performed by comparing the ETSL of different MVE dimensions. Due to the effects of artificial compliance two alternative approaches were studied and from the first alternative approach it was concluded that for a dimension of 75×75 µm the MVE can be considered a RVE. The other two approaches did not verify this and the convergence study was performed for fixed properties and a single mixed load case. Therefore, it was considered that these dimensions might not be representative for the total envelope of the numerical experiments.

The multiple fiber numerical experiments were performed for six load cases: uni-axial extension, pure shear, simple shear and three mixed loadings. An average ETSL was obtained by averaging four different realisations, i.e. fiber distributions. The results were comparable with the single fiber simulations. It was concluded that the pure shear load case results were spurious and therefore it was replaced with the simple shear load case. The bilinear TSL parameters from five load cases: uni-axial extension (mode I), simple shear (mode II) and three mixed load cases were used for the correlation.

The correlation and curve fitting of the results consisted of two steps. First, the mode I and II properties were fitted using the uni-axial extension and simple shear load case. Secondly, these parameters were fitted, by using one mixed load case, as a function of the mode mixity β. For the first step a multiple variable least squares fit was employed that provides the mode I and II initial slope, cohesive strength and fracture energy as a function of the five variables. For the mode mixity fitting of the initial slope an elliptical relation between the mode I and II properties was proposed. The curve fitting of the cohesive strength used a power relation between the mode I and II damage initiation at separation. For the mode mixity fitting of the fracture energy a Benzeggagh-Kenane (BK) power relation was used because this could easily be implemented in ABAQUS. As a result of the two step correlation the three bilinear TSL parameters could be defined as a function of the five variables x_i and the mode mixity β.

In the end the implementation of the macroscopic failure criterion in ABAQUS, in terms of a bilinear TSL, was shown and verified for a single cohesive element. The damage initiation, i.e. the combination of initial slope and cohesive strength, showed a perfect fit between the response of the single cohesive element and the macroscopic failure criterion. However, the fracture energy was underestimated for a mixed load cases and required further investigation. Along with some issues, further development and extension of the proposed method is required to have a functional and generalised failure criterion.

Acknowledgements

As a start I would like to thank my supervisor at the Delft University of Technology (DUT), Dr. Sergio Turteltaub, for the useful feedback an guidance during my masters thesis. Although the inspiring meetings were usually quite extensive I enjoyed a great amount of the discussions. Secondly, I would like to express my gratitude towards my supervisor at Airbus Defence and Space Netherlands (ADSN) who made an effortless collaboration between the DUT and ADSN possible. In addition I would like to thank my colleagues at ADSN, in particular Stanley Wong for the many tips about PYTHON in combination with ABAQUS. Last but not least I would like to thank my girlfriend for her excellent proof reading skills and the support during the last ten months.

Delft, University of Technology
January 27, 2016

N. van Hoorn

Table of Contents

Nomenclature

List of Acronyms

1D	One-Dimensional
2D	Two-Dimensional
3D	Three-Dimensional
ADSN	Airbus Defence and Space Netherlands
BC	Boundary Conditions
BVP	Boundary Value Problem
CFRP	Carbon-Fiber Reinforced Plastic
CTOD	Crack-Tip-Opening Displacement
CZM	Cohesive Zone Model
DOF	Degrees of Freedom
DUT	Delft University of Technology
EPFM	Elastic Plastic Fracture Mechanics
ETSL	Effective Traction-Separation Law
FE	Finite Element
FEA	Finite Element Analysis
FEM	Finite Element Method
LC	Load Case
LEFM	Linear Elastic Fracture Mechanics
LPF	Load Proportionality Factor

MVE	Microstructural Volume Element
PBC	Periodic Boundary Conditions
PBS	Portable Batch System
TSL	Traction-Separation Law
RVE	Representative Volume Element
SIF	Stress Intensity Factor
UD	Uni-Directional
XFEM	eXtended Finite Element Method

List of Symbols

β	Mode mixity
$\boldsymbol{\sigma}$	Stress tensor
$\boldsymbol{\varepsilon_L}$	Local strain tensor
$\boldsymbol{\varepsilon}$	Strain tensor
$\boldsymbol{n}$	Crack opening normal
δ	Crack opening / separation
δ_i	Separation at damage initiation
γ	Energy density
μ	Shear modulus
ν	Poisson's ratio
Π	Potential energy
σ	Stress
τ	Traction
θ	Crack angle
ε	Strain
A	Area
a	Crack length
d_F	Fiber diameter
E	Young's modulus
G	Strain energy release rate
G_f	Fracture energy
h	Height
J	J contour integral
K	Initial slope TSL
n	Number of data points
t_u	Cohesive strength
V_f	Fiber volume fraction
w	Width
F	Force
S	Sum of squared residuals

Chapter 1

Introduction

Throughout history, fracture of structures has always been present and this phenomena has not always been well understood. With the increasing complexity of structures, as in the aerospace sector, the demand of understanding fracture increased rapidly over the last several decades. Nowadays, fracture mechanics has grown to one of the most important disciplines within engineering. By understanding why and how structures fail one can employ a damage tolerant design philosophy. The understanding of fracture in isotropic materials, e.g. metals, is already studied extensively by engineers and scientists like Inglis, Griffith, Irwin and Rice [1, 2, 3, 4]. As a result of their work a range of models, criteria or theories are available to predict the fracture mechanisms [5, 6]. Even for anisotropic materials like fiber-reinforced composites, which have complex failure mechanisms, models are available [7, 8, 9, 10]. With the increase in computational power, numerical models became more and more capable, which supported the development and application of fracture mechanics technology [6]. Examples are the development of the Cohesive Zone Model (CZM) [11, 12, 13, 14] and later the eXtended Finite Element Method (XFEM) [15, 16]. In order to relate the fracture mechanisms on a microscopic scale to the macroscopic behaviour of the structure multiscale models became of interest around the year 2000.

Over the past decades an astounding amount of research has been devoted to the development of fracture models and computational methods in this field. However, there is still a gap to fill in the area of failure theories and criteria. From this gap in knowledge the thesis objective was formulated as presented on the next page.

The thesis objective is to develop a new macroscopic failure criterion for fiber-reinforced composites that incorporates distinct fracture mechanisms occurring at a microscopic level. The microscopic information will be integrated into the macroscopic failure criterion through multiscale finite element simulations on representative volume elements.

In order to achieve this objective in the scope of a masters thesis a few restrictions were established. First, this masters thesis presents a proof of concept study. Further development and modifications are required for a fully functioning and verified failure criterion. Secondly, the CZM approach with the use of cohesive elements was chosen over the XFEM for the following reasons. It is relatively simple to implement in the existing Finite Element Method (FEM) and it allows for multiple crack branching and coalescence. The XFEM seems promising but is relatively new and still in development to extend its capabilities. Thirdly, it was chosen to limit this research to a Two-Dimensional (2D) framework with a Uni-Directional (UD) Carbon-Fiber Reinforced Plastic (CFRP) material loaded transverse to the fibers. Further extension to a Three-Dimensional (3D) framework is preferred but within the time available not achievable. Research similar to the above is reported in [17, 18, 19] but this work is extended in this thesis to multiple load cases and correlation of the data into a failure criterion.

The thesis is structured as follows. A literature review in Chapter 2 will present a clear overview of subjects that contribute to the thesis objective along with the current understanding and the gap in knowledge. In Chapter 3 the FEM will be introduced along with the numerical implementation of the cohesive elements. The main methodology and the setup of the numerical experiments will be discussed in Chapter 4. The first step in achieving the thesis objective is to perform numerical experiments on a single fiber Microstructural Volume Element (MVE), of which the methodology and results are presented in Chapter 5. In order to extend this to a multiple fiber framework the sample size should be determined, see Chapter 6 for the approach and results. The methodology and results of the numerical experiments on the multiple fiber Representative Volume Element (RVE) will be given in Chapter 7. These results are then correlated into a failure criterion that describes the fracture behaviour at a macroscopic level, as will be explained in Chapter 8. In the end the conclusions and recommendations will be presented in Chapter 9.

Chapter 2

Literature Review

In this chapter a literature review is presented on subjects that will contribute to achieving the research objective. A clear overview of these subjects is given along with the current understanding and the gap in knowledge. As a start, in Section 2.1, some fundamental concepts in fracture mechanics are discussed. In Section 2.2 the cohesive zone approach is presented as the central method that will be used along the Finite Element Method (FEM) for this thesis. Another crucial aspect, the multiscale approach in fracture mechanics, is reviewed in Section 2.3.

2.1 Basics of Fracture Mechanics

The field of fracture mechanics has become one of the most important divisions in engineering. As a result, fracture mechanics as a whole is quite broad. In this section some main concepts, parameters and definitions are reviewed along with a few historic highlights.

2.1.1 Linear Elastic and Elastic Plastic Fracture Mechanics

The field of fracture mechanics was given a boost by the pioneering work of Griffith [2] in Linear Elastic Fracture Mechanics (LEFM) during World War I. Griffith based his work on the research Inglis [1] did a few years earlier. The main goal of both Griffith and Inglis was to understand and predict the fracture behaviour of structures. For example, Inglis defined the stress concentration factor (k_t) of an elliptical hole as follows.

$$k_t = \frac{\sigma_A}{\sigma_\infty} = 1 + \frac{2a}{b} \tag{2.1.1}$$

In this equation σ_∞ is the far field stress, σ_A is the stress at the tip of the semi-major axis a and b is the semi-minor axis of the elliptical hole. The work of Inglis is limited as mathematical difficulties arose when dealing with sharp cracks (high a/b), in the limit the stresses would go to infinity at the crack tip. To solve this non-physical behaviour Griffith used the energy balance in the structure. Although his work was neglected until the 1950's it is considered as one of the most famous developments in material science. Griffiths work has been generalised to the Griffith's failure criterion, i.e. the stress required to create a new surface (σ_f).

$$\sigma_f = \sqrt{\frac{2\gamma_s E}{\pi a}} \tag{2.1.2}$$

for plane stress and,

$$\sigma_f = \sqrt{\frac{2\gamma_s E}{(1-\nu^2)\pi a}} \tag{2.1.3}$$

for plane strain. In these equations, E is the materials Young's Modulus, a is the crack length and γ_s is the surface energy density. Griffith's criterion agrees with experimental observations if brittle materials, e.g. glass, are considered. For materials that experience ductility, e.g. metals, the surface energy according to Griffith's criterion is too high. Both Irwin [3] and Orowan [20] independently modified Griffith's criterion to account for the energy dissipation in plastic flow, see Equation 2.1.4. The *Critical energy release rate* has been defined as two times the surface energy density plus the plastic energy density (γ_p), i.e. $G_c = 2 \cdot (\gamma_s + \gamma_p)$.

$$\sigma_f = \sqrt{\frac{G_f E}{\pi a}} \quad \text{(plane stress)} \tag{2.1.4}$$

As a result of Irwins work an important parameter in fracture mechanics has been defined, the strain energy release rate, G, which is the rate of change in potential energy (Π) with respect to the crack area (A).

$$G = -\frac{d\Pi}{dA} \tag{2.1.5}$$

In the case the strain energy release rate reaches a critical value (G_f) the crack extends. This critical value is generally referred to as the *fracture energy* or *fracture toughness*.

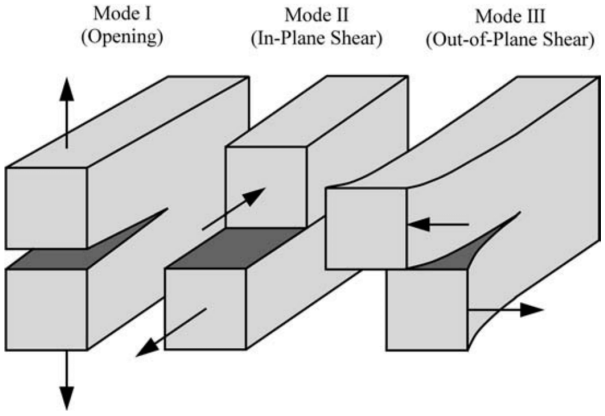

Figure 2.1.1: Three loading modes for fracture [6].

An alternative approach to the strain energy release rate is the stress intensity approach introduced by Westergaard and further developed by Irwin, Sneddon and Williams [6]. Their work led to definitions of the Stress Intensity Factor (SIF), i.e. K_I, K_{II} and K_{III} for mode I, II and III respectively. These three loading modes are given in Figure 2.1.1. For linear elastic materials the stresses in the field ahead of the crack tip can be written in terms of the SIF as in Equation 2.1.6 for mode I. Equal definitions can be written for mode II and III. The function $f_{ij}(\theta)$ is a trigonometric function depending on the stress σ_{ij} and the loading mode.

$$\lim_{x\to 0} \sigma_{ij}^{(I)} = \frac{K_{(I)}}{\sqrt{2\pi r}} f_{ij}^{(I)}(\theta) \tag{2.1.6}$$

The SIF can be used to determine the stresses around cracks and the fatigue properties. In addition the SIF can be related to the strain energy release rate, if all three modes are present this can be related as in Equation 2.1.7 [6]. Here, $E^{'}$ is either in plane stress or plane strain and μ is the shear modulus.

$$G = \frac{K_I^2}{E^{'}} + \frac{K_{II}^2}{E^{'}} + \frac{K_{III}^2}{2\mu} \tag{2.1.7}$$

In contrast to the definitions above that correspond to LEFM, the field of Elastic Plastic Fracture Mechanics (EPFM) tries to solve problems with plasticity around the crack tip. For instance, if the dimensions of a plastic region with non-linear material deformation is small compared to the dimensions of the structure the fracture can be considered brittle and LEFM is valid. According to Rabczuk [21] the size of the fracture process zone should be at least two orders smaller than the critical dimension of the structure. If this is not the case, EPFM methods should be applied. One important parameter in EPFM, introduced by Wells [22], is the Crack-Tip-Opening Displacement (CTOD). Note that there are different definitions of the CTOD, of which the most common is presented below.

$$\text{CTOD} = \frac{4}{\pi}\frac{G}{\sigma_{YS}} \tag{2.1.8}$$

In addition to the CTOD, Rice [23] introduced a second important parameter in EPFM, the *J contour integral*. The resulting value J is equal to the energy release rate in a nonlinear elastic body that contains a crack [6]. For nonlinear elastic materials J is equal to G in Equation 2.1.5 and this value can be evaluated at an arbitrary path Γ around the crack tip by the following integral [24]:

$$J = \int_{\Gamma}\left(w dy - \tau_i \frac{\partial u_i}{\partial x} ds\right) \tag{2.1.9}$$

where,

$$w = \int_0^{\varepsilon_{ij}} \sigma_{ij} d\varepsilon_{ij} \tag{2.1.10}$$

τ_i is the traction vector and u_i the displacement vector. J can be related to the CTOD by the equation below [6]. Here m is a dimensionless constant.

$$J = m\sigma_{YS} \cdot \text{CTOD} \tag{2.1.11}$$

2.1.2 Failure in Composite Materials

As the focus of this thesis is on composite materials and to be specific, fracture in Carbon-Fiber Reinforced Plastic (CFRP), one ought to know the failure modes and criteria of this material. Within a CFRP composite the following failure modes can occur,

- Matrix cracking
- Delamination
- Fiber/matrix debonding
- Fiber breakage

The matrix material can show brittle matrix cracking, i.e. the formation of microcracks, which is an intralaminar fracture mechanism. The coalescence of these cracks can ultimately lead to larger cracks and delamination. Delamination is one of the most common failure modes in composite materials and can be described as interlaminar debonding or interface cracking. Fiber/matrix debonding is an interesting failure mode for a microscopic model. This failure mode describes the adhesive interface failure of the fiber/matrix interface. The last failure

mode, which is probably the last failure mode that will occur is fiber breakage or fiber pull-out. This failure criterion describes complete failure of one or multiple fibers [24].

At which point the material fails depends on several factors, i.e. laminate layup and loading conditions. To predict failure several criteria have been developed. The most simple failure criteria assume that a ply can be considered homogeneous. To obtain detailed failure criteria one can look at the micromechanics, as has been done by Aboudi [25] who proposed a micromechanical failure criteria for Uni-Directional (UD) fiber composites. For failure on a macroscopic scale one generally refers to the homogeneous failure criteria. With these criteria it is assumed that for an UD ply the strength values mentioned below can describe the failure. In most cases these values are reduced to account for environmental effects and material scatter, which results in *material allowables* [26].

- X_t: Fiber tension strength
- X_c: Fiber compression strength
- Y_t: Matrix tension strength
- Y_c: Matrix compression strength
- S: Shear strength

The *maximum stress failure theory* compares the principal stresses (i.e. $\sigma_x, \sigma_y, \tau_{xy}$) with their corresponding (reduced) strengths mentioned above. If a value exceeds the strength the ply fails. The same concept holds for the *maximum strain failure theory* where the principal strains are compared to the allowable strains. To describe the interaction between principal stresses (or strains) Hill [27] proposed a combined failure theory.

$$F_x\sigma_x^2 + F_y\sigma_y^2 + F_{xy}\sigma_x\sigma_y + F_s\tau_{xy}^2 = 1 \tag{2.1.12}$$

Tsai modified Hill's failure criterion by writing it in terms of the material strengths X, Y and S (no difference in tension or compression), which lead to the Tsai-Hill failure criterion [26].

$$\frac{\sigma_x^2}{X^2} - \frac{\sigma_x\sigma_y}{X^2} + \frac{\sigma_y^2}{Y^2} + \frac{\tau_{xy}^2}{S^2} = 1 \tag{2.1.13}$$

In order to generalise the Tsai-Hill criteria, Tsai and Wu [7] added curve fitting to the Tsai-Hill criterion, which resulted in the Tsai-Wu failure criterion.

$$\frac{\sigma_x^2}{X^tX^c} + \frac{\sigma_y^2}{Y^tY^c} - \sqrt{\frac{1}{X^tX^c}\frac{1}{Y^tY^c}}\sigma_x\sigma_y + \left(\frac{1}{X^t} - \frac{1}{X^c}\right)\sigma_x + \left(\frac{1}{Y^t} - \frac{1}{Y^c}\right)\sigma_y + \frac{\tau_{xy}^2}{S^2} = 1 \tag{2.1.14}$$

There is still an ongoing discussion on which failure criteria is best and several people tried to come up with new failure criteria, for example, the Hashin-Rotem failure criteria [8] which

distinguishes between fiber or matrix failure. More recently the *LaRC03 failure criteria* were developed by Camanho and Dávila [10], which combine six separate failure criteria that describe fiber and matrix failure without the need of curve fitting. According to Dávila *et al.* this method shows a significant improvement compared to other failure criteria. The only problem with this criteria is that it requires several if statements that may complicate the failure assessment. There is a need for a simple and effective failure criterion, which is the objective of this thesis.

2.2 Cohesive Zone Approach in Finite Element Analysis

One of the models in solving fracture problems is the Cohesive Zone Model (CZM). In this section the CZM is reviewed with the focus on the numerical aspect. Two popular methods to numerically solve a CZM problem are the eXtended Finite Element Method (XFEM) and the interelement-separation method. However, for this thesis the focus is on the interelement-separation method. This method allows for multiple crack nucleation, branching and coalescence. It is true that the XFEM has advantages over the interelement-separation method, which will be mentioned in this section of the literature review.

2.2.1 Cohesive Zone Model

The CZM has been introduced to cope with the stress singularities in LEFM and to approximate nonlinear material separations. These stress singularities especially become a problem if the size of the cohesive zone becomes larger than the assumptions for LEFM, e.g. if the length scale l_{cz} (see Section 2.2.4) is larger than any characteristic length in the problem the CZM are necessary [28].

The first contributions to the CZM were made by Barenblatt [5] for brittle materials and by Dugdale [29] for yielding at the crack tip. A CZM describes the mechanisms in the damage zone in front of the crack tip, called the cohesive zone[1]. In the framework of the FEM a CZM can be implemented using cohesive elements. These elements are inserted between two bulk elements and describe the connection between the two elements. Crack opening is simulated by separation of the two connected elements. The amount of stress that can be transferred between the two elements is gradually reduced by means of a cohesive law (i.e. Traction-Separation Law (TSL)), Figure 2.2.2 shows some examples. For a Two-Dimensional (2D) element mesh the interface elements are 2D elements with zero-thickness and the thickness increases when separation occurs.

[1] Within the cohesive zone it is assumed that microcracks (or voids) are formed which results in stiffness degradation, see the top right of Figure 2.2.1.

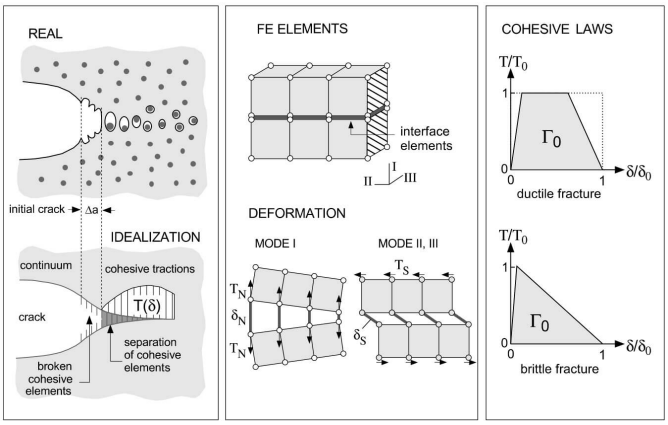

Figure 2.2.1: Basic concept of the CZM representing interface elements and cohesive laws [30].

A CZM is able to model multiple cracks, crack nucleation, crack bifurcation and complex fracture mechanisms [30, 31]. Other advantages include the easy incorporation in the FEM, its robustness and solving the model in parallel is straightforward [32]. Disadvantage include its mesh dependency [33], as will be discussed later on.

2.2.2 Intrinsic vs. Extrinsic Implementation

A CZM can be implemented in two different ways, *intrinsic* and *extrinsic*, each with its advantages and disadvantages. A few examples of an intrinsic implementation have been given in [11, 13, 14, 34, 12, 35, 36] and are characterised by adding the cohesive elements to the mesh *prior* to the simulation. An intrinsic TSL starts at zero traction, gradually increases until a maximum traction (or onset of damage point) and decrease with a certain relation to a zero traction at the maximum separation (softening), e.g. the TSL at the right of Figure 2.2.1. The advantage of an intrinsic implementation is that it is relatively easy and it works successful when the crack path is defined, for instance along interfaces [37]. A disadvantage is that the presence of interface elements in a large part of the model can reduce the stiffness of the model significantly. This is due to the initial slope (elastic part) of the TSL that results in an artificial compliance. Artificial compliance will be discussed in Section 4.2. In addition the number of Degrees of Freedom (DOF) is increased significantly by adding interface elements [37, 32, 33]. One solution to deal with the artificial compliance is to increase the so called dummy stiffness, i.e. the initial slope of the TSL. However, this brings along other issues with stable time steps among other aspects [36, 31, 32].

In contrast to an intrinsic implementation, the extrinsic approach adds interface elements adaptively to the mesh at the locations where failure occurs [38, 37, 32]. An extrinsic implementation eliminates the issues of the intrinsic implementation by initiating separation only when a failure criterion (e.g. based on maximum cohesive strength) is met. At this point the interface elements are added adaptively to the mesh, see for example in the article from

Park *et al.* [39]. Once separation is initiated the cohesive traction decreases as the separation increases, see the next section. A disadvantage of an extrinsic implementation is that an additional failure criteria is required and the adaptive implementation is more complex compared to an intrinsic approach. Next to this, a sophisticated data structure is required to store the Finite Element (FE) discretization as the mesh topology is changing over time [37, 32]. An example of such a data structure (TopS) is given in [40] and was applied by Zhang *et al.* [37]. Due to the change in mesh topology it is also difficult to solve the model in parallel [41] and there is a time discontinuity in the stress history [37]. In addition, numerical difficulties can occur when the material is elastically unloaded at the start of separation [42, 21].

2.2.3 Traction-Separation Laws

In this section an overview of the available TSLs will be given. A TSL is the cohesive law describing the non-linear separation mechanism between two elements. Some general examples are given in Figure 2.2.2. The initially elastic model, or intrinsic model, can be seen in Figure 2.2.2e. This TSL is linear and examples are given in [17, 19]. The other models can be considered as initially rigid, or extrinsic models, for example the Dugdale model [29] in Figure 2.2.2a. The decreasing slope models softening due to void growth and coalescence of cracks [30]. The case where the cohesive traction is increasing for an increasing crack opening (Figure 2.2.2f) is considered not feasible as the elements will have the tendency to close for an increasing stress.

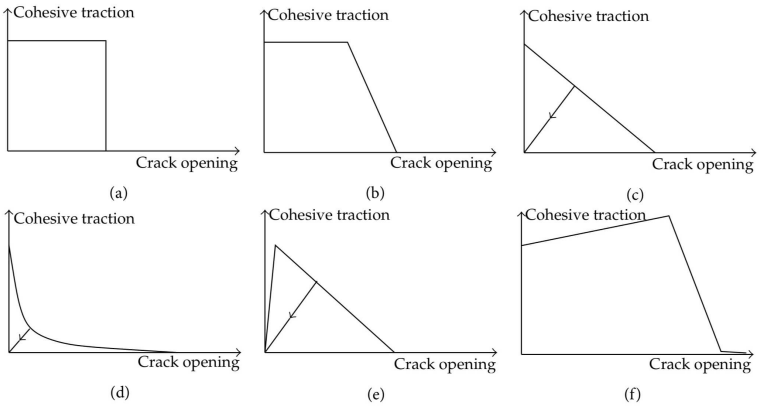

Figure 2.2.2: Examples of TSLs [21].

According to [30, 43, 17] the exact form of the TSL has only minor influence on the fracture characteristics. An advantage of the CZM is that only two parameters that describe a TSL are relevant for the fracture characteristics: e.g. the fracture energy and a cohesive strength [28, 17]. The fracture energy is equal to the area of the TSL and describes the energy that is required to form a new surface, see the equation below where τ_c is the cohesive traction and δ the crack opening or separation. The maximum crack opening δ_{max} is defined as the characteristic opening that results in a fully damaged element [30, 44].

$$G_f = \int_0^{\delta_{max}} \tau_c(\delta)\, d\delta \tag{2.2.1}$$

The form of the TSL describes the difference between ductile and brittle fracture. For example, (Quasi-)brittle fracture is usually described by a TSL as given in [11, 13, 12, 17, 19] and ductile fracture by a trapezoidal TSL [30, 45]. In general two categories, with sub-categories, of TSLs can be distinguished [31].

- One-Dimensional (1D) effective displacement TSL
  - Cubic polynomial [13]
  - Trapezoidal [34]
  - Smoothed trapezoidal [46]
  - Exponential [36]
  - Linear softening [38, 35]
  - Bi-linear softening
- General potential-based TSL
  - Polynomials [11, 47]
  - Based on universal binding energy [48, 49, 50]
  - Park-Paulino-Roesler polynomial based [51]

1D Effective Displacement Traction Separation Laws

1D effective displacement TSLs are represented by one effective displacement (separation) and traction. Tvergaard [13] proposed one of the first effective displacement TSLs in the form of a cubic polynomial (Figure 2.2.3a), which is based on the original TSL from Needleman [11] that only contained normal separation. This effective traction can be modified to represent other shapes of the TSL. A trapezoidal TSL has been proposed by Tvergaard and Hutchingson [34] (Figure 2.2.3b). This model is unable to account for different fracture energies in the normal and tangential direction [31]. In order to provide continuity in the derivatives the trapezoidal model of Tvergaard and Hutchingson has been modified by Scheider and Brocks [46], see Figure 2.2.3c. An exponential TSL as in Figure 2.2.3d is given by Ortiz and Pandolfi [36]. This model was modified by Camacho and Ortiz [38] to an extrinsic linear softening TSL by excluding the initial elastic slope of the TSL. According to Ortiz and Pandolfi [36] this extrinsic version is preferred as this deals with the stable time step difficulties [31]. A general application was published by Zhang *et al.* [37]. An intrinsic linear softening TSL proposed by Geubelle and Baylor [35], as in Figure 2.2.3e, which is a special case of the cubic polynomial TSL. Applications of the linear softening TSL can be found in [17, 19].

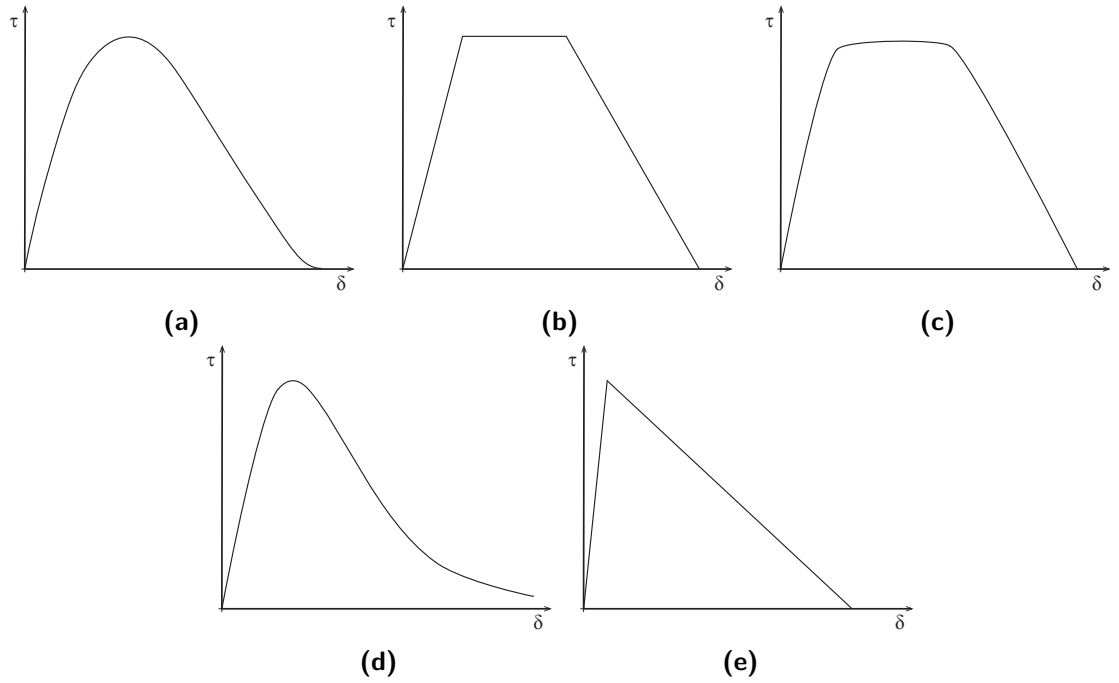

Figure 2.2.3: Examples of 1D effective displacement TSLs [31]: (a) cubic polynomial TSL proposed by Tvergaard [13] (b) trapezoidal TSL proposed by Tvergaard and Hutchingson [34] (c) modified trapezoidal TSL by Scheider and Brocks [46] (d) exponential TSL by Ortiz and Pandolfi [36] (e) linear softening TSL proposed by Geubelle and Baylor [35].

Overall there are limitations to the 1D effective displacement TSLs, of which the main limitation is that they represent only the fracture energy of one mode. This makes these models limited for mixed-mode calculations if the fracture energy in mode I is different than in mode II. In addition these models are unable to distinguish between positive or negative separation [31].

General Potential Based Traction Separation Laws

To overcome some of the limitations of 1D effective displacement TSLs the general potential-based TSLs have been introduced. These models are based on a potential that is a function of both the separation in normal direction and in tangential direction instead of an effective separation. A cubic-linear version of a potential-based TSL was introduced by Needleman [11]. The problem of this TSL is that it has issues with large shear, a large shear separation weakens the material behaviour [48, 31]. Therefore the model was revised by Freed and Banks-Sills [47], with initial applications for a bi-material interface. The difference with the model of Needleman that no tangential softening occurs, i.e. the traction in tangential direction can go to infinity [31].

In addition to the two models mentioned above models were introduced that are based on the universal binding energy between particles. A exponential-periodic version is given by Needleman [48] to cope with the large shear displacement issues of the above mentioned models. The problem is that only mode I fracture parameters are used, it does not include mode II parameters [31]. Therefore it was generalised by Beltz and Rice [49] to account for shear. The only difficulty using this model is that an additional length scale parameter is required that is hard to obtain [31]. In order to improve the model, Xu and Needleman [50] used exponential relations (i.e. Figure 2.2.2d) for both normal and shear traction, and therefore can represent fracture energy and cohesive strength in mode I and II.

The last mentioned model has been used extensively, but there are still Boundary Conditions (BC) related limitations, stiffness reduction due to the initial linear elastic part and a unrealistic finite crack opening [31]. Recently a new model, the general unified potential-based model or Park-Paulino-Roesler model, has been developed to tackle the problems of the former potential-based TSLs [51]. This model uses four fracture parameters for each mode: fracture energy, cohesive strength, shape parameters and an initial slope. The shape parameters are used because according to Park and Paulino [31] the shape has a significant influence on the fracture results, which is in direct contradiction with the statement made by Li *et al.* [43]. There are still limitations to the Park-Paulino-Roesler model, e.g. the four parameters are difficult to obtain, especially for shearing [51, 31].

To conclude, the choice of TSL should be made with caution, especially with respect to mode-mixity. It is also worth to mention that the CZM is a phenomenological approach so the choice of TSL is free as the correlation between the TSL and the results is unambiguous [30].

2.2.4 Numerical Implementation and Considerations

The type of CZM and the corresponding TSLs were discussed above and require a specific implementation in numerical software, like ABAQUS .

At first the *smeared* cohesive elements were introduced. With smeared cohesive element the interface between elements is represented by a thin film. These thin elements are not suitable to study interfacial crack growth as the thin elements have a high aspect ratio resulting in numerical difficulties, especially with convergence [28]. To overcome these problems *zero-thickness* elements have been introduced that are more suitable, these elements are nowadays known as cohesive elements. In [52, 32] the cohesive elements are implemented in ABAQUS and in addition an open source program [53] is available that can implement the interface elements in an existing mesh.

One of the drawbacks of the intrinsic methods is the mesh dependency [28, 33], i.e. a crack can only propagate along the element boundaries which might not be the preferred direction. This issue is minimised when the preferred crack direction is known, but up until now

the mesh dependency is still an active area of research. Rimoli and Rojas [33] performed an analysis of several meshing strategies. They compared a random mesh with a so called 4K mesh. For a structured mesh certain paths are preferred and the paths in other directions are less favourable. This is called *mesh-induced anisotropy*. In addition, the energy released by forming cracks is higher with a discrete mesh compared to a continuum, this effect is called the *mesh-induced toughness* [33].

For a random triangular mesh the mesh-induced anisotropy effect is smaller compared to a 4K mesh but the mesh-induced toughness effect is larger (due to a higher mean). Rimoli and Rojas proposed a compromise, i.e. a conjugate-directions mesh which is a basic k-mesh with barycentric subdivision. This mesh has a smaller relative error and a less mesh dependent crack path compared to a conventional 4K mesh. The mesh dependency is reduced but is still there.

To remove the before mentioned limitations of the intrinsic implementation of a CZM, extrinsic implementations were introduced as in [32, 38, 37]. In the framework of the extrinsic implementation, Park *et al.* [39] introduced an adaptive mesh refinement and coarsening scheme for a 4K mesh. This computational method is interesting as it reduces the computational cost significantly and removes the limitations of the intrinsic approach.

An important parameter within a CZM is the *cohesive zone length*. According to Turon *et al.* several definitions of the cohesive zone length are available and in general have the form indicated below where M is a certain coefficient [54]. In the end the cohesive zone length is a function of the Young's Modulus (E), fracture energy (G_f) and cohesive strength (t_u).

$$l_{cz} = ME\frac{G_f}{t_u^2} \tag{2.2.2}$$

2.3 Multiscale Approach for Fracture

Novel engineering materials like fiber-reinforced composites have an increasing complexity, which in turn lead to a structural assessment on different length scales. Therefore, to study the fracture mechanisms of a large complex structure on a macroscopic scale, the behaviour on a microscopic scale should be considered to get an appropriate representation.

2.3.1 Types of Multiscale Modelling

It can be said that a Finite Element Analysis (FEA) of composites requires at least a mesh as fine as the size of the fiber [55]. For instance, the microcracks in an epoxy or fiber-matrix

debonding on a microscopic scale can eventually result in a damage zone that on a macroscopic scale appears as a crack. One can model the full structure in detail on a single scale (brute-force) but this is computational expensive [56]. An alternative is to retrieve information on two length scales to give detailed information where needed. The coupling of the information at different length scales is the main goal of multiscale methods. Length scales range from nanoscopic (atomistic), microscopic (single fiber), mesoscopic (multiple fibers), macroscopic (laminate) to the full structure.

There are different methods available to couple the length scales and the fundamentals of these methods are in most cases for structures without damage, i.e. without discontinuities like cracks, delaminations etc. In general one can distinguish between the following three categories of multiscale methods:

- Concurrent methods
- Semi-concurrent methods
- Hierarchical or homogenisation based methods

Each of these methods have their distinct coupling techniques as can be seen in Figure 2.3.1. The hierarchical methods, as illustrated in Figure 2.3.1c, only exchange information from the fine scale to the coarse scale and are based on homogenisation methods. Homogenisation methods can be considered as *numerical homogenisation* as in [57, 17, 19], i.e. based on a unit cell. On the other hand there is *computational homogenisation* as in [58, 59, 60, 61, 62, 63, 64]. The latter seems promising according to the recent developments and will be discussed in more detail in Section 2.3.4.

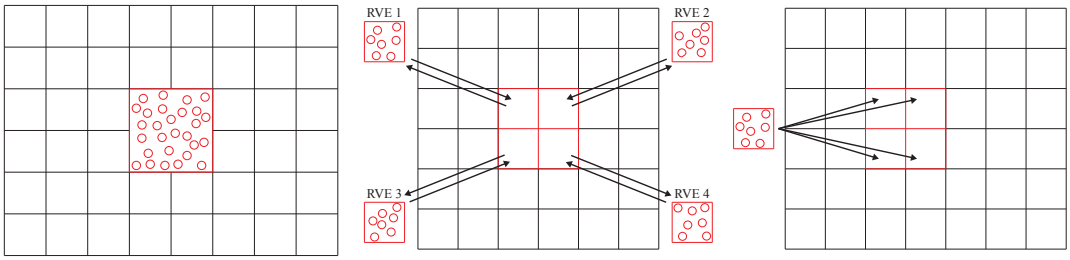

Figure 2.3.1: Categories of multiscale methods; (a) concurrent, (b) semi-concurrent and (c) hierarchical. The coarse scale is indicated in black and the fine scale in red.

For a fully concurrent method the information on fine- and coarse scale is simulated on both scales simultaneously. A fine scale simulation is for instance needed at locations with stress concentrations, discontinuities or other domains of interest. The coupling of the two scales is performed by linking the two scales at their interface. Examples can be found in [65, 66, 67, 68, 69] and applications to fracture originated later on as in [56, 70, 71]. A review of concurrent multiscale methods will be given in Section 2.3.2.

In contrast to concurrent multiscale methods, the semi-concurrent methods exchange the information from fine- to coarse scale and vice versa, as can be seen in Figure 2.3.3. The simulations at both scales is done separately, i.e. the coarse scale is localised to fine scale constitutive equations that can be solved and through homogenisation be translated back to the coarse scale. Semi-concurrent methods are generally more flexible compared to concurrent methods and can easily be solved in parallel [21]. One of the most used methods is FE^2 as introduced by Feyel and Chaboche [55] and extensions for fracture are reported in [58, 57, 72]. It should be noted that semi-concurrent methods like FE^2 are based on unit cell methods which can be classified as numerical homogenisation methods and thus show overlap with hierarchical multiscale methods.

Up until now there are some challenges regarding multiscale modelling, especially when discontinuities like cracks are concerned. There is still the need of an efficient method to transfer information between the length scales [21]. The most effective methods that have recently been published are the continuous-discontinuous computational homogenisation methods as in [62, 63, 64] but are still computationally expensive.

2.3.2 Concurrent Multiscale Methods

Concurrent multiscale methods as in Figure 2.3.1a analyse both scales simultaneously. The first concurrent multiscale methods originated for intact materials, especially in the field of atomistic modelling. Atomistic modelling is considered as the exact representation of the material behaviour. A full atomistic model is generally not computationally feasible with respect to computational cost. Examples of atomistic models include the quasi-continuum method and MAAD (Macroscopic, Atomistic, *Ab initio* Dynamics). The quasi-continuum method is a direct coupling method where the FE mesh aligns with the atoms, i.e. an atomistic-continuum coupling [68]. Due to the fact that there exists a domain that intersects the coarse and fine domain, concurrent methods are seen as a so called "handshake" methods.

In order to describe the undamaged domain by continuum models and the discontinuities by detailed models several methods were developed that are in line with the XFEM [56, 70, 71]. Loehnert and Belytschko [56] developed a multiscale project method for macro/micro-crack simulations. They considered two scales, a fine scale (l_1) and a coarse scale (l_0) where $l_0 \gg l_1$. On the coarse scale only cracks that are longer than a typical FE size are explicitly considered whereas in the fine scale both microcracks and coarse scale discontinuities are considered [56]. Conclusions of Loehnert and Belytschko were that the coarse scale mesh density had almost no influence on the SIF at the macro crack. The fine mesh density has more influence but between the densest and coarsest fine scale mesh only a 5% difference was observed. The fine scale domain size has only little (1%) influence on the accuracy of the SIF. In general the proposed method is effective when there is a significant separation of scales [56]. Guidault *et al.* [70] proposed a similar method based on a mixed *domain decomposition method*, i.e. there consist multiple domains with different length scales. Finer length scale domains are

obtained by refining the mesh in vicinity of the crack. The XFEM is required to describe the geometry of the crack independently of the mesh (on both scales) and the mixed domain coupling method provides coupling between the two scales.

2.3.3 Semi-concurrent Multiscale Methods

Semi-concurrent multiscale methods as in Figure 2.3.1b exchange data from the fine to coarse scale and vice versa. In contrast to concurrent multiscale methods it is not required to solve both scales simultaneously as the scales are decoupled, providing more flexibility. This avoids difficulties with the rapid transition from fine to coarse scale elements that result in ill-conditioned equilibrium equations and spurious reflections of the interface [68]. Compared to concurrent methods the reduction in computational effort is not significant [55, 68].

One method that is widely used as a basis for semi-concurrent multiscale methods is the FE^2 method proposed by Feyel and Chaboche [55], where the superscript "2" stands for the number of scales. For fiber-reinforced composites in most cases the microscopic and macroscopic scale are employed. Before the development of the FE^2 method phenomenological models were used. Phenomenological models define the constitutive equations based on experimental observations. The transition from microscopic to macroscopic scale is done using complex averaging processes to the constitutive equations [55]. This method is sufficient for materials with a random microstructure (metals) but not in the case of fiber-reinforced composites.

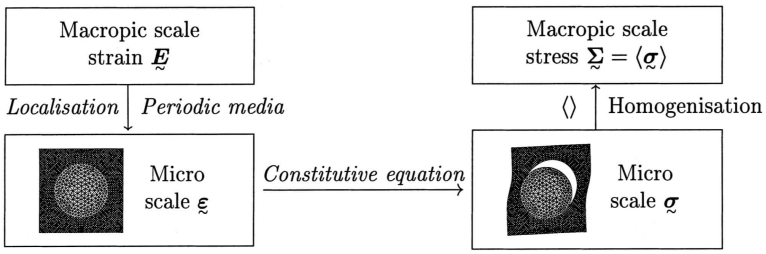

Figure 2.3.2: Schematic representation of the FE^2 methodology [55].

With the FE^2 method the constitutive equations are only defined on the microscopic scale and through homogenisation and localisation the macroscopic stresses and strains are computed, see Figure 2.3.2. The scale transition is realised by using the *periodic homogenisation theory* that describes a volume element by an infinite number of basic patterns (fibers) that are ordered periodically in space [55]. The first step is to localise the macroscopic strains by using periodic BCs on the basis cell, see more on period BCs in Section 2.3.5. The second step solves the microscopic Boundary Value Problem (BVP) resulting in microscopic stresses and strains. In the third step the microscopic stresses and strains are translated to the macroscopic scale through homogenisation techniques.

The FE^2 methodology is used as a starting point for semi-concurrent multiscale method for fracture. Kouznetsova was one of the first to extend the FE^2 methodology for fracture (gradient models) for her PhD thesis [73] and subsequently published by Kouznetsova *et al.* [58]. Later, others followed, like in [57, 72, 74]. The up-scaling from fine to coarse scale, i.e. step three in the FE^2 procedure, is realised using *computational homogenisation*. Computational homogenisation is classified as a *hierarchical multiscale method*. Therefore the semi-concurrent multiscale methods will be further discussed in Section 2.3.4 as part of hierarchical multiscale modelling.

2.3.4 Hierarchical or Homogenisation Based Multiscale Methods

Hierarchical multiscale methods as in Figure 2.3.1c are superposition based and translate the information from the fine scale to the coarse scale. Numerical or computational homogenisation techniques are used to translate this information. Compared to (semi-)concurrent multiscale methods hierarchical multiscale methods are widely used and most efficient [68]. The problem is that hierarchical models rely on the assumption of dissimilar length scales, i.e. $l_{cr} \ll l_{MVE} \ll l_{spec}$ for crack length, Microstructural Volume Element (MVE) dimensions and specimen dimensions respectively. For fracture problems this assumption is violated as the crack length can be in the same order as the dimensions of the MVE [57, 21].

One solution is to "hierarchically" enrich the discontinuities, which is similar to the XFEM. An example of multiscale hierarchical decomposition for intact materials is the Multiscale Enrichment method based on Partition of Unity (MEPU) given by Fish and Yuan [75]. The goal of Fish and Yuan was to develop a method for problems where there is no scale separation, i.e. $l_{cr} \sim l_{MVE}$. The MEPU method showed significantly better results than the quasi-continuum method that was discussed in Section 2.3.2 when heterogeneous materials are considered [75].

Homogenisation methods can generally be divided in *numerical* and *computational* homogenisation that will be discussed in the subsequent subsections.

Numerical Homogenisation

Numerical homogenisation is based on the repetition of a unit cell, which should not be confused with a Representative Volume Element (RVE)[2]. A unit cell is considered to represent a heterogeneity, like a single or multiple fiber(s), and is periodically repeated throughout the structure. This results in a ordered representation of the microstructure. A general problem of unit cell methods is that assumptions regarding the form of macroscopic constitutive

[2]The difference between MVE and RVE is that a RVE is considered representative for the material at a macroscopic level.

behaviour are made which are not valid for nonlinear problems [72, 74]. In addition, the representation of periodically spaced unit cells is not realistic for fiber-reinforced composites. Computational homogenisation is an alternative technique that overcomes the limitations of unit cell methods and is therefore discussed in more detail.

Computational Homogenisation

Computational homogenisation for the realisation of multiscale modelling is required when the behaviour of the structure becomes nonlinear, i.e. with large deformations and complex loading paths. Multiscale computational homogenisation, or global-local analysis, can be considered as a FE^2 method as mentioned in Section 2.3.3. In contrast to the numerical homogenisation that is based on the assumption of global periodicity, computational homogenisation is based on local periodicity. Local periodicity allows to model the effect of a non-uniform distribution of the microstructure on the macroscopic behaviour [73].

In general four categories of computational homogenisation techniques can be considered:

- First-order computational homogenisation
- Second-order (gradient enhanced) computational homogenisation
- Computational homogenisation for cohesive/adhesive interface problems
- Continuous-discontinuous computational homogenisation

The first two categories as reported in [73, 58] are generally applicable for intact materials. The first attempts to use computational homogenisation for fracture are related to adhesive or cohesive interfaces as in [59, 60, 72, 74]. Recently another extension to fracture problems is realised by continuous-discontinuous computational homogenisation as in [61, 62, 63, 64].

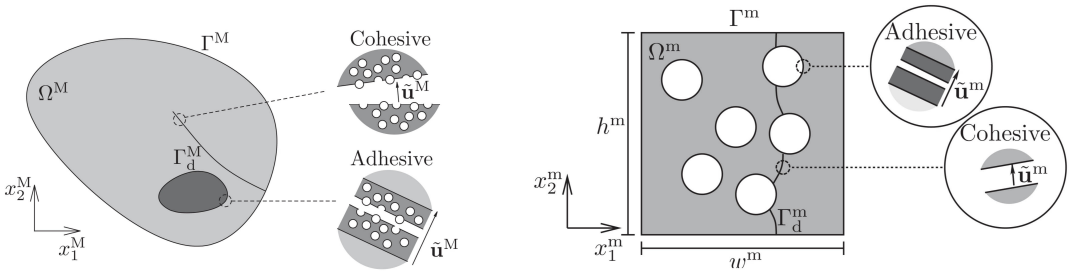

(a) Macroscopic model. **(b)** Microscopic model.

Figure 2.3.3: Schematic representation of the computational homogenisation method according to Verhoosel *et al.* [72].

One interesting computational homogenization technique for adhesive or cohesive interface problems worth mentioning is given by Verhoosel *et al.* [72]. Their method is based on an FE^2 setting where two scales are considered, macroscopic and microscopic scale. The macroscopic model is schematically represented in Figure 2.3.3a and can represent cohesive and

adhesive discontinuities. These discontinuities are then evaluated on a microscopic scale as in Figure 2.3.3b.

As can be seen there are two types of interfaces, adhesive and cohesive. For the adhesive layer averaging relations relate the macroscopic TSL to the response of the microscopic model. For the cohesive interface the relation is different. On the macroscopic scale a cohesive zone is only inserted when a failure criterion is met. On the microscopic scale the point of failure is not defined as interface elements are readily present. The model of Verhoosel *et al.* assumes that the macroscopic constitutive behaviour, before a failure criterion is met, is described by the homogenised microscopic properties [72]. For cohesive failure in Figure 2.3.4a the macroscopic crack is homogenised in the direction the microscopic crack. The same holds for adhesive failure but Verhoosel *et al.* considered two cases as in Figure 2.3.4b.

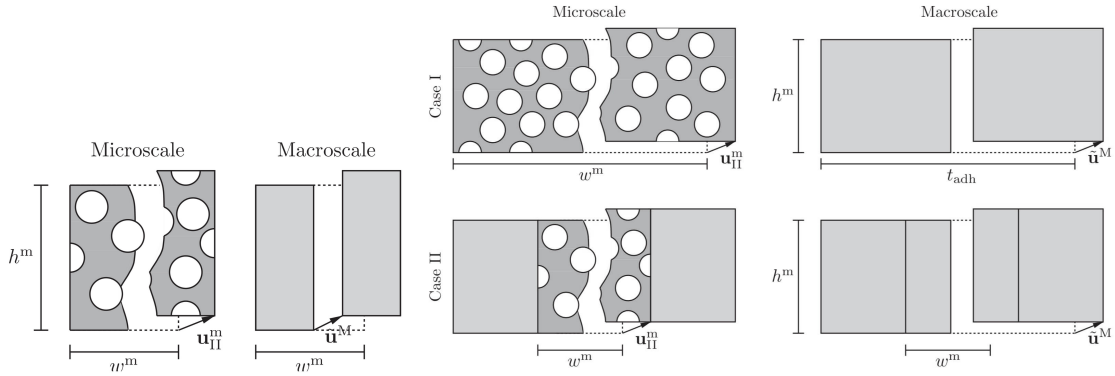

(a) Cohesive failure.

(b) Adhesive failure. Case I: the interface is considered as one RVE. Case II: periodicity of the RVE is taken into account

Figure 2.3.4: Details of the Verhoosel *et al.* homogenisation method [72].

In the end the homogenised macroscopic TSL is independent of the MVE dimensions [72]. This method is only applicable for a simple microstructure with discrete cracking. Therefore, it was modified by Nguyen *et al.* [74]. They employed a similar framework that shows modifications to allow diffusive damage and random microstructures with various loading conditions. In this model, next to the fiber and matrix phase there is an interfacial transition zone. In the model of Nguyen *et al.* a macroscopic TSL is obtained from the microscopic response that is independent of the MVE size. These macroscopic TSLs can be used in two ways; in a sequential homogenisation scheme[3] or in a semi-concurrent FE^2 scheme. For a FE^2 scheme there is direct coupling between the macroscopic and microscopic model. Nguyen *et al.* evaluated mixed loading and concluded that the macroscopic TSLs are independent of the MVE size. In addition the MVE was evaluated for two MVE sizes and the same conclusion have been drawn.

[3] In a sequential homogenisation scheme several simulations with different loading conditions are performed on the MVE, the resulting TSLs are saved and later used on the macroscopic scale as standard phenomenological constitutive laws, known as micromechanically derived TSLs.

2.3.5 Representative Volume Element Considerations

According to the former sections in this chapter it can be seen that at a microscopic scale in the majority of the methods a MVE is used. A MVE can be called representative if it accurately represent the higher scale structure when it is periodically reproduced. One can ask which conditions need to apply when a MVE can be considered a RVE. A study on the existence and size determination was performed by Gitman *et al.* [76]. According to them a RVE is defined as a sample that:

- is statistically representative for the macroscopic response
- contains sufficient inclusions and microscopic information
- increasing this volume should not lead to changes of the macroscopic behaviour
- is sufficiently smaller than the macroscopic structural dimensions

According to Kouznetsova [73] the second condition can lead to a considerably large RVE when all microstructural configurations of a random structure are considered. Therefore, a RVE is in most cases sufficiently defined by the third condition. In this case the minimum required size of the RVE depends on the material behaviour in addition to the microscopic constituents [73].

Gitman *et al.* compared different sizes of examples, with each different realisations, and samples with different volume fractions. A statistical analysis was performed on different samples in terms of stiffness, which is motivated by the fact that stiffness is relevant in multiscale homogenisation techniques [76]. According to analytical results the RVE should be approximately two times as large as the particle size to get a 95% accuracy and 4.5 times to get a 99% accuracy [76]. A short discussion on the sample shape was given by Cid Alfaro *et al.* [19] where a square and rectangular RVE are considered. Their conclusion was that there was almost no influence of the shape on the resulting traction-separation response. Analogous in [18] the effect of fiber volume fraction was investigated. For an increasing fiber volume fraction the peak of the traction-separation curve decreases and the softening slope increases [18].

Periodicity and Boundary Conditions

According to Gitman *et al.* there are two main aspects that determine a correct periodic representation of a RVE; periodicity of BCs and periodicity of the material. Periodicity of the material can be described as the *wall effect*. When there is a wall effect the particles are unable to penetrate through the boundaries of the RVE. Without the wall effect it is considered that the RVE belongs to a larger sample, thus inclusions are crossing the boundary of the RVE and reappear on the opposite side, for instance as on the right side of Figure 2.3.5. Periodicity of BCs prescribe that the displacement (or stress) should be equal on opposite edges as in the left of Figure 2.3.5. In general it should be taken into account that the RVE is part of a bulk structure.

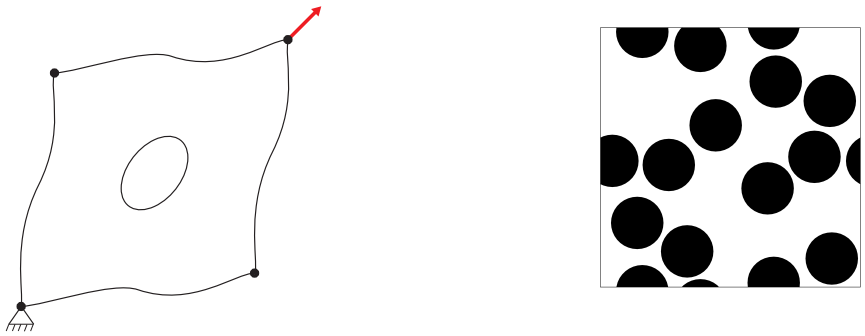

(a) **(b)**

Figure 2.3.5: Illustration of the (a) PBC and (b) the "no wall effect"

For a BC to be periodic the microscopic fluctuation field ($\Delta \boldsymbol{u}$) needs to satisfy the following conditions,

$$\Delta \boldsymbol{u}_L(s) = \Delta \boldsymbol{u}_R(s) \tag{2.3.1}$$

$$\Delta \boldsymbol{u}_T(s) = \Delta \boldsymbol{u}_B(s) \tag{2.3.2}$$

where s is the position on the left (L), right (R), top (T) or bottom (B) boundary. Gitman *et al.* concluded that the periodic BCs have almost no influence for tension loading and some influence for shear loading. For tension the periodic BCs are dominant and for shear the wall effect is dominant when considering the size of the RVE.

PBC provide a good estimation of the effective stiffness and respect periodicity [62]. Next to PBC alternative BC can be used for a RVE, of which an overview was given by Coenen *et al.* [62]. *Taylor BC* indicate that the fluctuation field should be zero at each point within the RVE, i.e. $\Delta \boldsymbol{w}_m = \boldsymbol{0}$. This results in a strong overestimation of the effective stiffness and fully suppresses the localisation band. For *linear BC* the same holds but then only for the boundary of the RVE, which still overestimates the stiffness and the localisation band is only constrained at the boundaries. *Minimal or traction BC* ensure that the traction normal to the boundary is equal for both sides, but it underestimates the effective stiffness and the localisation band is sensitive to spurious (false) localisation [62]. PBC have been employed by [73, 58, 59, 60, 72, 19, 74, 61, 62, 63]. It should be taken into account that the displacement may be periodic but the stress distribution may not be.

Chapter 3

Finite Element Method for Fracture Mechanics

The simulations performed for this thesis will be highly dependent on the Finite Element Method (FEM) due to the fact that these simulations are performed in ABAQUS, a Finite Element Analysis (FEA) package. This chapter will present the numerical aspect of the FEM. Starting with the basics in Section 3.1 and afterwards the numerical implementation of cohesive elements in Section 3.2.

3.1 Basics of the Finite Element Method

Computational methods have been developed to be able to numerically solve a Boundary Value Problem (BVP) on an arbitrary domain. In general these methods divide the continuum domain in small parts that can be numerically solved and the solution thereof gives an approximate representation of the continuum solution. Examples of the computational methods are the Discrete Element Method, Boundary Element Method, Finite Difference Method, Finite Volume Method. Beside these models the FEM has been developed. For structural analysis this method is preferred over the previous mentioned methods. Most methods for modelling crack growth are based on the FEM and the method is able to handle a complex geometry and loading [6]

With the FEM the structure is divided in a finite number of elements which are connected at the nodes, see Figure 3.1.1 for a Two-Dimensional (2D) example. The BVP consisting of the

governing equations and boundary conditions is discretized in a finite set of equations that can be solved. An example of the discretization of a domain including cohesive elements is illustrated in Figure 3.2.1.

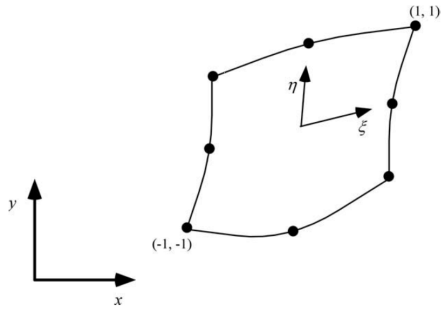

Figure 3.1.1: Local (ζ,η) and global coordinates (x,y) for a 2D FE [6].

The global coordinates (x,y) of any point in space are given as a function of the surrounding nodes $(i = 1,...,n)$ and shape functions (N_i) that are a function of the local coordinates (ζ,η),

$$x = \sum_{i=1}^{n} N_i(\zeta,\eta)\, x_i \tag{3.1.1a}$$

$$y = \sum_{i=1}^{n} N_i(\zeta,\eta)\, y_i \tag{3.1.1b}$$

Analogous to the equations above the displacements u and v, in x and y direction respectively, can be interpolated. Shape functions can be polynomials of any order (i.e. linear, quadratic, cubic, etc) and have to satisfy certain conditions. For example the condition in Equation 3.1.2 that describes that the value of the shape function (N_i) should be equal to one on node i and zero on the other nodes [77].

$$N_i(\zeta_j,\eta_j) = \delta_{ij} = \begin{cases} 1, & \text{for } i = j \\ 0, & \text{for } i \neq j \end{cases} \tag{3.1.2}$$

The main principle of FEM is solving the system described in Equation 3.1.3. In the case of an elastic analysis $\boldsymbol{K}$ is the global stiffness matrix which describes the properties of the structure, $\boldsymbol{u}$ is a vector containing all the Degrees of Freedom (DOF) (i.e. displacements) which are unknown and $\boldsymbol{F}$ are the forces applied to the system. With Equation 3.1.3 the displacement can be determined at any node, from which the stresses and strains can be determined. Next to elastic parameters, thermal, fluid or electrostatic parameters can be solved.

$$\boldsymbol{K}\boldsymbol{u} = \boldsymbol{F} \rightarrow \boldsymbol{u} = \boldsymbol{K}^{-1}\boldsymbol{F} \tag{3.1.3}$$

The global stiffness matrix is an assembly of the elemental stiffness matrices ($\boldsymbol{k}$) as in Equation 3.1.4 [6].

$$\boldsymbol{k} = \int\int \boldsymbol{B}^T \boldsymbol{D}\boldsymbol{B} \cdot \det|\boldsymbol{J}| d\zeta\eta \tag{3.1.4}$$

where the $\boldsymbol{D}$ matrix contains the stress-strain constitutive relations and $\boldsymbol{J}$ is the Jacobian,

$$\boldsymbol{J} = \begin{bmatrix} \dfrac{\partial x}{\partial \zeta} & \dfrac{\partial y}{\partial \zeta} \\ \dfrac{\partial x}{\partial \eta} & \dfrac{\partial y}{\partial \eta} \end{bmatrix} \tag{3.1.5}$$

the partial derivatives of the shape functions are given in the matrix $\boldsymbol{B}$, for 2D this results in,

$$\boldsymbol{B} = \begin{bmatrix} \dfrac{\partial N_i}{\partial x} & 0 \\ 0 & \dfrac{\partial N_i}{\partial y} \\ \dfrac{\partial N_i}{\partial y} & \dfrac{\partial N_i}{\partial x} \end{bmatrix} \tag{3.1.6}$$

Short Discussion on Mesh Density

As a finite number of elements is used there is the discussion of mesh[1] density. In the framework of this thesis the choice of mesh density depends on the cohesive zone length as discussed in Section 2.2.4. In this part of the literature review it was concluded that the general form of the equation that determines the cohesive zone length is as given in Equation 2.2.2. In literature it is argued that a certain number of elements are required per cohesive zone length. This number ranges from two to ten but in most literature a value of three is used. The worst case is defined by the smallest cohesive zone length, which is determined using a value of $2/3\pi$ for the coefficient M [54], the smallest Young's modulus and fracture energy and the highest cohesive strength in the model. This results in an approximate cohesive zone length of 0.034 mm. Taking three elements per cohesive zone length, the mesh density in terms of millimeter[2] should have a value of at least smaller than 0.011 mm.

[1] A mesh is the collection of all the finite elements.

[2] The mesh density in terms of millimeter indicates the edge length, which is specified by the node spacing in the MATLAB meshing script.

3.2 Numerical Implementation of Cohesive Elements

In the case cohesive elements are embedded within the mesh an additional term is added to the governing equations. In this case, the weak form in the domain Ω can be formulated as the variation in external, internal and cohesive surface work [53, 32].

$$\delta W^{\text{ext}} = \delta W^{\text{int}} + \delta W^{\text{coh}} \tag{3.2.1}$$

When discretizing the system as in Figure 3.2.1, the embedded cohesive elements will result in additional displacement DOF. In their turn these DOF result in additional components in the stiffness matrix, displacement vector and force vector as in Equation 3.1.3.

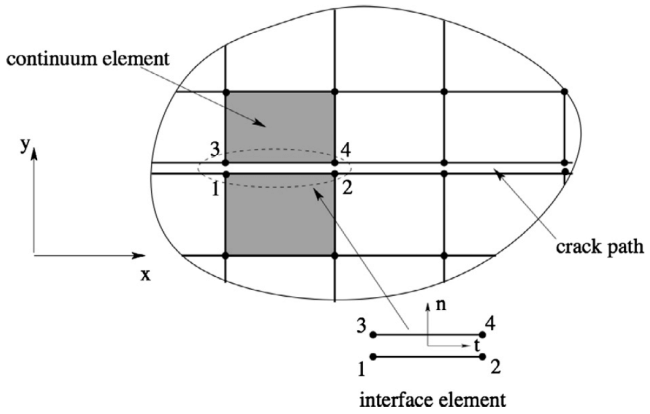

Figure 3.2.1: Discretization of the solid into bulk elements and zero-thickness cohesive elements [53].

The faces of the cohesive element are connected to the neighbouring bulk elements, i.e. the nodes are shared. Other options like tie constraints are available but not used in this thesis. The upper (node 3,4) and lower face (node 1,2) of the interface element can move relative to each other in thickness direction[3]. There are two integration points within the cohesive element, on the midpoint of face 2-3 and face 1-4. In each integration point a thickness direction is defined as in Figure 3.2.2.

The displacement fields of the cohesive element can be given by the equation below [53]. Here "+" stands for the upper face and "-" for the lower face.

$$\boldsymbol{u}^{+} = N_1 \boldsymbol{u}_3 + N_2 \boldsymbol{u}_4 \tag{3.2.2a}$$

$$\boldsymbol{u}^{-} = N_1 \boldsymbol{u}_1 + N_2 \boldsymbol{u}_2 \tag{3.2.2b}$$

[3]The thickness direction of the cohesive element is by default from the lower face towards the upper face.

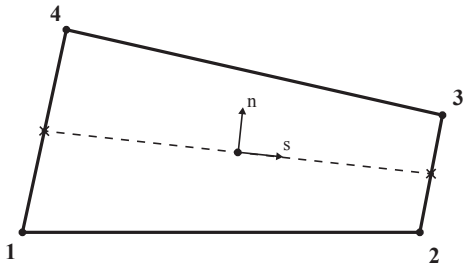

Figure 3.2.2: A 2D cohesive element with two integration points on the midpoints of face 2-3 and face 1-4. Indicated are the thickness directions in each integration point in the local (n, s) coordinate system.

The displacement jump can then be written in terms of the displacement fields,

$$\boldsymbol{u}(\boldsymbol{x}) = \boldsymbol{N}^{\text{int}}(\boldsymbol{u}^{+} - \boldsymbol{u}^{-}) \tag{3.2.3}$$

Implementing the above in the weak form gives a relation between the external, internal and cohesive force.

$$\boldsymbol{F}^{\text{ext}} = \boldsymbol{F}^{\text{int}} + \boldsymbol{F}^{\text{coh}} \tag{3.2.4}$$

Assembly of the relations of each component and linearization of the cohesive force vectors, by differentiating with respect to the displacement vector $\boldsymbol{u}$, results in the stiffness matrix of the cohesive elements as below [53].

$$\boldsymbol{K}_i^{\text{coh}} = \begin{bmatrix} \int_{\Gamma_d} \boldsymbol{N}^T \boldsymbol{Q}\boldsymbol{T}\boldsymbol{Q}^T \boldsymbol{N} d\Gamma & -\int_{\Gamma_d} \boldsymbol{N}^T \boldsymbol{Q}\boldsymbol{T}\boldsymbol{Q}^T \boldsymbol{N} d\Gamma \\ -\int_{\Gamma_d} \boldsymbol{N}^T \boldsymbol{Q}\boldsymbol{T}\boldsymbol{Q}^T \boldsymbol{N} d\Gamma & \int_{\Gamma_d} \boldsymbol{N}^T \boldsymbol{Q}\boldsymbol{T}\boldsymbol{Q}^T \boldsymbol{N} d\Gamma \end{bmatrix} \tag{3.2.5}$$

The assembly of the stiffness matrices of the bulk elements and cohesive elements results in a system of equations as in Equation 3.1.3 that can be solved.

In the case the cohesive elements are defined in terms of a Traction-Separation Law (TSL) the initial linear elastic behaviour is defined somewhat different to the bulk elements. The elements that have not been activated have a zero geometric thickness, but in ABAQUS a constitutive thickness[4] of 1.0 is used to ensure that the nominal strain is equal to the separation.

[4]The constitutive thickness of the cohesive element is the thickness that is used to define the constitutive behaviour. It can either be equal to the geometric (actual) thickness based on nodal coordinates or it can be defined.

In 2D the nominal traction stress vector has two components τ_n and τ_s, which represent the normal and shear traction respectively. Analogous the normal and shear separation are defined as δ_n and δ_s. The elastic behaviour of 2D cohesive elements is defined as below.

$$\boldsymbol{\tau} = \begin{bmatrix} \tau_n \\ \tau_s \end{bmatrix} = \begin{bmatrix} E_{nn} & E_{ns} \\ E_{ns} & E_{ss} \end{bmatrix} \begin{bmatrix} \varepsilon_n \\ \varepsilon_s \end{bmatrix} = \boldsymbol{E\varepsilon} \tag{3.2.6}$$

Once the cohesive elements meet the damage initiation criteria (peak of TSL) they are activated. From this point the stiffness of the cohesive elements is degraded by means of a damage evolution law (softening slope of TSL). For this a scalar damage variable, D, is defined that ranges from 0 to 1. Damage evolution can be defined in different ways, for this thesis a simple linear evolution based on energy is used.

In some cases the crack closes when the cohesive elements are unloaded. Within ABAQUS it is assumed that the unloading is always linear towards the origin of the TSL. Reloading occurs along the same line as the unloading path.

Chapter 4

Numerical Experiments: Methodology

In order to come up with a failure criterion that uses detailed information about the fracture mechanisms of a Carbon-Fiber Reinforced Plastic (CFRP) at a microscopic[1] level numerical experiments have to be performed. The samples that are considered for these numerical experiments are in the order of $1/10^{\text{th}}$ of a millimeter and are therefore difficult to be tested. There are methods available to test samples at this scale, but these methods are not always available and expensive in time and money. In Section 4.1 the general top-level methodology will be presented. An important issue with cohesive elements is artificial compliance, as was stipulated in Chapter 2, which is discussed in Section 4.2 along with the elastic stiffness of cohesive elements. In the end all the details of the pre- and post-processing will be given in Sections 4.3 and 4.4 respectively. The units used throughout the numerical experiments[2] are mm and MPa. Any load cases that are mentioned are summarized in Table 4.2.

4.1 General Outline

The top-level methodology in achieving the thesis objective is presented in this section. A *failure criterion* in this thesis is considered as mathematical relations that describe the fracture mechanisms in terms of a Traction-Separation Law (TSL) and can predict when a ma-

[1] The microscopic scale is used when the terms Microstructural Volume Element (MVE) and Representative Volume Element (RVE) are considered, i.e. it is at a level where one can distinguish the fibers and matrix material.

[2] Numerical experiments are simulations in ABAQUS that evaluate the behaviour, i.e. fracture mechanisms, for different input variables.

terial fails. A parametric study has to result in these mathematical relations. In the introduction it has already been mentioned that this parametric study will be performed on Two-Dimensional (2D) samples with an Uni-Directional (UD) CFRP material. In addition the material properties of the fiber and matrix will be kept constant, only the *cohesive* and *adhesive* properties[3] will be studied along with the fiber volume fraction.

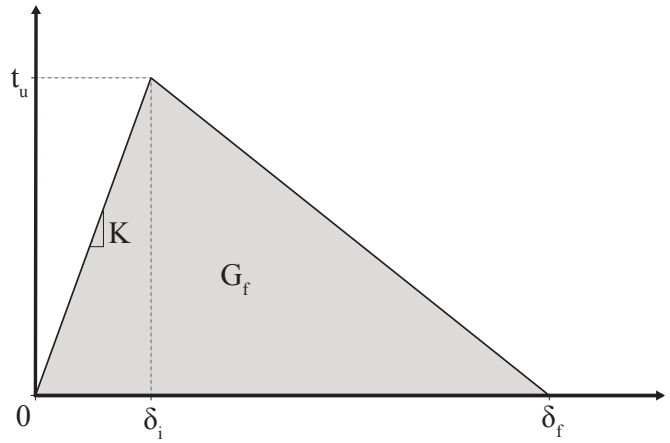

Figure 4.1.1: Bilinear intrinsic TSL used as input for the microscopic cohesive elements.

For this research it is chosen to pick a simple bilinear intrinsic TSL[4] (One-Dimensional (1D) effective) to describe the brittle fracture mechanisms as in Figure 4.1.1. This TSL will be used as input for the microscopic cohesive elements. There are three cohesive properties that define a bilinear intrinsic TSL; cohesive strength (t_u), fracture energy (G_f) and the elastic stiffness of the cohesive elements (K). It is chosen keep the elastic stiffness of the cohesive elements fixed, as will be discussed in Section 4.2. The cohesive strength is the maximum traction and is usually the point where damage initiates. The area of the TSL, or fracture energy, describes the amount of energy or work that is used to create the crack.

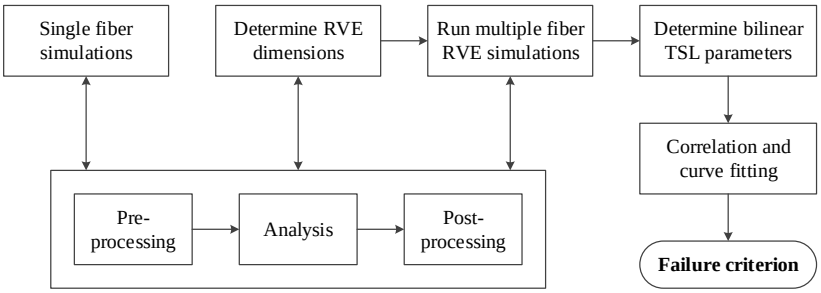

Figure 4.1.2: General outline of the thesis in terms of activities.

[3]The term cohesive is used for the interaction between similar materials (i.e. cracks in matrix material) and the term adhesive is used for the interaction between dissimilar materials (fiber-matrix debonding).

[4]Intrinsic indicates that the traction starts at zero for zero separation. Bilinear implies a linear initial slope and a linear softening slope.

In Figure 4.1.2 an overview of the steps towards the failure criterion are given. As a start single fiber simulations will be performed to get insight in the the effects of several parameters. Next to this, each simulation will be performed for a coarse, medium and fine mesh density to study the effect of mesh convergence. Each simulation will go through the three steps: pre-processing, analysis and post-processing. After the single fiber simulations the dimensions of the multiple fiber RVE, i.e. when it is considered representative, will be determined based on a convergence study. Once the dimensions are known the simulations on the multiple fiber RVE will be performed to study the effect of several variables. The fracture behaviour of each single simulation is summarised in a bilinear TSL that consists of three parameters. The three bilinear parameters of all simulations will be correlated using curve fitting which will result in the macroscopic failure criterion.

As mentioned above the single fiber simulations will study the variablessadf as listed below and in addition a mesh convergence study is performed.

- Interface cohesive strength ($t_u^{(i)}$)
- Fiber cohesive strength ($t_u^{(f)}$)
- Interface fracture energy ($G_f^{(i)}$)
- Fiber fracture energy ($G_f^{(f)}$)
- Fiber diameter (d_F)

The interface properties define the cohesive elements between the fiber and matrix. In addition, all cohesive variables are changed relative to the cohesive properties of the matrix material (i.e. smaller, equal, greater). Changing the five variables has an influence on the input TSL of the fiber and interface cohesive material. All the results are compared to a reference model. With preliminary simulations and the paper of Cid Alfaro [18] as a reference it was concluded that the reference model should have the properties as in Table 4.1.

Table 4.1: Cohesive element properties of the reference model.

Material	**Parameter**	**Value**	**Units**
Interface cohesive elements	$t_u^{(i)}$	25	N/mm^2
	$G_f^{(i)}$	0.025	N/mm
	$E_c^{(i)}$ / $K^{(i)}$	10^9	N/mm^3
Matrix cohesive elements	$t_u^{(m)}$	50	N/mm^2
	$G_f^{(m)}$	0.05	N/mm
	$E_c^{(m)}$ / $K^{(m)}$	10^9	N/mm^3
Fiber cohesive elements	$t_u^{(f)}$	100	N/mm^2
	$G_f^{(f)}$	0.1	N/mm
	$E_c^{(f)}$ / $K^{(f)}$	10^9	N/mm^3

The elastic stiffness of the cohesive elements is listed in the table, in Section 4.2 a discussion on how this parameter is obtained is given. It is assumed that the crack opening is mode independent[5], so the values in Table 4.1 that describe the input TSLs are applicable for both mode I and II. The absence of material properties in Table 4.1 is due to the confidentiality of these properties.

The second step in Figure 4.1.2 is to determine the RVE dimensions. The methodology and results are presented in Chapter 6. In addition to the original approach two other cases are considered for determining the RVE dimensions. For all the simulations in this chapter an arbitrary mixed load case (LC0 in Table 4.2) and the reference cohesive properties are used.

Table 4.2: Overview of the load cases with the components of the strain tensor as given in Equation 4.3.5.

Load case:	ε_{11}	ε_{22}	ε_{12}	ε_{21}	**Description**
LC0	0.05	0.1	0.07	0.07	arbitrary mixed
LC1	0.21	0	0	0	uni-axial extension
LC2	0	0	0.21	0.21	pure shear
LC3	0.07	0.07	0.07	0.07	equally mixed
LC4	0.035	0.07	0.105	0.105	high shear mixed
LC5	0.105	0.07	0.035	0.035	high uni-axial extension mixed
LC6	0	0	0.21	0	simple shear

The inputs for the curve fitting will result from the multiple fiber RVE simulations. Five loading cases, i.e. LC1 to 5 in Table 4.2, will be studied. The mode I load case is uni-axial extension[6] and initially the mode II load case is pure shear. During the curve fitting it became clear that the pure shear load case had to be be replaced by the simple shear load case. The strain components in Table 4.2 are in the microscopic coordinate system, i.e. $(1,2)$ as indicated in Figure 4.1.3. The local coordinate system (n,s) is aligned with the crack line. The same cohesive parameters as studied during the single fiber simulations will be studied, but now the fiber diameter is replaced with the fiber volume fraction.

[5]Mode independent indicates that there is no distinction between the mechanisms of normal (mode I) and shear (mode II) opening

[6]Uni-axial extension, in contrast to uni-axial tension, indicates that no Poisson's effect is present. The top and bottom edge nodes are pinned in y-direction due to the Periodic Boundary Conditions (PBC).

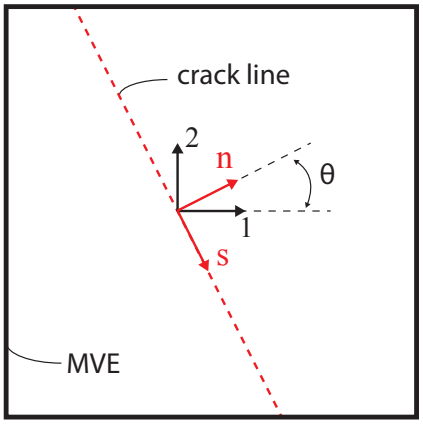

Figure 4.1.3: Illustration of the microscopic $(1,2)$ and local (n,s) coordinate systems. The crack angle θ is defined as the angle between the crack line and crack normal.

4.2 Artificial Compliance: Cohesive Element Elastic Stiffness

It has been mentioned that a bilinear intrinsic TSL will be used as input to the simulations. According to the discussion in Section 2.2.2 it was concluded that an issue with intrinsic TSLs is artificial compliance[7]. The severity of this issue increases with an increasing number of elements, or in this case sample size and mesh density. The only purpose of the cohesive elements is to simulate fracture, but in addition it has a significant effect on the global deformation. In a simple 1D linear-elastic case the strain (ε) can be determined as a function of the applied stress.

$$\varepsilon = \frac{\sigma}{E_b} \tag{4.2.1}$$

E_b is the Young's modulus of the bulk elements[8]. In the case a cohesive interface element is implemented an additional term has to be considered,

$$\varepsilon = \frac{\sigma}{E_b} + \frac{\sigma}{E_c} \tag{4.2.2}$$

As one can see this term can be minimised by increasing the elastic stiffness of the cohesive elements (E_c). The elastic stiffness of the cohesive elements is also called the penalty stiffness parameter that ensures a stiff connection before damage occurs. Ideally a value $E_c \to \infty$ is

[7] Artificial compliance is the apparent Young's modulus as a result of the implemented cohesive elements.

[8] Bulk material or elements refers to the fiber and matrix material or elements, distinguishing them from the cohesive material or elements.

preferred but this is not feasible because stable time step issues arise for too high values, resulting in convergence problems [36, 31, 32].

According to literature [78, 54] the elastic stiffness of the cohesive elements has to be sufficiently high compared to the maximum elastic stiffness of the bulk material. Blal *et al.* [79] proposed a relation for the factor that will result in an 'invisible' implementation of the cohesive elements.

$$\frac{E_c}{E_b} \geq \frac{75}{l_{mesh}} \tag{4.2.3}$$

The above equation is valid for a Poisson's ratio (ν) of 0.3. For the proposed mesh density for the simulations of l_{mesh} = 0.0005 mm this will result in a factor of 150000. This value is unfeasible high compared to the values used in literature, in common practice a factor of 1000 should be sufficient. A factor of 1000 results in a coarse mesh in which the fibers are not properly defined. With the above discussion and after the first simulations there was doubt about the exact value and therefore a small parametric study was performed.

In Figure 4.2.1 the results of this parametric study can be found for two load cases, uni-axial extension (LC1) and a mixed loading case (LC0) as in Table 4.2. The load cases will be explained in Section 4.3 and the post-processing procedure to obtain the above plots in Section 4.4. A sample with dimensions 25×25 µm is used because for a high factor convergence problems arise for samples with a higher number of elements.

One can see that when a factor of 100 is employed the fracture behaviour is not properly defined, i.e. the results show high artificial compliance resulting in a low apparent stiffness and a high resulting strain (Equation 4.2.2). For higher factors the fracture behaviour is better defined, resulting in a peak. Especially for LC1 this peak increases for higher factors and no convergence can be observed. To ensure stable simulations of models with a high number of cohesive elements the factor should not be too high. This is due to the numerical problems that arise when there are large differences in stiffness within the system that leads to an ill-conditioned Boundary Value Problem (BVP). Therefore, for the subsequent simulations in this thesis an elastic stiffness (E_c) of 10^9 MPa is used for the cohesive elements, which corresponds to a factor of 3623 (red line). In ABAQUS this is the value of E_{nn} and E_{ss} as in Equation 3.2.6. It is known that the results will be different for higher values, but in the end one cannot say for certain that those result will be correct without further investigating this issue.

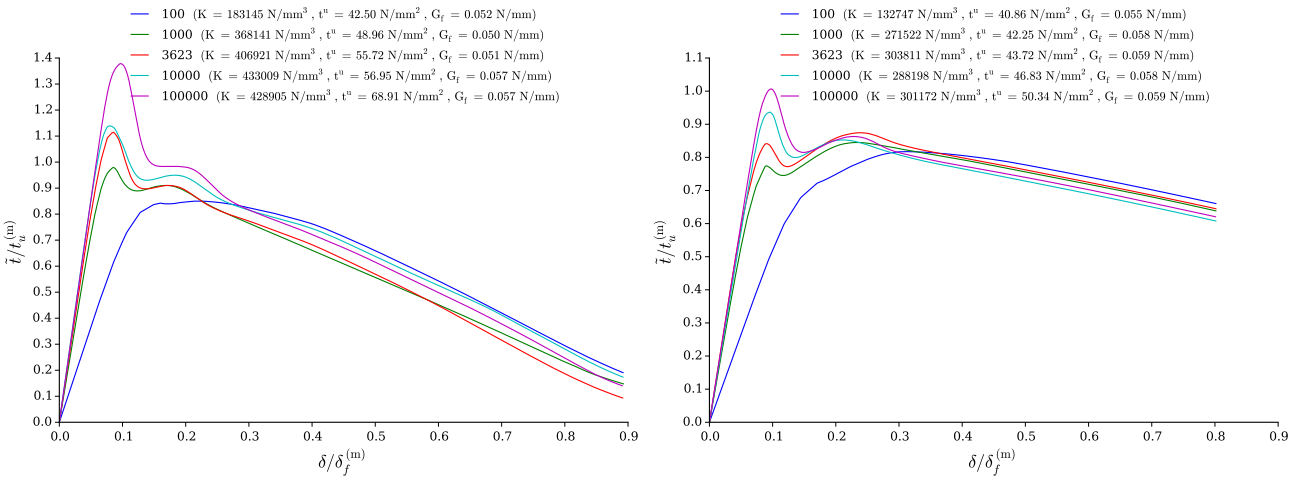

(a) Uni-axial extension (LC1). **(b)** Mixed loading (LC0).

Figure 4.2.1: Effect of the elastic stiffness of the cohesive elements for two load cases. Simulations were performed on a 25×25 µm multiple fiber sample and the factor is given by Equation 4.2.3.

4.3 Pre-Processing: Model Setup

In this section the pre-processing of the single and multiple fiber models will be discussed. In Section 4.3.1 the mesh generation script is explained followed by the implementation of cohesive elements in Section 4.3.2. The implementation of each PBC and the verification is presented in Section 4.3.3 followed by the generation of the ABAQUS input file in Section 4.3.4. At the end of the pre-processing the job[9] is submitted to the Delft University of Technology (DUT) cluster[10] for analysis, as explained in Section 4.3.5. All the separate steps in the pre-processing are bundled in one PYTHON script.

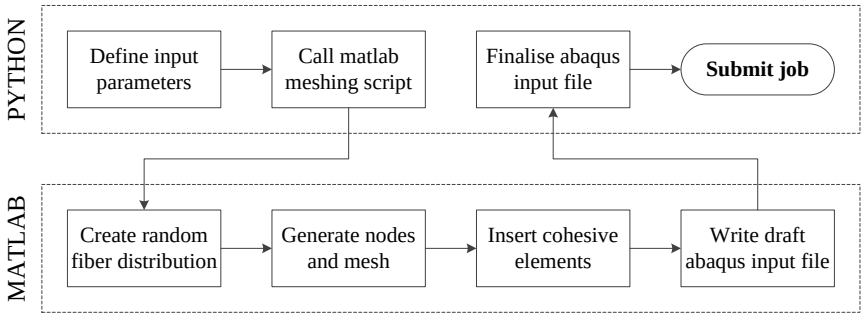

Figure 4.3.1: Activities of the pre-processing as part of Figure 4.1.2.

[9] The term job indicates the model that has to be analysed.
[10] The DUT cluster is a remote server on which calculations can be performed.

4.3.1 Mesh Generation

For the generation of multiple fiber meshes a random fiber distribution is required and for each simulation several realizations (i.e. different fiber distributions with the same amount of fibers) have to be generated. In addition the implementation of PBC is more convenient when utilizing an own made meshing script. In order to achieve this two options are available: either write a PYTHON script that generates a mesh in combination with ABAQUSor write a script in MATLAB. Because the implementation of cohesive elements is done MATLAB the second option is preferred. The MATLAB script consists of the steps shown in the bottom of Figure 4.3.1 and is explained below.

Using inputs like fiber volume fraction (V_f), mesh density and MVE dimensions the script starts with determining the number of fibers and node spacing. After this the location of each fiber origin is randomly picked from a predefined set of locations. From these locations the nodes on the fiber edge are generated. An important part in this step is that the no wall effect (see Section 2.3.5) is implemented, i.e. the fibers that go through the edge have to appear at the other side of the MVE. Analogous the nodes inside those fibers are generated with no wall effect and aligned with the edges of the MVE. In addition a random perturbation is added to the nodes inside the fiber, see Figure 4.3.2a and 4.3.3a for an example node distribution for a single and multiple fiber model respectively.

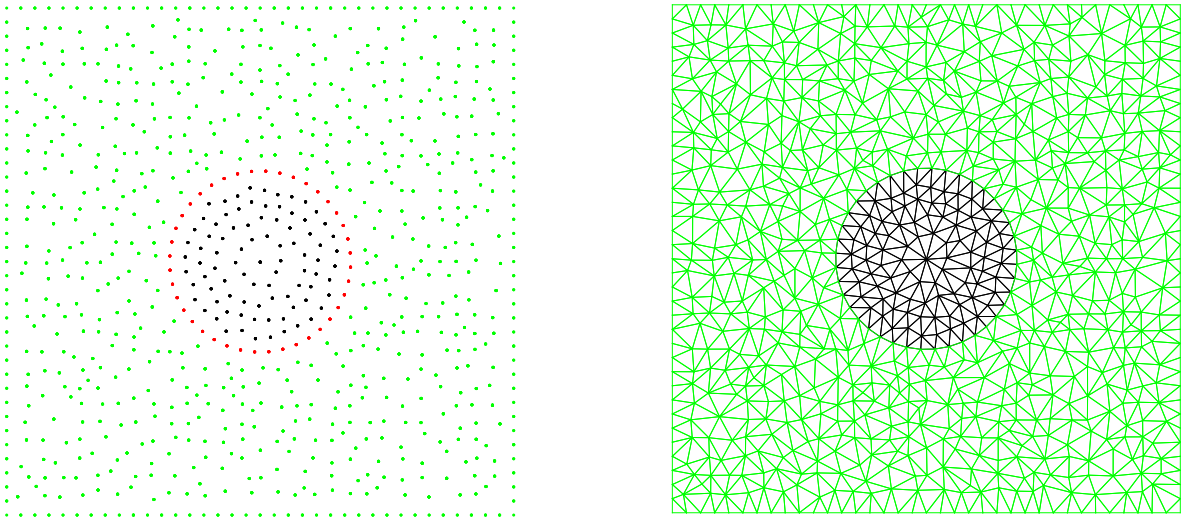

(a) Node distribution. **(b)** Final triangular mesh.

Figure 4.3.2: Example result of the MATLAB meshing script for a single fiber model.

The next step is to generate the matrix nodes between the fibers, which is done using two overlapping node distributions. The first distribution contains nodes that are radially extrapolated from the fiber edge nodes and the second distribution is a rectangular to fill up

the gaps. Nodes that are too close are removed and it is ensured that there are always some nodes between the neighbouring fibers. Just as with the fiber nodes, random perturbations are added to the matrix nodes. Together with the fiber perturbation this ensures a random mesh

In the end the node distribution is generated from which a triangular mesh is generated using the *delaunay* function of MATLAB. The choice for a random triangular mesh is proved to be essential when studying fracture with cohesive elements. For a quadrangular mesh the directions in which a crack can go at a node is limited (i.e. 0°, 90° or -90°). For a triangular mesh there are more directions in which the crack can go and therefore the mesh dependency is reduced, especially with a random mesh. An example node distribution for a single fiber MVE can be found in Figure 4.3.2a along with the final mesh in Figure 4.3.2b.

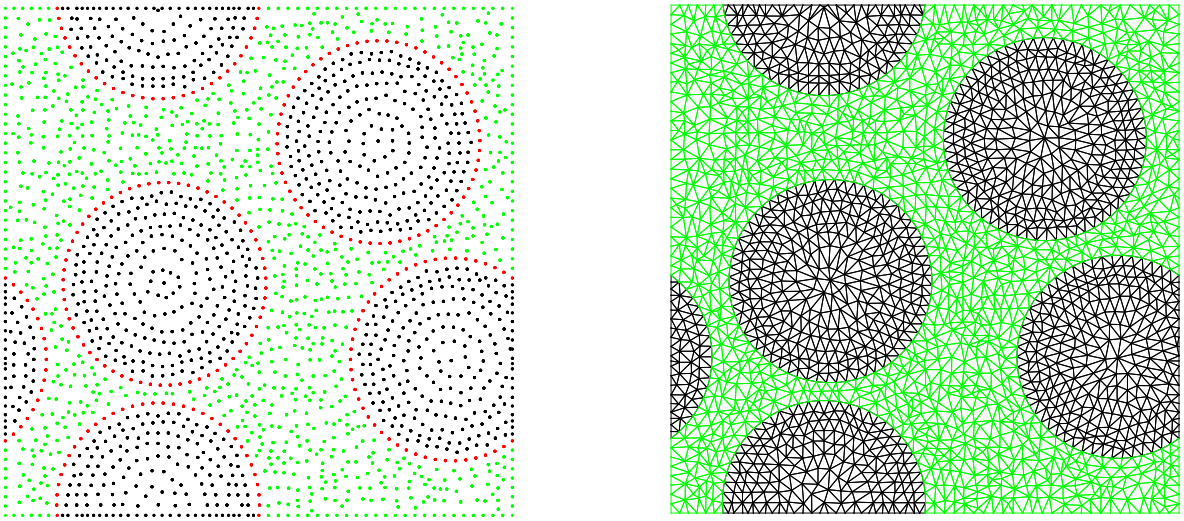

(a) Node distribution. **(b)** Final triangular mesh.

Figure 4.3.3: Example result of the MATLAB meshing script for a multiple fiber model.

In order to verify the mesh a quality check is done. For each element the aspect ratio is checked and it is ensured that its value is below 3.0. Elements that have a higher aspect ratio are corrected. At the end of the MATLAB script the node coordinates and element connectivity is written to an ABAQUS input file. The bulk elements are of the type CPE3, which is a three node linear plane strain element. Plain strain is chosen because one dimension, i.e. out-of-plane fiber length, is significantly larger than the width and height of the MVE. The cohesive elements are of the type COH2D4, a four node 2D cohesive element.

4.3.2 Implementation of Cohesive Elements

In the same MATLAB script as the mesh generation from the previous section, the implementation of cohesive elements is processed. The fundamentals of this part of the script were provided by two PhD students from the DUT, Sathiskumar Anusuya Ponnusami and Jayaprakash Krishnasamy. For this thesis modifications were made to make it more suitable and to decrease the computational time significantly. The script looks for common faces of the bulk elements. On these common faces the nodes are duplicated and subsequently the cohesive elements are defined, as illustrated in Figure 3.2.1. After this the all the nodes and elements, bulk and cohesive, are divided in sets.

4.3.3 Implementation of Periodic Boundary Conditions

As mentioned in Section 2.3.5 PBC are the preferred option for multiscale simulation and are implemented by the condition below. This condition states that the deformation field on the left edge should be equal to the deformation field on the right edge, same as for the top and bottom edge. This way the MVE can be repeated through space.

$$\Delta \boldsymbol{u}_L(s) = \Delta \boldsymbol{u}_R(s) \tag{4.3.1}$$

$$\Delta \boldsymbol{u}_T(s) = \Delta \boldsymbol{u}_B(s) \tag{4.3.2}$$

In a Finite Element (FE) model this translates to enforcing the displacement of node pairs. For example, a left-right node pair is defined as the nodes on the left and right edge that have the same y-coordinate. The meshing script from Section 4.3.1 already ensured that these node pairs exist at the correct location. Note that node pairs are only defined for nodes on the edge, not for the corner nodes.

For a model that does not contain cohesive elements the implementation is straightforward. Two dummy nodes are created, a left-right (LR) dummy and a top-bottom (TB) dummy node. The exact location of these nodes is not relevant. The displacement of each node pair is related to the displacement of one of these dummy nodes. Due to this the deformation loading can be applied to the dummy nodes only instead of each node pair separately. A deformation vector is applied to the dummy node, see Figure 4.3.4. For example, for a random left-right node pair this gives the two equations below.

$$u_1^{(R)} - u_1^{(L)} - \varepsilon_{11} w = 0 \tag{4.3.3}$$

$$u_2^{(R)} - u_2^{(R)} - \varepsilon_{21} w = 0 \tag{4.3.4}$$

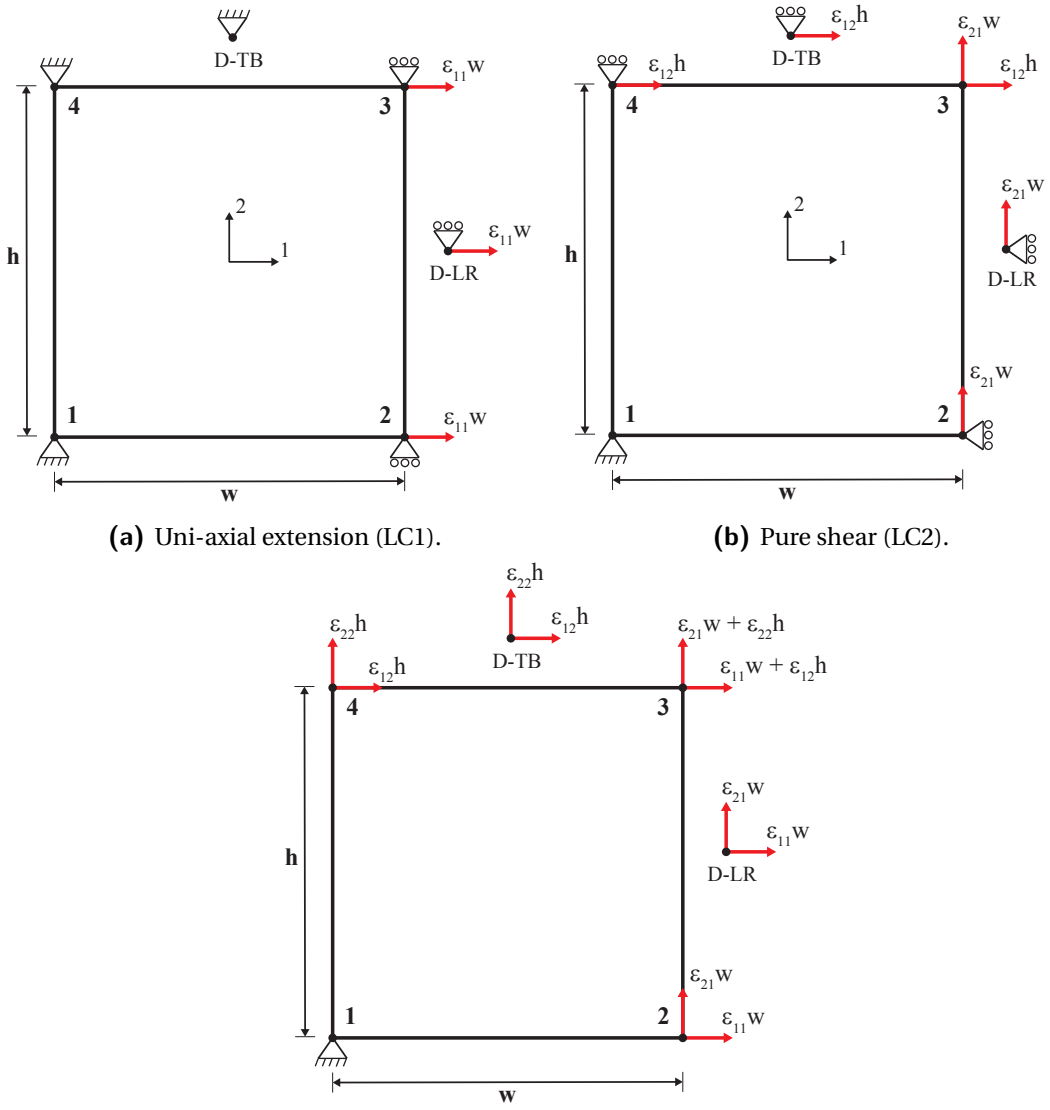

(a) Uni-axial extension (LC1).

(b) Pure shear (LC2).

(c) Mixed loading.

Figure 4.3.4: Illustration of the BC for three distinct load cases. The BC are given for the four corner nodes, the left-right dummy node (D-LR) and the top-bottom dummy node (D-TB).

For each node pair two equations exist, i.e. in 1 and 2 direction, and in the next section it is explained how to write this to the ABAQUS input file. The combination of different deformation loadings enforced on the dummy nodes result in a specific load case. In general the load case is described by the strain tensor ($\boldsymbol{\varepsilon}$).

$$\boldsymbol{\varepsilon} = \begin{bmatrix} \varepsilon_{11} & \varepsilon_{12} \\ \varepsilon_{21} & \varepsilon_{22} \end{bmatrix} \tag{4.3.5}$$

The strain is determined from the deformation by using the original geometry as a reference, i.e. *Lagrangian strain*. When calculating the displacement loading from the strain tensor input, small strains are assumed. In general this assumption is only valid for strains less than 1%. However, for fracture problems the strain can go up to 20%. This assumption will thus result in a certain error, but this error is equal for all the models that are compared and therefore it is assumed to have no effect on the correlation of the results. In the end the 2D displacement PBC for ABAQUS are calculated as below, where w and h are the width and height of the MVE respectively.

$$\boldsymbol{u} = \begin{bmatrix} \varepsilon_{11} & \varepsilon_{12} \\ \varepsilon_{21} & \varepsilon_{22} \end{bmatrix} \begin{bmatrix} w \\ h \end{bmatrix} = \begin{bmatrix} \varepsilon_{11} w + \varepsilon_{12} h \\ \varepsilon_{21} w + \varepsilon_{22} h \end{bmatrix} \tag{4.3.6}$$

The above explanation is valid for models without cohesive elements, the implementation for models with cohesive elements is similar. However, the nodes are duplicated a number of times, depending on the number of elements that connect to the original node. Therefore the node pairs are defined different compared to the model without cohesive elements. The issue is that, for example, on the top edge at coordinates $(x, h/2)$ the node is duplicated four times because four elements connect to that node, whereas on the bottom edge at location $(x, -h/2)$ the node is duplicated only three times. In this case there is an unequal number of nodes on the top and bottom edge. Several methods were tested to correctly define the node pairs, as a result the method illustrated in Figure 4.3.5 is preferred.

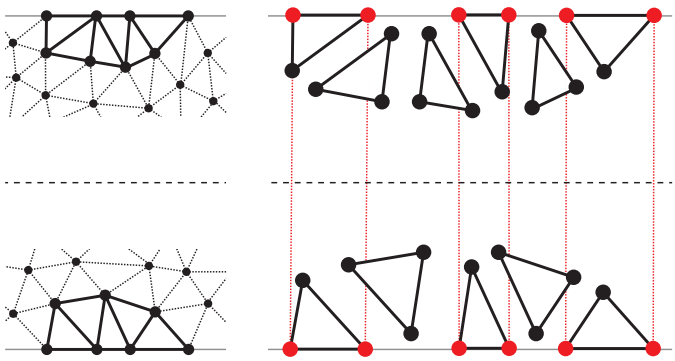

Figure 4.3.5: Method for defining the node pairs for a mesh with embedded cohesive elements. On the left a part of the top and bottom mesh is illustrated, with a detailed illustration on the right. The defined node pairs are indicated in red.

The left side of Figure 4.3.5 gives a part of the top and bottom mesh and on the right a detail of the left is given. It can be seen that only the nodes of the bulk elements that have a face on the edge are coupled, indicated in red. The bulk elements with nodes on the edge but all faces inside the MVE are coupled to the bulk elements through the cohesive elements. This method ensures identical node pairs and enforces the PBC. It should be mentioned that enforcing the displacement does not guaranty traction continuity along the boundaries, more on this in the next section.

Verification of Periodic Boundary Conditions

The implementation of PBC is verified by running three separate models. One single fiber model without cohesive elements and two multiple fiber element with and without cohesive elements. The results for the single fiber model can be seen in Figure 4.3.6 for two load cases; uni-axial extension and a mixed loading case, LC1 and 3 in Table 4.2 respectively. From these contour plots it is concluded that the displacement is indeed periodic, which is confirmed by checking the exact values at each node. For example, the difference in displacement of each left-right node pair in Figure 4.3.6a is exactly the imposed displacement of 5.88e-4 mm in x-direction and 0 mm in y-direction as determined in Equation 4.3.7 and 4.3.8.

$$\varepsilon_{11}\, w + \varepsilon_{12} h = (0.21) \cdot (28e\text{-}3) + (0) \cdot (28\text{e-}3) = 5.88\text{e-}4 \text{ mm} \tag{4.3.7}$$

$$\varepsilon_{21}\, w + \varepsilon_{22} h = (0) \cdot (28\text{e-}3) + (0) \cdot (28\text{e-}3) = 0 \text{ mm} \tag{4.3.8}$$

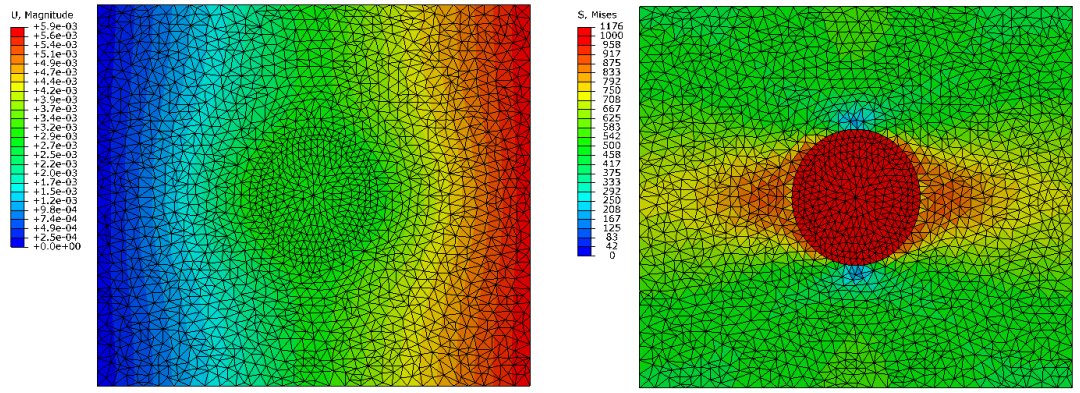

(a) LC1 displacement. **(b)** LC1 Von Mises stress.

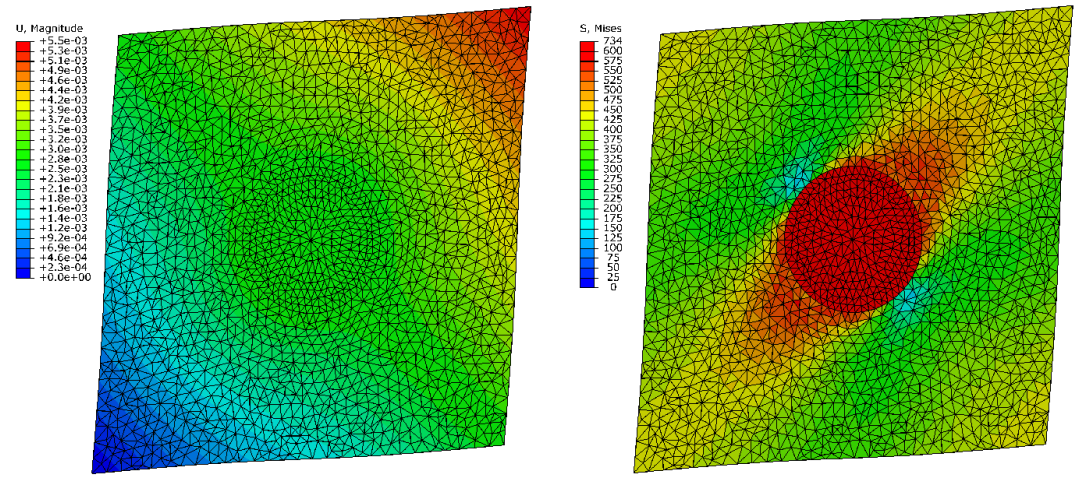

(c) LC3 displacement. **(d)** LC3 Von Mises stress.

Figure 4.3.6: Verification of the PBC for a single fiber model without cohesive elements.

The same holds for the mixed loading case. In terms of traction periodicity along the boundary it seems that the Von Mises stresses are periodic. However, comparing the exact element values shows a difference of approximately 0.2% for the Von Mises, σ_{11} and σ_{22} components. This is explained by the fact that the stresses are averaged with nodes inside that have no PBC applied. The error in the σ_{12} component is very high as there is almost no shear stress present at the edges (i.e. ≈ 0). Overall it is concluded that there is traction periodicity for this model.

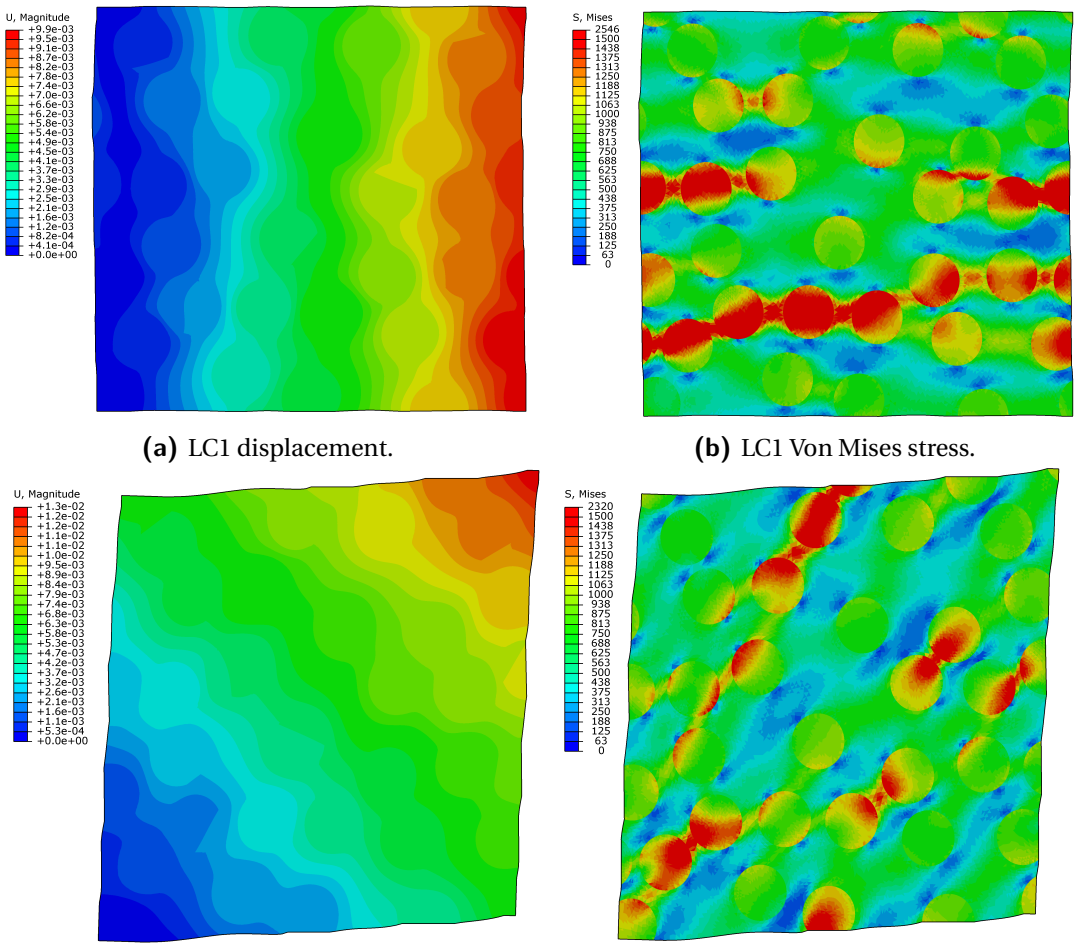

(a) LC1 displacement.

(b) LC1 Von Mises stress.

(c) LC3 displacement.

(d) LC3 Von Mises stress.

Figure 4.3.7: Verification of the PBC for a 75×75 µm multiple fiber model ($V_f = 40\%$) without cohesive elements.

The multiple fiber model without cohesive elements is shown above. Compared to the single fiber model the same conclusions are drawn. As the stress periodicity in Figure 4.3.7d is not clear the top and bottom locations indicated in Figure 4.3.8a are shown next to each other in Figure 4.3.8b. The stress field seems periodic but there are differences up to 10% in the exact value, again due to the interpolation with nodes that are not periodic. The difference is higher compared to the single fiber model because fibers are located at the edge resulting in higher stress differences. It is concluded that the traction along the boundary is semi-periodic.

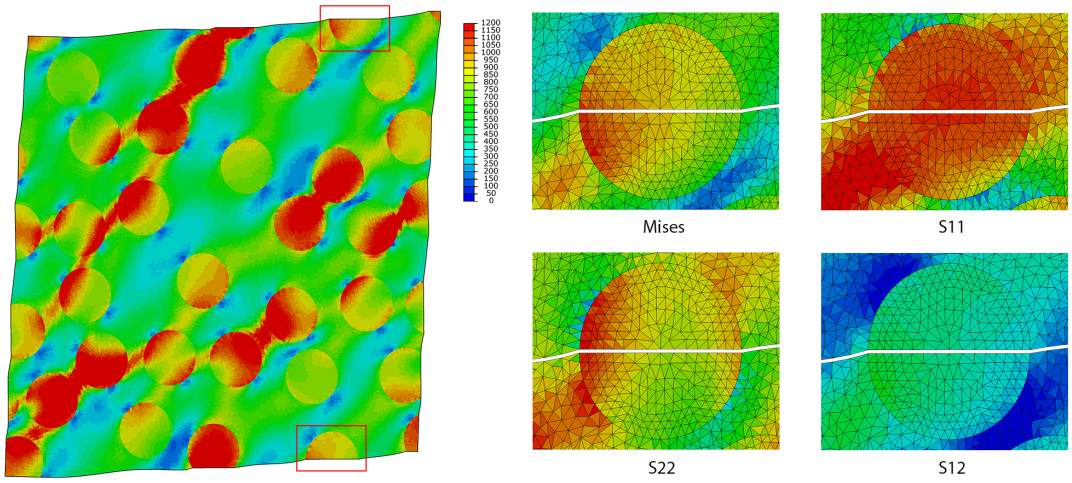

Figure 4.3.8: Detailed contour plot for the verification of PBC of the multiple fiber model without cohesive elements; (a) top and bottom locations of which the detailed contour plot is shown in (b) for the Von Mises stress, σ_{11}, σ_{22} and σ_{12}.

At last the PBC verification of the multiple fiber model with cohesive elements is performed, see Figure 4.3.9. On the general contour plots the displacement periodicity is visible, even with the discontinuity. The traction periodicity along the boundary is less clear, therefore the detail plots are given in Figure 4.3.9. The stresses do not align, which is due to the discontinuities. There are cohesive elements present between the bulk elements that result in a discontinuity in the stress, especially around cracks. In addition the definition of the node pairs as in Figure 4.3.5 has an influence on the traction at the boundary. Therefore, the traction along the boundary is not periodic.

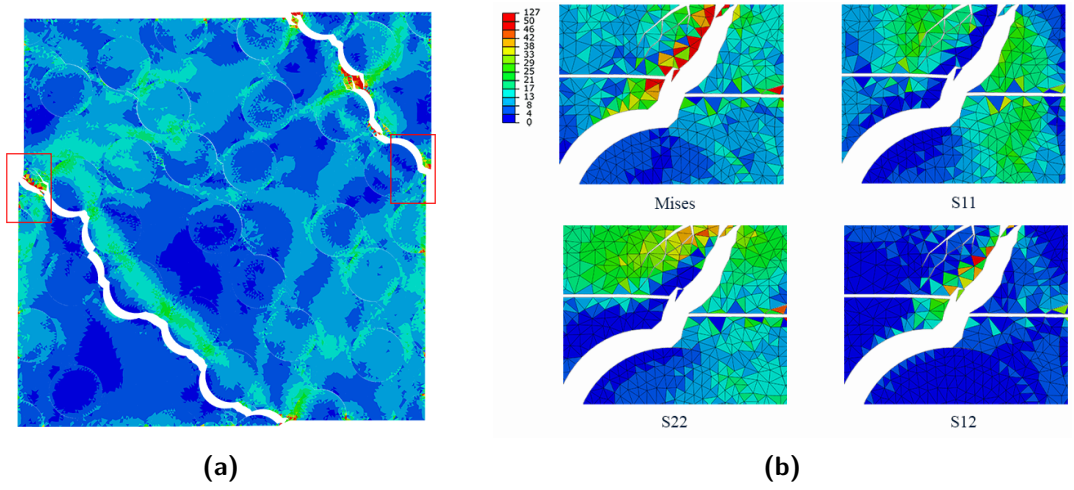

Figure 4.3.9: Detailed contour plot for the verification of PBC of the multiple fiber model with cohesive elements; (a) left and right locations of which the detailed contour plot is shown in (b) for the Von Mises stress, σ_{11}, σ_{22} and σ_{12}.

4.3.4 ABAQUS Input File

Once the MATLAB script is finished a basic input file has been written that includes the node coordinates, (cohesive) elements connectivity, element and node sets, sections and PBC equations. In this section each component in the ABAQUS input file is explained.

The first lines of the ABAQUS input file contain the heading that specifies the job and model name, the ABAQUS version and a preprint which is non-relevant for the current input files. After this the parts of the model are printed that include the nodes, elements, element sets and sections that belong to this specific part. In total there are three parts: the MVE part and two dummy parts. The definition of the MVE part is given above.

```
**
** PARTS
**
*Part, name=EXAMPLE
*Node
1, X-COORD, Y-COORD
...
*Element, type=CPE3
1, NODE 1, NODE 2, NODE 3,
...
*Element, type=COH2D4
N_b + 1, NODE 1, NODE 2, NODE 3, NODE 4,
...
*Elset, elset=NAME
ELEMENT 1, ELEMENT 2, ...
...
** Section: EXAMPLE-1
*Solid Section, elset=ELSET-1, controls=EC-1, material=MATERIAL-1
...
*Section: EXAMPLE-2
*Cohesive Section, elset=ELSET-2, controls=EC-2, material=MATERIAL-2, response=TRACTION SEPARATION
...
*End part
```

After the *End part statement the dummy parts are printed that only contain one node and nothing else. Either a solid section or a cohesive section is generated that refers to the material and controls generated later on. After the parts the assembly is printed that includes the main and dummy instances, node sets and equations.

```
**
** ASSEMBLY
**
*Assembly, name=Assembly
**
*Instance, name=EXAMPLE, part=EXAMPLE
*End Instance
...
*Nset, nset=NAME, instance=EXAMPLE
NODE 1, NODE 2, ...
...
*Equation
3
```

```
RIGHT_NODE_X, 1, 1, LEFT_NODE_Y, 1, -1, DUMMY_LR, 1, -1,
*EQUATION
3
RIGHT_NODE_X, 2, 1, LEFT_NODE_Y, 2, -1, DUMMY_LR, 2, -1,
...
*END ASSEMBLY
```

The equation statements describe Equation 4.3.4 where the first value after NODE is the Degrees of Freedom (DOF) and the second value the factor. The displacements of [0.1,0.0] in Equation 4.3.4 are replaced with the DUMMY_LR node on which the displacements are enforced. The above is as far as the MATLAB script goes, after this the PYTHON script takes over and writes the element controls, material properties, steps, boundary conditions and output requests. This is done so that these values can be easily modified by the PYTHON script for the parametric study. First the section controls are printed.

```
**
** ELEMENT CONTROLS
**
*SECTION CONTROLS, NAME=EC-X, ELEMENT DELETION=NO, VISCOSITY=0.001
1., 1., 1.
```

The above shows an example where element deletion is off and viscosity is added. In general for all the models in this thesis element deletion[11] is off and a viscosity of 0.001 is added to the cohesive elements. The viscosity is required to cope with the convergence problems with cohesive elements that have a high initial elastic stiffness.

```
**
** MATERIALS
**
*MATERIAL, NAME=EXAMPLE_BULK
*ELASTIC, E, ν
..
*MATERIAL, NAME=EXAMPLE_COHESIVE
*DAMAGE INITIATION, CRITERION=MAXS
t_u1, t_u2, t_u3
*DAMAGE EVOLUTION, TYPE=ENERGY
G_f
*ELASTIC, TYPE=TRACTION
E_c1, E_c2, E_c3
...
```

The example above of describes the material definition of the bulk material is a simple elastic material. For the cohesive elements a damage initiation criterion has to be defined, which is a maximum stress criterion. When the stress in the element is greater or equal to the cohesive strength (t_u) it is activated, the cohesive strength is assumed to be equal in normal, shear 1 and shear 2 direction. Next to this a damage evolution has to be defined that together with the damage initiation describes the input TSL. The type of the damage evolution is energy which requires the fracture energy (G_f) as input. The softening is linear as discussed before and opening is assumed mode independent. This is an important assumption because a mode

[11] With element deletion set to *on* the cohesive elements that are fully damaged are removed.

dependent model will require multiple input TSLs. In addition, no relation between mode I (normal) and mode II (opening) is defined.

```
**
STEP: GENERAL_STEP
**
*STEP, NAME=GENERAL_STEP, NLGEOM=YES, INC=N_max
*STATIC, STABILIZE, ALLSDTOL=0.005
Δt_init, 1, Δt_min, Δt_max, 1
```

The load step is defined as given above. The maximum number of increments is given by n_{max} and is used to terminate a model. There is stabilization in order for the model to be able to converge and the time steps; initial, minimum and maximum are in general; 0.001, 1e-24, 0.1 respectively. Next to the stabilization the number of attempts for each iteration is increased to 30. As part of the step input, the boundary conditions are written.

```
**
** BOUNDARY CONDITIONS
**
** NAME: BC_DUMMY_LR TYPE: DISPLACEMENT/ROTATION
*BOUNDARY
DUMMY_LR, 1, 1, ε_11 w
DUMMY_LR, 2, 2, ε_21 w
```

The above shows as an example the BC for the left-right dummy node which has a displacement loading of $[\varepsilon_{11}w, \varepsilon_{21}w]$. The BC for the top-bottom node can be written analogous with a displacement loading of $[\varepsilon_{12}h, \varepsilon_{22}h]$. The BC on the dummy nodes enforce the BC on the edge nodes through the equations discussed before. In addition to these BC the BC of the corner nodes are written. The bottom left corner node is fixed, the bottom right corner node has a displacement loading equal to the left-right dummy node, the top left corner node a displacement loading equal to the top-bottom dummy node and the top right corner node BC is described by Equation 4.3.6. All the boundary conditions for a uni-extension loading, pure shear loading and a mixed load case are visually illustrated in Figure 4.3.4.

After the BC the field output request are written, which are element stress (S), element volume (EVOL) and node displacement (U). The output is only requested each approximate 0.001 time step for pure shear and 0.002 otherwise, in order to minimise the size of the output file. No history output is required and at *END STEP line the ABAQUS input file is finished.

```
**
** OUTPUT REQUESTS
**
*RESTART, WRITE, FREQUENCY=0
**
FIELD OUTPUT: F-OUTPUT-1
**
*OUTPUT, FIELD, TIME INTERVAL=0.001, TIME MARKS=NO
* NODE OUTPUT
U,
*ELEMENT OUTPUT, DIRECTION=YES
S, EVOL,
*END STEP
```

4.3.5 Submitting the Jobs

Once the ABAQUS input file is written with all required parameters the job is submitted to the DUT cluster for an ABAQUS 6.14-1 standard analysis. The operating system of this cluster is Fedora Core 12 in a Linux environment and is accesses via a secure shell. For the here are 25 multi-cpu compute nodes available. Each node has two Intel Xeon E5520 (quadcore) processors and 24 GB1333 ECC RAM. A Portable Batch System (PBS) script is used to manage the job on the cluster and an example is given below. The PBS file and ABAQUS input file are copied to the cluster using an sftp client within PYTHON. Subsequently the job is submitted by the command QSUB EXAMPLE.PBS.

```
#PBS -O JOB_NAME
#PBS -L NODES=1:PPN=1
#PBS -L MEM=3GB
#PBS -L WALLTIME=75:00:00
#PBS -N JOB_NAME
#PBS -S /BIN/CSH
#PBC -W STAGEOUT=$TMPDIR/MODEL_NAME.ODB@HPC12:OUTPUT_LOCATION
#PBC -W STAGEOUT=$TMPDIR/MODEL_NAME.MSG@HPC12:OUTPUT_LOCATION
#PBS -W STAGEOUT=$TMPDIR/MODEL_NAME.DAT@HPC12:OUTPUT_LOCATION
CD $PBS_O_WORKDIR
CP INP_LOCATION $TMPDIR
CD $TMPDIR
MODULE LOAD ABAQUS
ABAQUS JOB=JOB_NAME INTERACTIVE CPUS=1
EXIT 0
```

A small investigation was done to study the effect of parallel analysis, which concluded that a single core analysis is the most efficient (nodes=1:ppn=1). Using for example 16 cores can reduce the total computational time, but in total 20 ABAQUS tokens are required and instead of 4 parallel jobs (requires 20 tokens) only one job can be submitted at once.

In general 3gb of memory was more than enough. The simulations are performed in a temporary directory on the local disc of the node ($TMPDIR). The stageout commands state that at the end of the PBS script, no matter how it ends, the indicated files are copied to the output location. This is useful when the walltime[12] is reached.

4.4 Post-Processing Approach

In this section the post-processing of the single and multiple fiber models will be discussed. The first step is to extract the relevant data from the ABAQUS output file, see Section 4.4.1. From extracted data the Effective Traction-Separation Law (ETSL) can be plotted as explained in Section 4.4.2. In the end additional plotting is discussed in Section 4.4.3. All the separate steps in the pro-processing are bundled in one PYTHON script.

[12] Walltime is the maximum amount of time the job is allowed to run, after exceeding the walltime the job is aborted.

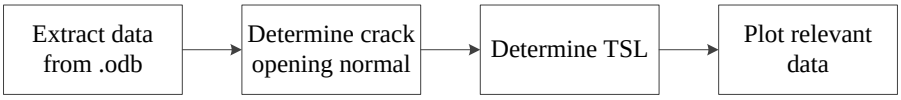

Figure 4.4.1: Activities of the post-processing as part of Figure 4.1.2.

4.4.1 Extract Data

For determining the traction at each iteration the average stress of all the elements is required. In addition to determine the crack orientation angle the node displacement at the last iteration is needed. In the end the following data is extracted using a PYTHON script;

- Load Proportionality Factor (LPF) at each iteration
- Average stress components at each iteration
- Node displacement at last iteration

The extraction of the LPF at each frame (i) and node displacement of each element (j) at the last iteration ($n_{frames} - 1$) is quite straightforward as shown below.

```
LPF[I] = ODB_FILE.STEPS['GENERAL_STEP'].FRAMES[I].FRAMEVALUE
U_NODE[J] = ODB_FILE.STEPS['GENERAL_STEP'].FRAMES[n_frames - 1].FIELDOUTPUTS['U'].VALUES[J].DATA
```

The extraction of the average stress is done by averaging the stress of all the bulk elements (i.e. $j = 1, 2, .., n$) using the equation below.

$$\boldsymbol{\sigma}_{avg,i} = \frac{1}{w \cdot h} \sum_{j=1}^{n} \left(\boldsymbol{\sigma_j} \cdot A_j \right) \tag{4.4.1}$$

where,

$$\boldsymbol{\sigma_j} = \begin{bmatrix} \sigma_{11} & \sigma_{12} \\ \sigma_{12} & \sigma_{22} \end{bmatrix} \tag{4.4.2}$$

The stress tensor ($\boldsymbol{\sigma}$) contains the three stress components of and A_j is the area each bulk element j. At each iteration i the stress tensor and element volume of each bulk element j are extracted using the ABAQUS command below.

```
EVOL[J] = ODB_FILE.STEPS['GENERAL_STEP'].FRAMES[I].FIELDOUTPUTS['EVOL'].VALUES[J].DATA
S_ELEM[J] = ODB_FILE.STEPS['GENERAL_STEP'].FRAMES[I].FIELDOUTPUTS['S'].VALUES[J].DATA
```

4.4.2 Micro- to Macroscopic Coupling

The coupling between the microscopic MVE and the resulting macroscopic behaviour is done in terms of an ETSL[13]. The first step in determining the ETSL is to define the crack line orientation in terms of a crack normal vector, i.e. n as in Figure 4.1.3. This normal vector can then be multiplied with the average stress tensor, in microscopic coordinates, to get the traction along the crack line at each increment.

$$\boldsymbol{\sigma} = \begin{bmatrix} \sigma_{11} & \sigma_{12} \\ \sigma_{12} & \sigma_{22} \end{bmatrix} \begin{bmatrix} n_1 \\ n_2 \end{bmatrix} = \begin{bmatrix} n_1\sigma_{11} + n_2\sigma_{12} \\ n_1\sigma_{12} + n_2\sigma_{22} \end{bmatrix} = \begin{bmatrix} \tau_1 \\ \tau_2 \end{bmatrix} \tag{4.4.3}$$

In order to get the crack normal it is determined which elements have failed at the last increment. For this the displacement of each node is used together with the element connectivity. First the critical opening or separation (δ_f) is determined based on the fracture energy, maximum cohesive strength and elastic stiffness of the cohesive elements.

$$\delta_f = \frac{2G_f}{t_u} - \frac{t_u}{E_c} \tag{4.4.4}$$

Note that for each cohesive element set, i.e. matrix, fiber or interface, the critical opening is different as the input properties vary. When either the normal (δ_n) or shear (δ_s) opening, see Figure 4.4.2, is larger than the critical value the element has failed. In the case that no elements have reached the critical opening a certain percentage of the elements with the highest opening is selected.

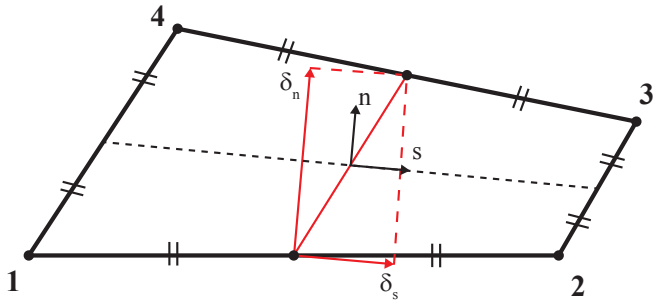

Figure 4.4.2: Illustration of the normal and shear opening of a cohesive element. The opening separations are the components of the vertex between the mid nodes of edge 1-2 and 3-4 in the local (n,s) coordinate system.

For each failed element the opening direction in terms of a unit vector can be determined. After transforming these unit vectors to the microscopic $(1,2)$ coordinate system the weighted average, of all the unit vectors, results in the crack opening normal in $(1,2)$ coordinates. For

[13] In this context, effective indicates that it is an average fracture response of the MVE.

the weight the total opening of the cohesive interface element is considered. An example for a single fiber model subject to LC1 see Figure 4.4.3.

$$\theta = \tan^{-1}\left(\frac{n_2}{n_1}\right) \tag{4.4.5}$$

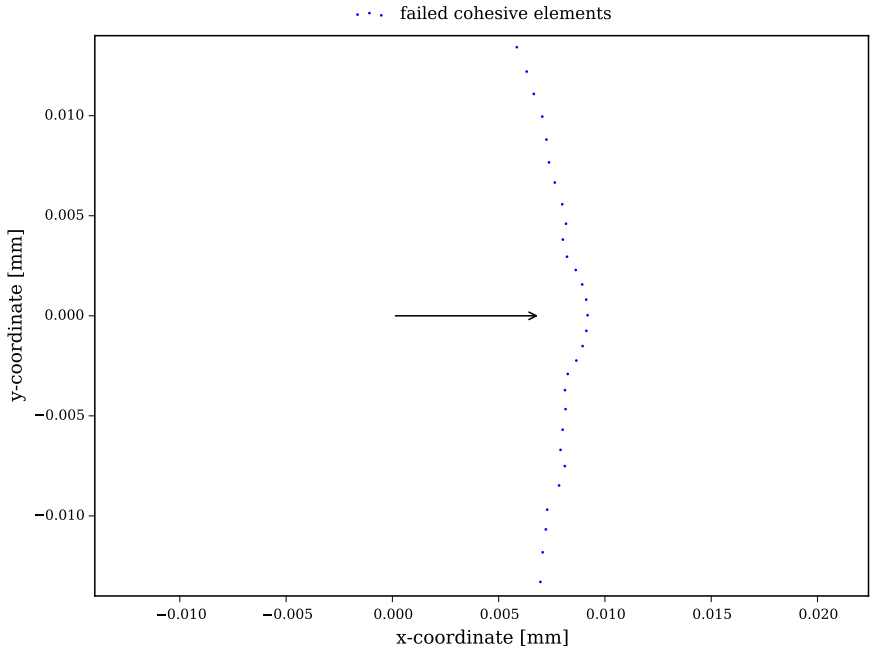

Figure 4.4.3: Example crack opening normal (arrow) for a single fiber model subject to LC1 based on the individual opening direction of the failed cohesive elements.

From the crack opening normal the crack angle (θ) as in Figure 4.1.3 is determined by Equation 4.4.5. Moreover, the traction vector at each increment can be determined using Equation 4.4.3. The total traction (i.e. magnitude) at each increment (i) is subsequently determined with;

$$\tau_i = \sqrt{\tau_1^2 + \tau_2^2} \tag{4.4.6}$$

and at each increment the average separation is determined by multiplying the applied displacement with the LPF of that increment. Once this is done the final ETSL can be plotted.

$$\delta_i = \mathrm{LPF}_i \sqrt{(\varepsilon_{11} w + \varepsilon_{12} h)^2 + (\varepsilon_{21} w + \varepsilon_{22} h)^2} \tag{4.4.7}$$

4.4.3 Plotting and Curve Fitting

For the single fiber models a combined plot with the coarse, medium and fine mesh density ETSL are plotted along with the input TSL of the fiber, matrix and interface cohesive elements, see Appendix A.

For the multiple fiber models identical plots are made but now instead of the coarse, medium and fine mesh models the different realisations are plotted. In addition an average of the the realisations is required, which is obtained using data averaging on the data points of all realisations. The data averaging is performed for separation values ranging from zero to the maximum available separation[14]. At each separation value the average traction of all realisations is determined, if no data point is present at this separation value it is determined using linear interpolation between the data points of the corresponding realisation.

In some cases extrapolation of the ETSL is required. The slope of the linear extrapolated part is based on the average fracture energy of all realisations. Examples of multiple fiber ETSLs, curve fitting and extrapolation can be found in Appendix B.

When results have to be compared, plots are generated that contain the fitted ETSL (or ETSL of the fine mesh density models in the case of single fiber comparison) of models that are to be compared. In this case the maximum cohesive strength and fracture energy are to be compared. The fracture energies are determined using a simple trapezoidal rule up until the maximum available separation as indicated in the plot. In order to study the crack patterns of the models that are compared an additional PYTHON script is written that prints the crack patterns at relevant frames.

[14]The maximum available separation is defined as the value at which data of all realisations is available. For example, realisation 1 goes up to a separation of 0.1 mm but realisation 2 only to 0.08 mm. In this case the data averaging is performed up until 0.08 mm.

Chapter 5

Single Fiber Results and Discussion

The results of the single fiber numerical experiments will be presented in this chapter. The pre- and post-processing are performed according to the methods described in Chapter 4. Additional information will be provided in Section 5.1 after which the results are presented in the subsequent sections. In the end some concluding remarks will be given in Section 5.7. The detailed Effective Traction-Separation Law (ETSL) of each model can be found in Appendix A.

5.1 Methodology

As mentioned in Section 4.1 the single fiber numerical experiments have to provide insight in the effect of the cohesive properties and fiber diameter[1] as listed below. The results will be presented by means of an ETSL and the fine mesh density models will be compared.

- Section 5.2: interface cohesive strength
- Section 5.3: fiber cohesive strength
- Section 5.4: interface fracture energy
- Section 5.5: fiber fracture energy
- Section 5.6: fiber diameter

[1] The effect of fiber diameter in the single fiber simulations is equivalent to the effect of fiber volume fraction for the multiple fiber simulations.

Based on the paper of Cid Alfaro [18] a fiber diameter (d_F) of 10 µm is chosen, see Figure 5.1.1a. The width and height of the Microstructural Volume Element (MVE) are 28 µm resulting in a fiber volume fraction of 10%. To study the effect of fiber diameter the diameter is increased to 20 µm as in Figure 5.1.1b, resulting in a fiber volume fraction of 40%. The fiber is located exactly in the center of the MVE.

(a) Reference model ($d_F = 10$ µm). **(b)** Modified model ($d_F = 20$ µm).

Figure 5.1.1: Fiber distributions for a 28×28 µm single fiber model.

The cohesive properties are changed with respect to the reference properties as in Table 4.1. The properties are normalised with the properties of the matrix cohesive elements. In this way the properties are tested for values smaller (0.5), equal (1.0) and greater (2.0) compared to the properties of the matrix cohesive elements.

Each effect is studied for three load cases; uni-axial extension (LC1), pure shear (LC2) and an arbitrary mixed loading case (LC0). Refer to Table 4.2 for the applied strain values. In addition, three mesh densities will be evaluated: a coarse, medium and fine mesh density. According to the short discussion on mesh density in Section 3.1 a mesh density of at least 11 µm is required. For a fiber radius of 5 µm this results in 3 nodes on the fiber arc, which is not feasible and thus more are nodes are required. This indicates that the mesh density is fine enough in any case. For the coarse, medium and fine mesh it was chosen to place 20, 40, 80 nodes on the fiber arc resulting in a mesh density of 1.57 µm , 0.785 µm and 0.393 µm respectively.

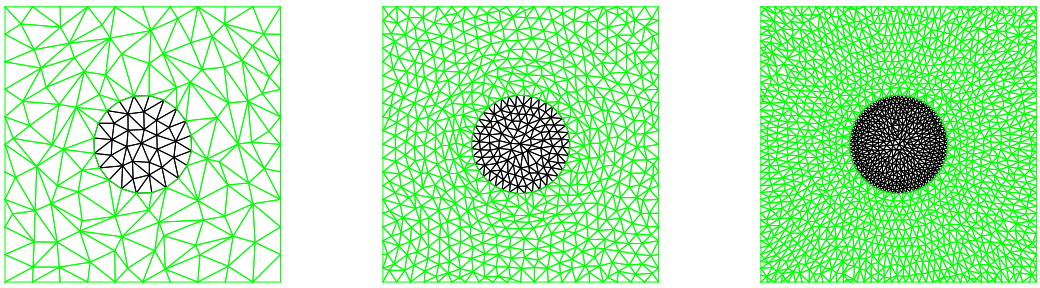

(a) Coarse mesh density. **(b)** Medium mesh density. **(c)** Fine mesh density.

Figure 5.1.2: FE meshes of the reference single fiber model.

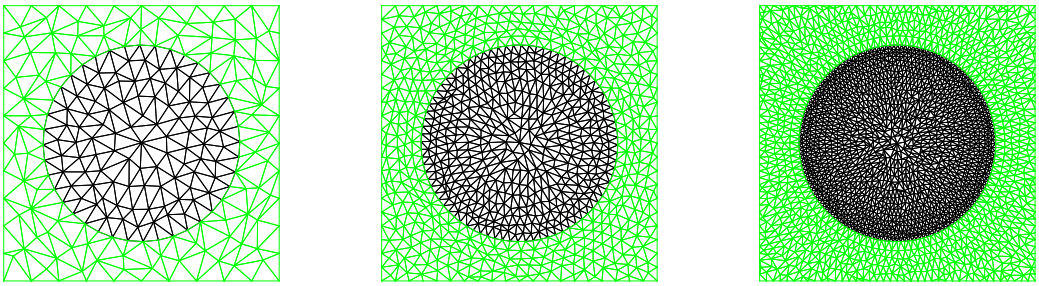

(a) Coarse mesh density. **(b)** Medium mesh density. **(c)** Fine mesh density.

Figure 5.1.3: FE meshes of the increased fiber diameter single fiber model.

The FE mesh of the coarse, medium and fine models are illustrated in Figure 5.1.2. These meshes will be used for all the single fiber simulations except for the simulations with an increased fiber diameter of which the meshes are shown in Figure 5.1.3. It can be observed that the node distribution around the fiber is not totally random. This is due to the fact that no random perturbation is applied to the nodes yet at the point in the research where the single fiber meshes where generated. If the node distribution is not totally random the fracture pattern will be too mesh dependent. For the multiple fiber simulations the MATLAB meshing script was improved. The properties of the six meshes shown above are given in Table 5.1. Note that the number of nodes are excluding the two dummy nodes.

Table 5.1: Properties of the single fiber meshes shown in Figure 5.1.2 and 5.1.3.

Mesh density	**# nodes**	**# bulk elements**	**# cohesive elements**
REFERENCE MODEL			
Coarse: 1.57 µm	840	280	400
Medium: 0.785 µm	3900	1300	1910
Fine: 0.393 µm	9426	3142	6433
INCREASED FIBER DIAMETER MODEL			
Coarse: 1.57 µm	1326	442	643
Medium: 0.785 µm	5094	1698	2507
Fine: 0.393 µm	14370	4790	7105

Of all the nodes only about 17-18% are the original nodes, thus due to the cohesive elements the number of nodes is increased about a factor 5.5. This indicates the significant effect the cohesive elements have on the Degrees of Freedom (DOF). About 40% of the elements are bulk elements and the linear increase in mesh density results in a linear increase in nodes and elements. The model with an increased fiber diameter has an increased number of nodes and elements compared to the reference model, which is explained by the denser mesh at the fiber arc.

5.2 Effect of Interface Cohesive Strength

The first effect on single fiber models that is studied is the effect of interface cohesive strength. Compared to the reference model this value is changed from 25 MPa, factor 0.5 compared to the matrix cohesive strength, to a factor 1.0 and 2.0. The results for LC1 are given in Figure 5.2.1.

It is clearly observed that the maximum cohesive strength and fracture energy of the ETSL with a factor 1.0 and 2.0 is higher compared to the reference model. There is no difference in the initial slope of the ETSL and the models with a factor 1.0 and 2.0 are almost identical. Looking at the crack patterns in Figure 5.2.4a explains why these two models are almost identical. In the case the cohesive strength of the interface cohesive elements is equal than the matrix material the crack is more likely to initiate in the matrix material. For the factor 2.0 the fiber-matrix interface is not the weak point anymore and the damage will always initiate in the matrix. For the pure shear load case and mixed load case, in Figure 5.2.2 and 5.2.2 respectively, the same can be concluded.

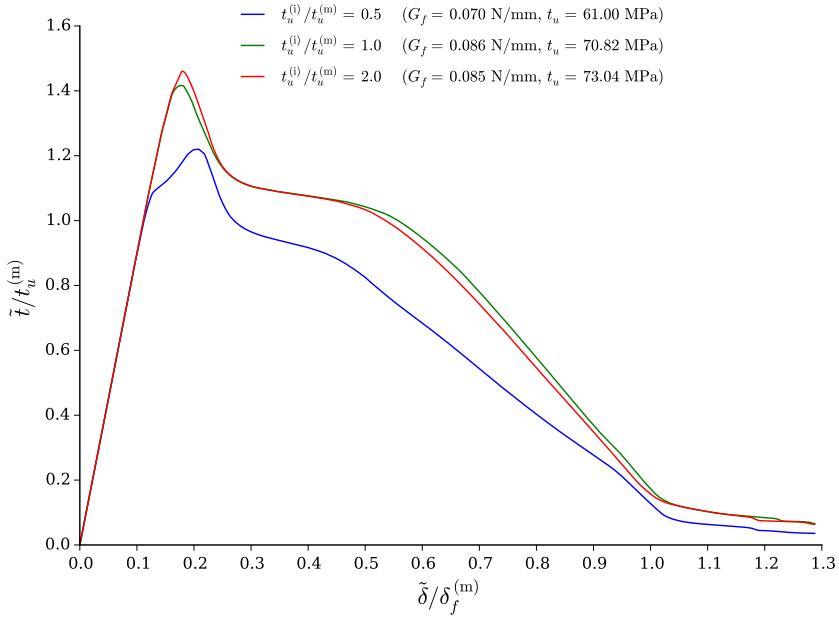

Figure 5.2.1: Effect of interface cohesive strength ($t_u^{(i)}$) on the fracture mechanism, in terms of a ETSL, of the single fiber model subjected to uni-axial extension (LC1).

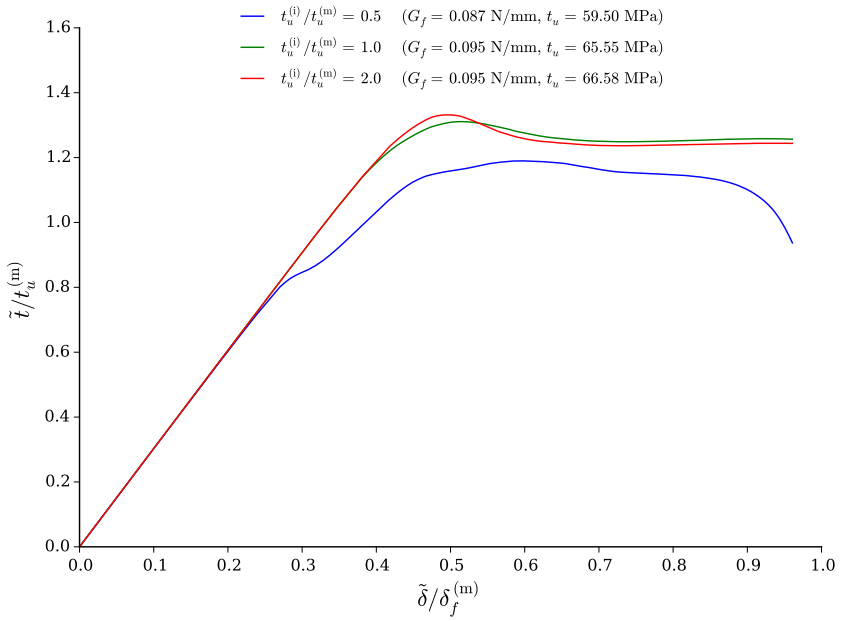

Figure 5.2.2: Effect of interface cohesive strength ($t_u^{(i)}$) on the fracture mechanism, in terms of a ETSL, of the single fiber model subjected to pure shear (LC2).

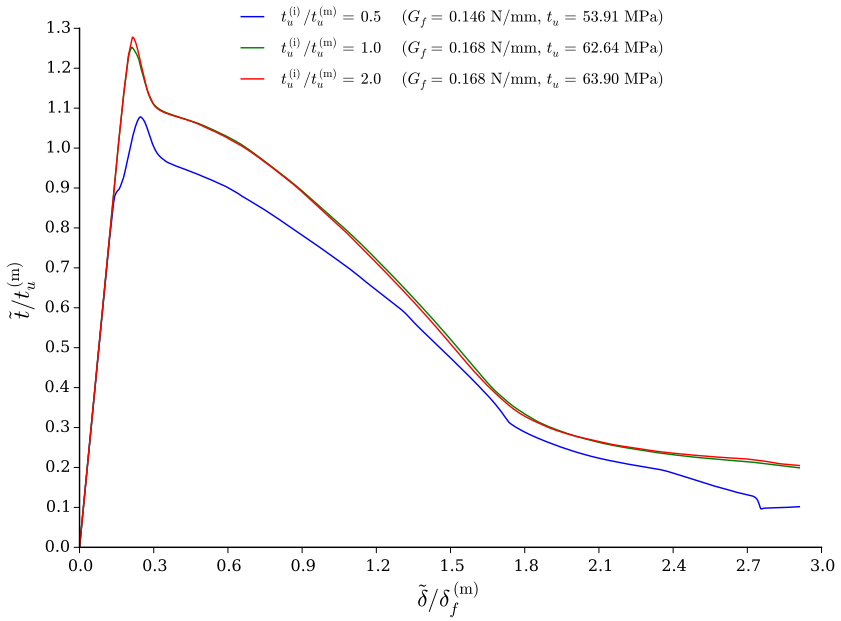

Figure 5.2.3: Effect of interface cohesive strength ($t_u^{(i)}$) on the fracture mechanism, in terms of a ETSL, of the single fiber model subjected to a mixed loading (LC0).

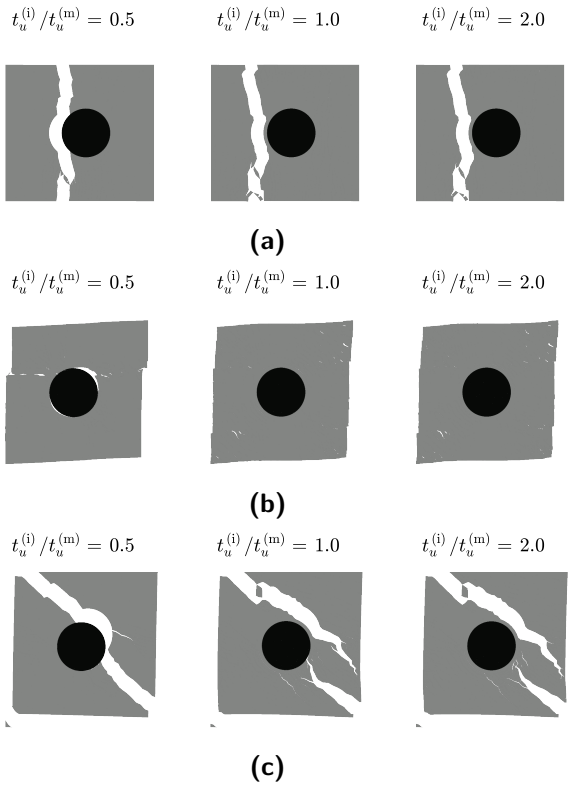

Figure 5.2.4: Crack patterns corresponding to; (a) Figure 5.2.1, (b) Figure 5.2.2 and (c) Figure 5.2.3.

5.3 Effect of Fiber Cohesive Strength

The second effect that is studied is the effect of the fiber cohesive strength, of which the results are presented in this section. In contrast to the previous section the cohesive strength of the fiber cohesive elements is changed from 100 MPa (factor 2.0) in the reference model to 50 MPa (factor 1.0) and 25 MPa (factor 0.5). The results of the three load cases are given in Figure 5.3.1 to 5.3.3.

In general the maximum cohesive strength decreases for lower factors. Especially for 0.5 due to the crack initiating in the fiber, see Figure 5.3.4. Moreover, for LC1 and 0 the fracture energy is higher in this case. This is due to the higher input fracture energy of the fiber cohesive elements, i.e. once the crack initiates in the fiber it takes more energy to propagate compared to crack initiation in the matrix or interface. For LC2 the fracture energy is lower when the crack initiates in the fiber. However, it is expected that if the ETSL goes up to zero traction[2] runs the same effect as for the other load cases will be present. Again, there is not much difference between factor 2.0 and 1.0 because in these cases the fiber-matrix interface is still the weak point.

[2]Due to convergence problems the simulations of the pure shear load case abort early.

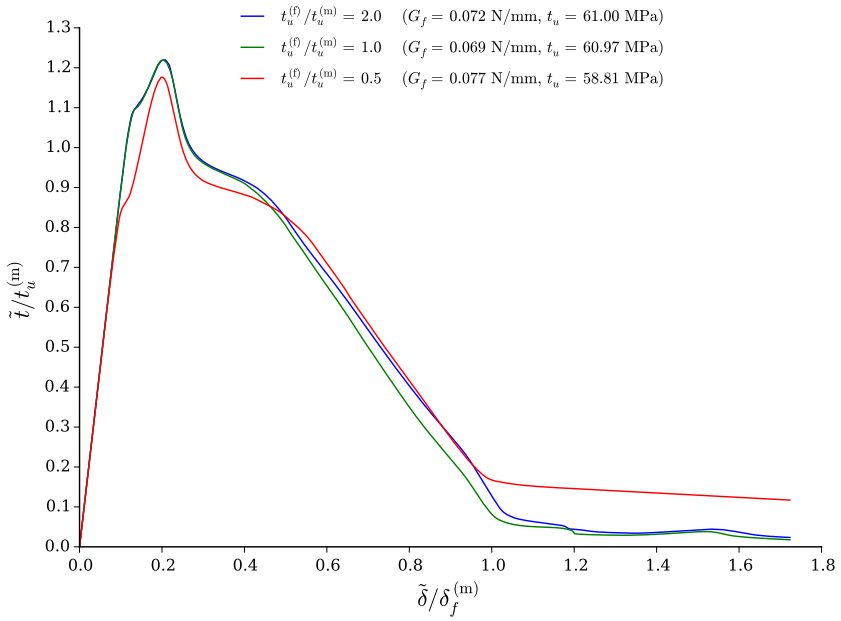

Figure 5.3.1: Effect of fiber cohesive strength ($t_u^{(f)}$) on the fracture mechanism, in terms of a ETSL, of the single fiber model subjected to uni-axial extension (LC1).

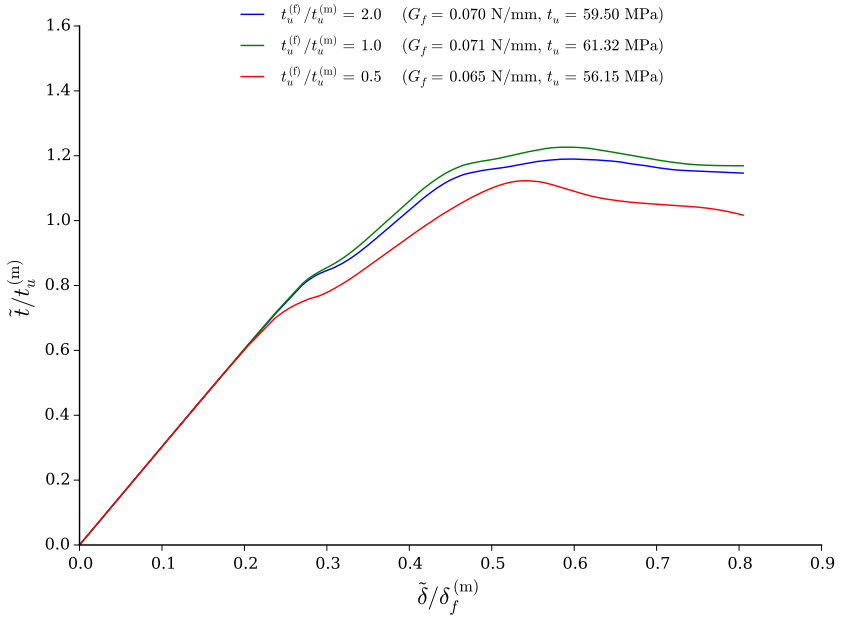

Figure 5.3.2: Effect of fiber cohesive strength ($t_u^{(f)}$) on the fracture mechanism, in terms of a ETSL, of the single fiber model subjected to pure shear (LC2).

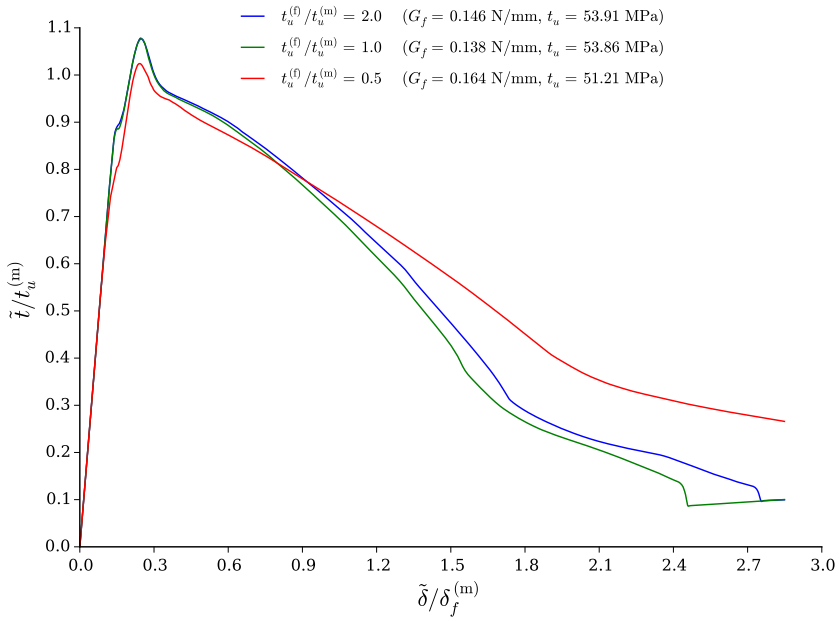

Figure 5.3.3: Effect of fiber cohesive strength ($t_u^{(f)}$) on the fracture mechanism, in terms of a ETSL, of the single fiber model subjected to a mixed loading (LC0).

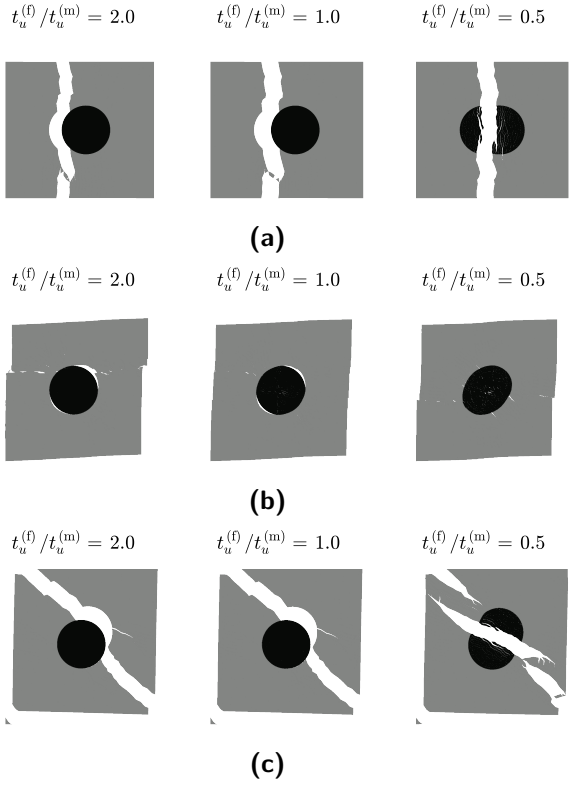

Figure 5.3.4: Crack patterns corresponding to; (a) Figure 5.3.1, (b) Figure 5.3.2 and (c) Figure 5.3.3.

5.4 Effect of Interface Fracture Energy

Next to the maximum cohesive strength, the fracture energy is the second parameters that defines the input Traction-Separation Law (TSL). Starting with the effect of interface fracture energy for the three load cases. The reference value of 0.025 N/mm (factor 0.5) is increased to 0.05 N/mm (factor 1.0) and 0.1 N/mm (factor 2.0). For uni-axial extension and the mixed load case almost no difference is observed in the maximum cohesive strength. A small difference is observed for LC0 due to a different fracture pattern, see Figure 5.4.4c. There is a small increase in fracture energy visible in the ETSLs of Figure 5.4.1 and 5.4.3, which indicates that more energy is required to fully crack the model. For pure shear in Figure 5.4.2 there is a difference in maximum cohesive strength as well as the fracture energy, which is due to the shearing behaviour.

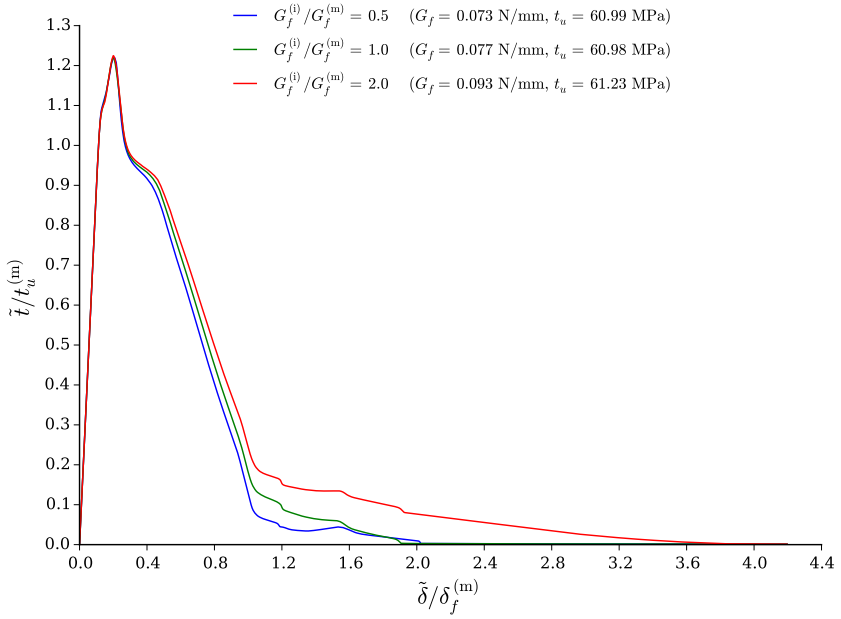

Figure 5.4.1: Effect of interface fracture energy ($G_f^{(i)}$) on the fracture mechanism, in terms of a ETSL, of the single fiber model subjected to uni-axial extension (LC1).

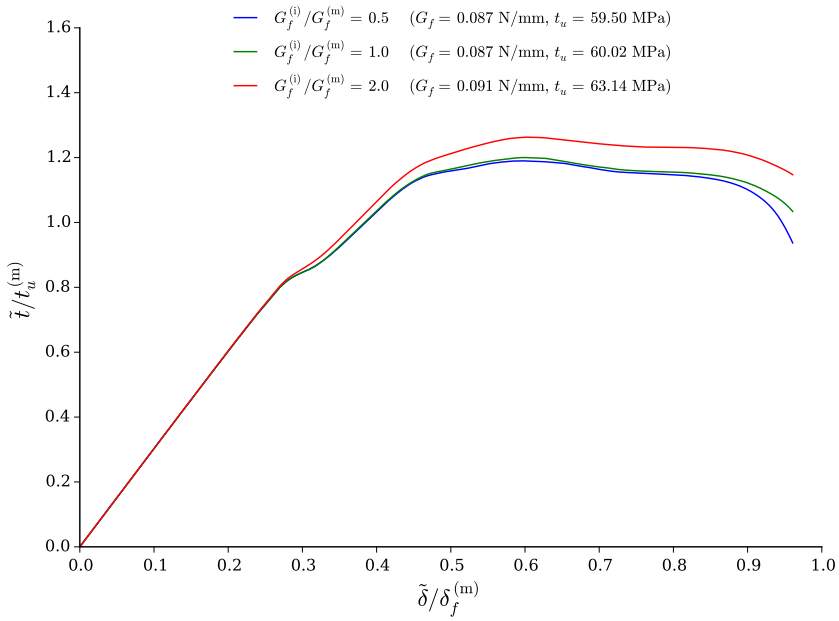

Figure 5.4.2: Effect of interface fracture energy ($G_f^{(i)}$) on the fracture mechanism, in terms of a ETSL, of the single fiber model subjected to pure shear (LC2).

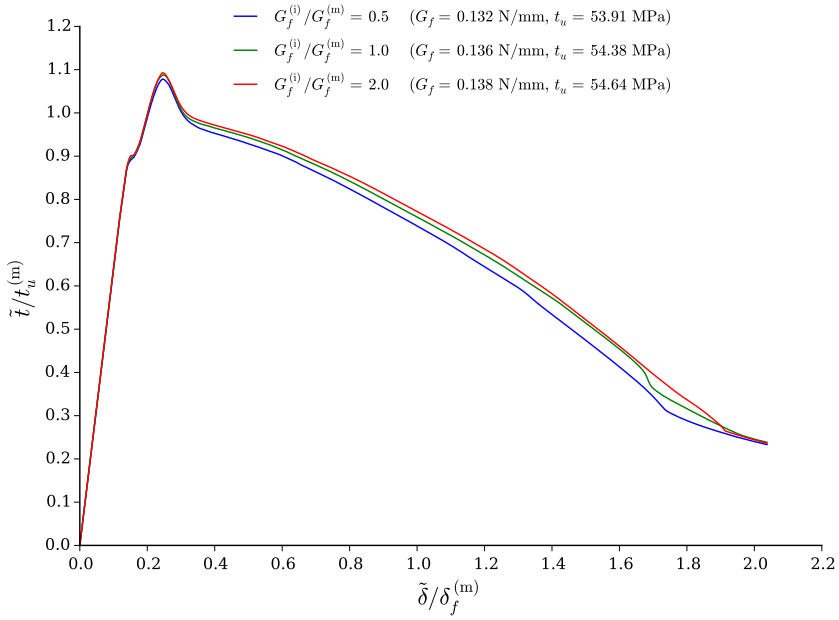

Figure 5.4.3: Effect of interface fracture energy ($G_f^{(i)}$) on the fracture mechanism, in terms of a ETSL, of the single fiber model subjected to a mixed loading (LC0).

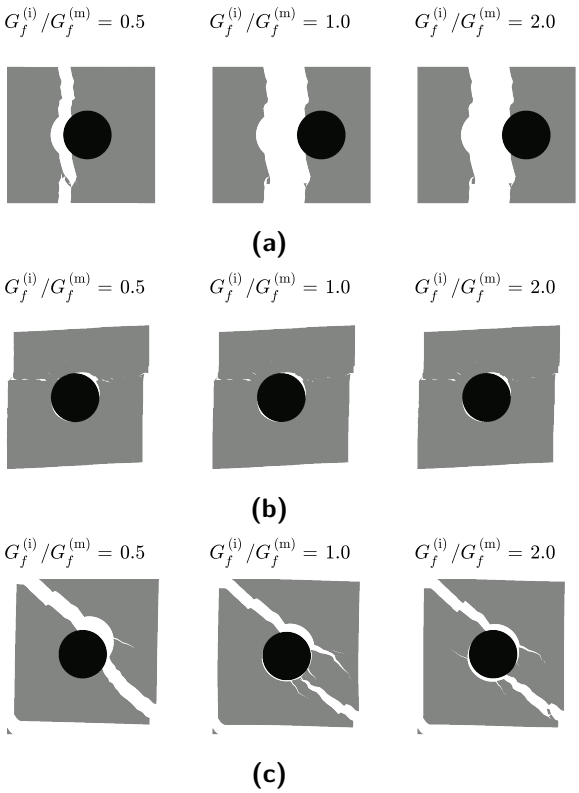

Figure 5.4.4: Crack patterns corresponding to; (a) Figure 5.4.1, (b) Figure 5.4.2 and (c) Figure 5.4.3.

5.5 Effect of Fiber Fracture Energy

The fourth effect that is studied is the effect of fiber fracture energy. The reference value of 0.1 N/mm (factor 2.0) is decreased to 0.05 N/mm (factor 1.0) and 0.025 N/mm (factor 0.5). From the results presented in Figure 5.5.1 to 5.5.4 it can be concluded that there is no noticeable difference when changing the fiber fracture energy. This is due to the fact that there is no interaction with the fiber cohesive elements because no cracks are initiated in the fiber. For LC1 and LC0 there is a small difference in fracture energy which can be explained by a small, although not visible, change in fracture pattern.

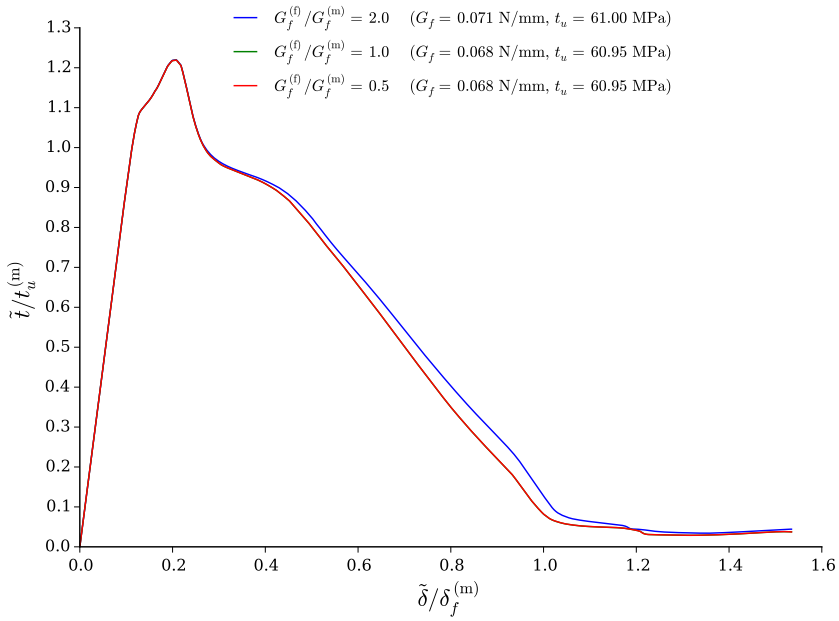

Figure 5.5.1: Effect of fiber fracture energy ($G_f^{(f)}$) on the fracture mechanism, in terms of a ETSL, of the single fiber model subjected to uni-axial extension (LC1).

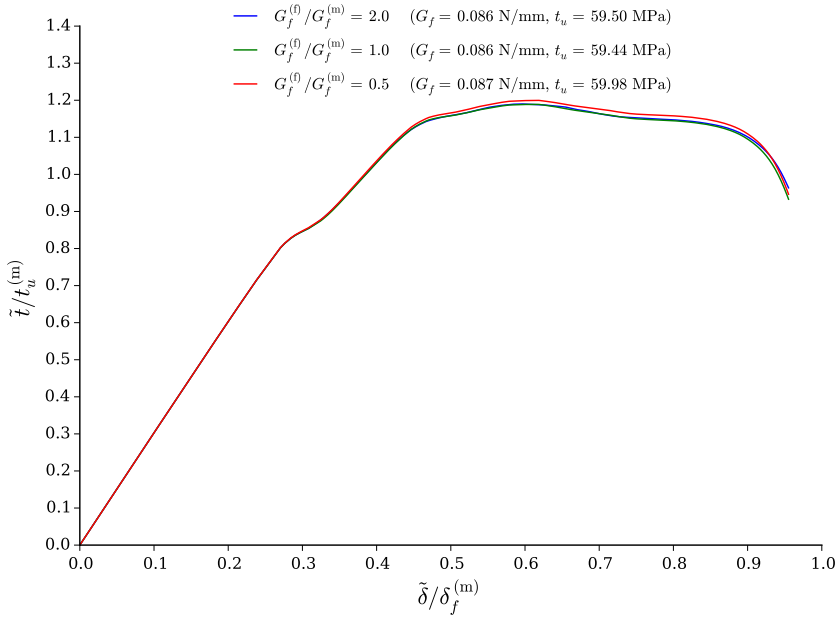

Figure 5.5.2: Effect of fiber fracture energy ($G_f^{(f)}$) on the fracture mechanism, in terms of a ETSL, of the single fiber model subjected to pure shear (LC2).

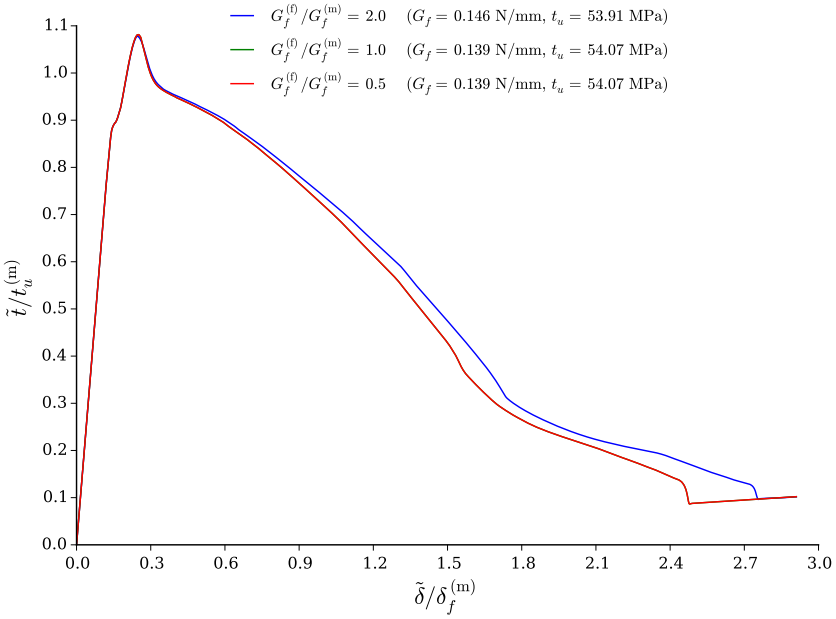

Figure 5.5.3: Effect of fiber fracture energy ($G_f^{(f)}$) on the fracture mechanism, in terms of a ETSL, of the single fiber model subjected to a mixed loading (LC0).

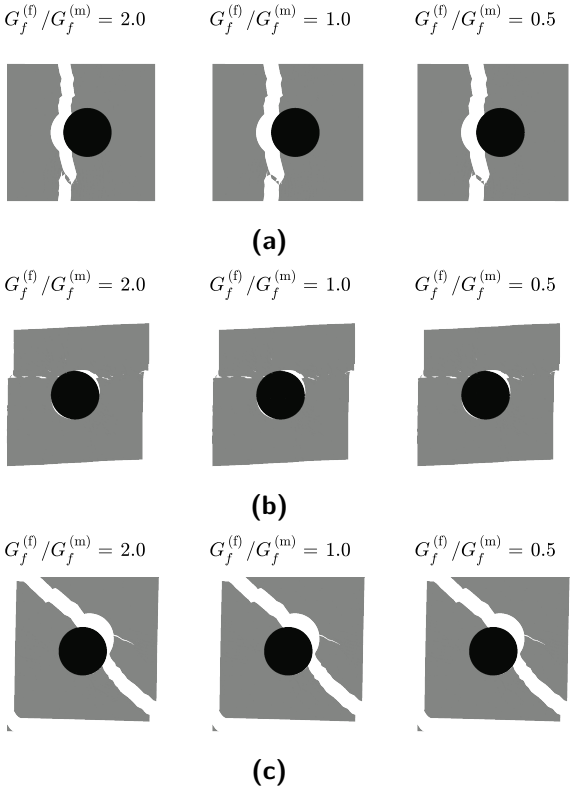

Figure 5.5.4: Crack patterns corresponding to; (a) Figure 5.5.1, (b) Figure 5.5.2 and (c) Figure 5.5.3.

5.6 Effect of Fiber Diameter

The last effect that is studied is the increase in fiber diameter. The diameter is increased by a factor two, from 10 µm to 20 µm . For each load case it is observed that for a higher fiber diameter the initial slope of the ETSL increases and the fracture energy decreases. The increase in initial slope is due to a higher effective stiffness of the model as a results of more fiber compared to the reference model. The fracture energy decreases because less energy is required to fully crack the model, there is less matrix material available. For the pure shear load case in Figure 5.6.2 it is observed that also the maximum cohesive strength decreases as a result of a larger fiber-matrix interface. In addition the crack pattern is different according to Figure 5.6.4b.

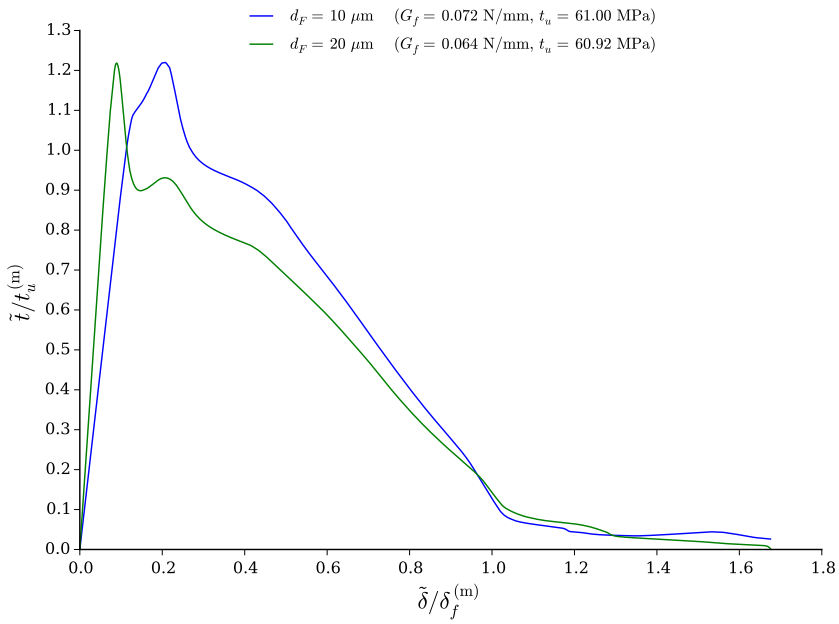

Figure 5.6.1: Effect of fiber diameter on the fracture mechanism, in terms of a ETSL, of the single fiber model subjected to uni-axial extension (LC1).

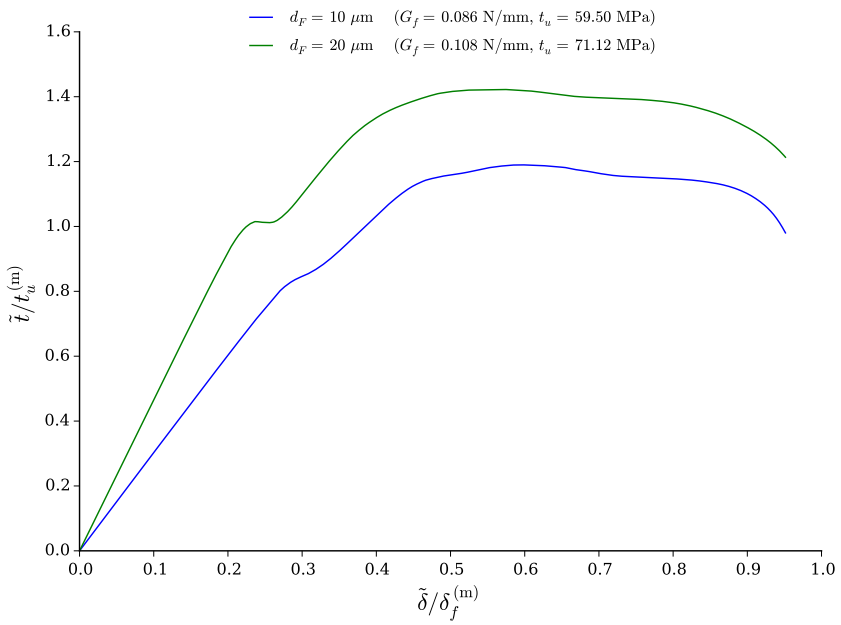

Figure 5.6.2: Effect of fiber diameter on the fracture mechanism, in terms of a ETSL, of the single fiber model subjected to pure shear (LC2).

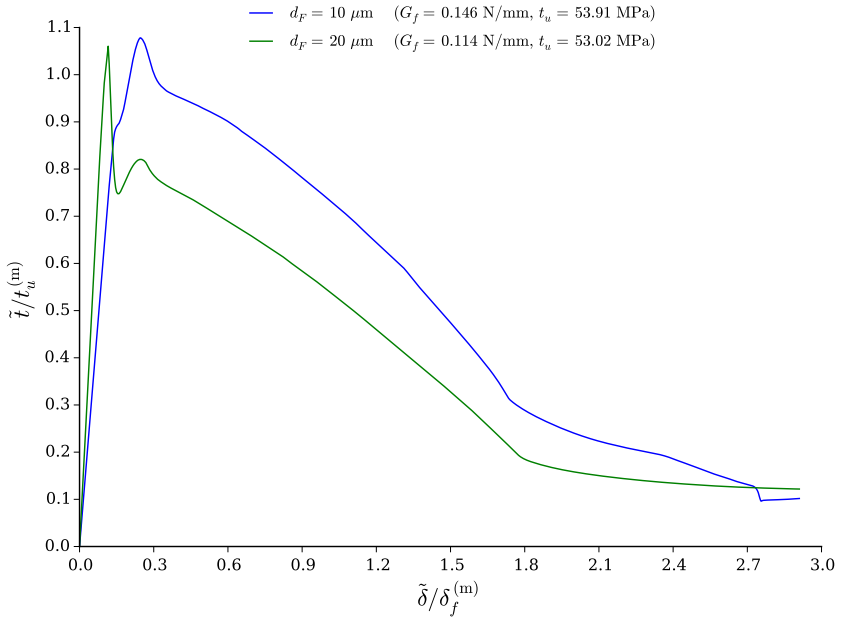

Figure 5.6.3: Effect of fiber diameter on the fracture mechanism, in terms of a ETSL, of the single fiber model subjected to a mixed loading (LC0).

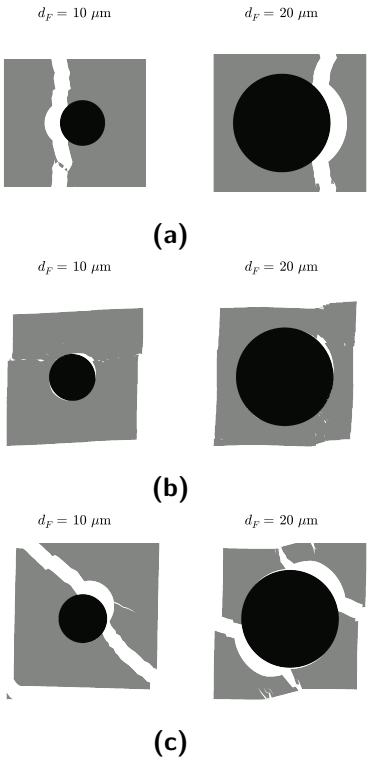

Figure 5.6.4: Crack patterns corresponding to; (a) Figure 5.6.1, (b) Figure 5.6.2 and (c) Figure 5.6.3.

5.7 Concluding Remarks

The effect of the cohesive parameters of the interface and fiber cohesive elements relative to the cohesive properties of the matrix cohesive properties has been presented in this chapter. In addition the effect of fiber diameter was studied. The results were given by comparing the ETSLs of the fine mesh density models. Overall the single fiber simulations gave insight in the influence of cohesive parameters and the choice of mesh density for the multiple fiber models.

Increasing the interface cohesive strength has a strong influence on the maximum cohesive strength and fracture energy. In the case this value is higher or equal to the matrix cohesive strength the crack will initiate within the matrix or at the fiber-matrix interface. This results in a higher maximum cohesive strength and fracture energy. There is only a small difference between a factor 1.0 and 2.0.

Decreasing the fiber cohesive strength has a strong influence on the maximum cohesive strength and a small influence on the fracture energy. In the case the fiber is the weak point, i.e. for a factor 0.5, the crack will initiate within the fiber. It is expected that for a factor greater

than 0.5 but smaller than 1.0 the crack will initiate on the fiber-matrix interface but will first propagate through the fiber before propagating within the matrix. Although cracks within the fiber are not expected to occur in 'real life' it is good to get a complete overview.

Increasing the interface fracture energy has almost no influence on the maximum cohesive strength, except when some small changes in fracture patterns occur. The total fracture energy increases for higher factors as more energy is required to fully open a interface cohesive element. The decrease in fiber fracture energy has no influence on the ETSL. An increasing fiber diameter increases the initial slope of the ETSL and decreases the fracture energy.

In Appendix A a comparison of the coarse, medium and fine mesh density models can be found. It is difficult to identify mesh convergence when looking at each simulation separately. The results for pure shear are spurious, there is no clear convergence visible in most cases. From the uni-axial extension and mixed load case it is concluded that the coarse or medium mesh density is not sufficient. However, in the case a fine mesh density a multiple fiber model will result in a high number of DOF. The simulations would simply take up too much time. Therefore, a compromise between the medium and fine mesh density was chosen for the remainder of the simulations, i.e. 0.5 μm.

Chapter 6

Size Determination of Microstructural Volume Elements

Before the multiple fiber numerical experiments can be performed the dimensions of the Microstructural Volume Element (MVE) has to be determined that ensures it is representative for the larger structure. In Section 2.3.5 of the literature review some Representative Volume Element (RVE) considerations were mentioned that will be used in this chapter. First in Section 6.1 the methodology of three approaches mentioned in the three subsequent sections is explained. At the end of this chapter some concluding remarks are given.

6.1 Methodology

Obviously, the methodology to determine the dimensions of the RVE is to determine the fracture response for different MVE dimensions. It is expected that convergence can be seen for an increasing MVE size. The first step is to determine the variables like cohesive parameters, fiber volume fraction, load cases, number of realisations[1] and MVE dimensions.

If all of these parameters are variable the number of simulations would be too high. Therefore, it is chosen to limit the simulations to a fixed volume fraction and only one load case with the cohesive properties as listed in Table 4.1. A volume fraction of 40% is chosen and an

[1] The fiber distribution of multiple fiber models can be realised in different ways. In order to get an average response a certain number of realisations are simulated.

arbitrary mixed load case is applied, see LC0 in Table 4.2. The response is averaged over five realisations for six different sample sizes ranging from 25×25 µm to 150×150 µm .

It was mentioned that there are three approaches, this is due to problems related to artificial compliance. For a discussion on artificial compliance one can refer to Section 4.2. During the first comparison of the results obtained with the original approach it was concluded that no clear conclusion could be drawn, as will be explained in Section 6.2. In order to tackle the problem with artificial compliance two alternative approaches were studied.

- Case I: Keep the number of cohesive elements constant over all the MVE sizes
- Case II: Reduce the elastic stiffness of the cohesive elements for smaller MVE sizes

The first case ensures that there is an equal amount of cohesive elements and thus an equivalent artificial compliance on all the MVE sizes. The second case lowers the elastic stiffness of the cohesive elements to ensure an equal amount of artificial compliance, even when the number of cohesive elements is not equal. Due to limited time the 125 and 150 µm models were excluded in the alternative approaches, because the analysis of these models took the longest. As the results are compared to the 100×100 µm model of the original approach only the 25, 50 and 75 models have to be analysed in the alternative approaches.

6.2 Original Approach

In this section the results and discussion of the original approach in determining the MVE size is presented. An overview of the fiber distributions are given in Figure 6.2.1 to 6.2.6 for 25, 50, 75, 100, 125 and 150 µm MVEs respectively.

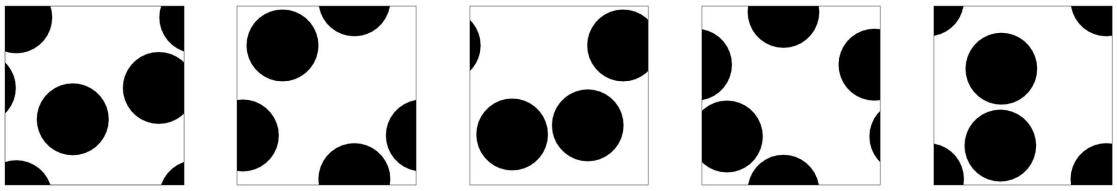

(a) R1 **(b)** R2 **(c)** R3 **(d)** R4 **(e)** R5

Figure 6.2.1: Different realisations for the 25×25 µm MVE.

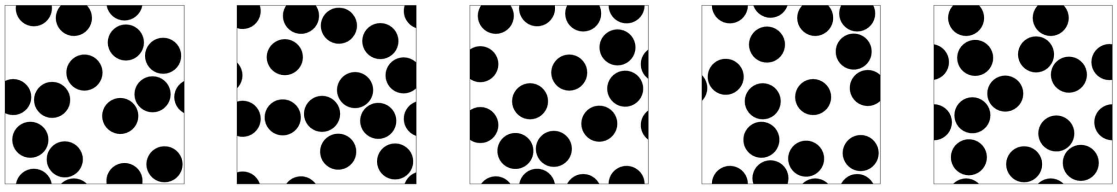

(a) R1 **(b)** R2 **(c)** R3 **(d)** R4 **(e)** R5

Figure 6.2.2: Different realisations for the 50×50 µm MVE.

(a) R1 **(b)** R2 **(c)** R3 **(d)** R4 **(e)** R5

Figure 6.2.3: Different realisations for the 75×75 µm MVE.

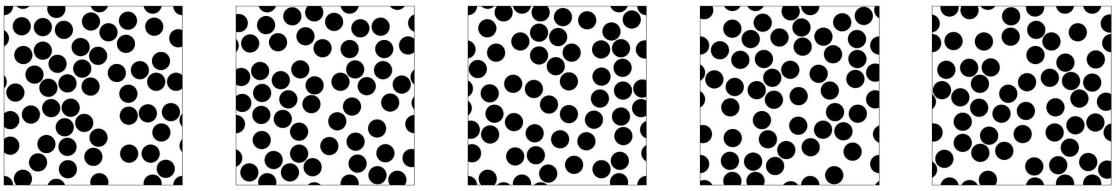

(a) R1 **(b)** R2 **(c)** R3 **(d)** R4 **(e)** R5

Figure 6.2.4: Different realisations for the 100×100 µm MVE.

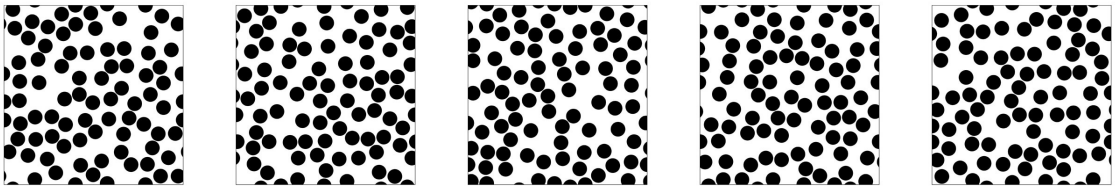

(a) R1 **(b)** R2 **(c)** R3 **(d)** R4 **(e)** R5

Figure 6.2.5: Different realisations for the 125×125 µm MVE.

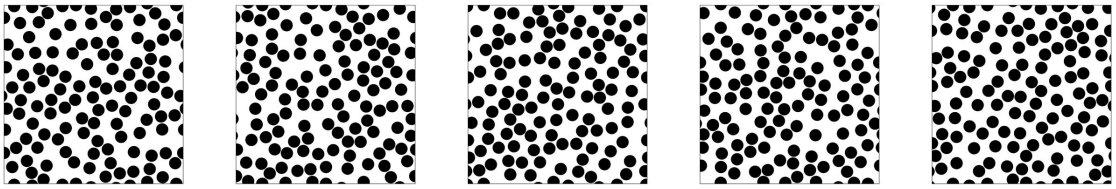

(a) R1 **(b)** R2 **(c)** R3 **(d)** R4 **(e)** R5

Figure 6.2.6: Different realisations for the 150×150 µm MVE.

The individual ETSLs of each realisation and the averaging is given in Appendix B.1. The average Effective Traction-Separation Law (ETSL) of each MVE size is compared in Figure 6.2.7. The effect of artificial compliance increases for an increasing MVE size, as can clearly be observed by a decreasing slope of the linear elastic part. Moreover, the softening slope of the ETSL is significantly higher resulting in an increase in fracture energy. Due to the additional cohesive elements more energy can be absorbed before the model is fully cracked. No conclusions regarding convergence can be obtained from these results.

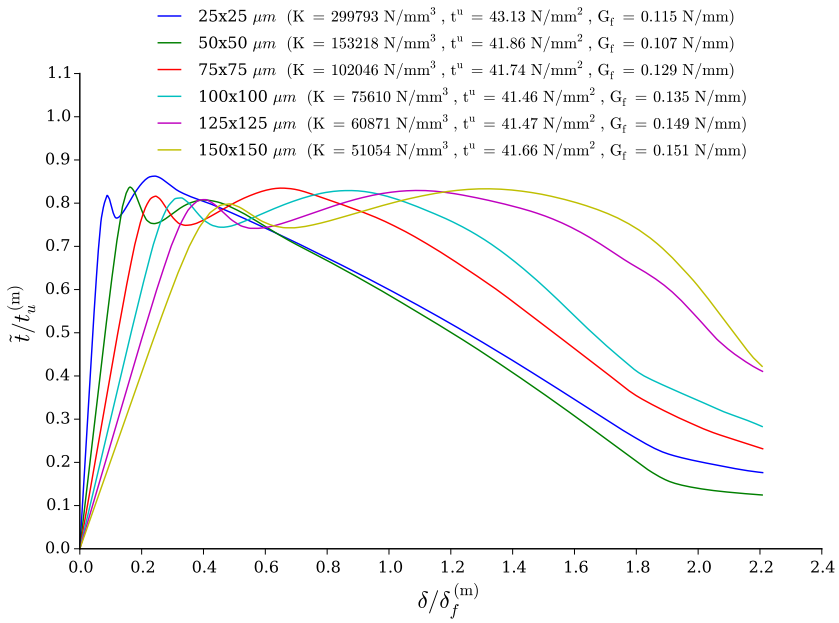

Figure 6.2.7: Comparison of the ETSLs of different MVE sizes, original approach.

A conclusion that can be drawn from the above results is that after damage initiation (first peak) the traction drops but increases again afterwards. After a thorough investigation it is concluded that this is due to the following. The first time the traction drops the elements along the fiber-matrix interface are activated and start opening, because this is the weak point with the lowest cohesive strength. At some point the interface of each fiber is fully separated and the crack has to propagate into the matrix material. Due the fact that the cohesive strength of the matrix cohesive elements is higher it is harder to propagate and therefore the traction is able to increase again. The second drop in traction indicates matrix cracking.

6.3 Alternative Approach: Case I

For the first alternative approach the number of elements is kept constant for each MVE size. In order to achieve this it is infeasible to change the mesh density. For the 25×25 µm model this will simply result in a too small mesh density resulting in numerical difficulties within the MATLAB meshing script. An alternative is to keep the MVE dimensions constant, i.e. 100×100 µm , and increase the fiber diameter to represent smaller MVE sizes. This approach is justified by the fact that it has to be determined how many details, i.e. fibers, have to be present within the MVE in order to be representative. Due to the fact that the mesh is changed different realisations have been generated and are presented in Figure 6.3.1 to 6.3.3.

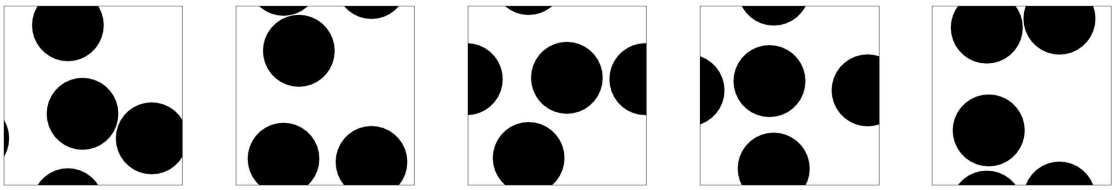

(a) R1 **(b)** R2 **(c)** R3 **(d)** R4 **(e)** R5

Figure 6.3.1: Different realisations for the 25×25 µm MVE.

(a) R1 **(b)** R2 **(c)** R3 **(d)** R4 **(e)** R5

Figure 6.3.2: Different realisations for the 50×50 µm MVE.

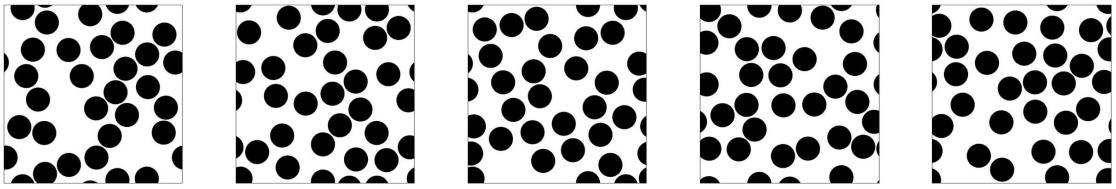

(a) R1 **(b)** R2 **(c)** R3 **(d)** R4 **(e)** R5

Figure 6.3.3: Different realisations for the 75×75 µm MVE.

In order to check if the number of cohesive elements is equal for each MVE dimension the resulting meshes are compared to the meshes of the 100×100 µm MVEs of the original approach in Table 6.1. It can be seen that there is a maximum difference of 2% in the number of cohesive elements, which is acceptable.

Table 6.1: Difference in number of cohesive elements in the models of the alternative approach case I, compared to the 100×100 µm model.

Realisation	**25×25 μm**	**50×50 μm**	**75×75 μm**	**100×100 μm**
1	86384	86266	87451	87604
2	86542	86331	87656	87904
3	87355	85764	87594	87541
4	87484	85310	87651	87607
5	86038	85811	87661	87517
average	**86761**	**85896**	**87603**	**87635**
error [%]	-1,00	-1,98	-0,04	0,00

The detailed results can be found in Appendix B.2 and the average ETSL of each MVE size is plotted in Figure 6.3.4. In contrast to the original approach the initial slope of each ETSL

aligns, which indicates an equal amount of artificial compliance. For an increasing MVE size the maximum cohesive strength decreases, which is due to a higher probability of fiber-matrix interface cracks due to an increasing number of fibres. In addition the fracture energy increases for an increasing MVE size. From these results conclusions can be drawn, which will be given in Section 6.5.

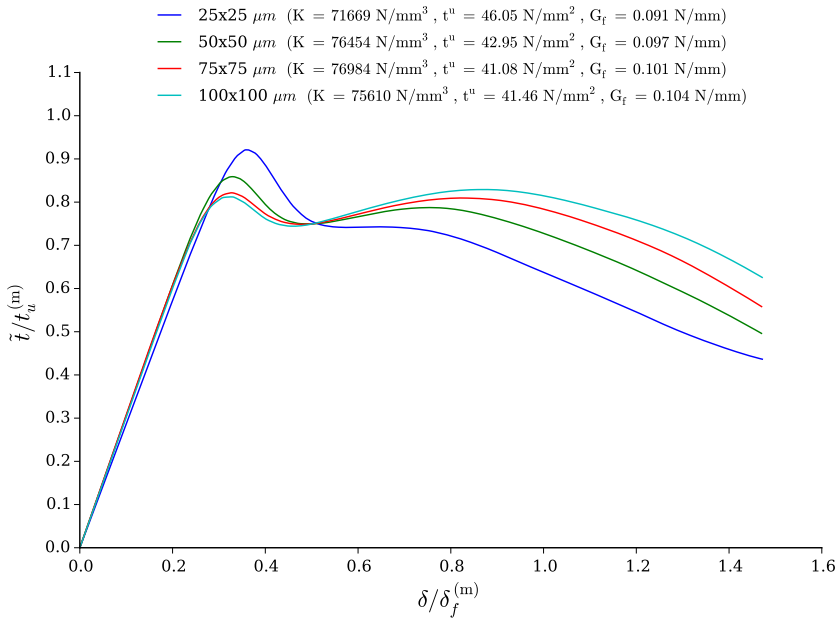

Figure 6.3.4: Comparison of the ETSLs of different MVE sizes, alternative approach: case I.

6.4 Alternative Approach: Case II

For the second alternative approach the elastic stiffness of the cohesive elements is decreased for a decreasing MVE size. In this way the initial slope will be aligned, just as in the previous section. As there is no clear relation between the number of cohesive elements and the initial slope of the ETSL the elastic stiffness has to be obtained by trial and error. Compared to the original elastic stiffness of 10e9 N/mm^3 it is concluded that the elastic stiffness should be decreased to 1.2e7, 6e7 and 1.15e8 N/mm^3 for the 25, 50 and 75 µm models respectively. The same fiber distributions as for the original approach are used as only a material parameter is changed, not the geometry.

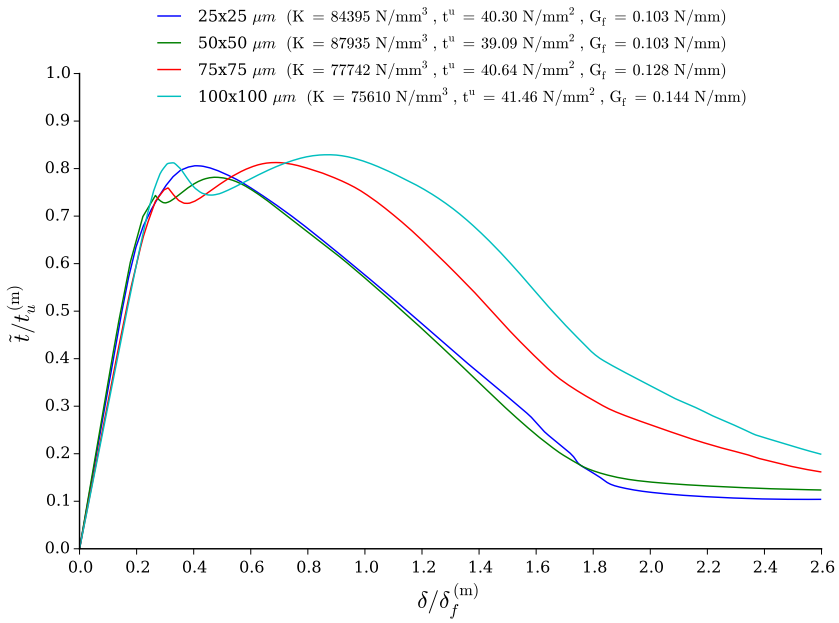

Figure 6.4.1: Comparison of the ETSLs of different MVE sizes, alternative approach: case II.

The results of the second alternative approach are given in Figure 6.4.1 and details on the ETSLs can be found in Appendix B.3. Again the initial slope is quite in line with the 100×100 µm model. However, no clear convergence in the maximum cohesive strength can be seen. The only aspect that can be observed is the nature of the ETSL after the first peak. For example, only one peak is present for the smallest MVE in contrast to two peaks for the other MVE sizes. The overall conclusions of this chapter are presented in the next section.

6.5 Concluding Remarks

The goal of this chapter was to determine the dimensions of the MVE in which it contains enough microstructural details in order to be representative for a larger part of the structure, i.e. a RVE. Three approaches have been presented of which for only one convergence was observed. According to the first alternative approach, where the number of cohesive elements was kept constant, it can be concluded that a MVE size of 75×75 µm is representative. However, this is not observed for the other two approaches.

Due to the limited time available within a masters thesis it was chosen to continue with the 75×75 µm as RVE dimensions. It is recognized that this might not be representative for all load cases, fiber volume fractions and for changes in material/cohesive properties. A more detailed study should be performed in order to give a definitive conclusion on this matter. For now these RVE dimensions are suitable to demonstrate the method that is proposed in this thesis.

Chapter 7

Multiple Fiber Representative Volume Element Simulations and Results

According to the results from the previous chapter the dimensions of the Representative Volume Element (RVE) is determined to be 75×75 μm . In this chapter the results of the numerical experiments, similar to Chapter 5, will be presented. The methodology of this parametric study will be explained in Section 7.1, followed by the results of the effects of: interface cohesive strength, fiber cohesive strength, interface fracture energy, fiber fracture energy and fiber volume fraction in Section 7.2 to 7.6. Concluding remarks on the results of this chapter will be given in Section 7.7.

7.1 Methodology

To determine the sensitivity of the cohesive variables and the fiber volume fraction the properties below are evaluated using the procedure discussed in Section 4.1:

- Section 7.2: interface cohesive strength
- Section 7.3: fiber cohesive strength
- Section 7.4: interface fracture energy
- Section 7.5: fiber fracture energy
- Section 7.6: fiber volume fraction

First, a reference model with properties as in Table 4.1 and a fiber volume fraction of 40% is generated. These reference properties and fiber volume fraction are evaluated, independently of each other, for values smaller, equal and greater to the matrix reference properties. Instead of five realisations used before now only four realisations are averaged. This is done to limit total the number of simulations.

To study the effect of fiber volume fraction three volume fractions are used; 30%, 40% and 50%. This results in 12 fiber distributions as given in Figure 7.1.1, Figure 7.1.2 and 7.1.3. To study the effects of cohesive variables the fiber distributions as in Figure 7.1.2 is used. Note that the fiber distributions below are different compared to Figure 6.2.3 due to the fact that improvements to the meshing script were made.

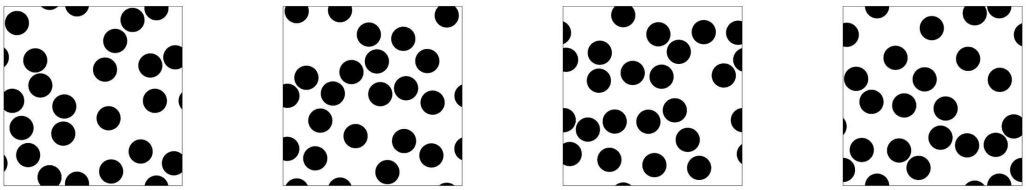

(a) R1 **(b)** R2 **(c)** R3 **(d)** R4

Figure 7.1.1: Four realisations used for the 30% fiber volume fraction simulations.

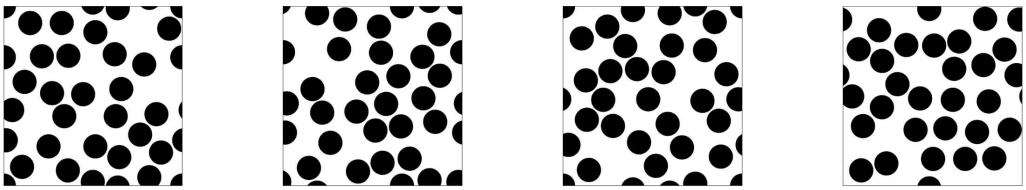

(a) R1 **(b)** R2 **(c)** R3 **(d)** R4

Figure 7.1.2: Four realisations used for the 40% fiber volume fraction simulations.

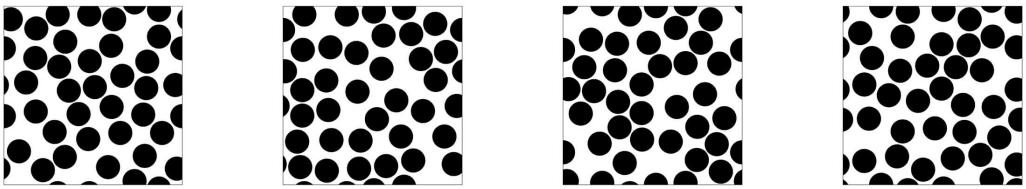

(a) R1 **(b)** R2 **(c)** R3 **(d)** R4

Figure 7.1.3: Four realisations used for the 50% fiber volume fraction simulations.

The meshes of the above fiber distributions have the mesh properties listed in Table 7.1, where the average of all four realisations is given. The number of nodes, thus Degrees of Freedom (DOF), and elements increase for a higher volume fraction due to the increase in number of fibers, resulting in a longer computational time and a higher influence of artificial compliance. However, it is assumed that this influence is negligible for the purpose of this

thesis. For future simulations an alignment factor is implemented in the meshing script that ensures an approximate equal number of nodes and elements for each volume fractions.

Table 7.1: Average properties of all four realisations of the multiple fiber meshes shown in Figure 7.1.1, Figure 7.1.2 and Figure 7.1.3.

Fiber volume fraction	# nodes	# bulk elements	# cohesive elements
30%	105335	35112	52488
40%	112454	37485	56036
50%	116547	38849	58070

As mentioned in Section 4.1 the multiple fiber simulations will be done for the five load cases given in Table 4.2. However, during the post-processing of the results and curve fitting (Chapter 8) it was observed that there is a significant difference in simple shear ($\varepsilon_{12} \neq 0$ and $\varepsilon_{21} = 0$) and pure shear ($\varepsilon_{12} = \varepsilon_{21} \neq 0$), see Figure 7.1.4 for the reference model. In addition, for the implementation of the failure criterion in ABAQUS the mode II properties correspond to a simple shear loading of the cohesive element. More details will be given in Chapter 8.

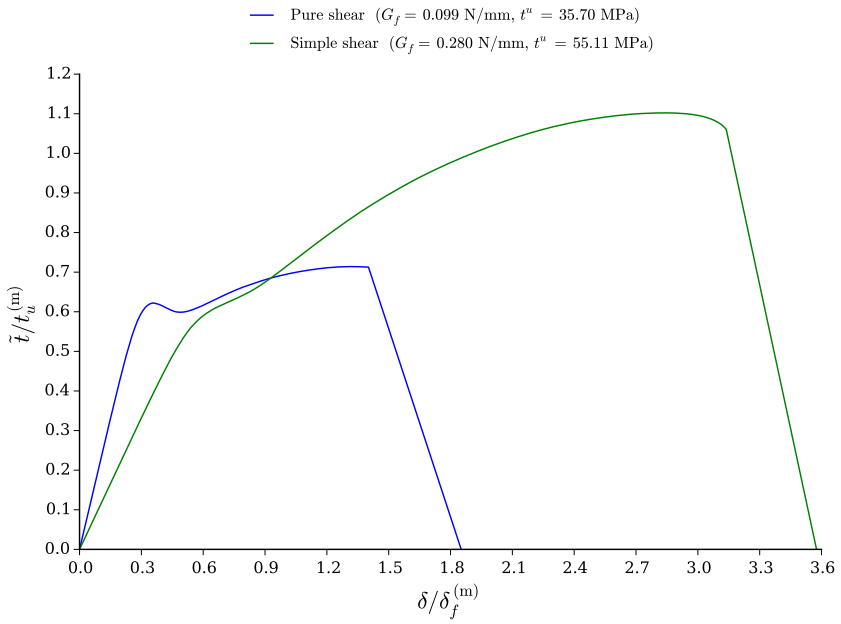

Figure 7.1.4: Difference in ETSL for a simple and pure shear loading.

Due to the above an additional load case is evaluated, i.e. a simple shear case with $\varepsilon_{12} = 0.21$ and $\varepsilon_{21} = 0$, denoted by LC6. The ETSL plots are generated using the procedure mentioned in Section 4.4.3 and detailed plots can be found in Appendix B.4 to B.8.

7.1.1 Short Discussion on Fiber Distribution

A short study on the effect of fiber distribution is performed that in addition gives the opportunity to verify mesh dependency. A fiber volume fraction of 35% for the 75×75 μm results in 25 fibers that can be structurally placed. The realisations of the random fiber distribution models are given in Figure 7.1.5a to 7.1.5d and the structured distribution as in Figure 7.1.5e. Note that for the results of the structured distribution also the average of four identical realisations, but with different meshes, is used.

(a) R1 **(b)** R2 **(c)** R3 **(d)** R4 **(e)** Structured

Figure 7.1.5: Effect of fiber distribution; (a) - (d) random fiber distributions and (e) a structured distribution for a fiber volume fraction of 35%.

For the uni-axial extension load case the results are given in Figure 7.1.6. The random fiber distribution results in an approximate 10% lower maximum cohesive strength and fracture energy. For the pure shear and mixed load case, LC2 and LC3, similar results are observed. The lower strength is explained by the fact that the stress is not evenly distributed for a random fiber distribution, resulting in earlier damage initiation at stress concentrations. As a result the fracture energy is also lower for a random fiber distribution.

The structured fiber distribution simulations have been averaged over four identical realisations with different meshes. Looking at the ETSL of each realisation, as in Figure 7.1.7, the effect of mesh dependency can be investigated. Again these results are for uni-axial extension. The ETSLs align perfectly until $\tilde{\delta}/\delta_f^m \approx 1.0$, after which they deviate. This is explained by the difference in fracture pattern. The mesh has a strong influence on the fracture pattern but almost no effect on the resulting ETSL. For the mixed load case the same conclusions can be drawn. However, for the pure shear load case there is already a significant difference between the peak of each ETSL. From this it is concluded that for pure shear the results are spurious and unreliable.

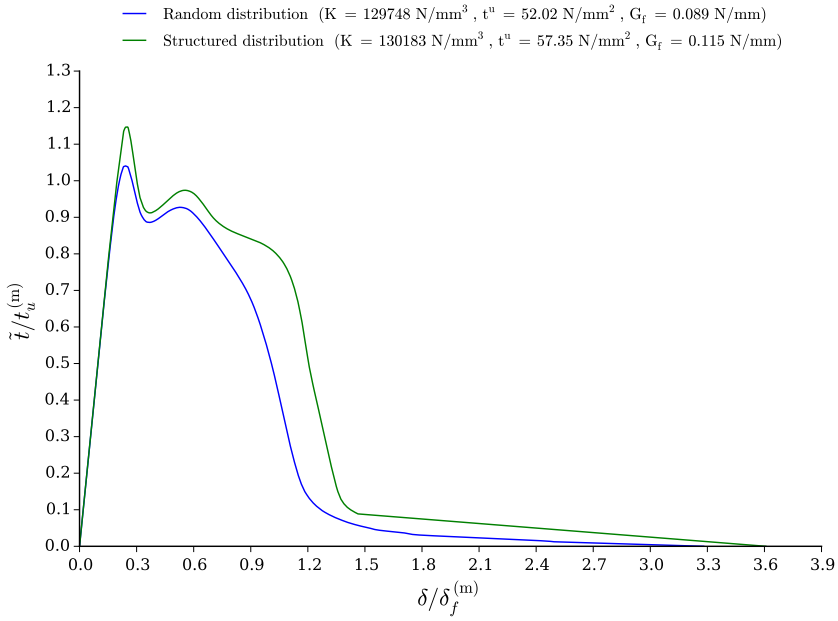

Figure 7.1.6: Effect of fiber distribution: comparing the ETSL of a random and structured fiber distribution subjected to uni-axial extension (LC1).

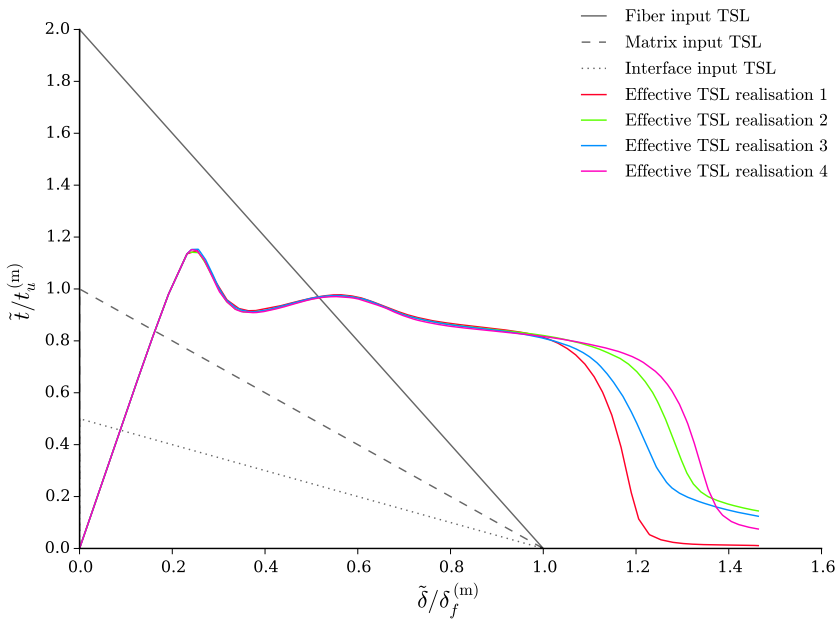

Figure 7.1.7: ETSLs of the four identical realisations of the structured fiber distribution subjected to uni-axial extension (LC1).

7.2 Effect of Interface Cohesive Strength

As with the single fiber results the first effect studied is the effect of interface cohesive strength, i.e. the bonding strength between the fiber and matrix. Compared to the reference model this value is changed from 25 MPa, factor 0.5 compared to the matrix cohesive strength, to a factor 1.0 and 2.0. From the single fiber results it was concluded that once the factor $t_u^{(i)}/t_u^{(m)}$ is larger or equal to 1.0 the crack propagates through the matrix and thus there is an increase in maximum cohesive strength and fracture energy. In addition, there is not much difference between a factor 1.0 and 2.0.

The same is observed during the multiple fiber simulations as can be seen in Figure 7.2.1 to 7.2.6. The difference in maximum cohesive strength and fracture energy between a factor 0.5 and 1.0 (or 2.0) is higher compared to the single fiber results due to a higher volume fraction (40% vs. 10%). In general the above applies for each load case. However, for the shear loading (LC2 and LC6) there is a difference between a factor 1.0 and 2.0. This is explained by the larger spread in ETSL between each realisation.

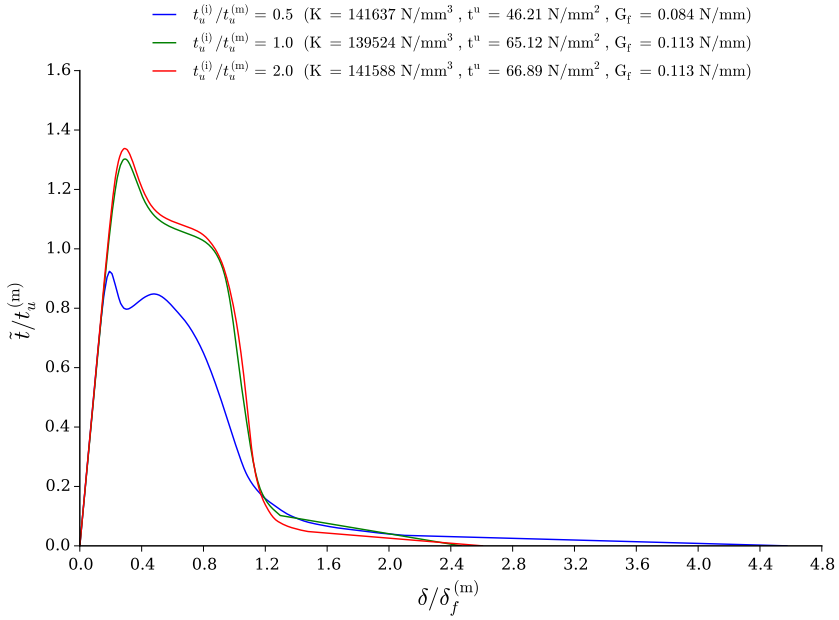

Figure 7.2.1: Effect of interface cohesive strength ($t_u^{(i)}$) on the fracture mechanism, in terms of a ETSL, of the multiple fiber model subjected to uni-axial extension (LC1).

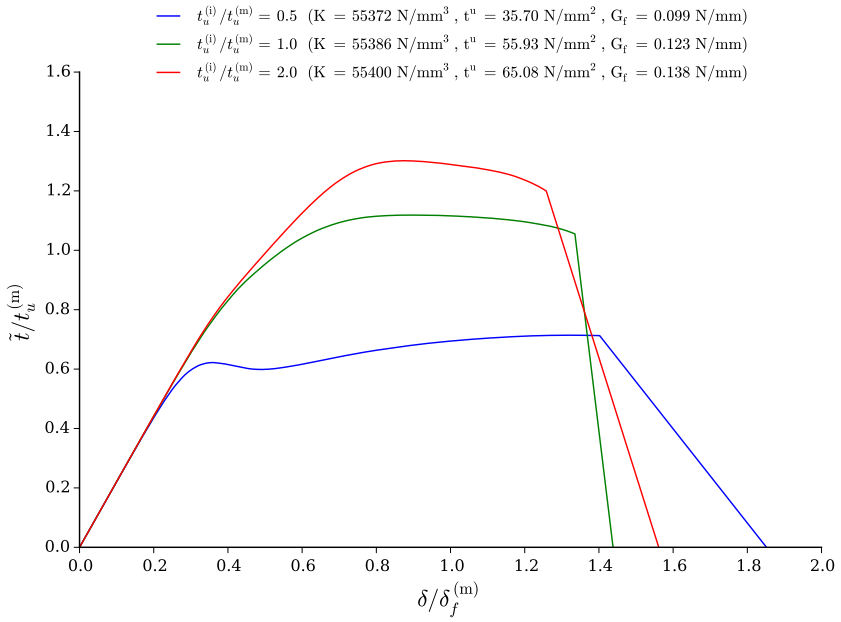

Figure 7.2.2: Effect of interface cohesive strength ($t_u^{(i)}$) on the fracture mechanism, in terms of a ETSL, of the multiple fiber model subjected to pure shear (LC2).

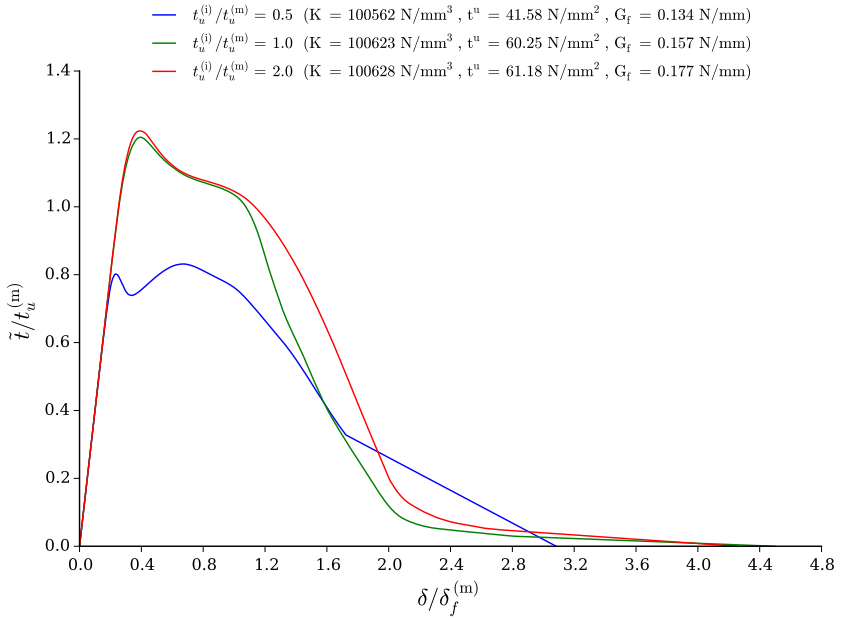

Figure 7.2.3: Effect of interface cohesive strength ($t_u^{(i)}$) on the fracture mechanism, in terms of a ETSL, of the multiple fiber model subjected to a mixed loading (LC3).

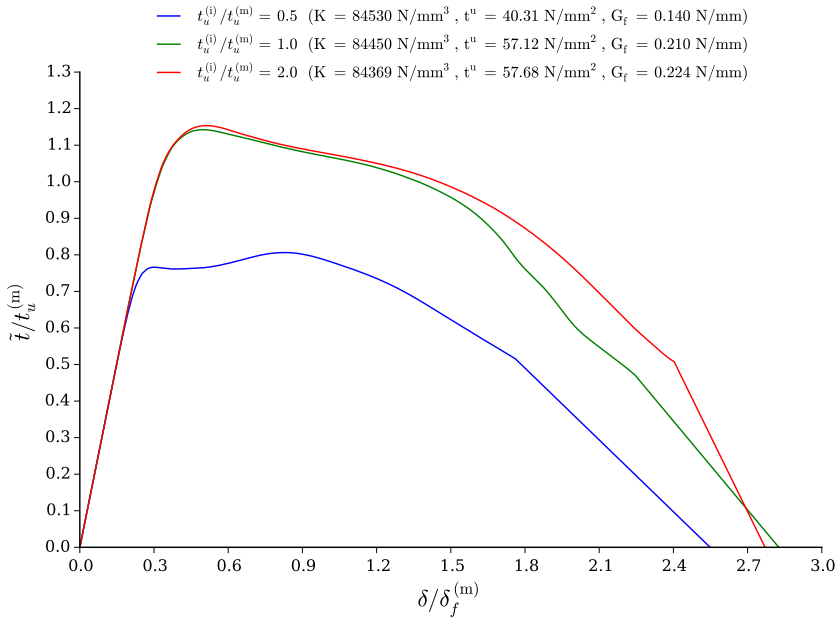

Figure 7.2.4: Effect of interface cohesive strength ($t_u^{(i)}$) on the fracture mechanism, in terms of a ETSL, of the multiple fiber model subjected to a mixed loading (LC4).

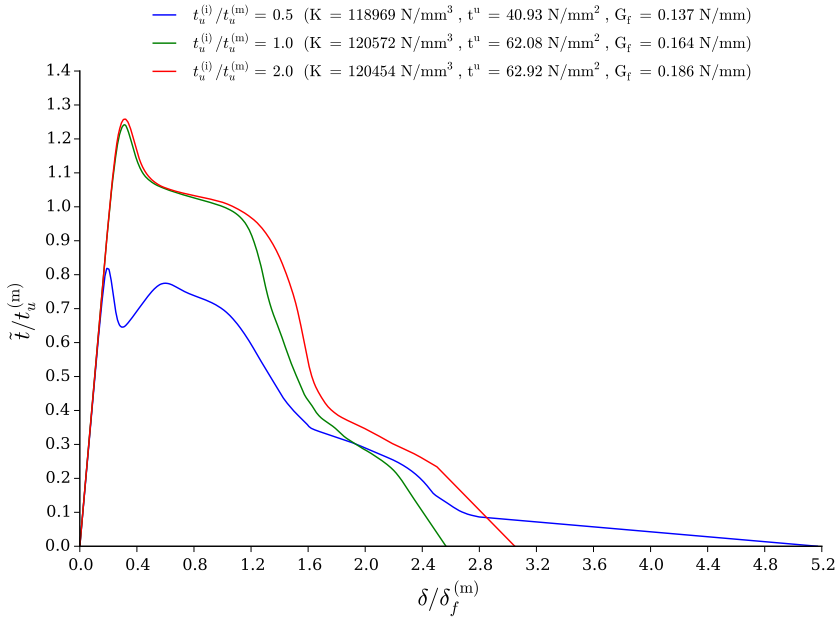

Figure 7.2.5: Effect of interface cohesive strength ($t_u^{(i)}$) on the fracture mechanism, in terms of a ETSL, of the multiple fiber model subjected to a mixed loading (LC5).

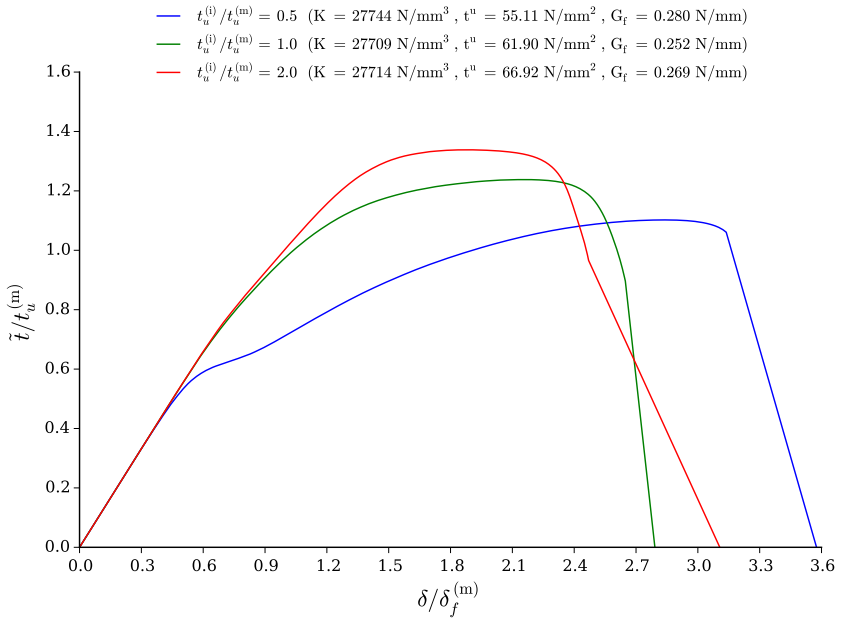

Figure 7.2.6: Effect of interface cohesive strength ($t_u^{(i)}$) on the fracture mechanism, in terms of a ETSL, of the multiple fiber model subjected to simple shear (LC6).

7.3 Effect of Fiber Cohesive Strength

The second effect that is studied is the effect of the fiber cohesive strength. In contrast to the previous section the cohesive strength of the fiber cohesive elements is changed from 100 MPa (factor 2.0) in the reference model to 50 MPa (factor 1.0) and 25 MPa (factor 0.5). The results can be observed in Figure 7.3.1 to 7.3.6. In Section 5.3 it was observed that for a factor 0.5 the maximum cohesive strength was lower and the fracture energy higher compared to a factor of 1.0 and 2.0. In addition there is not much difference in a factor 1.0 and 2.0 due to the fact that the crack does not initiate in the fiber for these factors.

Identical results are observed in this section. Again, for pure shear in Figure 7.3.2 the results are spurious and not suitable for future use (fitting). The simple shear results in Figure 7.3.6 are in line with the other load cases and therefore suitable for the curve fitting. The difference in fracture energy between a factor 0.5 and 1.0 (or 2.0) is significant, especially compared to the single fiber results, which is due to the increased number of fibers compared to the single fiber models.

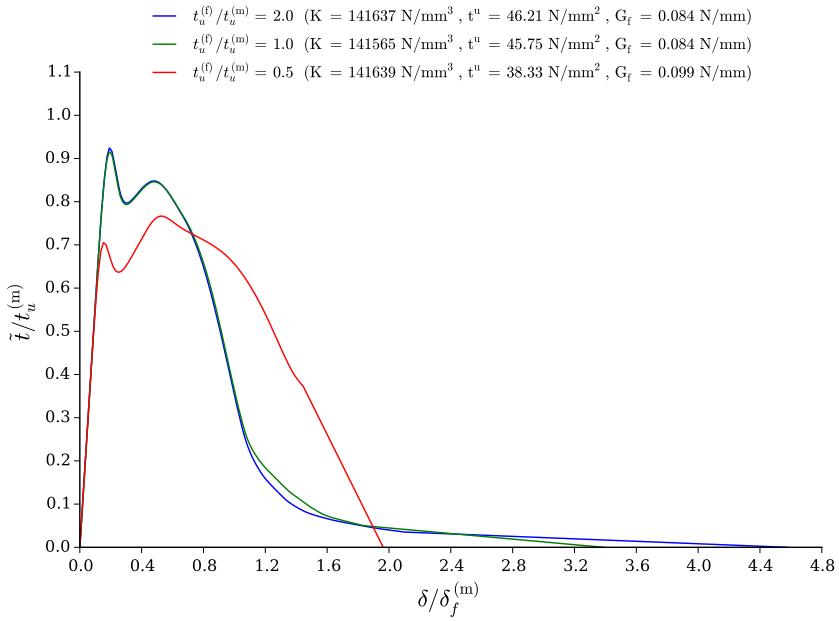

Figure 7.3.1: Effect of fiber cohesive strength ($t_u^{(f)}$) on the fracture mechanism, in terms of a ETSL, of the multiple fiber model subjected to uni-axial extension (LC1).

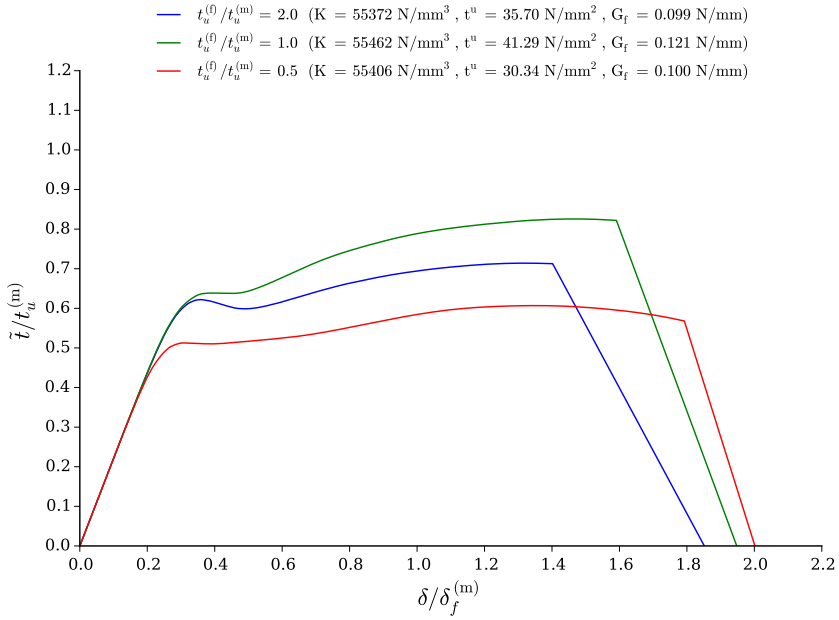

Figure 7.3.2: Effect of fiber cohesive strength ($t_u^{(f)}$) on the fracture mechanism, in terms of a ETSL, of the multiple fiber model subjected to pure shear (LC2).

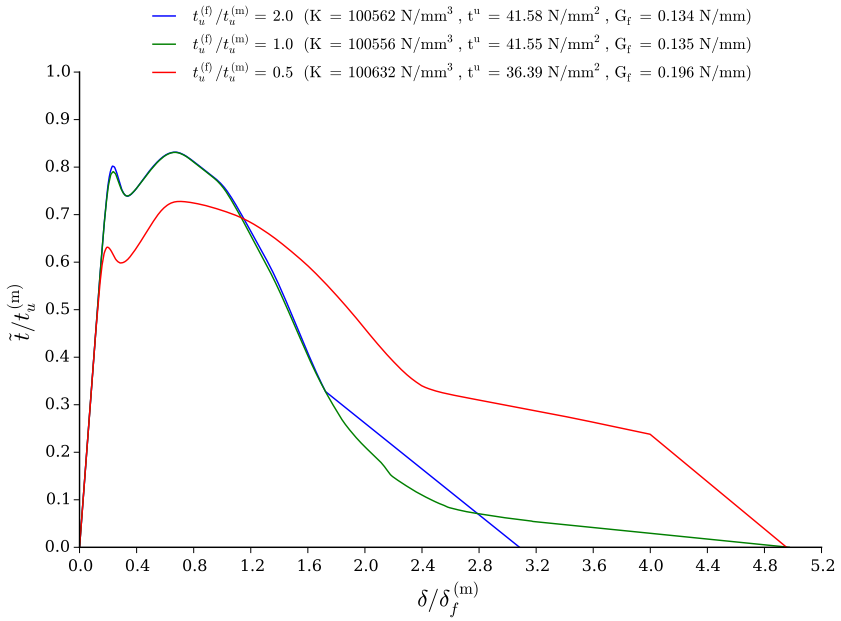

Figure 7.3.3: Effect of fiber cohesive strength ($t_u^{(f)}$) on the fracture mechanism, in terms of a ETSL, of the multiple fiber model subjected to a mixed loading (LC3).

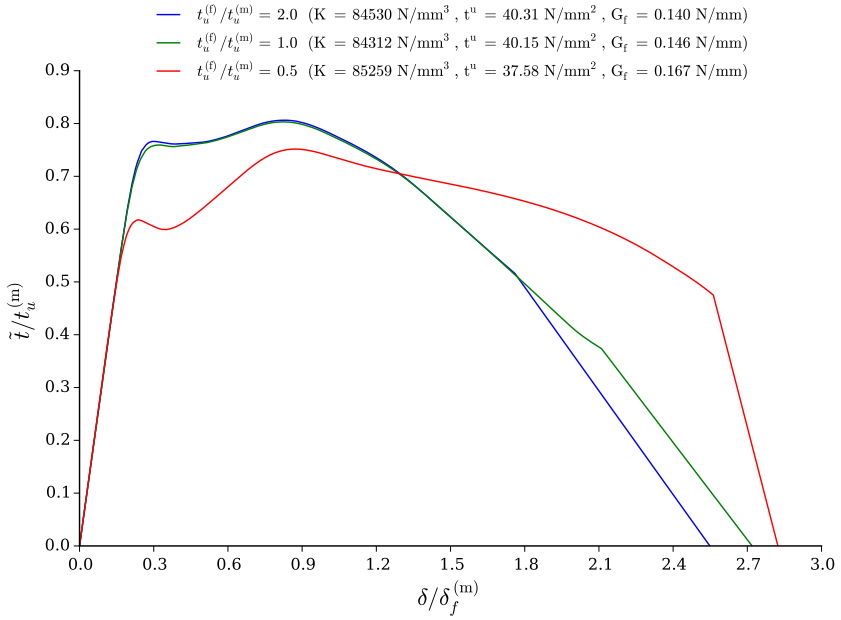

Figure 7.3.4: Effect of fiber cohesive strength ($t_u^{(f)}$) on the fracture mechanism, in terms of a ETSL, of the multiple fiber model subjected to a mixed loading (LC4).

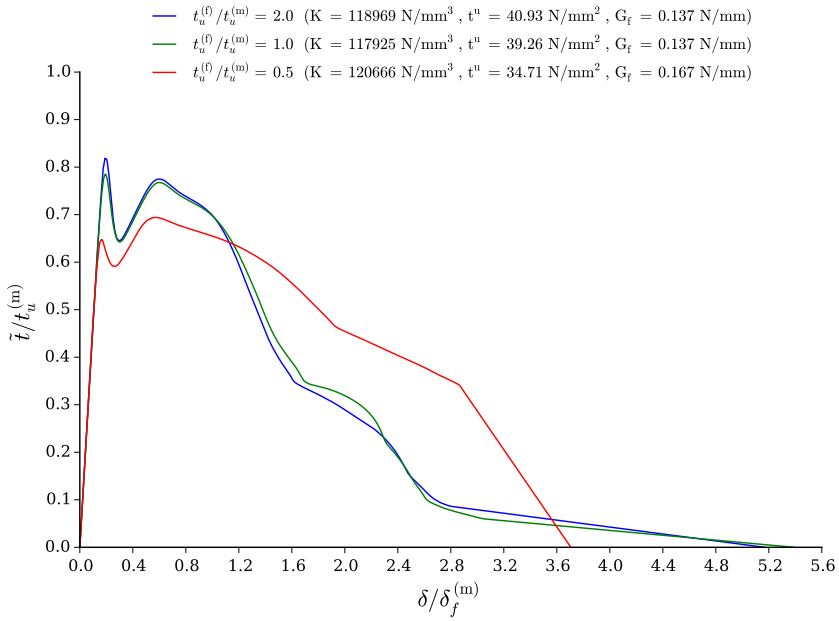

Figure 7.3.5: Effect of fiber cohesive strength ($t_u^{(f)}$) on the fracture mechanism, in terms of a ETSL, of the multiple fiber model subjected to a mixed loading (LC5).

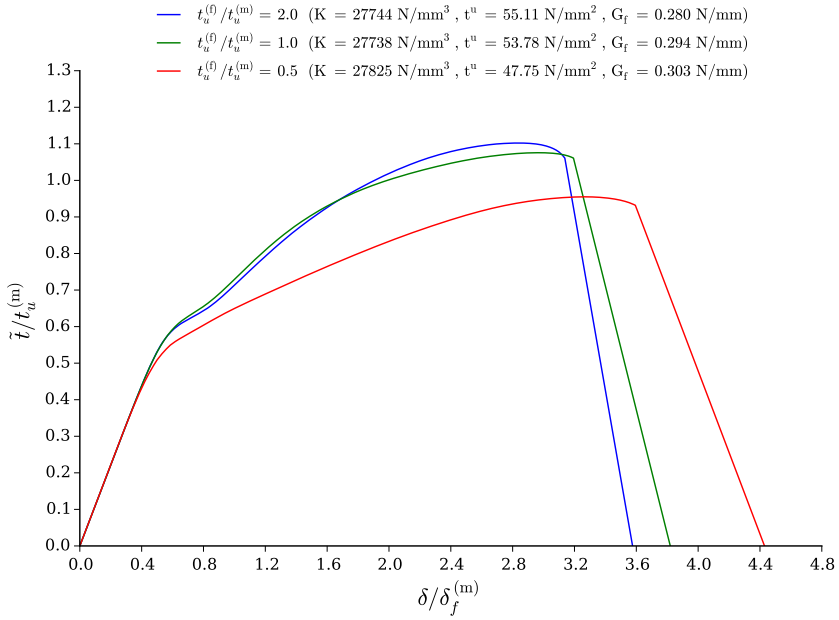

Figure 7.3.6: Effect of fiber cohesive strength ($t_u^{(f)}$) on the fracture mechanism, in terms of a ETSL, of the multiple fiber model subjected to simple shear (LC6.

7.4 Effect of Interface Fracture Energy

The effect of interface fracture energy is the third cohesive parameters that is studied. The reference value of 0.025 N/mm (factor 0.5) is increased to 0.05 N/mm (factor 1.0) and 0.1 N/mm (factor 2.0). The single fiber results showed a small change in fracture energy, but almost no change in maximum cohesive strength.

For the results in Figure 7.4.1 to 7.4.6 with respect to the maximum cohesive strength the same can be concluded. Also, for LC1, LC3, LC4 and LC5 the softening slope of the ETSL increases for a higher factor, as expected. For the shear load cases, LC2 and LC6, this is not the case. In the case of pure shear the fracture energy decreases for a higher factor and for the simple shear case there is not much difference. This is mainly explained by the different fracture mechanism, i.e. there are shear bands along which the elements slide along each other.

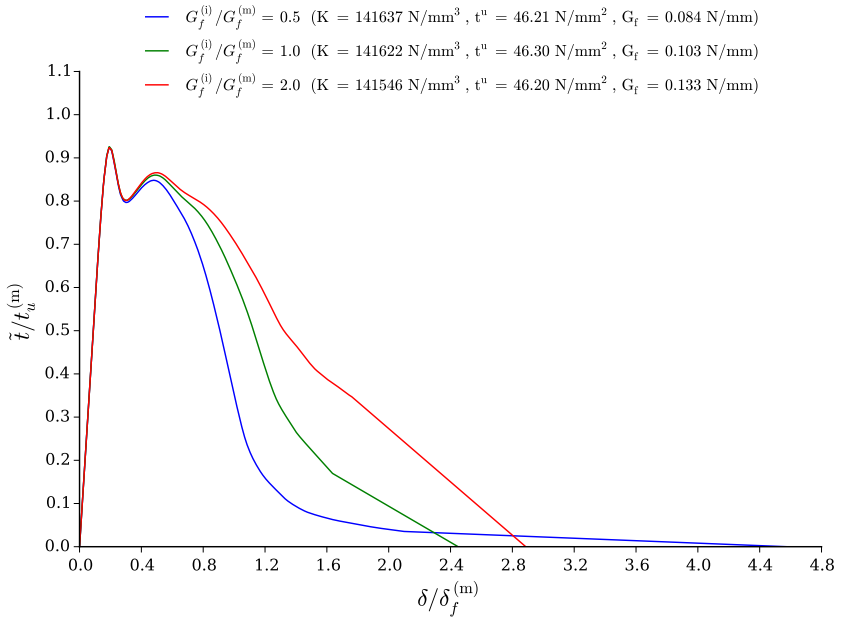

Figure 7.4.1: Effect of interface fracture energy ($G_f^{(i)}$) on the fracture mechanism, in terms of a ETSL, of the multiple fiber model subjected to uni-axial extension (LC1).

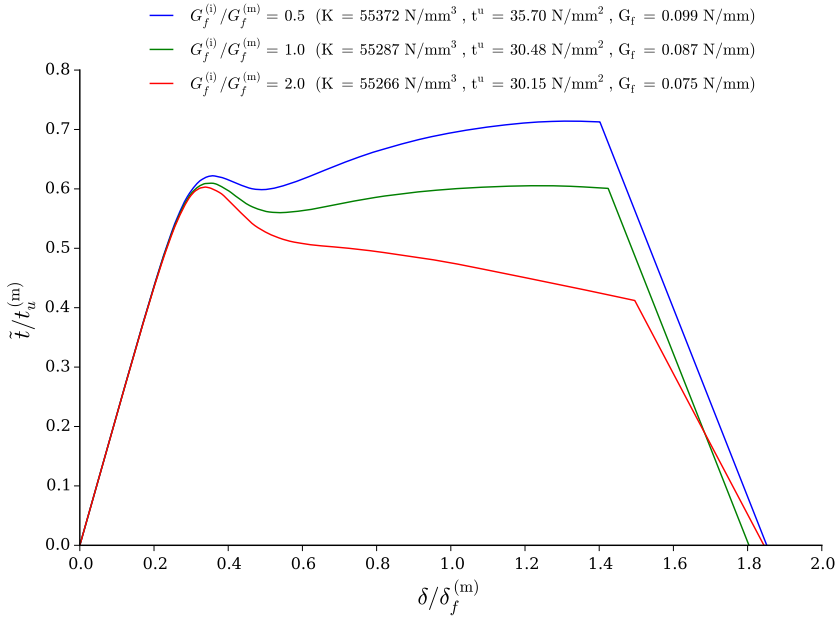

Figure 7.4.2: Effect of interface fracture energy ($G_f^{(i)}$) on the fracture mechanism, in terms of a ETSL, of the multiple fiber model subjected to pure shear (LC2).

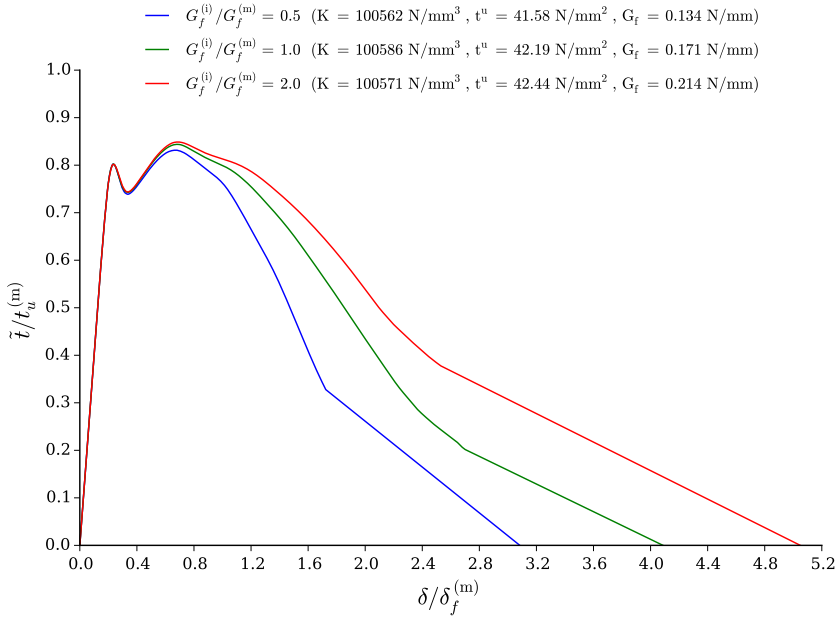

Figure 7.4.3: Effect of interface fracture energy ($G_f^{(i)}$) on the fracture mechanism, in terms of a ETSL, of the multiple fiber model subjected to a mixed loading (LC3).

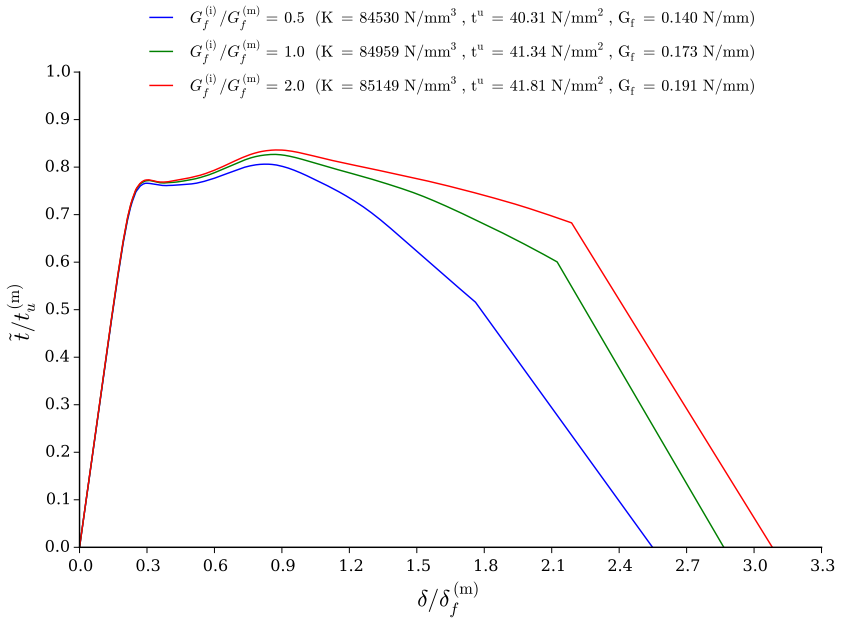

Figure 7.4.4: Effect of interface fracture energy ($G_f^{(i)}$) on the fracture mechanism, in terms of a ETSL, of the multiple fiber model subjected to a mixed loading (LC4).

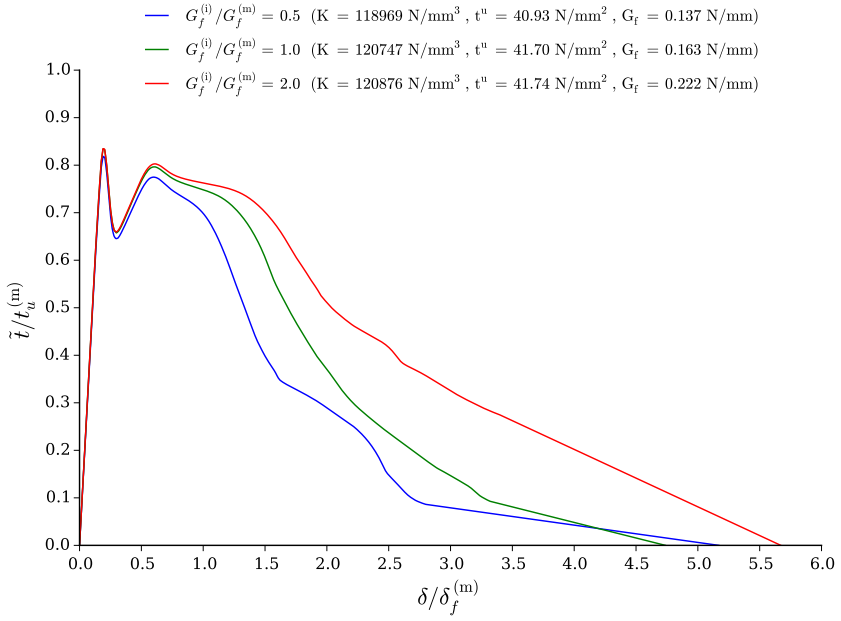

Figure 7.4.5: Effect of interface fracture energy ($G_f^{(i)}$) on the fracture mechanism, in terms of a ETSL, of the multiple fiber model subjected to a mixed loading (LC5).

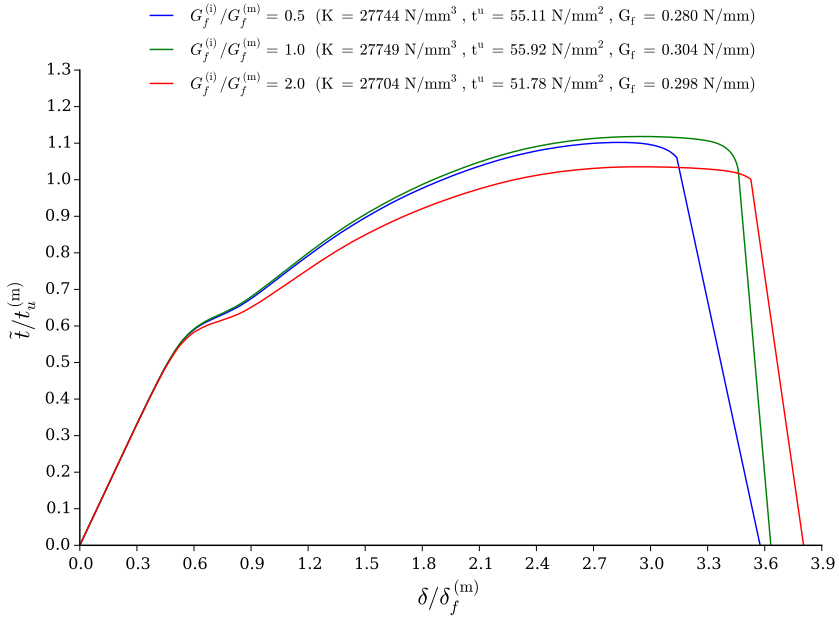

Figure 7.4.6: Effect of interface fracture energy ($G_f^{(i)}$) on the fracture mechanism, in terms of a ETSL, of the multiple fiber model subjected to simple shear (LC6).

7.5 Effect of Fiber Fracture Energy

The last cohesive parameter that is studied is the fiber fracture energy. The reference value of 0.1 N/mm (factor 2.0) is decreased to 0.05 N/mm (factor 1.0) and 0.025 N/mm (factor 0.5). The single fiber results showed little to no effect due to the fact that the crack does not interact with the fiber.

For the results in Figure 7.5.1 to 7.5.6 the same can be concluded, except for the pure shear load case in Figure 7.5.2 due to the spurious effects. These effects are not visible with the simple shear results. It is expected that the fiber fracture energy will have an influence similar to the interface fracture energy in the case the crack initiates in the fiber, i.e. for a $t_u^{(f)}/t_u^{(m)} < 1$.

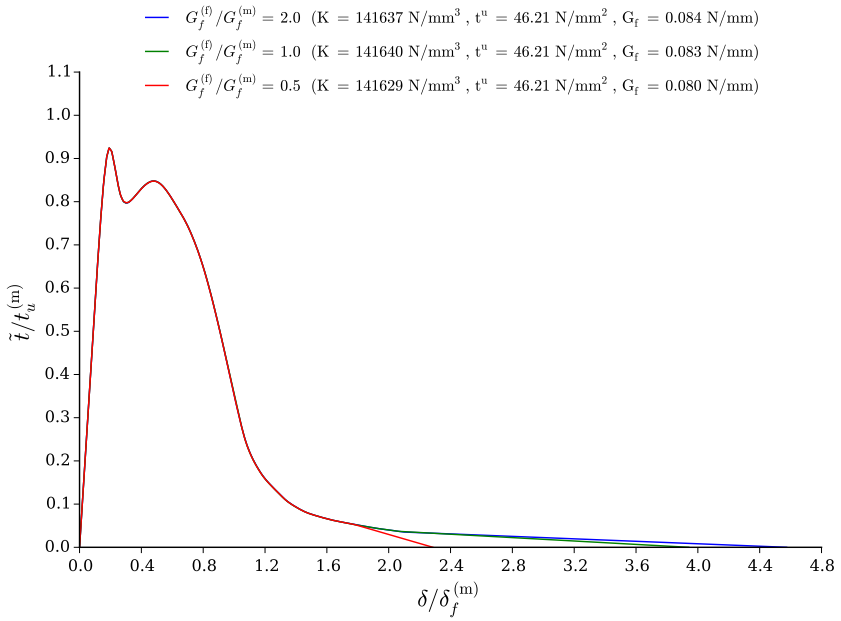

Figure 7.5.1: Effect of fiber fracture energy ($G_f^{(f)}$) on the fracture mechanism, in terms of a ETSL, of the multiple fiber model subjected to uni-axial extension (LC1).

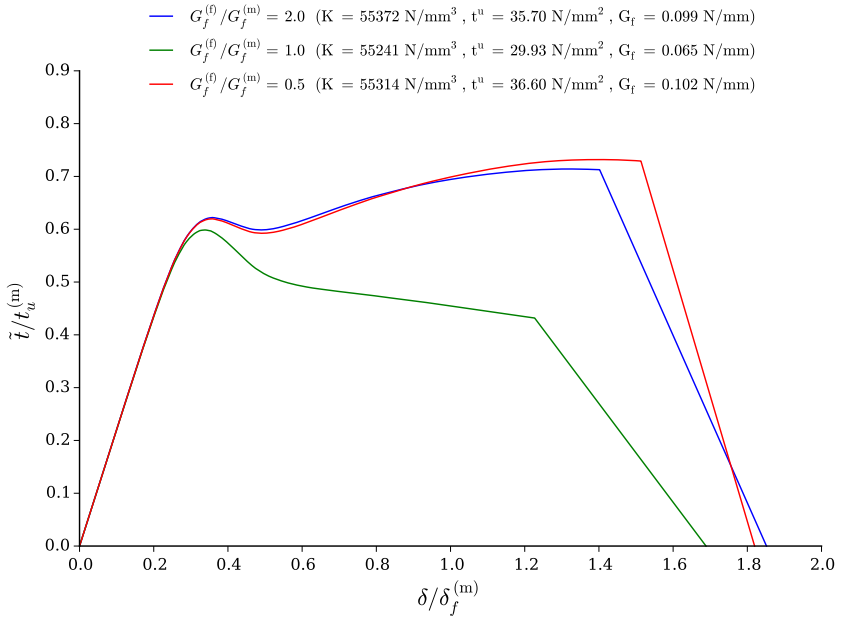

Figure 7.5.2: Effect of fiber fracture energy ($G_f^{(f)}$) on the fracture mechanism, in terms of a ETSL, of the multiple fiber model subjected to pure shear (LC2).

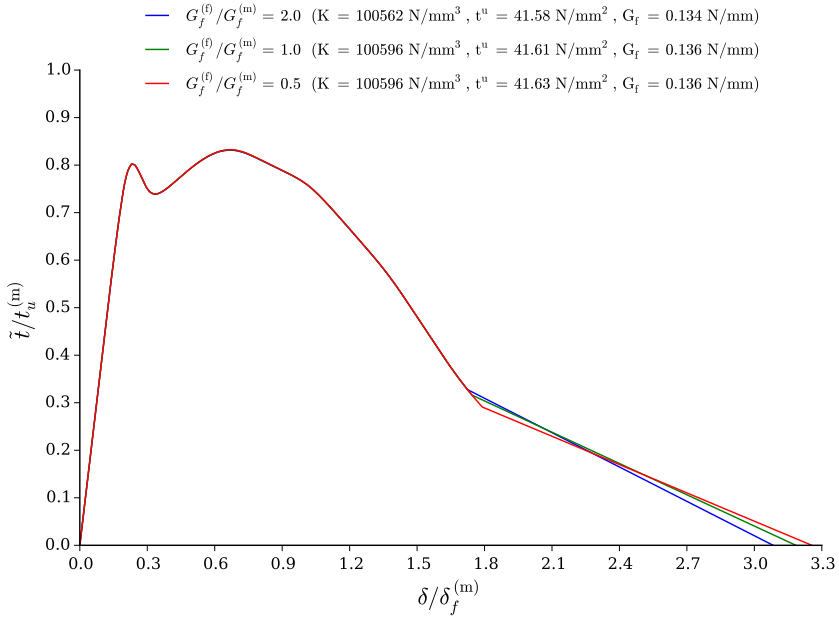

Figure 7.5.3: Effect of fiber fracture energy ($G_f^{(f)}$) on the fracture mechanism, in terms of a ETSL, of the multiple fiber model subjected to a mixed loading (LC3).

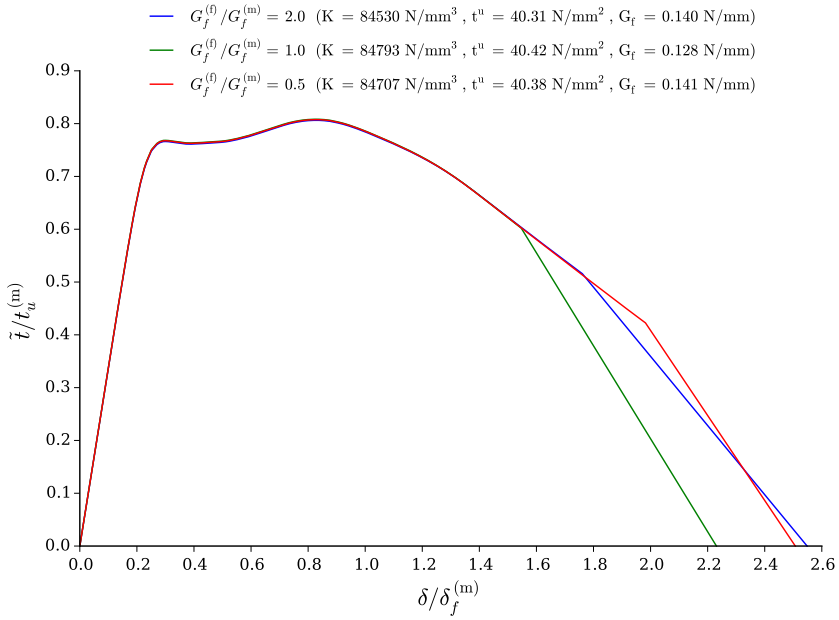

Figure 7.5.4: Effect of fiber fracture energy ($G_f^{(f)}$) on the fracture mechanism, in terms of a ETSL, of the multiple fiber model subjected to a mixed loading (LC4).

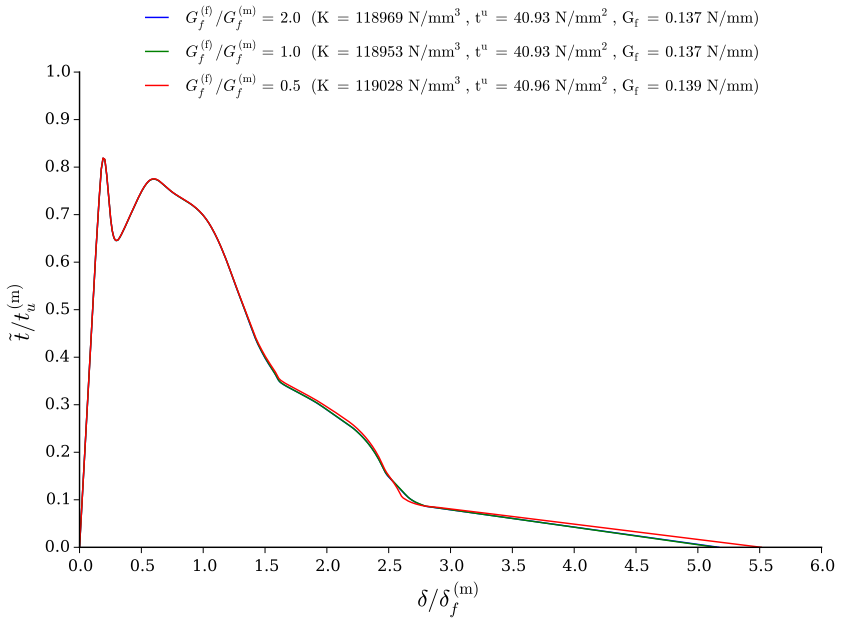

Figure 7.5.5: Effect of fiber fracture energy ($G_f^{(f)}$) on the fracture mechanism, in terms of a ETSL, of the multiple fiber model subjected to a mixed loading (LC5).

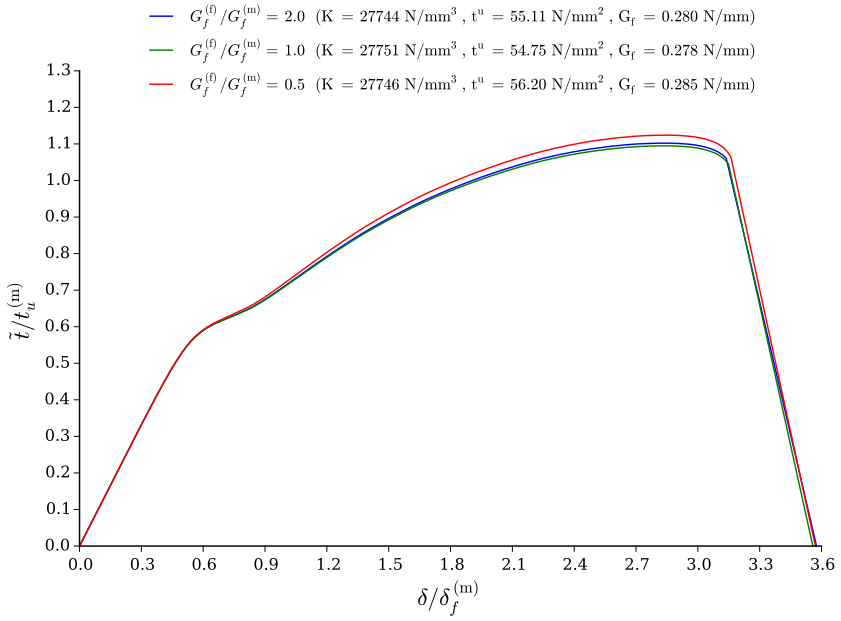

Figure 7.5.6: Effect of fiber fracture energy ($G_f^{(f)}$) on the fracture mechanism, in terms of a ETSL, of the multiple fiber model subjected to simple shear (LC6).

7.6 Effect of Fiber Volume Fraction

Next to the parameters of the cohesive element the effect of fiber volume fraction is studied. The reference model has a volume fraction of 40%, which is changed to 30% and 50% by increasing the number of fibers. Note that the cohesive parameters are kept constant. Similar to the effect of fiber diameter for the single fiber results it is expected that the slope will increase for a higher fiber volume fraction, the maximum cohesive strength is about constant and the fracture energy decreases.

In Figure 7.6.1 to 7.6.6 the result of each load case is presented. The slope increases for a higher volume fraction in all cases, as expected. However, changes in the maximum cohesive strength are observed. For most load cases the maximum cohesive strength increases for a higher volume fraction. In addition, the fracture energy decreases for a higher volume fraction except for the shear load cases due to identical reasons as mentioned in the previous sections.

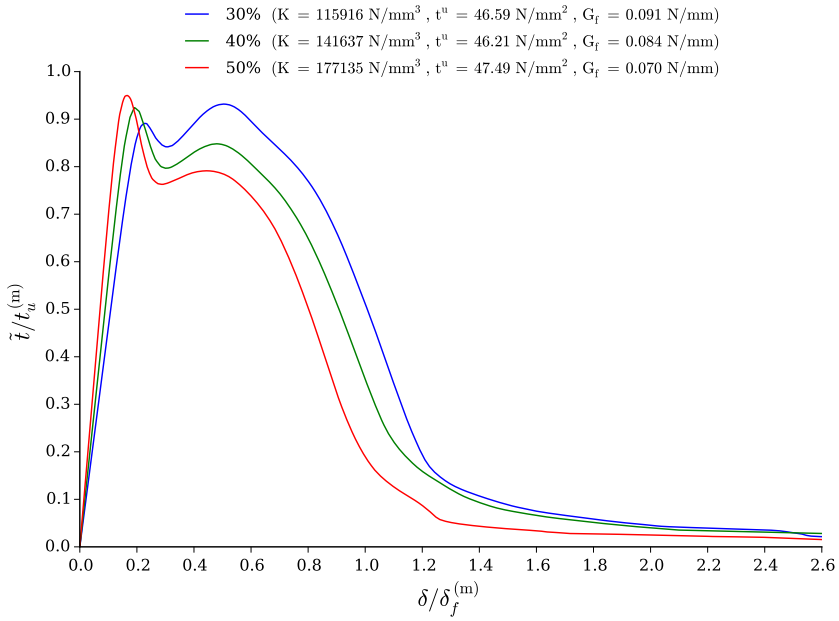

Figure 7.6.1: Effect of fiber volume fraction (V_f) on the fracture mechanism, in terms of a ETSL, of the multiple fiber model subjected to uni-axial extension (LC1).

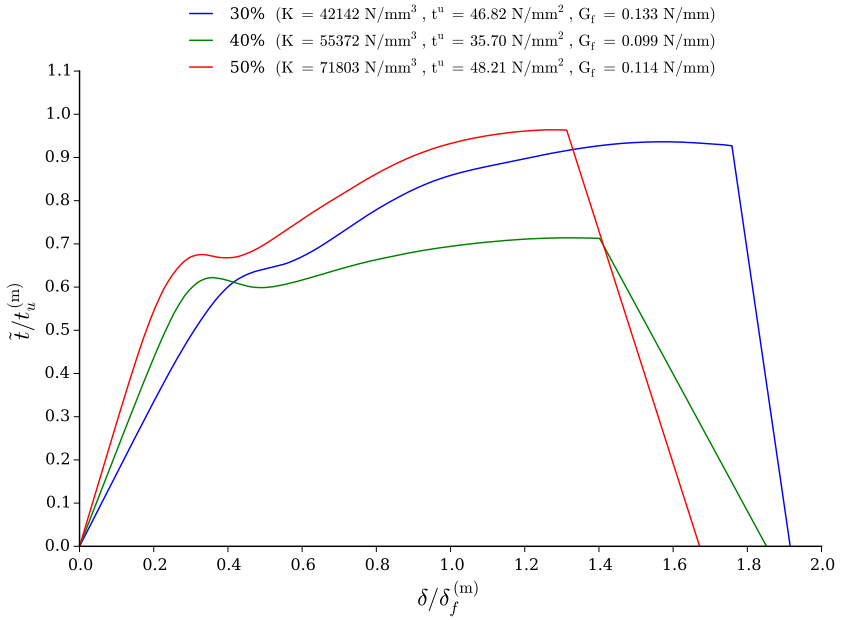

Figure 7.6.2: Effect of fiber volume fraction (V_f) on the fracture mechanism, in terms of a ETSL, of the multiple fiber model subjected to pure shear (LC2).

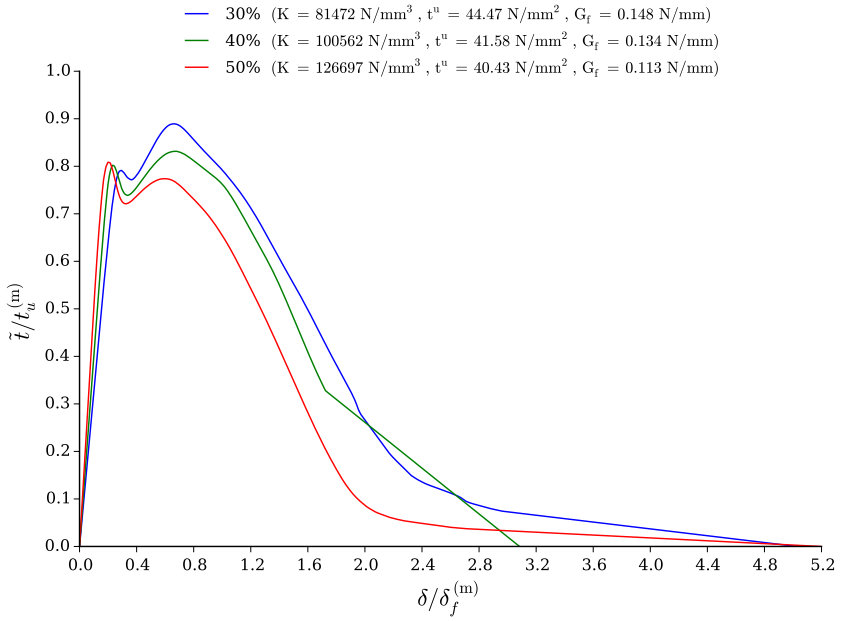

Figure 7.6.3: Effect of fiber volume fraction (V_f) on the fracture mechanism, in terms of a ETSL, of the multiple fiber model subjected to a mixed loading (LC3).

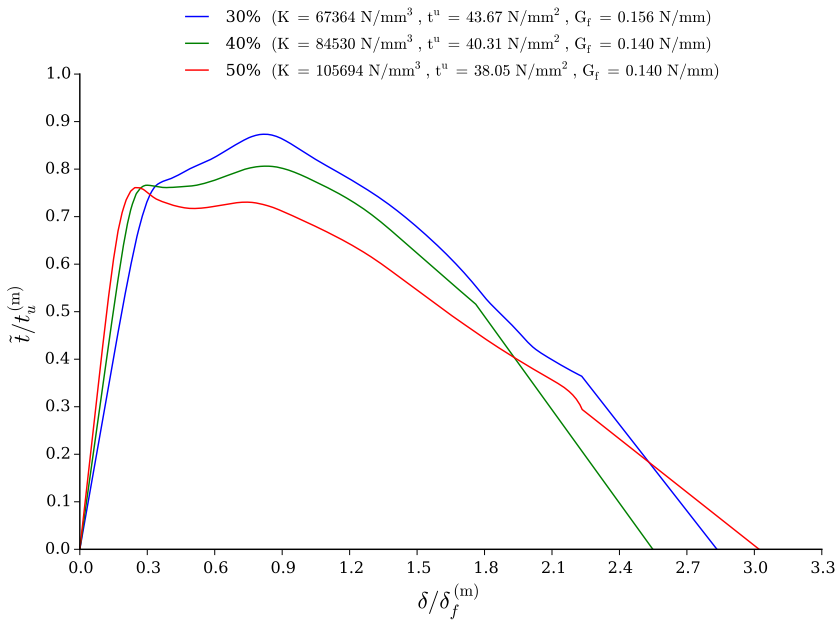

Figure 7.6.4: Effect of fiber volume fraction (V_f) on the fracture mechanism, in terms of a ETSL, of the multiple fiber model subjected to a mixed loading (LC4).

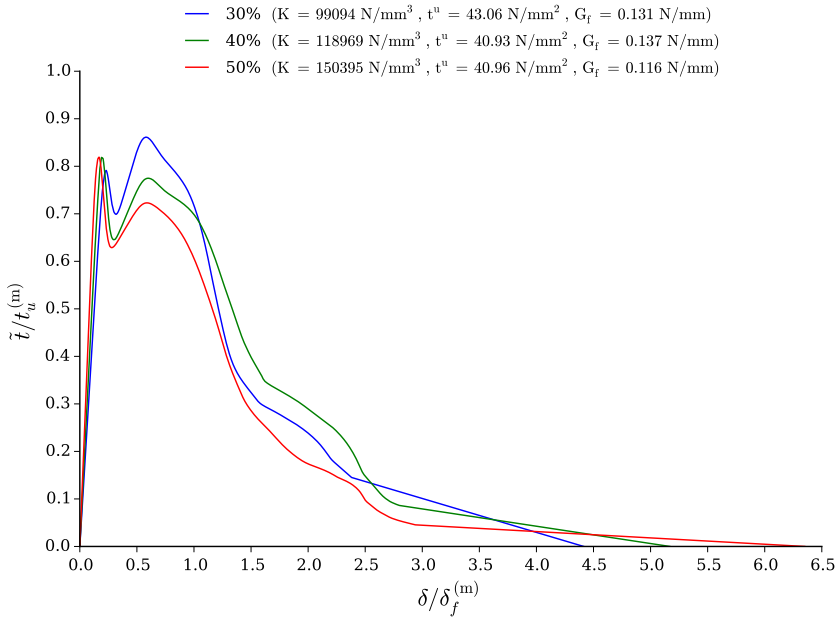

Figure 7.6.5: Effect of fiber volume fraction (V_f) on the fracture mechanism, in terms of a ETSL, of the multiple fiber model subjected to a mixed loading (LC5).

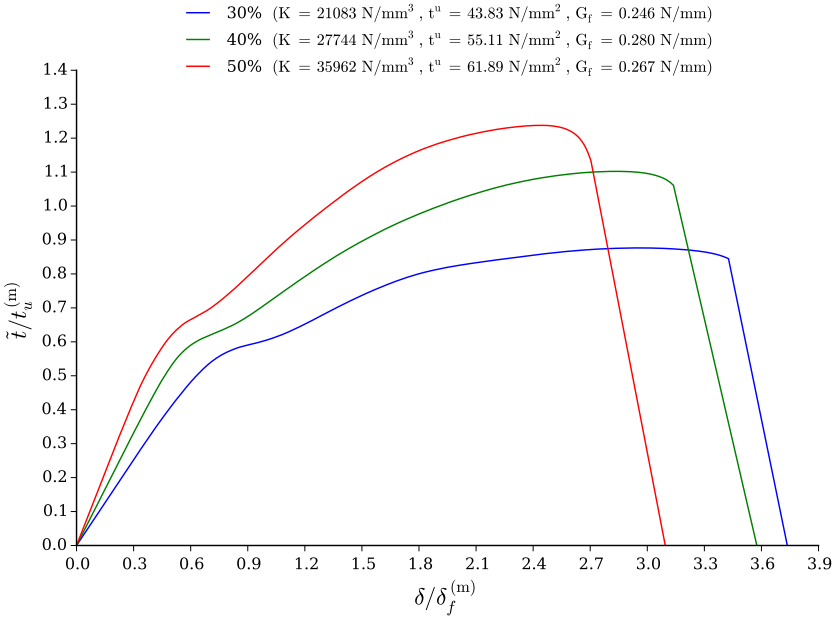

Figure 7.6.6: Effect of fiber volume fraction (V_f) on the fracture mechanism, in terms of a ETSL, of the multiple fiber model subjected to simple shear (LC6).

7.7 Concluding Remarks

In this chapter the effect of cohesive parameters and fiber volume fracture on the fracture mechanisms of the multiple fiber RVE were studied for a total of six load cases. In general the results are similar to the single fiber results and therefore identical conclusions can be drawn, see Section 5.7. The only additional conclusion that is drawn is that the effect of fiber fracture energy method is flawed. Due to the fact that the crack does not initiate in the fiber it appears to have no influence on the fracture response. During a future study the effect should be studied with a fiber cohesive strength equal to a factor 0.5. In addition, it is concluded that the results of the pure shear load case are spurious and therefore not suitable for future use. Instead the simple shear load case gives far better results. The other load cases show consistent results.

The computational time for each model was quite high due to a large number of DOF, i.e. ranging from approximately 20 hours (uni-axial extension) to 70 hours (pure/simple shear). However, due to the fact that these simulations only have to be performed once the computational time is less important to the required accuracy.

For the curve fitting it is important that all the results of the multiple fiber simulations are combined into a single equation for each parameter of the failure criterion in terms of a Traction-Separation Law (TSL). It is observed that the fracture pattern has a strong influence on the effect of the cohesive parameters, for instance there is almost no effect of fiber fracture energy because the crack does not interact with the fibers. In the next chapter it is discussed how the results are assembled into one equation.

Chapter 8

Effective Model: Correlation and Results

From the results presented in Chapter 7 a failure criterion has to be formulated. The first step is to determine the effective parameters for each data point[1], see Section 8.1. After this there are two separate stages of curve fitting in Section 8.2 and 8.3. On the one hand the results of mode I (LC1) and mode II (LC6) are fitted and on the other hand the mode mixity is fitted using the mixed load cases. In the end the assembly of the failure criterion and implementation in ABAQUS is discussed in Section 8.4.

8.1 Determining Effective Parameters

In this section the effective parameters of the resulting Effective Traction-Separation Law (ETSL) for each data point are determined. For each load case there are 11 data points, i.e. the reference case and per effect studied two cases. The parameters of each data point are given in Table 8.1. For each data point an ETSL has been generated and from this ETSL three parameters can be determined that describe a bilinear Traction-Separation Law (TSL); the initial slope (K), maximum cohesive strength (t_u) and fracture energy (G_f). A bilinear TSL is chosen as it is the most simple TSL and can easily be implemented in ABAQUS . It should be noted that the results of pure shear LC2 are neglected because the results were spurious and unreliable, instead the results of simple shear LC6 are utilised.

[1] A data point is the result of a simulation in terms of the three parameters of a bilinear TSL.

Table 8.1: Description of the data points corresponding to all simulations. For each load case the data points are identical.

#	$t_u^{(i)}/t_u^{(m)}$	$t_u^{(f)}/t_u^{(m)}$	$G_f^{(i)}/G_f^{(m)}$	$G_f^{(f)}/G_f^{(m)}$	V_f	**Description**
1	0.5	2.0	0.5	2.0	0.4	Reference case
2	1.0	2.0	0.5	2.0	0.4	$t_u^{(i)} \times 2$
3	2.0	2.0	0.5	2.0	0.4	$t_u^{(i)} \times 4$
4	0.5	1.0	0.5	2.0	0.4	$t_u^{(f)} \times 0.5$
5	0.5	0.5	0.5	2.0	0.4	$t_u^{(f)} \times 0.25$
6	0.5	2.0	1.0	2.0	0.4	$G_f^{(i)} \times 2$
7	0.5	2.0	2.0	2.0	0.4	$G_f^{(i)} \times 4$
8	0.5	2.0	0.5	1.0	0.4	$G_f^{(f)} \times 0.5$
9	0.5	2.0	0.5	0.5	0.4	$G_f^{(f)} \times 0.25$
10	0.5	2.0	0.5	2.0	0.3	$V_f = 30\%$
11	0.5	2.0	0.5	2.0	0.5	$V_f = 50\%$

The goal is to find a versatile and consistent method that determines the parameters of the ETSL and can be scripted using PYTHON . The first parameter, the initial slope, is relatively easy to determine by dividing the traction by the separation of the first increment point. Just as simple is the determination of the maximum cohesive strength, which is just the maximum of the ETSL. The fracture energy of the resulting bilinear TSL is assumed equal to the fracture energy of the ETSL.

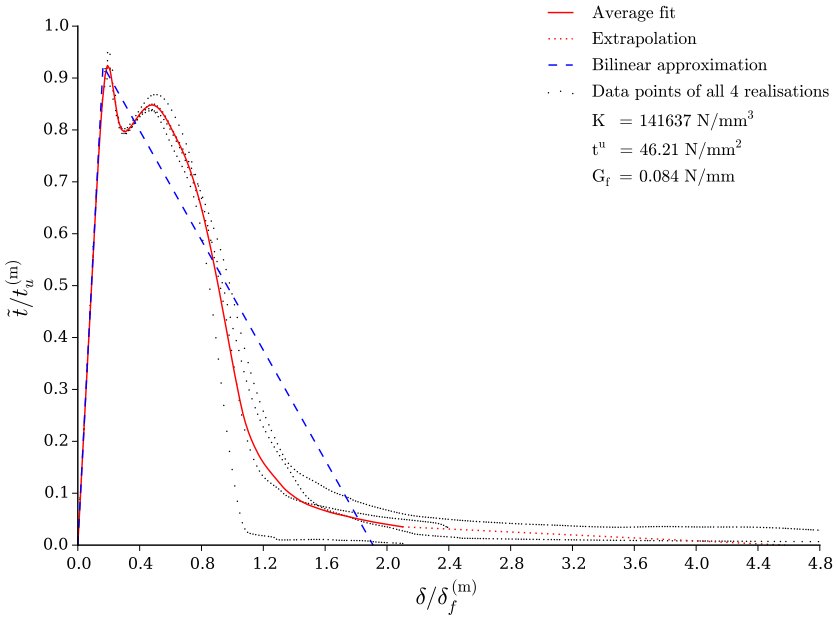

Figure 8.1.1: Illustration of the bilinear TSL for the reference model subjected to uni-axial extension (LC1).

The procedure above gives an overall good bilinear approximation, of which examples are shown in Figure 8.1.1 and 8.1.2, i.e. the bilinear TSL for the model with reference properties for LC1 and LC6 respectively. From the data points of all realisations an average ETSL is determined, which is extrapolated to zero traction and from this curve the effective bilinear TSL is derived. In Figure 8.1.1 the maximum cohesive strength aligns perfectly with the peak of the ETSL. However, for the case in Figure 8.1.2 the bilinear TSL starts deviating from the ETSL. Although the shape of the bilinear TSL is different, the physical behaviour in terms of maximum cohesive strength and fracture energy is assumed similar to the ETSL.

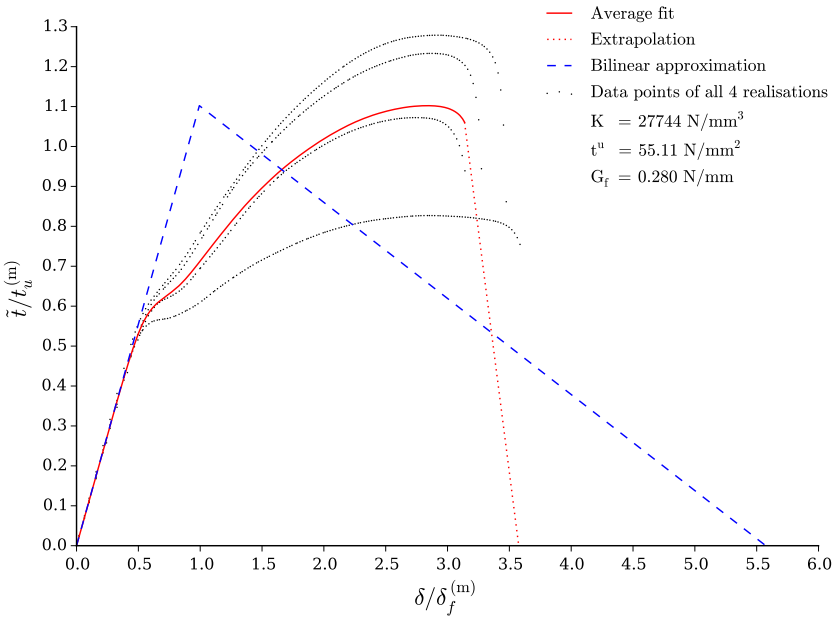

Figure 8.1.2: Illustration of the bilinear TSL for the reference model subjected to simple shear (LC6).

The above are just two examples, the bilinear TSL of each data point is given in Appendix B. For each data point and load case the three parameters that describe a bilinear TSL are listed: the initial slope in Table 8.2, the maximum cohesive strength Table 8.3 and the fracture energy in Table 8.5. In addition the initiation at separation (δ_i) is determined using Equation 8.1.1 and is given in Table 8.4. All these values will be used for the curve fitting in Section 8.2 and 8.3.

$$\delta_i^{LCi} = \frac{t_u^{LCi}}{K^{LCi}} \tag{8.1.1}$$

Table 8.2: Initial slope of the bilinear TSL for each data point and load case. Units are N/mm^3.

#	K^{LC1}	K^{LC3}	K^{LC4}	K^{LC5}	K^{LC6}
1	141637	100562	84530	118969	27744
2	139524	100623	84450	120572	27709
3	141588	100628	84369	120454	27714
4	141565	100556	84312	117925	27738
5	141639	100632	85259	120666	27825
6	141622	100586	84959	120747	27749
7	141546	100571	85149	120876	27704
8	141640	100596	84793	118953	27751
9	141629	100596	84707	119028	27746
10	115916	81472	67364	99094	21083
11	177135	126697	105694	150395	35962

Table 8.3: Maximum cohesive strength, i.e. peak, of the bilinear TSL for each data point and load case. Units are N/mm^2.

#	${t_u}^{LC1}$	${t_u}^{LC3}$	${t_u}^{LC4}$	${t_u}^{LC5}$	${t_u}^{LC6}$
1	46.21	41.58	40.31	40.93	55.11
2	65.12	60.25	57.12	62.08	61.90
3	66.89	61.18	57.68	62.92	66.92
4	45.75	41.55	40.15	39.26	53.78
5	38.33	36.39	37.58	34.71	47.75
6	46.30	42.19	41.34	41.70	55.92
7	46.20	42.44	41.81	41.74	51.78
8	46.21	41.61	40.42	40.93	54.75
9	46.21	41.63	40.38	40.96	56.20
10	46.59	44.47	43.67	43.06	43.83
11	47.49	40.43	38.05	40.96	61.89

Table 8.4: Separation at damage initiation for each data point and load case. Units are µm.

#	${\delta_i}^{LC1}$	${\delta_i}^{LC3}$	${\delta_i}^{LC4}$	${\delta_i}^{LC5}$	${\delta_i}^{LC6}$
1	0.326	0.413	0.477	0.344	1.986
2	0.467	0.599	0.676	0.515	2.234
3	0.472	0.608	0.684	0.522	2.415
4	0.323	0.413	0.476	0.333	1.939
5	0.271	0.362	0.441	0.288	1.716
6	0.327	0.419	0.487	0.345	2.015
7	0.326	0.422	0.491	0.345	1.869
8	0.326	0.414	0.477	0.344	1.973
9	0.326	0.414	0.477	0.344	2.025
10	0.402	0.546	0.648	0.435	2.079
11	0.268	0.319	0.360	0.272	1.721

Table 8.5: Fracture energy, i.e. area, of the bilinear TSL for each data point and load case. Units are N/mm.

#	${G_f}^{LC1}$	${G_f}^{LC3}$	${G_f}^{LC4}$	${G_f}^{LC5}$	${G_f}^{LC6}$
1	0.084	0.134	0.140	0.137	0.280
2	0.113	0.157	0.210	0.164	0.252
3	0.113	0.177	0.224	0.186	0.269
4	0.084	0.135	0.146	0.137	0.294
5	0.099	0.196	0.167	0.167	0.303
6	0.103	0.171	0.173	0.163	0.304
7	0.133	0.214	0.191	0.222	0.298
8	0.083	0.136	0.128	0.137	0.278
9	0.080	0.136	0.141	0.139	0.285
10	0.091	0.148	0.156	0.131	0.246
11	0.070	0.113	0.140	0.116	0.267

8.2 Mode I and II Parameter Curve Fitting

Now that the bilinear TSL parameters of each data point are known from the previous section, the correlation and curve fitting can be performed. In this section the parameters of the mode I and mode II load case are fitted, i.e. the uni-axial extension and simple shear load case respectively. The goal is to define an equation for each parameter that can reproduce the values for any data point with random variables[2]. For instance as in the form shown below.

[2]In this context a parameter is either the initial slope (K), maximum cohesive strength (t_u) or fracture energy (G_f). The term variable refers to the four cohesive input variables and the fiber fraction.

In the end the mode I and mode II properties are used in ABAQUS for fracture simulations on a macroscopic scale.

$$K^{I,II} = f^{I,II}(x_1, x_2, x_3, x_4, x_5) \tag{8.2.1}$$

$$t_u^{I,II} = g^{I,II}(x_1, x_2, x_3, x_4, x_5) \tag{8.2.2}$$

$$G_f^{I,II} = h^{I,II}(x_1, x_2, x_3, x_4, x_5) \tag{8.2.3}$$

where,

$$x_1 = \frac{t_u^{(i)}}{t_u^{(m)}}, \quad x_2 = \frac{t_u^{(f)}}{t_u^{(m)}}, \quad x_3 = \frac{G_f^{(i)}}{G_f^{(m)}}, \quad x_4 = \frac{G_f^{(f)}}{G_f^{(m)}}, \quad x_5 = V_f$$

The equations above are fitted to the bilinear TSL parameters of the uni-axial extension and simple shear load case using a multiple variable least squares fit. A multiple variable least squares fit is performed by solving a linear system of equations as given below.

$$\boldsymbol{A}^T \boldsymbol{A}\boldsymbol{c} = \boldsymbol{A}^T \boldsymbol{y} \tag{8.2.4}$$

where $\boldsymbol{c}$ is a vector containing the unknown coefficients of the multiple variable equation, $\boldsymbol{y}$ is a vector with the data points to which the curve is fitted and $\boldsymbol{A}$ contains the values of each variable x_i. For instance, if each variable is assumed to vary linearly as in Equation 8.2.5 the linear system of equations can be assembled for n data points.

$$y = c_0 + c_1 x_1 + c_2 x_2 + c_3 x_3 + c_4 x_4 + c_5 x_5 \tag{8.2.5}$$

$$\underbrace{\begin{pmatrix} 1 & x_1^{(1)} & x_2^{(1)} & x_3^{(1)} & x_4^{(1)} & x_5^{(1)} \\ 1 & x_1^{(2)} & x_2^{(2)} & x_3^{(2)} & x_4^{(2)} & x_5^{(2)} \\ \vdots & \vdots & \vdots & \vdots & \vdots & \vdots \\ 1 & x_1^{(n)} & x_2^{(n)} & x_3^{(n)} & x_4^{(n)} & x_5^{(n)} \end{pmatrix}}_{\boldsymbol{A}} \underbrace{\begin{pmatrix} c_0 \\ c_1 \\ c_2 \\ c_3 \\ c_4 \\ c_5 \end{pmatrix}}_{\boldsymbol{c}} = \underbrace{\begin{pmatrix} y^{(1)} \\ y^{(2)} \\ \vdots \\ y^{(n)} \end{pmatrix}}_{\boldsymbol{y}} \tag{8.2.6}$$

The linear system in Equation 8.2.6 can easily be solved for the unknown coefficients in $\boldsymbol{c}$ using the $\boldsymbol{A}$ matrix and its transpose and the data points in the $\boldsymbol{y}$ vector to which the data has to be fitted. However, the dependence on a variable may not always be linear and another function might give a better fit. Therefore the Equation 8.2.5 is generalised to be able to accommodate for power laws[3], see Equation 8.2.7.

[3] A power law is preferred over a polynomial or exponential as the behaviour is more monotonic. In addition

$$y = c_0 + c_1 x_1^{b_1} + c_2 x_2^{b_2} + c_3 x_3^{b_3} + c_4 x_4^{b_4} + c_5 x_5^{b_5} \tag{8.2.7}$$

The above relation is nonlinear, i.e. the $\boldsymbol{A}$ matrix becomes of the form below where each column $\boldsymbol{x_i} = x_i^{(1)}, x_i^{(2)}, ..., x_i^{(n)}$ has an unknown power b_i.

$$\boldsymbol{A} = \begin{pmatrix} \mathbf{1} & \boldsymbol{x_1}^{b_1} & \boldsymbol{x_2}^{b_2} & \boldsymbol{x_3}^{b_3} & \boldsymbol{x_4}^{b_4} & \boldsymbol{x_5}^{b_5} \end{pmatrix} \tag{8.2.8}$$

In order to solve this nonlinear system of equations each power b_i is determined separately for each variable. Before this is done tolerances are used to determine if the dependence on an individual variable is constant ($b_i = 0$), linear ($b_i = 1$) or otherwise. In the case $b_i = 0$ the column of the corresponding variable in the $\boldsymbol{A}$ matrix is removed. In case it is otherwise, a power law fit of an individual variable is performed.

An example for the effect of variable $x_1 = t_u^{(i)} / t_u^{(m)}$ on the maximum cohesive strength for LC1 will be shown below. The effect of variable x_1 is given by the first three data points in Table 8.1, i.e. $x_1 = 0.5, 1.0, 2.0$. The corresponding maximum cohesive strengths from Table 8.3 are 46.21, 65.12, 66.89 respectively. In this case the power law fit is described by;

$$t_u^{LC1} = y = c_1 x_1^{b_1} \tag{8.2.9}$$

which is linearised by taking the natural logarithmic of both sides;

$$\log(y) = \log(c_1 x_1^{b_1}) = \log(c_1) + b_1 \cdot \log(x_1) \tag{8.2.10}$$

which is a linear equation that can be solved using Equation 8.2.4 where;

$$\boldsymbol{A} = \begin{pmatrix} 1 & \log(0.5) \\ 1 & \log(1.0) \\ 1 & \log(2.0) \end{pmatrix} \tag{8.2.11}$$

$$\boldsymbol{y} = \begin{pmatrix} \log(46.21) \\ \log(65.21) \\ \log(66.89) \end{pmatrix} \tag{8.2.12}$$

As a result a value of 0.267 is found for b_1. In some cases a simple shift of the power law, i.e. $x_i - x0_i$, can result in a better fit. Therefore another minimisation over the above method is

the effect of each individual variable is represented by only three data points. A polynomial with order two can produce a perfect fit through those three data points but outside the range of these data points the polynomial fit may be significantly off.

performed for $x0_i$ in the range from -4 to 0. If $x_{0,i}$ is not zero this value has to be subtracted from the corresponding vector $(x_i - x_{0,i})_i^b$ in Equation 8.2.8.

The above procedure is performed for each variable separately and the resulting b_i can now be implemented in Equation 8.2.8. Subsequently the multiple variable system as in Equation 8.2.4 is solved.

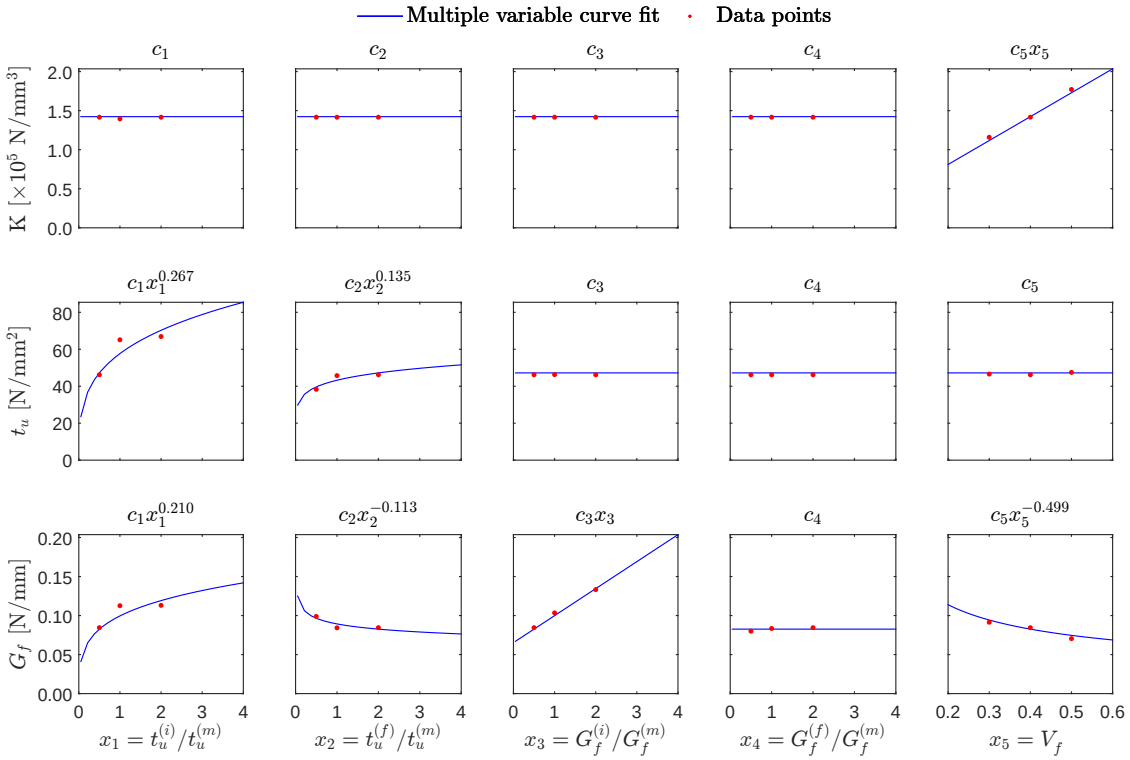

Figure 8.2.1: Multiple variable least squares fit of the three bilinear TSL parameters as a function of the five variables for mode I (uni-axial extension). The effect of each variable is shown individually. Note that the five x-axes are applicable for the subplots in vertical direction and the three y-axes are applicable for the subplots in horizontal direction.

With the above procedure the results for the mode I parameters can be illustrated as in in Figure 8.2.1. Here the values of K, t_u and G_f for each data point of LC1 from Table 8.2 to 8.5 are plotted. In addition the fitted curves, as in the equations Equation 8.2.13 to 8.2.15, are plotted for each variable separately[4]. From these equations it is observed that the initial slope, K^I, is only depending on the fiber volume fraction x_5, which is expected because the cohesive properties do not change the linear elastic behaviour of the Representative Volume Element (RVE). The maximum cohesive strength, t_u^I depends only on the input cohesive strengths. The fracture energy G_f^I depends on all variables except the fiber fracture energy x_4. However, this is mainly due to the fracture pattern that does not interact with the fiber

[4]One variable (x_i) is evaluated for the range 0 to 4 (or 0.2 to 0.6 for V_f) while keeping the other variables constant at the reference value of data point 1.

cohesive elements. It is expected that if the effect of fiber fracture energy was studied with $x_2 = 0.5$ instead of 1.0 a similar effect as the effect of interface fracture energy will be observed. This is one of the limitations of the method, the fracture pattern has a significant influence on the parameters, especially the fracture energy.

$$K^I = \quad 19874 + 306096 \cdot x_5 \tag{8.2.13}$$

$$t_u^I = -48.71 + 62.00 \cdot x_1^{0.267} + 40.43 \cdot x_2^{0.135} \tag{8.2.14}$$

$$G_f^I = -0.200 + 0.125 \cdot x_1^{0.210} + 0.088 \cdot x_2^{-0.113} + 0.034 \cdot x_3 + 0.048 \cdot x_5^{-0.499} \tag{8.2.15}$$

Table 8.6: Comparison of the mode I bilinear TSL parameters of the original data points and the predicted values of the curve fit functions; Equation 8.2.13, 8.2.14 and 8.2.15.

#	K^{LC1} N/mm^3	K^I N/mm^3	error	${t_u}^{LC1}$ N/mm^2	${t_u}^I$ N/mm^2	error	${G_f}^{LC1}$ N/mm	${G_f}^I$ N/mm	error
1	141637	142313	0.48%	46.21	47.21	2.16%	0.084	0.083	2.22%
2	139524	142313	2.00%	65.12	57.68	11.43%	0.113	0.100	11.57%
3	141588	142313	0.51%	66.89	70.27	5.05%	0.113	0.119	5.39%
4	141565	142313	0.53%	45.75	43.25	5.47%	0.084	0.089	5.93%
5	141639	142313	0.48%	38.33	39.64	3.42%	0.099	0.097	2.39%
6	141622	142313	0.49%	46.30	47.21	1.97%	0.103	0.100	3.40%
7	141546	142313	0.54%	46.20	47.21	2.18%	0.133	0.135	0.95%
8	141640	142313	0.47%	46.21	47.21	2.16%	0.083	0.083	0.98%
9	141629	142313	0.48%	46.21	47.21	2.16%	0.080	0.083	3.25%
10	115916	111703	3.63%	46.59	47.21	1.34%	0.091	0.094	3.13%
11	177135	172922	2.38%	47.49	47.21	0.60%	0.070	0.075	5.93%

Comparing the values of the original data points and the values determined by the equations above gives the results in Table 8.6. Overall the error is acceptable, for the maximum cohesive strength and fracture energy prediction of data point 2 the highest error is observed. In Figure 8.2.1 the difference between the data point and multiple variable curve fit is clearly visible. This is due to the change in fracture pattern, i.e. for $x_1 \geq 1$ the crack propagates through the matrix and thus the effective maximum cohesive strength and fracture energy is higher. As mentioned before, there is only little difference between a factor 1.0 or 2.0. In order to fit this data better more data points are required.

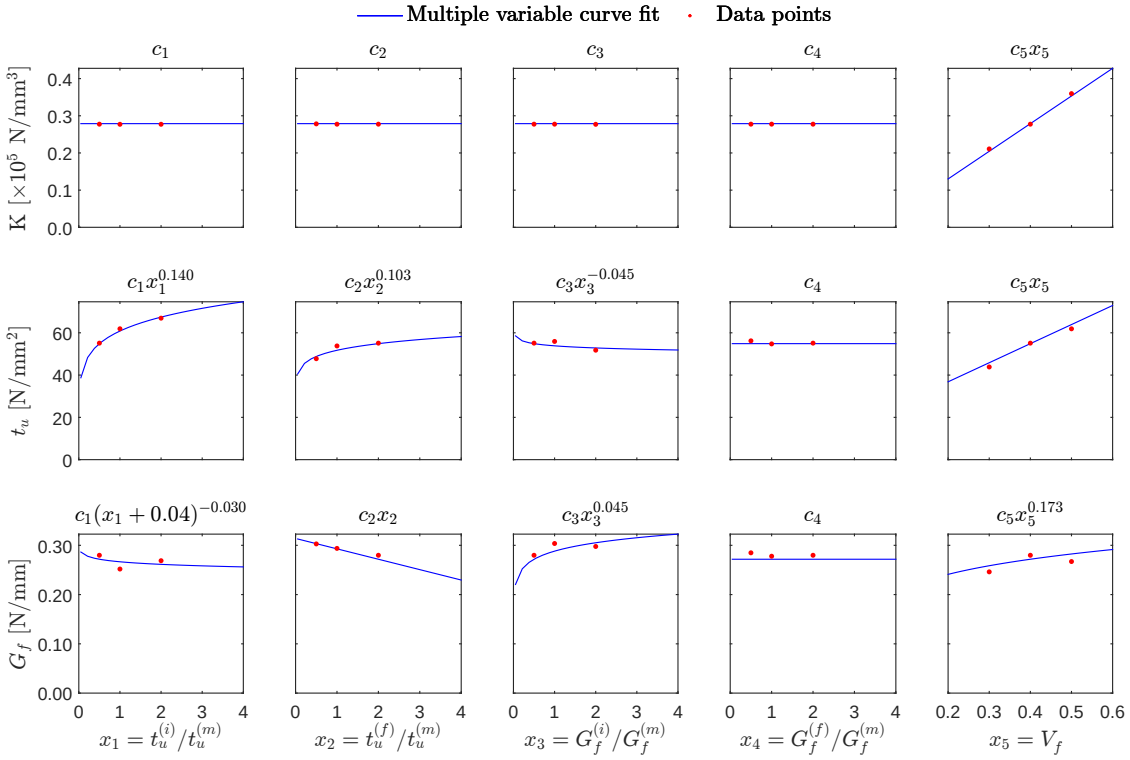

Figure 8.2.2: Multiple variable least squares fit of the three bilinear TSL parameters as a function of the five variables for mode II (simple shear). The effect of each variable is shown individually. Note that the five x-axes are applicable for the subplots in vertical direction and the three y-axes are applicable for the subplots in horizontal direction.

For the mode II curve fitting the results are summarised in Figure 8.2.2, with the corresponding equations in Equation 8.2.16 - 8.2.18. Again the initial slope, K is only dependent on the fiber volume fraction. The maximum cohesive strength, t_u, is now also depending on the interface fracture energy and fiber volume fraction. The same holds for the fracture energy. This is partly explained by the difference in loading condition. The other part is due to the method used for the determination of the bilinear TSL parameters in Section 8.1. In the end the errors between the original data points and predicted values, listed in Table 8.7, are acceptable.

$$K^{II} = -1873 + 74393 \cdot x_5 \tag{8.2.16}$$

$$t_u^{II} = -118.84 + 64.56 \cdot x_1^{0.140} + 42.22 \cdot x_2^{0.103} + 32.63 \cdot x_3^{-0.045} + 90.26 \cdot x_5 \tag{8.2.17}$$

$$G_f^{II} = -0.750 + 0.263 \cdot (x_1 + 0.04)^{-0.030} - 0.021 \cdot x_2 + 0.541 \cdot x_3^{0.045} + 0.317 \cdot x_5^{0.173} \tag{8.2.18}$$

Table 8.7: Comparison of the mode II bilinear TSL parameters of the original data points and the predicted values of the curve fit functions; Equation 8.2.16, 8.2.17 and 8.2.18.

#	K^{LC2} N/mm^3	K^{II} N/mm^3	error	$t_u{}^{LC2}$ N/mm^2	$t_u{}^{II}$ N/mm^2	error	$G_f{}^{LC2}$ N/mm	$G_f{}^{II}$ N/mm	error
1	27744	27884	0.51%	55.11	54.87	0.44%	0.280	0.272	2.88%
2	27709	27884	0.63%	61.90	60.84	1.72%	0.252	0.267	5.85%
3	27714	27884	0.61%	66.92	67.42	0.75%	0.269	0.261	2.75%
4	27738	27884	0.53%	53.78	51.73	3.81%	0.294	0.293	0.31%
5	27825	27884	0.21%	47.75	48.81	2.22%	0.303	0.303	0.18%
6	27749	27884	0.49%	55.92	53.84	3.72%	0.304	0.288	5.10%
7	27704	27884	0.65%	51.78	52.83	2.04%	0.298	0.305	2.54%
8	27751	27884	0.48%	54.75	54.87	0.22%	0.278	0.272	2.21%
9	27746	27884	0.50%	56.20	54.87	2.37%	0.285	0.272	4.59%
10	21083	20445	3.03%	43.83	45.84	4.58%	0.246	0.259	5.05%
11	35962	35323	1.78%	61.89	63.90	3.25%	0.267	0.282	5.75%

8.3 Mode Mixity Curve Fitting

In the previous section the bilinear TSL parameters for pure mode I and pure mode II were fitted. At this point a mode I and II TSL can be generated for a data point with random variables. In this section the mode mixity is fitted, i.e. how do the mode I and II TSL interact with each other in the case of a mixed loading. The resulting equations for the three bilinear TSL parameters will represent the resulting failure criterion.

The first step is to find a method to determine the expected crack opening normal ($\boldsymbol{n}$) as a function of the input strain tensor, see Equation 4.3.5. The crack opening normal is required to determine the macroscopic strain tensor, which in turn is required to determine the mode mixity. The idea is that the microscopic RVE represents one single cohesive element on the macroscopic scale. The response of the macroscopic cohesive element loaded with $\boldsymbol{\varepsilon_L}$ should be equal to the response of the microscopic RVE loaded with $\boldsymbol{\varepsilon}$. The relation between the microscopic and macroscopic scale is illustrated in Figure 8.3.1.

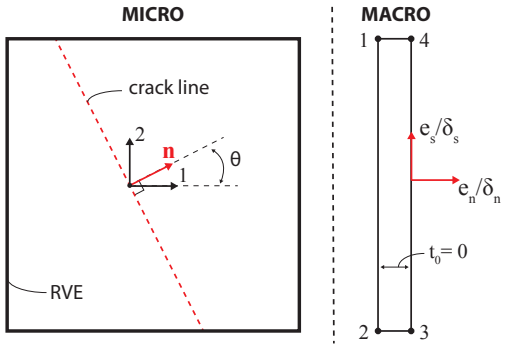

Figure 8.3.1: Illustration of the relation between the microscopic RVE and the single macroscopic cohesive element. The macroscopic strains are described by Equation 8.3.4 and the cohesive element has an initial thickness of zero mm ($t_0 = 0$).

It is expected that the crack opening normal ($\boldsymbol{n}$) aligns with the highest principal strain direction, which is obtained by solving the eigenvalue problem below.

$$(\boldsymbol{\varepsilon} - \lambda \boldsymbol{I}) = \boldsymbol{0} \tag{8.3.1}$$

Solving this eigenvalue problem gives two eigenvalues;

$$\lambda_{1,2} = \frac{(e_{11} + e_{22}) \pm \sqrt{e_{11}^2 + e_{22}^2 + 4e_{12}e_{21} - 2e_{11}e_{22}}}{2} \tag{8.3.2}$$

With the maximum eigenvalue, $\lambda_m = \max(\lambda_{1,2})$, the crack opening direction is equal to the eigenvector corresponding to the largest eigenvalue. Which is equivalent to the equation below.

$$\boldsymbol{n} = \begin{bmatrix} n_1 \\ n_2 \end{bmatrix} = \begin{bmatrix} (\lambda_m - e_{22}) / e_{21} \\ 1 \end{bmatrix} \tag{8.3.3}$$

The crack angle as in Figure 4.1.3 is determined by Equation 4.4.5. Comparing this angle with the actual average crack angle from the simulations in Chapter 7 gives the results in Table 8.8. The error is acceptable and thus the above method is valid.

Table 8.8: Comparison of the predicted crack angle (θ) and the average crack angle of the simulations (θ_{sim}) subjected to a mixed loading.

	$\boldsymbol{\theta}$	$\boldsymbol{\theta_{sim}}$	**error**
LC3	45.0°	44.2°	1.18%
LC4	49.7°	48.7°	2.05%
LC5	31.7°	32.6°	2.76%

$$\boldsymbol{\varepsilon_L} = \begin{bmatrix} e_n \\ e_s \end{bmatrix} = \boldsymbol{\varepsilon} \cdot \frac{\boldsymbol{n}}{|\boldsymbol{n}|} \tag{8.3.4}$$

Multiplying the normalised expected crack opening normal with the applied strain tensor gives the normal (mode I) and shear (mode II) strain along the crack, i.e. $\boldsymbol{\varepsilon_L}$ as in the equation above. The $|\boldsymbol{n}|$ is the magnitude of $\boldsymbol{n}$.

As discussed in Section 3.2 the constitutive thickness of the cohesive element is equal to 1.0, the default setting in ABAQUS , so that $\delta_n = e_n$ and $\delta_s = e_s$. From this fact the macroscopic separation ratio can be determined using Equation 8.3.5. For pure mode I this ratio is 0 ($\delta_s = 0$) and for pure mode II it is ∞ ($\delta_n = 0$).

Table 8.9: Macroscopic strain fractions (α) and mode mixity parameter (β) for each load case.

	$\boldsymbol{\alpha}$ [-]	$\boldsymbol{\beta}$ [rad]	**Description**
LC1	0	0	Mode I
LC3	1	0.25π	Mixed mode equal
LC4	1.18	0.28π	Mixed mode ($e_{12} > e_{11}$)
LC5	0.62	0.18π	Mixed mode ($e_{12} < e_{11}$)
LC6	∞	0.50π	Mode II

$$\alpha = \frac{\delta_s}{\delta_n} = \frac{n_2}{n_1} \overset{(n_2=1)}{=} \frac{e_{21}}{\lambda_m - e_{22}} \tag{8.3.5}$$

$$\beta = \tan^{-1}\alpha \tag{8.3.6}$$

The resulting mode mixity parameter (β) is expressed as in Equation 8.3.6 in terms of an angle. As a result the mode mixity for each load case can be determined as listed in Table 8.9. The goal of this section is to find the three parameters of a bilinear TSL as a function of the mode mixity, the mode I and the mode II properties, for example in the form as shown below.

$$K^\beta = f^\beta(\beta, K^I, K^{II}) \tag{8.3.7}$$

$$t_u^\beta = g^\beta(\beta, t_u^I, t_u^{II}) \tag{8.3.8}$$

$$G_f^\beta = h^\beta(\beta, G_f^I, G_f^{II}) \tag{8.3.9}$$

8.3.1 Initial Slope Mode Mixity Fitting

In order to find the initial slope as a function of the mode mixity, mode I and II properties curve fitting has to be performed. It is chosen to go with an elliptical relation between the mode I and II properties, i.e. as illustrated in Figure 8.3.2. In this way the mode I and II properties will always be exact. This elliptical curve is described by Equation 8.3.10 where examples for the variable m_k are illustrated in Figure 8.3.2.

$$\left(\frac{K^{I*}}{K^I}\right)^{m_k} + \left(\frac{K^{II*}}{K^{II}}\right)^{m_k} = 1 \tag{8.3.10}$$

where,

$$K^{I*} = K^I \cos\beta^{2/m_k} \tag{8.3.11}$$

$$K^{II*} = K^{II} \sin\beta^{2/m_k} \tag{8.3.12}$$

As a result K^{β} is described by,

$$K^{\beta} = \sqrt{\left(K^{I}\cos\beta^{2/m_k}\right)^2 + \left(K^{II}\sin\beta^{2/m_k}\right)^2} \tag{8.3.13}$$

In the above relation only the power m_k is unknown and this is the parameter that is fitted using to one or multiple mixed load cases by minimising the sum of squared residuals (S). The sum of squared residuals is determined by Equation 8.3.14 where n are the number of data points, y_i is the actual value and r_i is the predicted value. It was studied if better results would be obtained if multiple load cases were used for fitting. Therefore, for the results in the subsequent sections either LC3 or LC4 and LC5 are used for the curve fitting. Any combination of load cases can be used but ideally only one load case is required. The other load cases are used for verification.

$$S = \sum_{i=1}^{n} \left(y_i - r_i\right)^2 \tag{8.3.14}$$

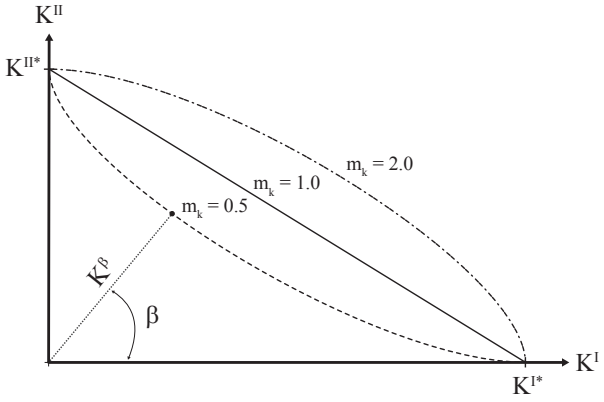

Figure 8.3.2: Illustration of the elliptical relation in Equation 8.3.10 between the mode I and II parameters. The angle β is a function of the mode mixity and K^{β} is equal to the distance between the origin and any point on the ellipse.

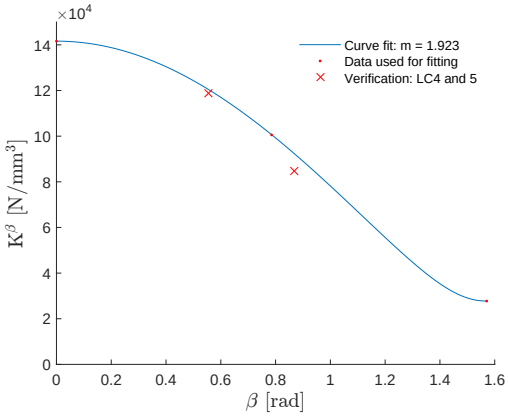

Figure 8.3.3: Example of the initial slope mode mixity fitting of data point 1 using only LC3. The curve fit is described by Equation 8.3.13 with m_k determined by Equation 8.3.15.

Applying the above procedure to the initial slopes (K) of the TSL for mode I and II as listed in Table 8.2 gives a power m_k for each data point. There are several ways one can deal with these powers for each data point; take the individual value, the mean value or use a multiple variable least squares fit (MLSQ) to describe the power by a function. Using the individual power of each data point gives the best curve fit but multiple definitions for the power m_k. Taking the mean value gives a single definition but the results will be less accurate. For the multiple variable least squares fit the same procedure as in Section 8.2 is used, which gives the power as a function of the five variables.

Table 8.10: Powers m_k, corresponding to Equation 8.3.13, that result in the best initial slope fit for each data point.

	LC3	LC4 AND LC5
#	$\boldsymbol{m_k}$	$\boldsymbol{m_k}$
1	1.918	1.642
2	2.002	1.730
3	1.924	1.661
4	1.921	1.622
5	1.921	1.689
6	1.920	1.682
7	1.922	1.692
8	1.920	1.649
9	1.921	1.648
10	1.879	1.621
11	1.951	1.655
avg	**1.927**	**1.663**

For each data point and load case the actual value for K and guessed value can be compared and verified using the load cases that are not used for the fitting. The average errors of all data points for using either the individual, mean or MLSQ value of the power are listed in Table 8.11. Either LC3 or both LC4 and LC5 are used for the fitting and as a comparison $m_k = 1$ and $m_k = 2$ (independent of load case used) given. Note that for LC1 (mode I) and LC6 (mode II) the error is always 0% due to the elliptical relation between the mode I and II properties.

Table 8.11: Average error between the actual and predicted initial slope of all data points using several methods. Using Equation 8.3.13 and either m_k from Table 8.10, the mean or a multiple variable least squares fit as a function of the variables.

	LC3			LC4 AND LC5				
	Individual	**Mean**	**MLSQ**	**Individual**	**Mean**	**MLSQ**	$\boldsymbol{m_k = 1}$	$\boldsymbol{m_k = 2}$
LC1	0.00%	0.00%	0.00%	0.00%	0.00%	0.00%	0.00%	0.00%
LC3	0.00%	0.33%	0.21%	5.57%	5.55%	5.56%	28.35%	1.33%
LC4	9.26%	9.27%	9.27%	1.80%	1.82%	1.81%	27.51%	11.05%
LC5	0.82%	0.83%	0.90%	2.37%	2.36%	2.36%	14.45%	1.18%
LC6	0.00%	0.00%	0.00%	0.00%	0.00%	0.00%	0.00%	0.00%

It can be seen that there is not much difference when either the individual value for each data point, the mean or a multiple variable least square fit is used. Using only LC3 gives a good fit except for LC4, using both LC4 and LC5 gives better results for LC4. However, the results of using only LC3 are preferred, especially when taking into account that only one mixed load case is required which reduces the number of simulations. The mean value gives good results and because this value is close to a power of 2, using $m_k = 2$ also gives acceptable results. In the end it is chosen to go with the multiple variable least squares fit using LC3 as in Equation 8.3.15 as this gives the best results. Here it is also taken into account that if more data points are added the mean value might result in higher errors.

$$m_k = -9.781 + 11.576 \cdot x_1^{0.002} + 0.359 \cdot x_5 \tag{8.3.15}$$

8.3.2 Maximum cohesive strength mode mixity fitting

The second parameter of the bilinear TSL is the maximum cohesive strength. In order to fit this parameter the separation at damage initiation (δ_i) was determined as in Table 8.4. This is done because the curve fitting of the maximum cohesive strength is not straightforward due to the fact that the values of the mixed cases are lower compared to the values of both mode I and II. In the end the maximum cohesive strength is determined by multiplying the fitted slope (K^β) with the fitted separation at damage initiation (δ_i^β), as will be discussed in Section 8.3.4.

Table 8.12: Powers $m_{d,1}$ and $m_{d,2}$, corresponding to Equation 8.3.16, that result in the best separation at damage initiation fit for each data point.

	LC3		LC4 AND LC5	
#	$\boldsymbol{m_{d,1}}$	$\boldsymbol{m_{d,2}}$	$\boldsymbol{m_{d,1}}$	$\boldsymbol{m_{d,2}}$
1	0.244	4.250	0.247	4.332
2	0.326	3.743	0.361	3.463
3	0.343	3.841	0.381	3.523
4	0.246	4.165	0.212	4.850
5	0.239	3.989	0.240	4.222
6	0.255	4.189	0.256	4.313
7	0.252	4.012	0.250	4.170
8	0.243	4.236	0.246	4.324
9	0.246	4.279	0.250	4.356
10	0.339	3.543	0.339	3.750
11	0.164	4.833	0.140	5.550
avg	**0.263**	**4.098**	**0.265**	**4.262**

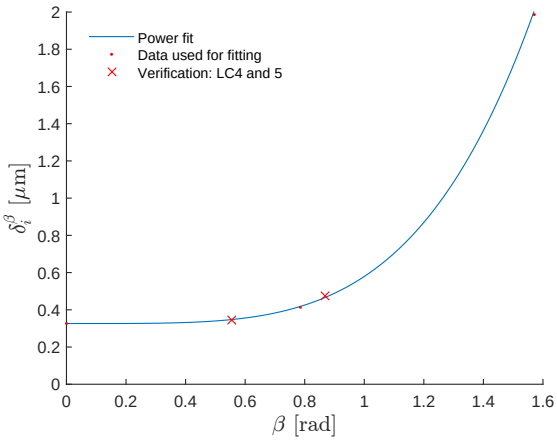

Figure 8.3.4: Example of the separation at initiation (δ_i) mode mixity fitting of data point 1 using only LC3. The curve fit in the form of a power law as described by Equation 8.3.16 with $m_{d,1}$ and $m_{d,2}$ determined by Equation 8.3.17 and 8.3.18.

From the results in Table 8.4 it can be seen that the mode II (LC6) separation is significantly higher compared to the other separations. In this case it is reasonable to use a power law that has an y-intercept at δ_i^I as in Equation 8.3.16. The power fitting is done using a simple least squares fit as has been done with Equation 8.2.9 in Section 8.2. An example for data point 1 is given in Figure 8.3.4, where the two parameters $m_{d,1}$ and $m_{d,2}$ are determined using only LC3 and fitted with the multiple variable least squares fit equations in Equation 8.3.17 and 8.3.18.

$$\delta_i^\beta = m_{d,1} \cdot \beta^{m_{d,2}} + \delta_i^I \tag{8.3.16}$$

Just as with the fitting in Section 8.3.1 either the individual value for $m_{d,1}$ and $m_{d,2}$ of each data point, the mean values or the values as a result of a multiple variable least squares fit can be taken. The resulting average errors of all data points are listed in Table 8.13. The error with LC1 (mode I) is always zero, in contrast with the initial slope fitting the results of LC6

(mode II) are not zero. Overall the curve fit using only LC3 gives better results and it is best to approximate the constants $m_{d,1}$ and $m_{d,2}$ using a multiple variable least squares fit.

Table 8.13: Average error between the actual and predicted separation at damage initiation of all data points using several methods. Using Equation 8.3.16 and either the individual $m_{d,1}$ and $m_{d,2}$ from Table 8.12, the mean values or a multiple variable least squares fit as a function of the variables.

	LC3			LC4 AND LC5		
	Individual	**Mean**	**MLSQ**	**Individual**	**Mean**	**MLSQ**
LC1	0.00%	0.00%	0.00%	0.00%	0.00%	0.00%
LC3	0.00%	4.83%	0.61%	2.16%	3.99%	2.07%
LC4	3.96%	5.79%	3.92%	5.32%	6.12%	5.52%
LC5	1.66%	2.98%	1.78%	0.53%	2.65%	0.99%
LC6	0.00%	5.07%	1.32%	6.90%	10.12%	7.52%

The multiple variable least squares fit of the two parameters as in Table 8.12 is given by the equations below. These equations are depending on more variables compared to Equation 8.3.15 due to the fact that the power law fit is sensitive to small changes in the constants $m_{d,1}$ and $m_{d,2}$. Therefore, the tolerance that is used to determine if the dependence on a variable is constant is lowered. However, the main dependence is still on the variable $x_5 = V_f$.

$$m_{d,1} = \quad 0.590 + 0.297 \cdot x_1^{0.245} + 0.689 \cdot x_2^{0.015} - 0.005 \cdot x_3^{0.025} - 0.933 \cdot x_4^{-0.007} - 0.874 \cdot x_5 \tag{8.3.17}$$

$$m_{d,2} = -18.397 + 4.571 \cdot x_1^{-0.073} + 2.758 \cdot x_2^{0.046} - 0.110 \cdot x_3 + 12.454 \cdot x_4^{-0.005} + 6.450 \cdot x_5 \tag{8.3.18}$$

8.3.3 Fracture energy mode mixity fitting

For the mode mixity fitting of the fracture energy a method that is compatible with an ABAQUS implementation is preferred. One of the methods to relate the mode I and II fracture energy (i.e. critical energy release rate) is the Benzeggagh-Kenane (BK) expression, see Equation 8.3.19 [80]. For the implementation in ABAQUS only the mode I and II fracture energy and a power m_g have to be specified.

$$G_f^\beta = G_f^I + \left(G_f^{II} - G_f^I\right)\left(\frac{G_{shear}}{G_{total}}\right)^{m_g} \tag{8.3.19}$$

Here, G_{shear} is the work done due to shear (i.e. G_{II}) and G_{total} is the total work done, i.e. $G_{total} = G_I + G_{II}$. These parameters are not known before the simulation and thus a different expression is required. Using the derivation from Turon *et al.* [80] the relation in Equation 8.3.20 is determined.

$$\frac{G_{shear}}{G_{total}} = \frac{\alpha_s^2}{1+2\alpha_s^2-2\alpha_s} \tag{8.3.20}$$

where α_s is given by:

$$\alpha_s = \frac{\delta_s}{\delta_n+\delta_s} \overset{\delta_s=\delta_n\tan\beta}{=} \frac{\delta_n\tan\beta}{\delta_n+\delta_n\tan\beta} = \frac{\tan\beta}{1+\tan\beta} \tag{8.3.21}$$

The relation between α_s and β is derived above and substituted in Equation 8.3.20. After some trigonometry simplifications the resulting modified BK law is given as a function of β.

$$G_f^\beta = G_f^I + \left(G_f^{II} - G_f^I\right)\left(\frac{1-\cos(2\beta)}{2}\right)^{m_g} \tag{8.3.22}$$

Table 8.14: Powers m_g, corresponding to Equation 8.3.22, that result in the best fracture energy fit for each data point.

	LC3	LC4 AND LC5
#	$\boldsymbol{m_g}$	$\boldsymbol{m_g}$
1	1.970	1.750
2	1.658	0.732
3	1.294	0.599
4	2.033	1.745
5	1.072	1.384
6	1.557	1.428
7	1.021	0.882
8	1.900	2.011
9	1.884	1.627
10	1.449	1.338
11	2.224	1.574
avg	**1.642**	**1.370**

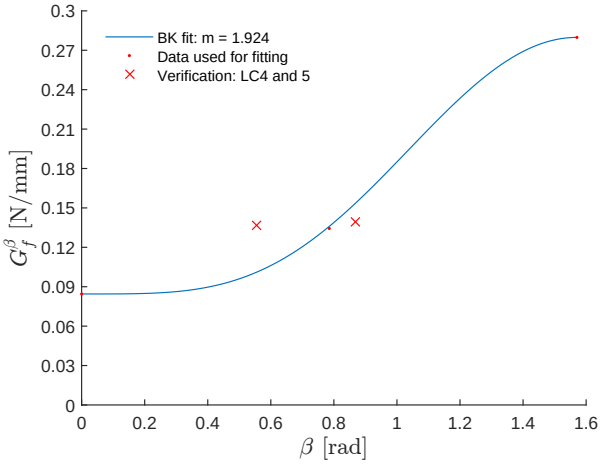

Figure 8.3.5: Example of the fracture mode mixity fitting of data point 1 using only LC3. The curve fit is in the form of a BK law described by Equation 8.3.22 with m_g determined by Equation 8.3.23.

The resulting power of the curve fit where the sum of squared residuals is minimised is listed in Table 8.14. Subsequently the actual values can be compared with the predicted value using Equation 8.3.22 by either taking the individual power m_g for each data point, the mean or a multiple variable least squares fit. See Table 8.15 for the average error over all data points.

Table 8.15: Average error between the actual and predicted fracture energy of all data points using several methods. Using Equation 8.3.22 and either m_g from Table 8.14, the mean or a multiple variable least squares fit as a function of the variables.

	LC3			LC4 AND LC5				
	Individual	**Mean**	**MLSQ**	**Individual**	**Mean**	**MLSQ**	$m_g = 1$	$m_g = 2$
LC1	0.00%	0.00%	0.00%	0.00%	0.00%	0.00%	0.00%	0.00%
LC3	0.00%	9.03%	2.81%	10.40%	12.64%	10.53%	23.01%	8.93%
LC4	13.18%	13.56%	13.61%	12.21%	19.44%	13.13%	29.11%	9.08%
LC5	22.44%	22.85%	22.72%	16.35%	16.58%	17.21%	6.32%	28.37%
LC6	0.00%	0.00%	0.00%	0.00%	0.00%	0.00%	0.00%	0.00%

It is observed that the errors in Table 8.15 are significantly higher compared to the errors observed in the previous two subsections. This is because the BK law does not perfectly align with the values for LC4 and LC5 as in Figure 8.3.5. However, using only LC3 for fitting and taking the multiple variable least squares fit of the power m_g gives results that are tolerable. Especially due to the fact that this is easily implemented in ABAQUS, onwhich will be discussed further in Section 8.4.

$$m_g = -1.649 - 0.432 \cdot x_1 + 0.961 \cdot x_2^{0.439} - 0.615 \cdot x_3 + 0.945 \cdot x_4^{0.032} + 3.984 \cdot x_5^{0.850} \tag{8.3.23}$$

8.3.4 Results Summary

Overall it is determined that when performing the parameter mode mixity fitting using only one mixed load case, i.e. LC3, is sufficient. The powers for each parameter are determined using a multiple variable least squares fit with the result as in Equation 8.3.15, 8.3.17, 8.3.18 and 8.3.23. The maximum cohesive strength is determined using Equation 8.1.1. Using this procedure the predicted parameters for each data point can be determined and compared to the actual parameter, see Table 8.16, 8.17 and 8.18. Note that only the mixed load cases are compared due to the fact that the mode I and mode II properties always align with the LC1 and LC6 properties, except for the mode II separation at crack initiation. This is due to the power fit, which will result in a small error (average 1.35%) in the predicted maximum cohesive strength of mode II.

Overall the results are acceptable with the highest errors in the initial slope of LC4 and the fracture energies of LC4 and LC5. At this point the comparison between the data points is performed using the data points from the simulations, but in theory the bilinear TSL parameters of a random data point (i.e. with random variables) can be determined for any load case.

Table 8.16: Comparison actual and predicted initial slope for the mixed load cases. The initial slope is predicted using Equation 8.3.13 and the powers m_k are determined with Equation 8.3.15.

#	K^{LC3} N/mm^3	$K^{0.25\pi}$ N/mm^3	**error** %	K^{LC4} N/mm^3	$K^{0.28\pi}$ N/mm^3	**error** %	K^{LC5} N/mm^3	$K^{0.18\pi}$ N/mm^3	**error** %
1	100562	100650	0.09	84530	92371	9.28	118969	120547	1.33
2	100623	99496	1.12	84450	91394	8.22	120572	118944	1.35
3	100628	101210	0.58	84369	93013	10.24	120454	120852	0.33
4	100556	100600	0.04	84312	92325	9.50	117925	120486	2.17
5	100632	100662	0.03	85259	92386	8.36	120666	120554	0.09
6	100586	100640	0.05	84959	92362	8.71	120747	120535	0.18
7	100571	100583	0.01	85149	92308	8.41	120876	120469	0.34
8	100596	100653	0.06	84793	92374	8.94	118953	120550	1.34
9	100596	100645	0.05	84707	92366	9.04	119028	120541	1.27
10	81472	81601	0.16	67364	74692	10.88	99094	98236	0.87
11	126697	126883	0.15	105694	116687	10.40	150395	151324	0.62
avg			**0.21**			**9.27**			**0.90**

Table 8.17: Comparison actual and predicted maximum cohesive strength for the mixed load cases. The maximum cohesive strength is predicted using the predicted initial slope, Equation 8.1.1, Equation 8.3.16 and the powers $m_{d,1}$ and $m_{d,2}$ are determined with Equation 8.3.17 and 8.3.18.

#	${t_u}^{LC3}$ N/mm^2	${t_u}^{0.25\pi}$ N/mm^2	**error** %	${t_u}^{LC4}$ N/mm^2	${t_u}^{0.28\pi}$ N/mm^2	**error** %	${t_u}^{LC5}$ N/mm^2	${t_u}^{0.18\pi}$ N/mm^2	**error** %
1	41.58	42.08	1.20	40.31	43.04	6.75	40.93	41.88	2.31
2	60.25	57.90	3.90	57.12	58.29	2.04	62.08	58.95	5.04
3	61.18	62.39	1.99	57.68	63.40	9.92	62.92	61.81	1.75
4	41.55	41.68	0.31	40.15	42.52	5.90	39.26	41.55	5.82
5	36.39	36.34	0.13	37.58	37.48	0.27	34.71	35.29	1.67
6	42.19	42.26	0.16	41.34	43.19	4.47	41.70	42.04	0.82
7	42.44	42.43	0.01	41.81	43.32	3.61	41.74	42.13	0.94
8	41.61	41.82	0.49	40.42	42.72	5.70	40.93	41.77	2.06
9	41.63	41.55	0.17	40.38	42.41	5.02	40.96	41.67	1.74
10	44.47	44.58	0.24	43.67	45.40	3.95	43.06	43.58	1.19
11	40.43	40.54	0.28	38.05	41.02	7.79	40.96	42.00	2.55
avg			**0.81**			**5.04**			**2.35**

Table 8.18: Comparison actual and predicted fracture energy for the mixed load cases. The fracture energy is predicted using Equation 8.3.22 and the powers m_g are determined with Equation 8.3.23.

#	$G_f{}^{LC3}$ N/mm	$G_f{}^{0.25\pi}$ N/mm	**error** %	$G_f{}^{LC4}$ N/mm	$G_f{}^{0.28\pi}$ N/mm	**error** %	$G_f{}^{LC5}$ N/mm	$G_f{}^{0.18\pi}$ N/mm	**error** %
1	0.134	0.136	1.19	0.140	0.153	9.83	0.137	0.101	26.37
2	0.157	0.155	0.97	0.210	0.168	20.15	0.164	0.128	21.95
3	0.177	0.177	0.43	0.224	0.191	14.64	0.186	0.143	23.12
4	0.135	0.154	13.83	0.146	0.173	18.90	0.137	0.112	18.81
5	0.196	0.180	8.14	0.167	0.198	18.76	0.167	0.136	18.72
6	0.171	0.169	1.60	0.173	0.187	7.80	0.163	0.128	21.07
7	0.214	0.215	0.53	0.191	0.229	19.57	0.222	0.179	19.46
8	0.136	0.135	0.07	0.128	0.153	19.22	0.137	0.100	26.85
9	0.136	0.136	0.05	0.141	0.154	9.26	0.139	0.098	29.46
10	0.148	0.145	2.04	0.156	0.159	2.08	0.131	0.113	13.74
11	0.113	0.110	2.07	0.140	0.127	9.47	0.116	0.081	30.35
avg			**2.81**			**13.61**			**22.72**

8.4 Failure Criterion

The procedure in the previous three sections resulted in equations that represent the effective bilinear TSL for random variables x_i and β. As mentioned before this bilinear TSL is considered as the resulting fracture mechanism on the macroscopic scale that incorporates details from the microscopic RVE. The equations that represent the failure criterion are the following:

$$K^{\beta} = \sqrt{\left(K^{I}\cos\beta^{2/m_k}\right)^2 + \left(K^{II}\sin\beta^{2/m_k}\right)^2} \tag{8.4.1}$$

$$t_u^{\beta} = K^{\beta}\cdot m_{d,1}\cdot\beta^{m_{d,2}} + \frac{t_u^I}{K^I} \tag{8.4.2}$$

$$G_f^{\beta} = G_f^I + \left(G_f^{II} - G_f^I\right)\left(\frac{1-\cos(2\beta)}{2}\right)^{m_g} \tag{8.4.3}$$

where,

$$K^I = \quad 19874 + 306096\cdot x_5 \tag{8.4.4}$$

$$K^{II} = -1873 + 74393\cdot x_5 \tag{8.4.5}$$

$$m_k = -9.781 + 11.576\cdot x_1^{0.002} + 0.359\cdot x_5 \tag{8.4.6}$$

$$t_u^I = -48.71 + 62.00\cdot x_1^{0.267} + 40.43\cdot x_2^{0.135} \tag{8.4.7}$$

$$m_{d,1} = \quad 0.590 + 0.297\cdot x_1^{0.245} + 0.689\cdot x_2^{0.015} - 0.005\cdot x_3^{0.025} - 0.933\cdot x_4^{-0.007} - 0.874\cdot x_5 \tag{8.4.8}$$

$$m_{d,2} = -18.397 + 4.571\cdot x_1^{-0.073} + 2.758\cdot x_2^{0.046} - 0.110\cdot x_3 + 12.454\cdot x_4^{-0.005} + 6.450\cdot x_5 \tag{8.4.9}$$

$$G_f^I = -0.200 + 0.125 \cdot x_1^{0.210} + 0.088 \cdot x_2^{-0.113} + 0.034 \cdot x_3 + 0.048 \cdot x_5^{-0.499} \tag{8.4.10}$$

$$G_f^{II} = -0.750 + 0.263 \cdot (x_1 + 0.04)^{-0.030} - 0.021 \cdot x_2 + 0.541 \cdot x_3^{0.045} + 0.317 \cdot x_5^{0.173} \tag{8.4.11}$$

$$m_g = -1.649 - 0.432 \cdot x_1 + 0.961 \cdot x_2^{0.439} - 0.615 \cdot x_3 + 0.945 \cdot x_4^{0.032} + 3.984 \cdot x_5^{0.850} \tag{8.4.12}$$

In the above x_i is given by the variables in Section 8.2 and the mode mixity β by Equation 8.3.6. Now this has been established a suggested implementation in ABAQUS is discussed. For the microscopic RVE the input TSL for the fiber, matrix or interface cohesive elements was assumed mode-independent. For the implementation of the cohesive elements in the macroscopic model a mode-dependent approach is presented.

8.4.1 Macroscopic Implementation

The macroscopic failure criterion in the previous represents the fracture mechanism by means of a bilinear TSL. The goal is to give this fracture behaviour as input for a single cohesive element on the macroscopic scale, such that the behaviour is equal to the microscopic RVE. During the simulation the mode mixity of each individual macroscopic cohesive element is variable, each load step a different mode mixity will be observed.

The softening part of the TSL can easily be implemented in ABAQUS using the BK mode mixity behaviour as in Equation 8.4.3. Only the power m_g, mode I and mode II properties have to be specified by the user and then ABAQUS ensures a fracture energy depending on the mode mixity. In order to align the initial slope of the TSL, i.e. damage initiation, with the mode mixity the following procedure is proposed. The elastic stiffness of the cohesive element is defined by K^I and K^{II}, or E_{nn} and E_{ss} in ABAQUS as in Equation 3.2.6. The maximum cohesive strength is aligned using the MAXE damage initiation criterion. For this criterion the mode I and mode II separation at initiation have to be defined, see below. Here δ_i^β is obtained using Equation 8.3.16.

$$\delta_i^I = \frac{\delta_i^\beta}{\sqrt{1 + \tan\beta^2}} \tag{8.4.13}$$

$$\delta_i^{II} = \delta_i^I \cdot \tan\beta \tag{8.4.14}$$

The dependency of the above relations on the mode mixity is given in Figure 8.4.1 where the effective separation (δ_i^β) is obtained for data point 1.

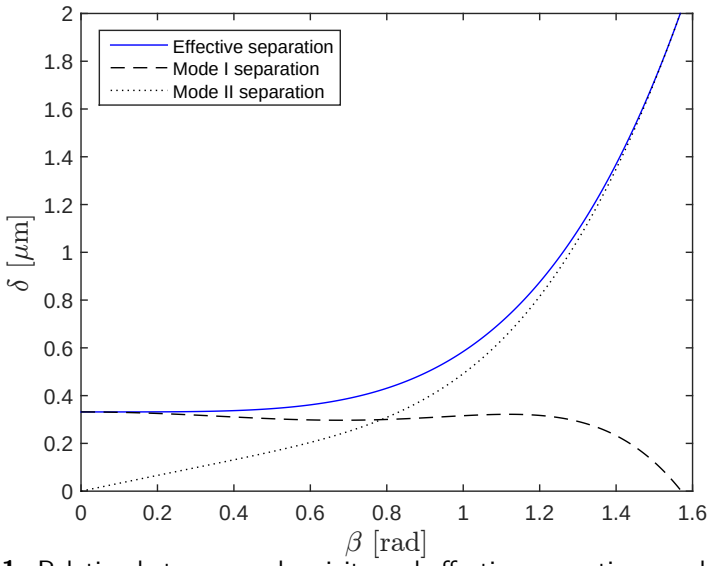

Figure 8.4.1: Relation between mode mixity and effective separation, mode I and mode II separation for data point 1.

In ABAQUS it is possible to define material properties on an user defined field variable. For example, if we take five points from the above plot the material definition as below can be written in the ABAQUS input file.

```
*MATERIAL, NAME=COHESIVE
*DAMAGE INITIATION, CRITERION=MAXE, DEPENDENCIES=1, TOLERANCE=0.001
  0.0003317,    1E-10,          0.,     ,    0.
  0.0003111,    0.0001289,      0.,     ,    0.3927
  0.0002995,    0.0002995,      0.,     ,    0.7854
  0.0003194,    0.0007711,      0.,     ,    1.1781
  1E-10.,       0.0020128,      0.,     ,    1.5708
*DAMAGE EVOLUTION, TYPE=ENERGY, MIXED MODE BEHAVIOR=BK, POWER=1.9244
  0.0826,    0.2717,    0.
*DEPVAR
  1,
*ELASTIC, TYPE=TRACTION
  142313.,    27884.1,    0.
*USER DEFINED FIELD
*INITIAL CONDITIONS, TYPE=SOLUTION
  COHESIVE_ELEMENTS,    0.7854
```

The damage initiation has one dependency, which is β, ranging from 0 to $\pi/2$ in the last column. ABAQUS determines the actual value for δ_i^I and δ_i^{II}, first and second column respectively, by interpolating between the given data. The value of the normal and shear separation can never be zero. Therefore, a value of 1e-10 is used. Note that more points should be added to increase the accuracy. All values in the above example correspond to the cohesive properties of data point 1.

The user defined field statement refers to a field variable that is given by use of the USDFLD subroutine[5]. In this subroutine the mode mixity β has to be defined, i.e. as in Equation 8.3.6.

[5]The USDFLD subroutine is called at the start of the increment for each material point, i.e. elements that

Also the initial conditions of this variable have to be specified for each cohesive element. It is preferred to start at a mode mixity of $\pi/4$ (LC3) because the extremes (0 or $\pi/2$) can result in damage initiation at the first iteration. The proposed USDFLD subroutine that defines the mode mixity β is presented below.

```
      SUBROUTINE USDFLD(FIELD,STATEV,PNEWDT,DIRECT,T,CELENT,TIME,DTIME,CMNAME,ORNAME,NFIELD,
     1 NSTATV,NOEL,NPT,LAYER,KSPT,KSTEP,KINC,NDI,NSHR,COORD,JMAC,JMATYP,MATLAYO,LACCFLA)
C
      INCLUDE 'ABA_PARAM.INC'
C
      CHARACTER*80 CMNAME,ORNAME
      CHARACTER*3 FLGRAY(15)
      DIMENSION FIELD(NFIELD),STATEV(NSTATV),DIRECT(3,3),T(3,3),TIME(2)
      DIMENSION ARRAY(15),JARRAY(15),JMAC(*),JMATYP(*),COORD(*)
C GET ELASTIC STRAIN AND SAVE IT INTO 'ARRAY'
      CALL GETVRM('E',ARRAY,JARRAY,FLGRAY,JRCD,JMAC,JMATYP,MATLAYO,LACCFLA)
C ASSIGN STRAIN VALUE TO FIELD VARIABLE: ARRAY(1) = E11, ARRAY(4) = E12
      IF (ARRAY(1) == 0 .AND. ARRAY(4) == 0) THEN
          FIELD(1) = 0.7854
      ELSE
          FIELD(1) = ATAN(ABS(ARRAY(4))/ABS(ARRAY(1)))
      END IF
C ASSIGN STATE VARIABLES
      STATEV(1) = FIELD(1)
C
      RETURN
      END
```

Using the above procedure the response a cohesive element should align with the input failure criterion as in Equation 8.4.1 to 8.4.3. In order to verify this a single zero-thickness cohesive element is modeled in ABAQUS. The model contains a single COH2D4 element as in Figure 8.3.1. Nodes 1 and 2 are fixed and on nodes 3 and 4 a displacement load (e_n, e_s) is applied. The material properties are equal to the example above but now a total of 50 lines are used to define the initiation criterion as a function of β.

In ABAQUS the output stress of the cohesive element has two components: normal and shear stress. The effective maximum cohesive strength (t_u^{ABQ}) is determined analogous as in Equation 4.4.6. The separation at damage initiation and failure are determined with the normal and shear separation, which are in turn determined with the Load Proportionality Factor (LPF) and applied loading. The effective separation is determined similar to the effective maximum cohesive strength. From the effective separation at initiation and effective maximum cohesive strength the initial slope (K^{ABQ}) is determined using Equation 8.1.1.

have the corresponding material properties assigned. Using GETVRM the data from the previous increment can be obtained.

Table 8.19: Verification of the bilinear TSL parameters in Equation 8.4.1 to 8.4.3 and the response of a single cohesive element in ABAQUS. The parameters are determined using (x_i) corresponding to data point 1 in Table 8.1.

	K^{β} N/mm^3	K^{ABQ} N/mm^3	**error**	t_u^{β} N/mm^2	t_u^{ABQ} N/mm^2	**error**	G_f^{β} N/mm	G_f^{ABQ} N/mm	**error**
LC1	142313	135057	5.10%	47.21	48.22	2.13%	0.083	0.085	2.80%
LC3	101131	99639	1.48%	42.83	43.94	2.59%	0.132	0.108	18.36%
LC4	92810	89938	3.09%	43.75	45.03	2.92%	0.149	0.126	15.81%
LC5	121121	117669	2.85%	42.74	43.58	1.96%	0.099	0.094	4.93%
LC6	27884	27694	0.68%	56.12	56.27	0.26%	0.272	0.273	0.45%

The single cohesive element is subjected to the five load cases used earlier for the curve fitting and the results are given in Table 8.19. In general the maximum cohesive strength of the single cohesive element in ABAQUS is a little higher compared to the result of the failure criterion, which is due to a small tolerance in ABAQUS. The errors in damage initiation, i.e. the combination of K and t_u, are acceptable and thus it can be verified that the method proposed in this section is verified. However, there is a relative large error in the fracture energy of LC3 and LC4. For LC3 G_f^{β} and G_f^{ABQ} should align as this is the load case used for the mode mixity fitting. The issue might be in the relation between G_{shear}/G_{total} and β in Equation 8.3.20. In order to solve this an alternative relation to the BK law can be used for the curve fitting. In ABAQUS the damage evolution can then be given by means of a tabular input with a dependence on β, similar to the definition of the separation at damage initiation. Unfortunately there is not enough time to investigate and verify this method.

Chapter 9

Conclusions and Recommendations

9.1 Conclusions

Fracture models and criteria for composite materials have seen a significant development over the past decades. In addition, the increase in computational power supported the development of computational methods to solve fracture problems. One approach in predicting fracture is the multiscale approach, which uses microscopic details for the macroscopic fracture behaviour. Failure criteria in this area are often limited to simple load cases and are not able to distinguish different fracture mechanisms, i.e. matrix or interface cracking. In order to fill this gap in knowledge the thesis objective was formulated as follows:

The thesis objective is to develop a new macroscopic failure criterion for fiber-reinforced composites that incorporates distinct fracture mechanisms occurring at a microscopic level. The microscopic information will be integrated into the macroscopic failure criterion through multiscale finite element simulations on representative volume elements.

A single macroscopic failure criterion was developed that accounts for, in a unified format, the distinct microscopic failure mechanisms such as matrix cracking, fiber debonding, fiber cracking and combinations thereof. In a Two-Dimensional (2D) framework multiple fiber numerical experiments were performed on a microscopic scale. The general outline of these numerical experiments was discussed in Chapter 4 and showed a fully scripted procedure for efficient pre- and post-processing. Fracture was simulated using an intrinsic implementation of cohesive elements that follow a simple bilinear Traction-Separation Law (TSL). The resulting fracture mechanism was expressed in terms of an Effective Traction-Separation Law (ETSL).

The fundamentals for the numerical experiments were established during the single fiber simulations in Chapter 5. The effect of five variables x_i was studied: the interface cohesive strength, fiber cohesive strength, interface fracture energy, fiber fracture energy and fiber diameter (or fiber volume fraction). The four cohesive properties were studied relative to the matrix cohesive properties. Three load cases were investigated: uni-axial extension, pure shear and a mixed load case. Over the course of these numerical experiments the method and corresponding scripts were improved. A mesh convergence study was performed from which the mesh density for further simulations was established. In addition, the initial effects of the five variables were observed.

Before the multiple fiber numerical experiments could be performed the Representative Volume Element (RVE) dimensions had to be determined. After the convergence study in Chapter 6 it was concluded that the RVE can be considered representative for a dimension of 75×75 µm. However, it was taken into account that these dimensions might not be representative for all load cases, fiber volume fractions and for changes in material/cohesive properties. These RVE dimensions were considered suitable to demonstrate the method that was proposed in this thesis.

For the multiple fiber numerical experiments a total of six load cases were studied: uni-axial extension, pure shear, simple shear and three mixed load cases. The five variables studied were identical to the variables during the single fiber numerical experiments. During the numerical experiments it was concluded that the pure shear results were spurious and therefore not suitable for correlation, the simple shear load case was used instead. For both the single and multiple fiber numerical experiments the following was concluded. The interface cohesive strength has a strong influence on the maximum cohesive strength and fracture energy due to the change in fracture pattern. For factors 1.0 and 2.0 the crack initiates in the matrix and thus a higher maximum cohesive strength and fracture energy is observed. There is almost no difference between a factor 1.0 and 2.0. The fiber cohesive strength has an identical influence, for a factor 0.5 the crack initiates in the fiber resulting in a higher maximum cohesive strength and a small increase in fracture energy. There is almost no difference between a factor 1.0 and 2.0. A higher interface fracture energy only has an influence on the fracture energy as more energy is required for the crack to propagate. The fiber fracture energy has almost no influence on the ETSL due to the fact that the crack does not interact with the fiber, this effect should have been studied with a fiber cohesive strength factor of 0.5. The increase in fiber volume fraction (or fiber diameter) results in a higher initial slope of the ETSL and decreases the fracture energy.

The main objective of this thesis was to use the microscopic results for the development of a macroscopic failure criterion. Therefore, each ETSL as a result of the multiple fiber numerical experiments was approximated by a bilinear TSL that has three parameters: an initial slope K, cohesive strength t_u (peak) and fracture energy G_f (area). For each data point and load case these three parameters were determined. On the macroscopic scale the mode I and mode II properties were to be defined. The uni-axial extension (mode I) and simple shear (mode II) bilinear TSL parameters were correlated using a multiple variable least squares fit. Due

to this all the mode I and II parameters could be given as a function of the five variables x_i. Overall the error between the curve fit and the actual data points turned out to be acceptable.

In addition to the mode I and II properties the mode mixity was implemented in the failure criterion. A mode mixity parameter β was introduced. The initial slope was fitted using an elliptical relation between the mode I and II parameters, the cohesive strength was defined by a power relation between the separation at damage initiation and the fracture energy was approximated by a Benzeggagh-Kenane (BK) power relation. Only LC3 was used for the mode mixity fitting and LC4 and LC5 were used for verification. The resulting equations showed a good fit for the damage initiation, but there was a relatively large error in the fracture energy. In the end the three bilinear TSL parameters were described by the five variables x_i and the mode mixity β. The relatively simple equations for the three parameters of the bilinear TSL resemble the macroscopic failure criterion. Returning to the thesis objective, it can be seen that the resulting macroscopic failure criterion indeed incorporates the distinct fracture mechanisms at the microscopic scale. For this proof of concept study the level of detail and applicability of this failure criterion is considered sufficient. However, in order for this failure criterion to be used as a functional tool in the design process some issues encountered during this thesis have to be solved and the method should be extended.

To complete the procedure proposed in this thesis the implementation of the macroscopic failure criterion was discussed. The proposed implementation in ABAQUS was verified with a single macroscopic cohesive element model. The resulting response of this cohesive element showed a perfect alignment of the damage initiation with the macroscopic failure criterion. However, the fracture energy was underestimated, which lead to one of the recommendations in the next section.

Overall the proposed method for the development of the macroscopic failure criterion is innovative and efficient. Additional data points can easily be added to the curve fitting, by running additional simulations, to increase the accuracy. The main advantage is that these simulations only have to be performed once. Moreover, the effect of other variables can be added in order to generalise the failure criterion.

9.2 Recommendations

In the previous section it was concluded that the thesis objective has been achieved. However, during the research some issues were encountered that could not be solved within the time available.

- The fiber fracture energy had no effect on the fracture mechanisms, i.e. there was no dependence on variable x_4. This was due to the fact that the crack does not interact with the fiber. In order to capture the effect of fiber fracture energy additional simulations with a fiber cohesive strength factor (x_2) of 0.5 should be performed and added to the curve fitting.

- During the implementation of the macroscopic failure criterion it was discovered that the fracture energy of a cohesive element subjected to a mixed loading is underestimated. This problem should be investigated and resolved before the method is implemented on a full macroscopic model.
- Some simulations were aborted before the traction dropped to zero, in which case an extrapolation of the ETSL was performed. In order to increase the accuracy the maximum number of steps should be increased and convergence problems should be mitigated. This will increase the computational time.

Next to the above issues there is always room for improvement. The ultimate goal is to generalise the proposed method to a fully functional tool that can be applied for fracture control in composite materials. For the recommendations proposed below the increase in complexity should not be underestimated.

- For this thesis a 2D framework was assumed. To generalise the proposed method the extension to Three-Dimensional (3D) should be made, which is considered relatively easy. Howerver, this will increase the number of load cases, variables and will result in an additional fracture mode (III).
- The extension to 3D will implicate a significant increase in the number of cohesive elements. To reduce, or completely remove, the effect of artificial compliance an extrinsic implementation of cohesive elements is preferred. This will result in a more complex data structure and post-processing procedure.
- For the implementation of cohesive elements in the RVE mode-independent properties were assumed. It would be interesting to see the effect of the mode I and mode II (and mode III for 3D) cohesive properties. This will increase the number of variables, and thus number of simulations, significantly.
- A better evaluation of the RVE dimensions should be performed. A similar procedure as proposed in this thesis can be used but it should be extended to multiple load cases. This procedure can only be successful when utilising an extrinsic implementation of cohesive elements to remove the effects of artificial compliance.
- For this thesis a simple bilinear TSL was assumed as input and as output. According to each resulting ETSL of the multiple fiber models a more sophisticated TSL might give better results. However, this will probably increase the number of parameters to define this TSL.
- A generalised failure criterion will require the effect of more variables, i.e. all cohesive properties separately instead of relative to the matrix properties. In addition, the effect of material properties of the fiber and matrix should be taken into account. For this thesis only three data points per variable were used, i.e. smaller, equal and greater. This should be increased to increase the accuracy of the curve fitting.
- At last, for the multiple fiber simulations only the average of four realisations was considered. To increase the accuracy this number should be increased at least above five.

Appendix A

Single Fibre Effective Traction-Separation Laws

In this appendix the detailed Effective Traction-Separation Law (ETSL) of all the single fiber simulations, discussed in Chapter 5, are presented. Each simulation is performed for three mesh densities; coarse, medium and fine as indicated in Table 5.1. In total three load cases are considered; uni-axial extension (LC1), pure shear (LC2) and a mixed load case (LC0) as listed in Table 4.2.

For each load case the effect of five variables is studied with respect to the reference case in Figure A.1 to A.3.

- Figure A.4 to A.9: interface cohesive strength
- Figure A.10 to A.15: fiber cohesive strength
- Figure A.16 to A.21: interface fracture energy
- Figure A.22 to A.27: fiber fracture energy
- Figure A.28 to A.30: fiber diameter

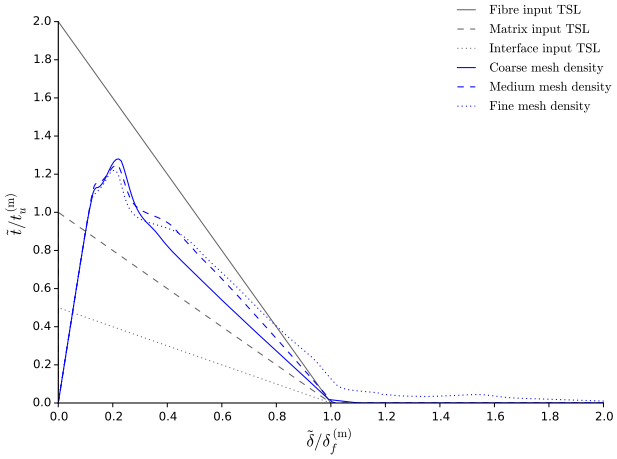

Figure A.1: Reference, LC1: ETSLs of the coarse, medium and fine mesh models combined.

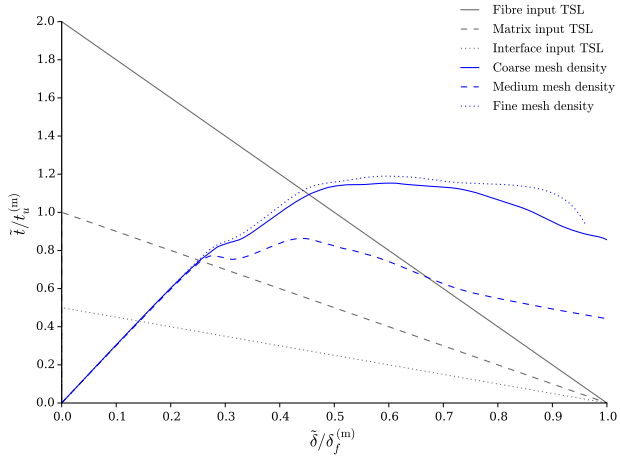

Figure A.2: Reference, LC2: ETSLs of the coarse, medium and fine mesh models combined.

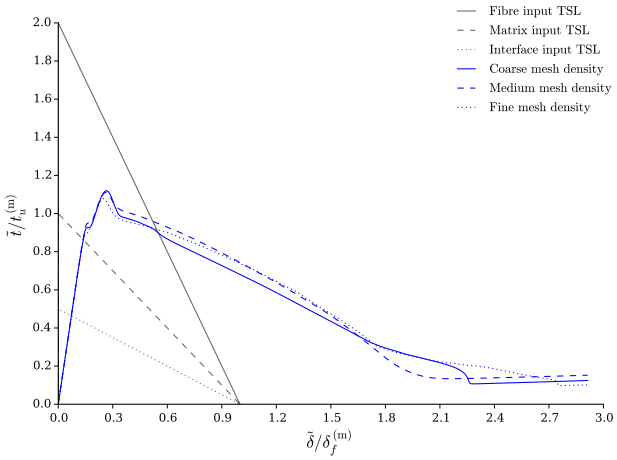

Figure A.3: Reference, LC0: ETSLs of the coarse, medium and fine mesh models combined.

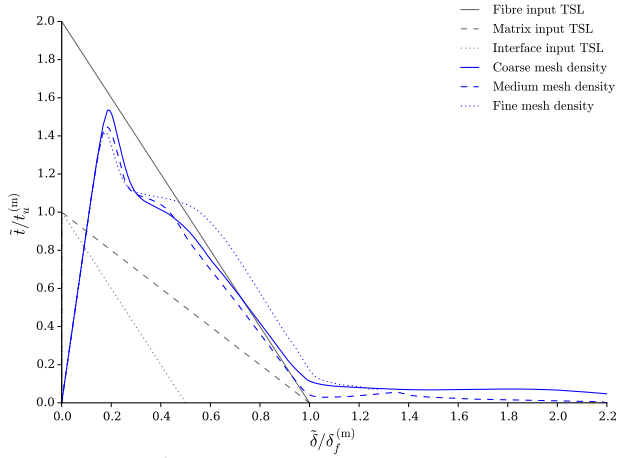

Figure A.4: $t_u^{(i)}$ × 2, LC1: ETSLs of the coarse, medium and fine mesh models combined.

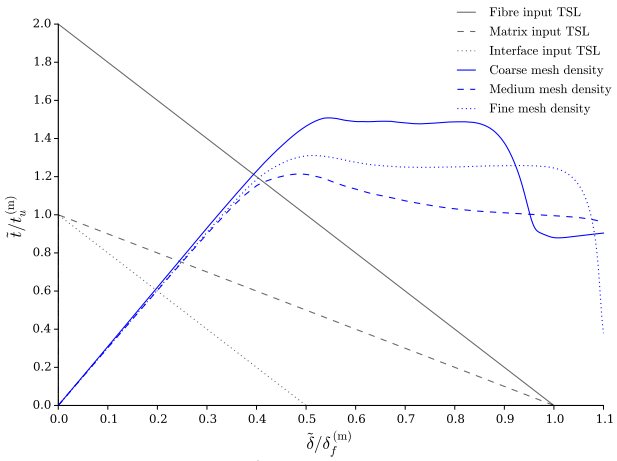

Figure A.5: $t_u^{(i)}$ × 2, LC2: ETSLs of the coarse, medium and fine mesh models combined.

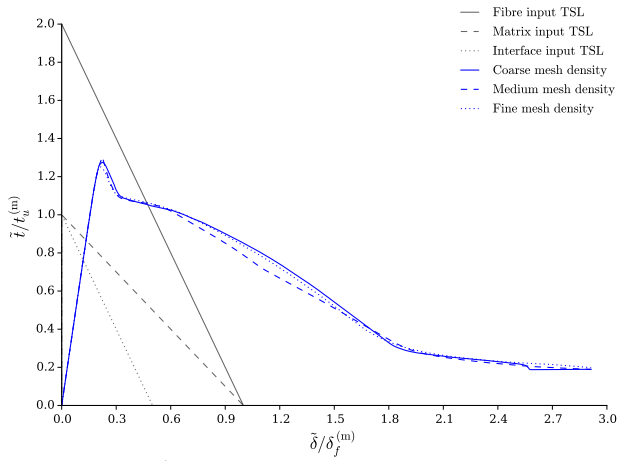

Figure A.6: $t_u^{(i)}$ × 2, LC0: ETSLs of the coarse, medium and fine mesh models combined.

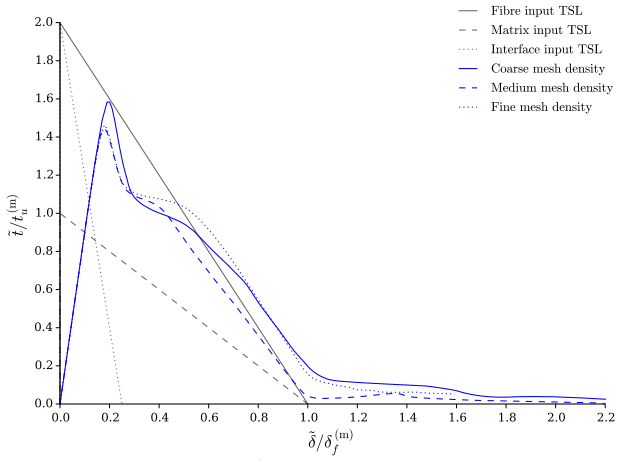

Figure A.7: $t_u^{(i)}$ × 4, LC1: ETSLs of the coarse, medium and fine mesh models combined.

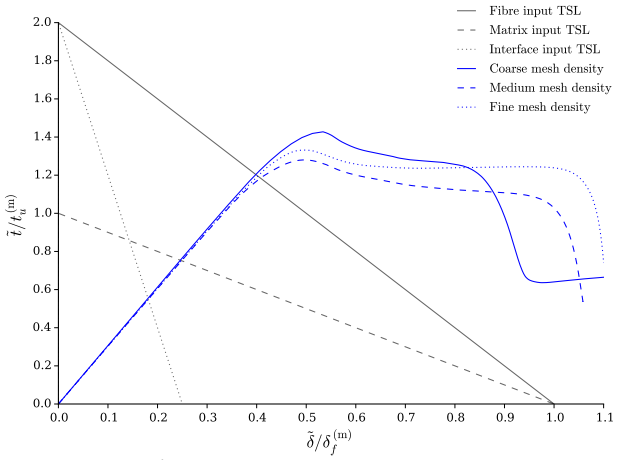

Figure A.8: $t_u^{(i)}$ × 4, LC2: ETSLs of the coarse, medium and fine mesh models combined.

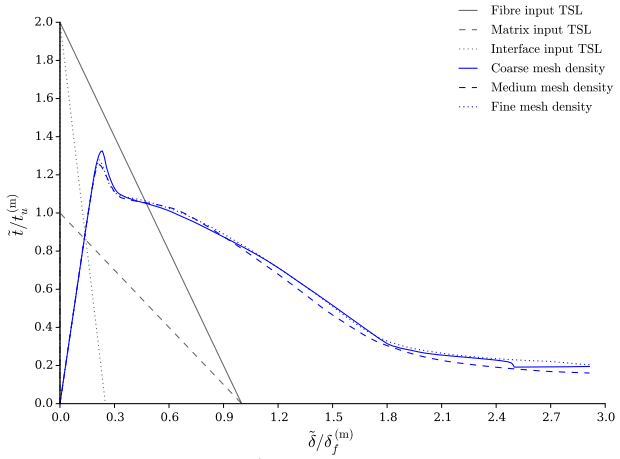

Figure A.9: $t_u^{(i)}$ × 4, LC0: ETSLs of the coarse, medium and fine mesh models combined.

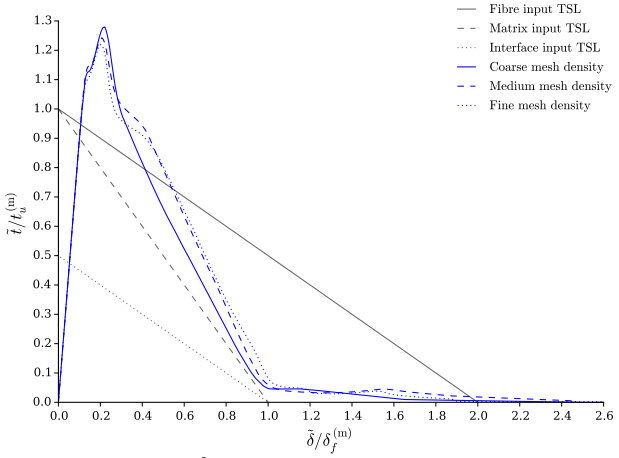

Figure A.10: $t_u^{(f)}$ × 0.5, LC1: ETSLs of the coarse, medium and fine mesh models combined.

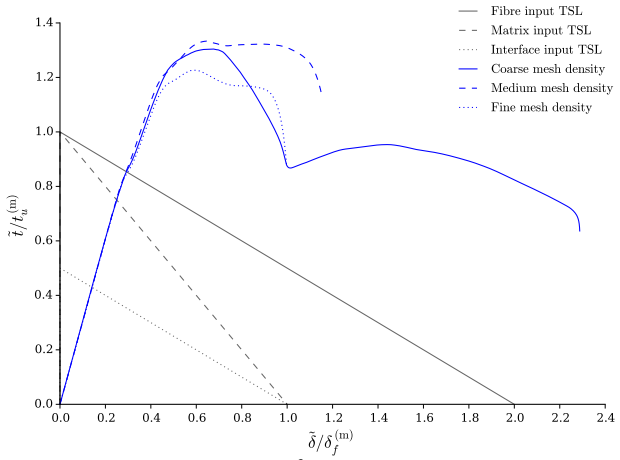

Figure A.11: $t_u^{(f)}$ × 0.5, LC2: ETSLs of the coarse, medium and fine mesh models combined.

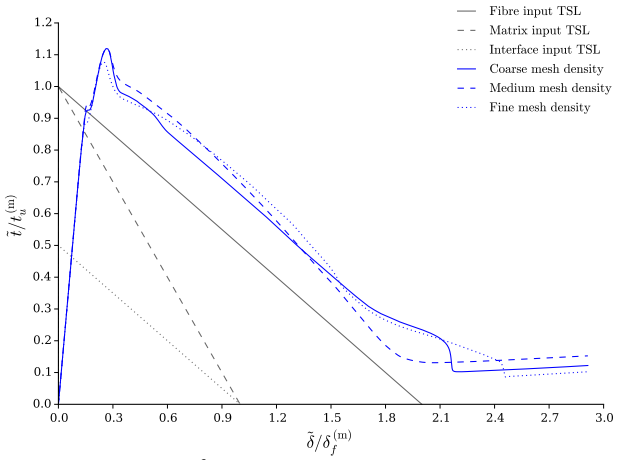

Figure A.12: $t_u^{(f)}$ × 0.5, LC0: ETSLs of the coarse, medium and fine mesh models combined.

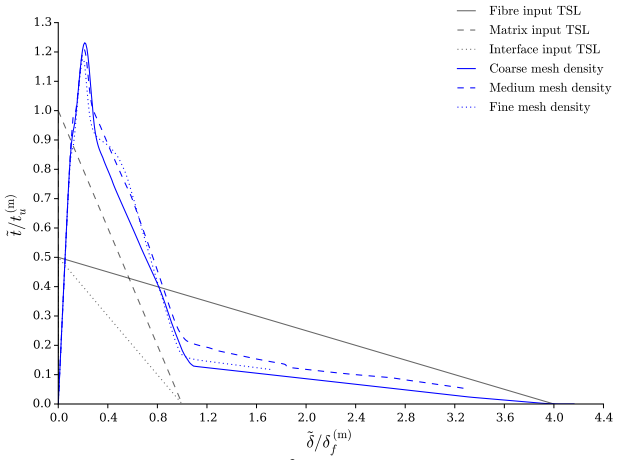

Figure A.13: $t_u^{(f)}$ × 0.25, LC1: ETSLs of the coarse, medium and fine mesh models combined.

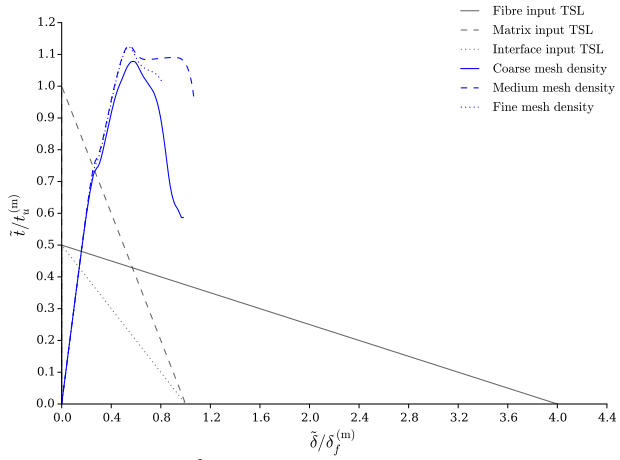

Figure A.14: $t_u^{(f)}$ × 0.25, LC2: ETSLs of the coarse, medium and fine mesh models combined.

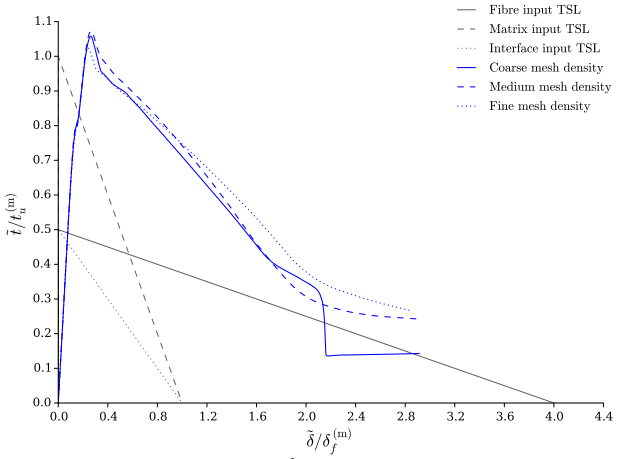

Figure A.15: $t_u^{(f)}$ × 0.25, LC0: ETSLs of the coarse, medium and fine mesh models combined.

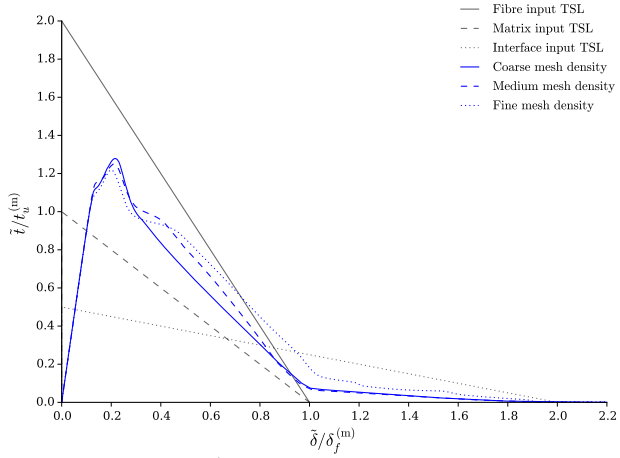

Figure A.16: $G_f^{(i)}$ × 2, LC1: ETSLs of the coarse, medium and fine mesh models combined.

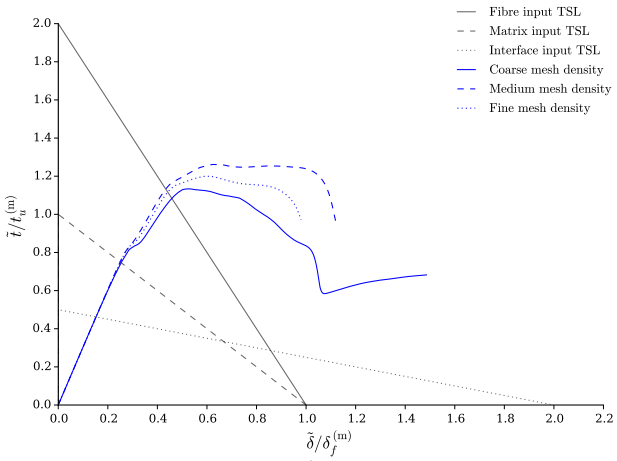

Figure A.17: $G_f^{(i)}$ × 2, LC2: ETSLs of the coarse, medium and fine mesh models combined.

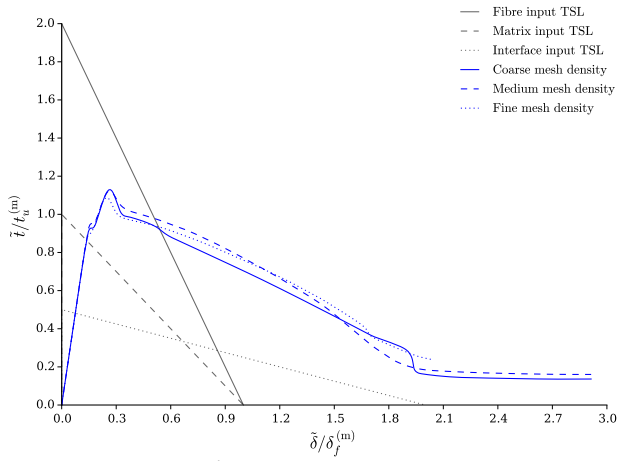

Figure A.18: $G_f^{(i)}$ × 2, LC0: ETSLs of the coarse, medium and fine mesh models combined.

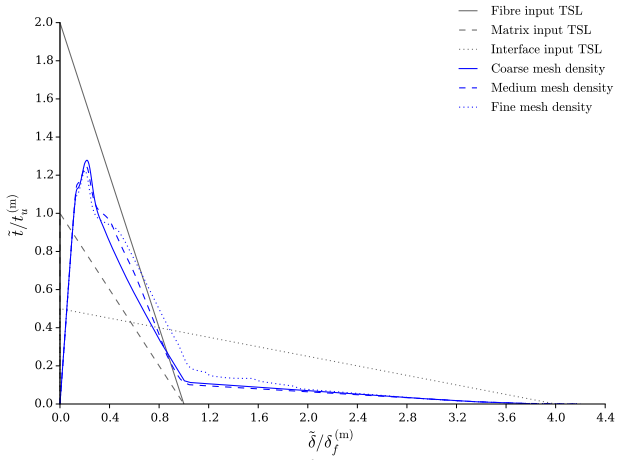

Figure A.19: $G_f^{(i)}$ × 4, LC1: ETSLs of the coarse, medium and fine mesh models combined.

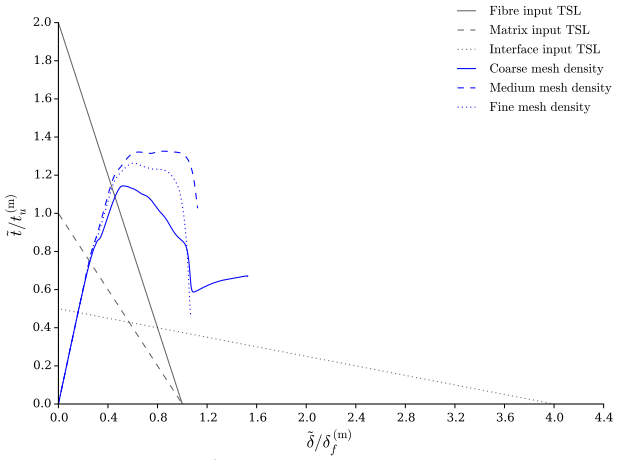

Figure A.20: $G_f^{(i)}$ × 4, LC2: ETSLs of the coarse, medium and fine mesh models combined.

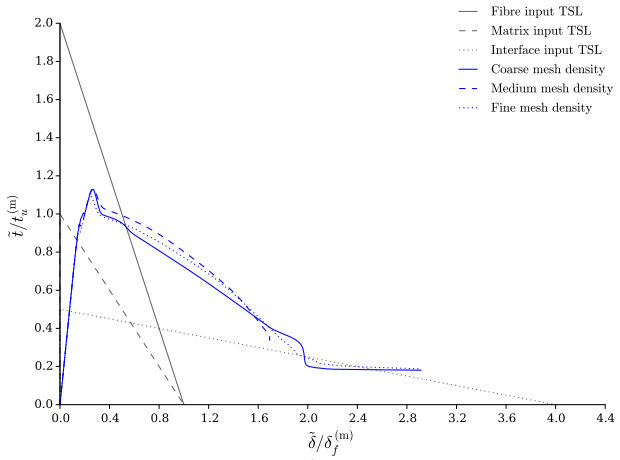

Figure A.21: $G_f^{(i)}$ × 4, LC0: ETSLs of the coarse, medium and fine mesh models combined.

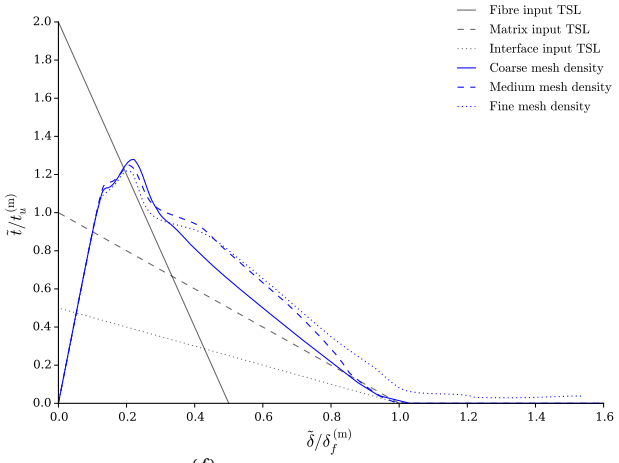

Figure A.22: $G_f^{(f)}$ × 0.5, LC1: ETSLs of the coarse, medium and fine mesh models combined.

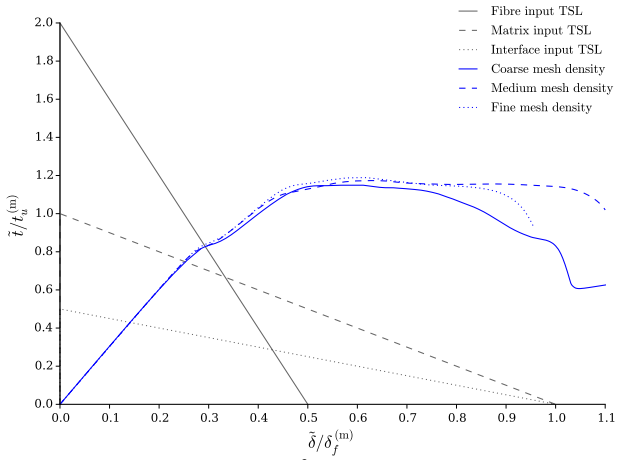

Figure A.23: $G_f^{(f)}$ × 0.5, LC2: ETSLs of the coarse, medium and fine mesh models combined.

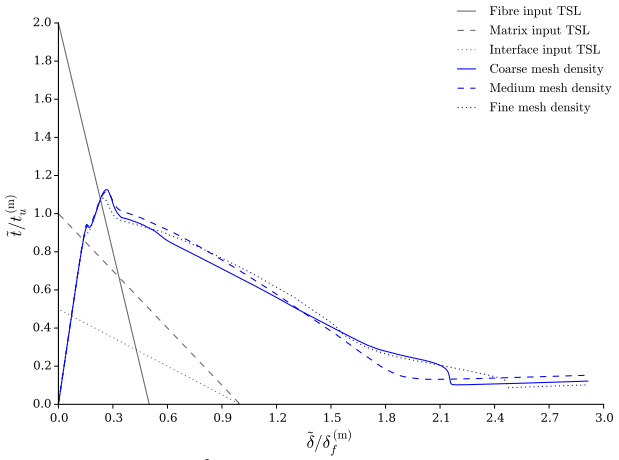

Figure A.24: $G_f^{(f)}$ × 0.5, LC0: ETSLs of the coarse, medium and fine mesh models combined.

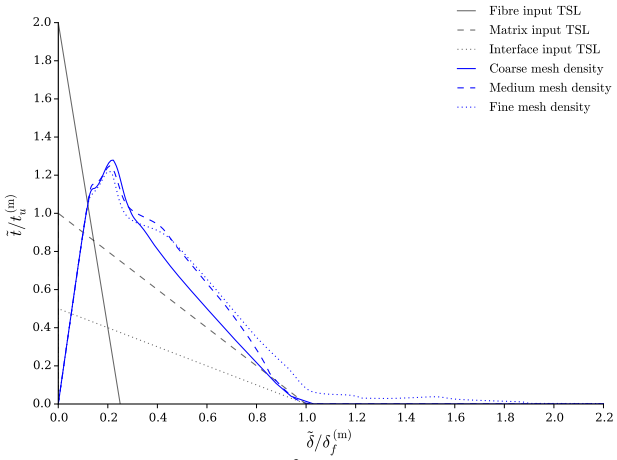

Figure A.25: $G_f^{(f)}$ × 0.25, LC1: ETSLs of the coarse, medium and fine mesh models combined.

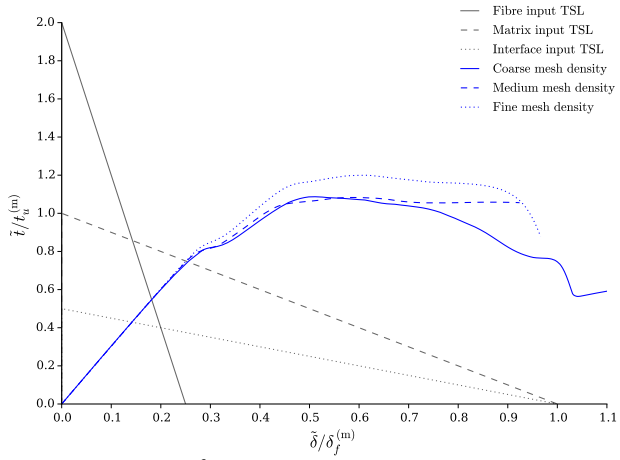

Figure A.26: $G_f^{(f)}$ × 0.25, LC2: ETSLs of the coarse, medium and fine mesh models combined.

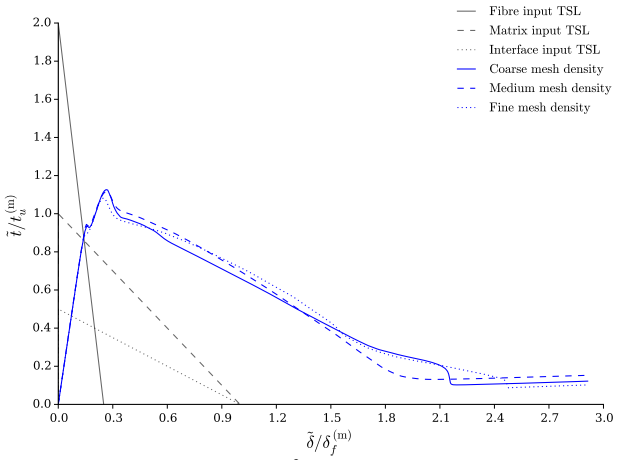

Figure A.27: $G_f^{(f)}$ × 0.25, LC0: ETSLs of the coarse, medium and fine mesh models combined.

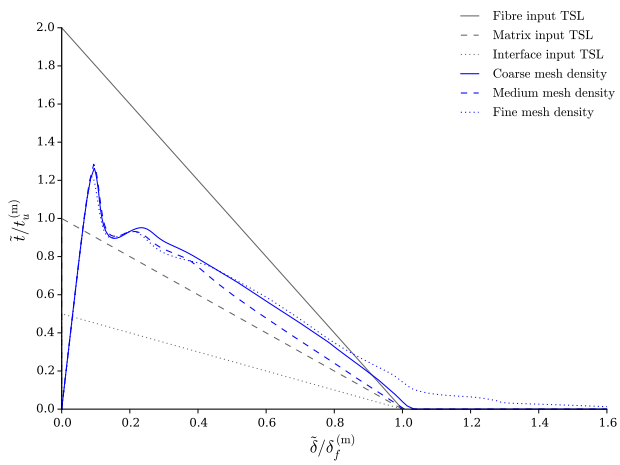

Figure A.28: d_F × 2, LC1: ETSLs of the coarse, medium and fine mesh models combined.

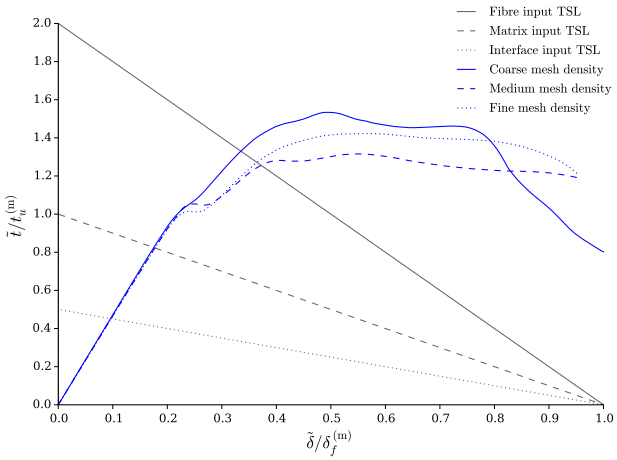

Figure A.29: d_F × 2, LC2: ETSLs of the coarse, medium and fine mesh models combined.

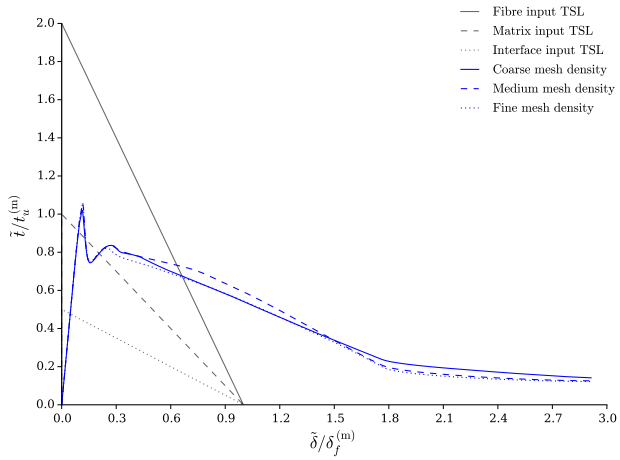

Figure A.30: d_F × 2, LC0: ETSLs of the coarse, medium and fine mesh models combined.

Appendix B

Multiple Fibre Effective Traction-Separation Laws

In this appendix the detailed Effective Traction-Separation Law (ETSL) of all the multiple fiber simulations are presented. First the detailed ETSL of the Representative Volume Element (RVE) size determination is presented in Section B.1, B.2 and B.3 for the three approaches as in Chapter 6.

Subsequently the detailed ETSL of the results presented in Chapter 7 are presented for a total of six load cases, i.e. LC1 to LC6 as in Table 4.2. For each load case the effect of five variables is studied with respect to the reference case, i.e. the models with a fiber volume fraction of 40% in Section B.8.

- Section B.4: interface cohesive strength
- Section B.5: fiber cohesive strength
- Section B.6: interface fracture energy
- Section B.7: fiber fracture energy
- Section B.8: fiber volume fraction

B.1 Size Determination of Microstructural Volume Elements: Original Approach

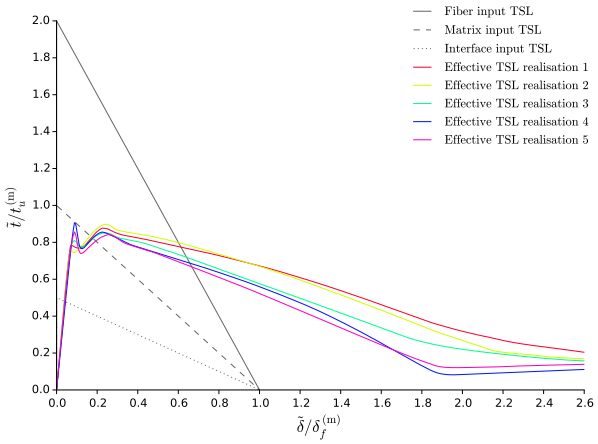

Figure B.1.1: 25×25 μm: ETSLs.

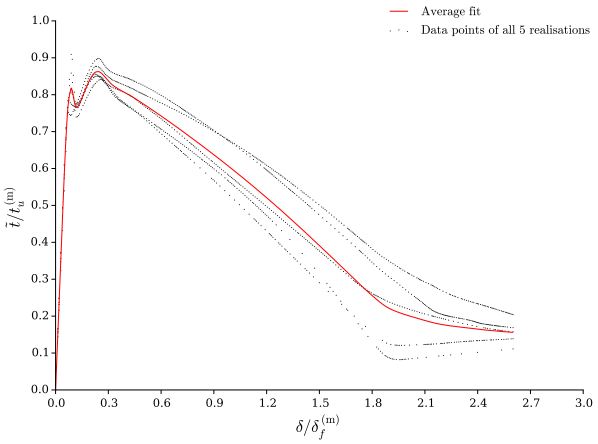

Figure B.1.2: 25×25 μm: average fit.

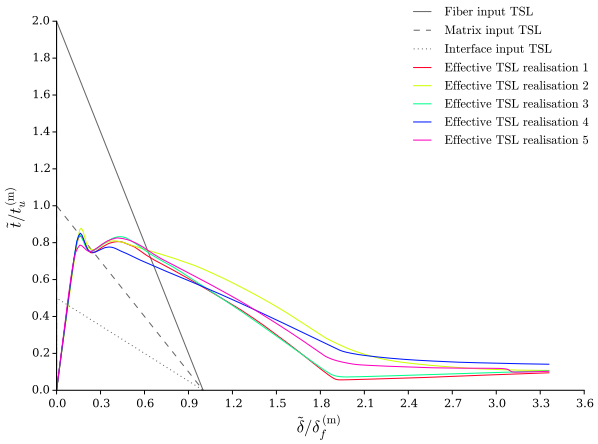

Figure B.1.3: 50×50 μm: ETSLs.

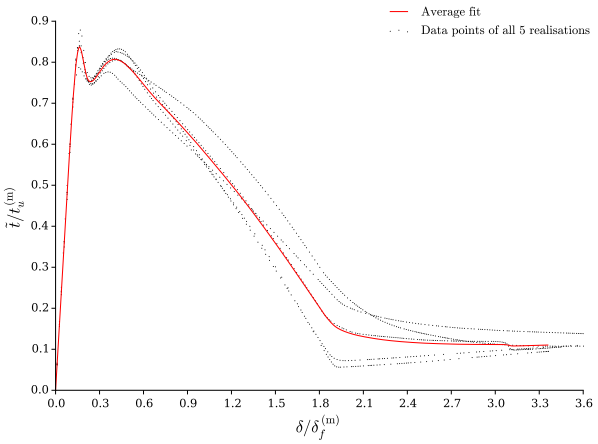

Figure B.1.4: 50×50 μm: average fit.

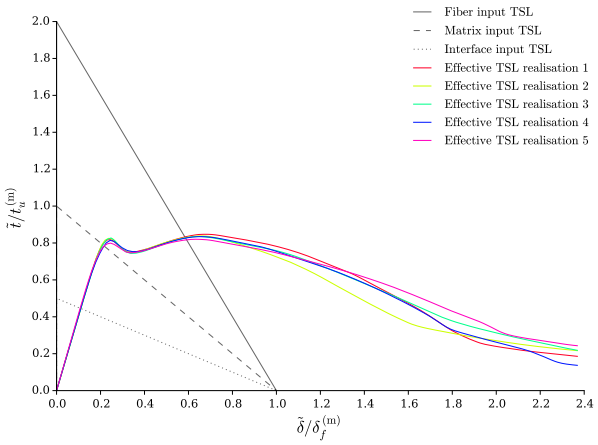

Figure B.1.5: 75×75 μm: ETSLs.

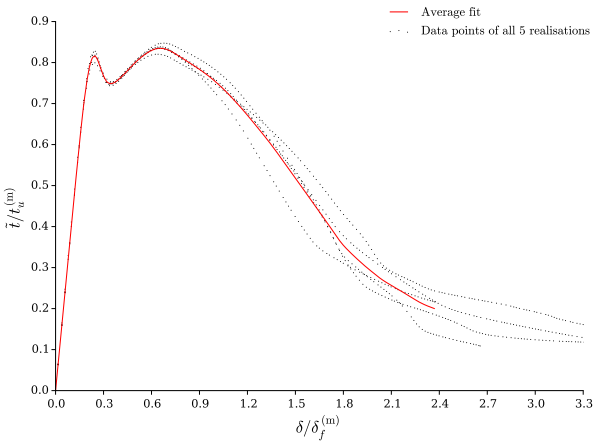

Figure B.1.6: 75×75 μm: average fit.

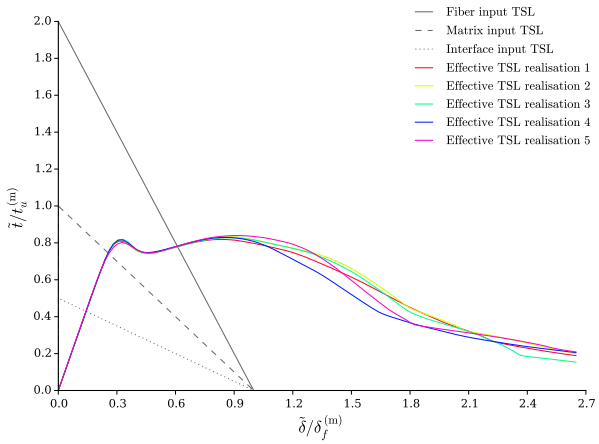

Figure B.1.7: 100×100 μm: ETSLs.

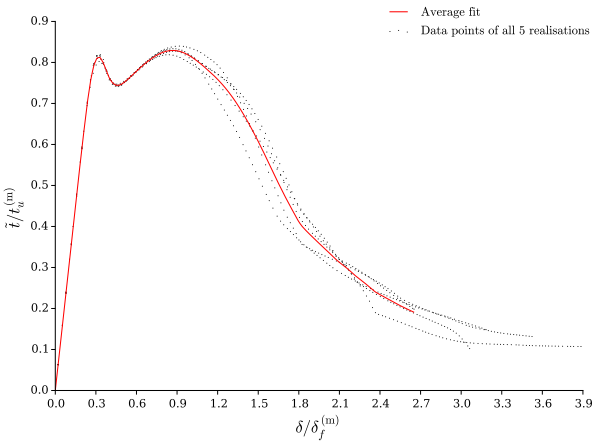

Figure B.1.8: 100×100 μm: average fit.

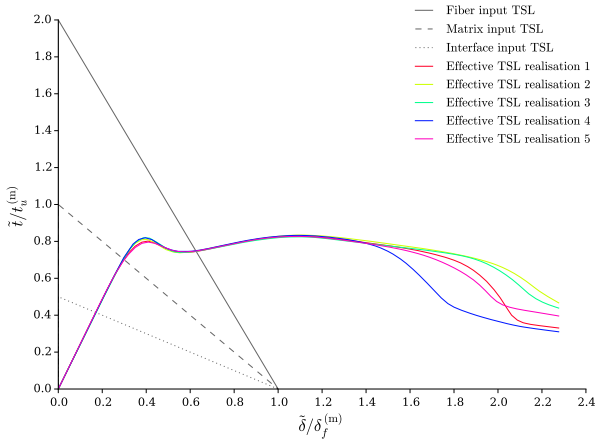

Figure B.1.9: 125×125 μm: ETSLs.

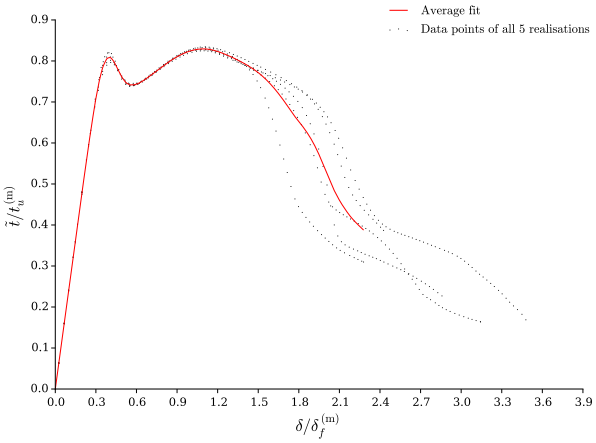

Figure B.1.10: 125×125 μm: average fit.

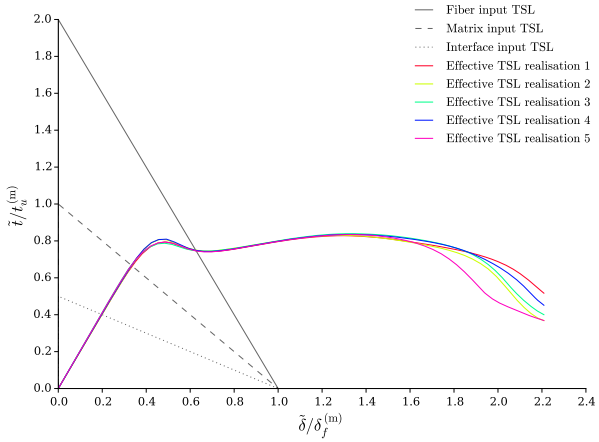

Figure B.1.11: 150×150 μm: ETSLs.

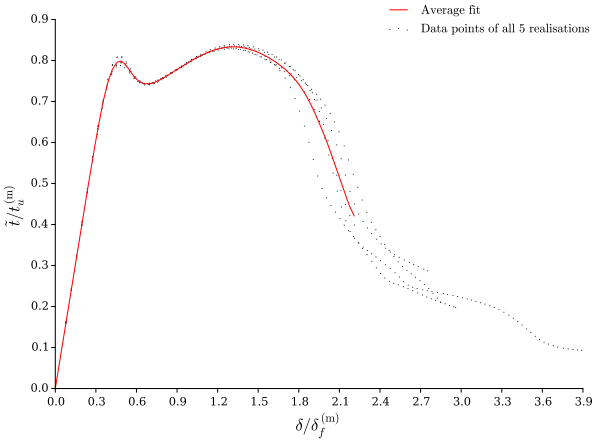

Figure B.1.12: 150×150 μm: average fit.

B.2 Size Determination of Microstructural Volume Elements: Case I

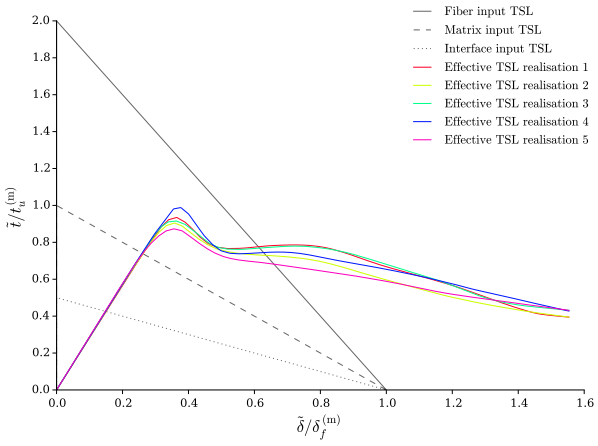

Figure B.2.1: 25×25 μm: ETSLs.

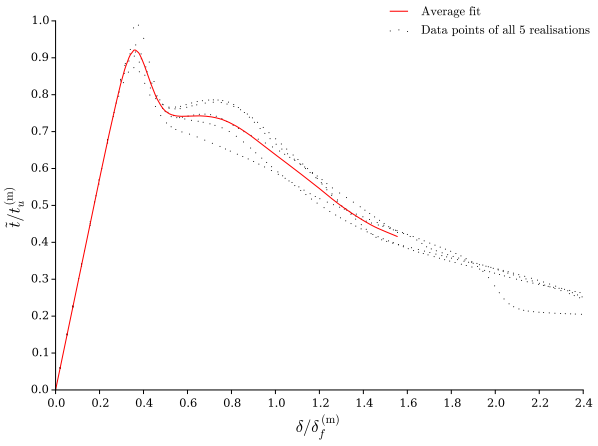

Figure B.2.2: 25×25 μm: average fit.

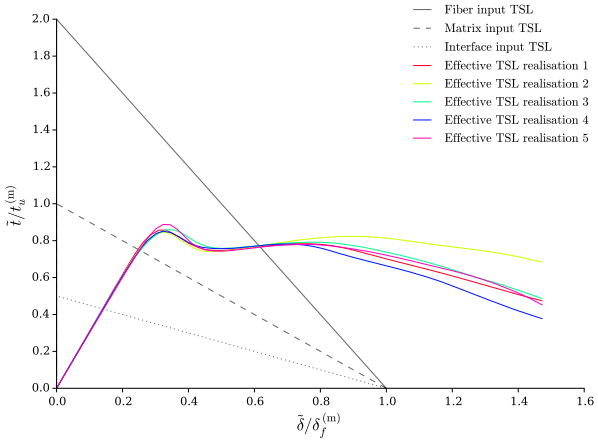

Figure B.2.3: 50×50 μm: ETSLs.

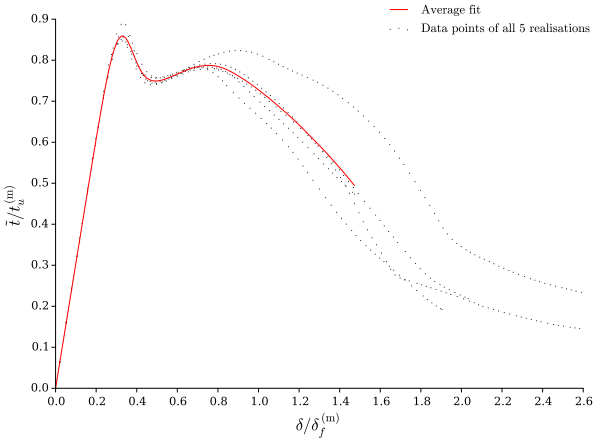

Figure B.2.4: 50×50 μm: average fit.

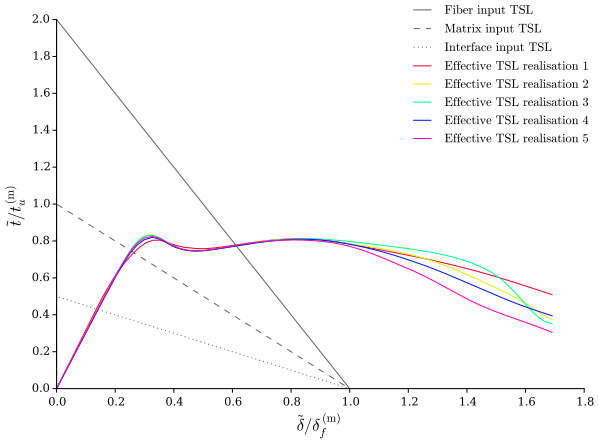

Figure B.2.5: 75×75 μm: ETSLs.

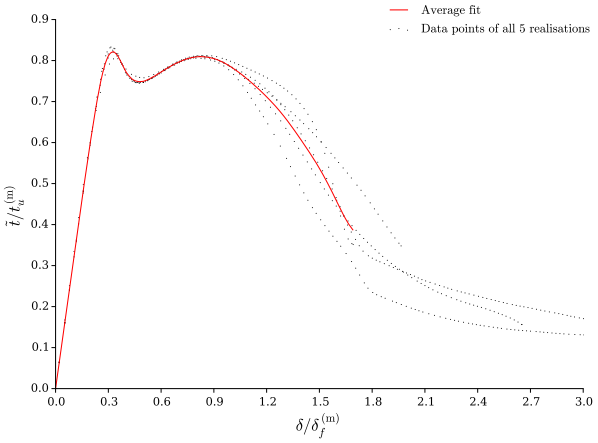

Figure B.2.6: 75×75 μm: average fit.

B.3 Size Determination of Microstructural Volume Elements: Case II

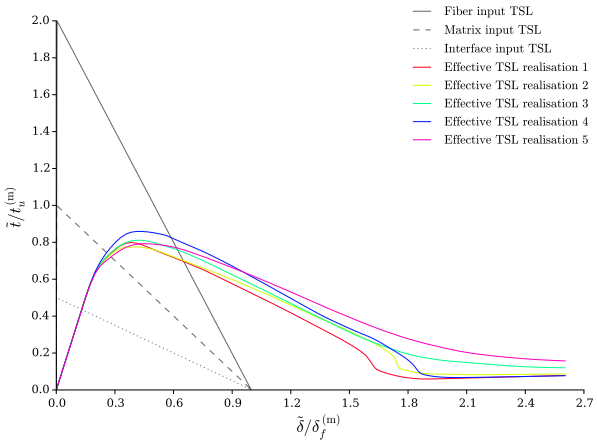

Figure B.3.1: 25×25 μm: ETSLs.

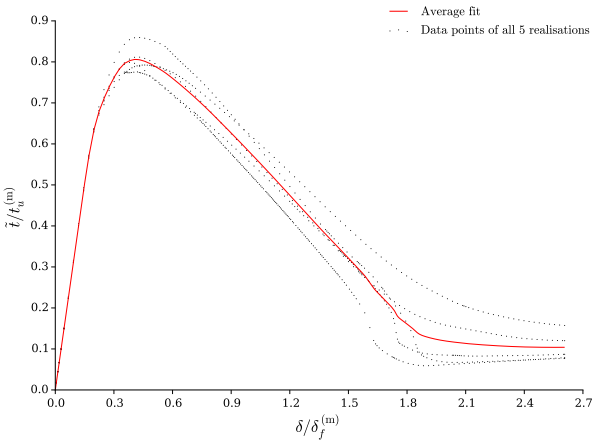

Figure B.3.2: 25×25 μm: average fit.

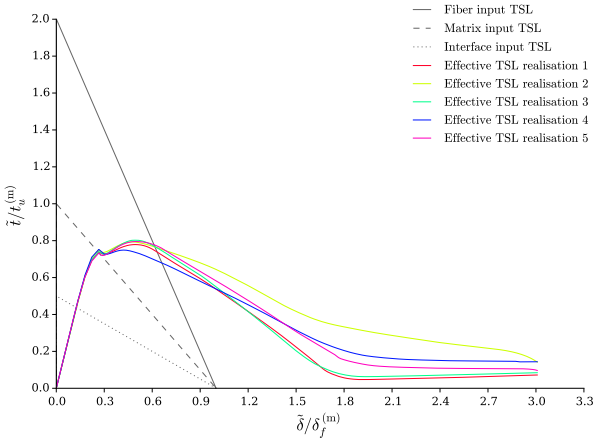

Figure B.3.3: 50×50 μm: ETSLs.

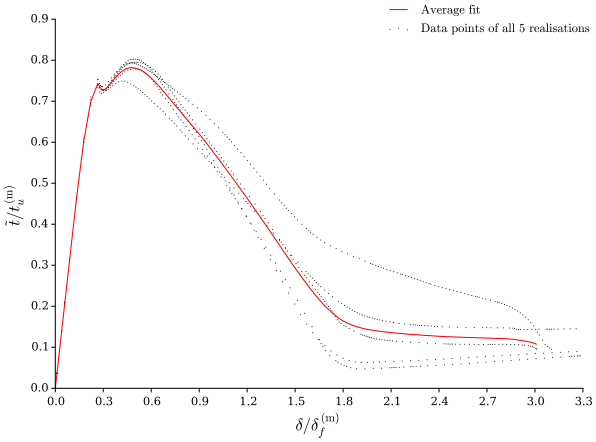

Figure B.3.4: 50×50 μm: average fit.

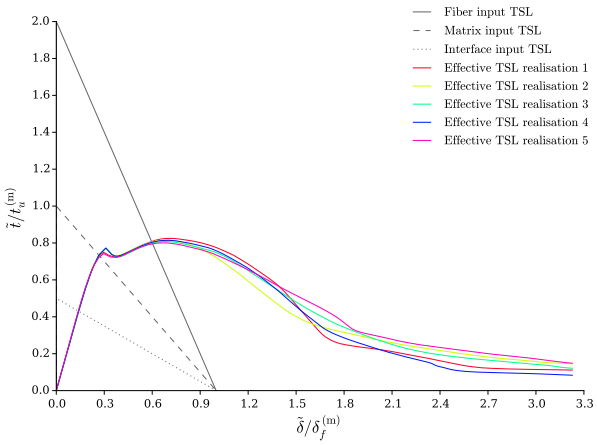

Figure B.3.5: 75×75 μm: ETSLs.

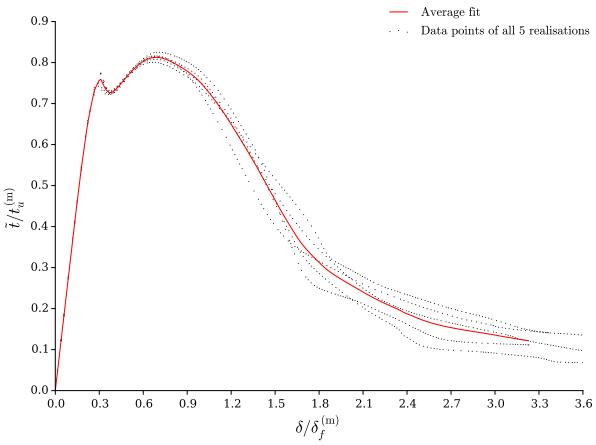

Figure B.3.6: 75×75 μm: average fit.

B.4 Effect of Interface Cohesive Strength

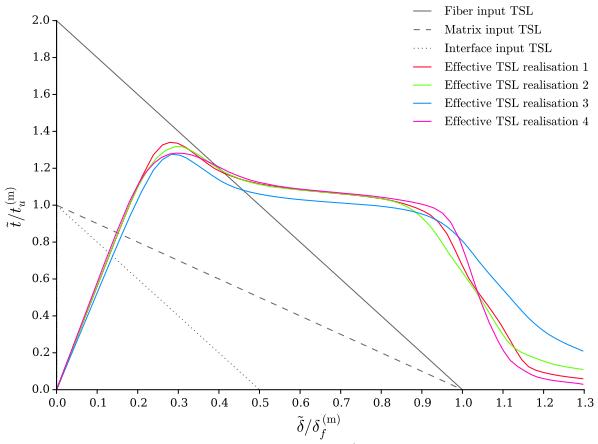

Figure B.4.1: LC1, $t_u^{(i)}/t_u^{(m)} = 1.0$: ETSLs.

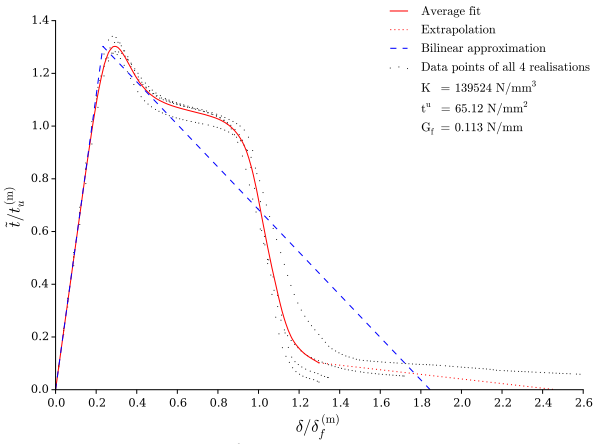

Figure B.4.2: LC1, $t_u^{(i)}/t_u^{(m)} = 1.0$: average fit.

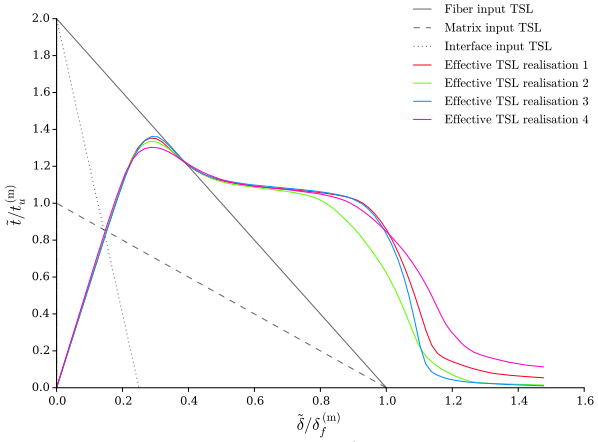

Figure B.4.3: LC1, $t_u^{(i)}/t_u^{(m)} = 2.0$: ETSLs.

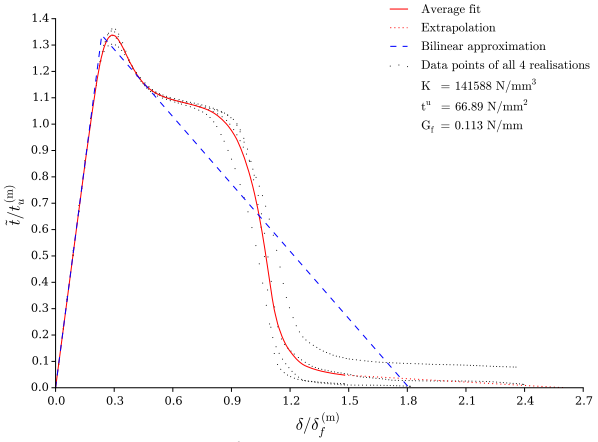

Figure B.4.4: LC1, $t_u^{(i)}/t_u^{(m)} = 2.0$: average fit.

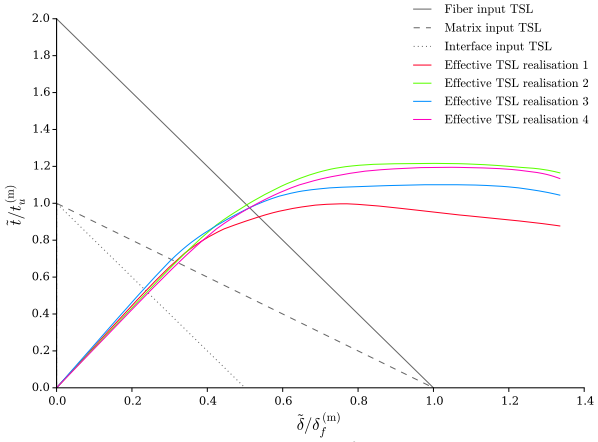

Figure B.4.5: LC2, $t_u^{(i)}/t_u^{(m)} = 1.0$: ETSLs.

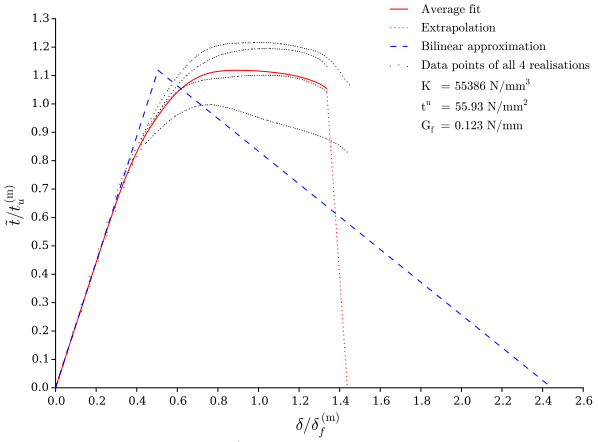

Figure B.4.6: LC2, $t_u^{(i)}/t_u^{(m)} = 1.0$: average fit.

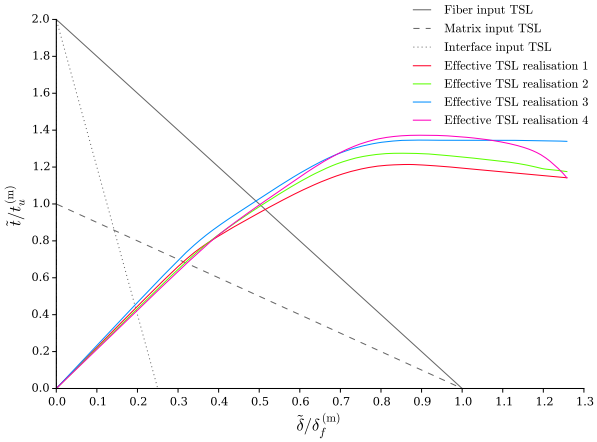

Figure B.4.7: LC2, $t_u^{(i)}/t_u^{(m)} = 2.0$: ETSLs.

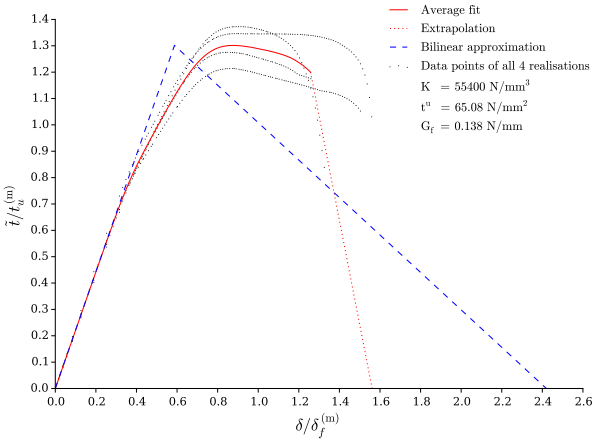

Figure B.4.8: LC2, $t_u^{(i)}/t_u^{(m)} = 2.0$: average fit.

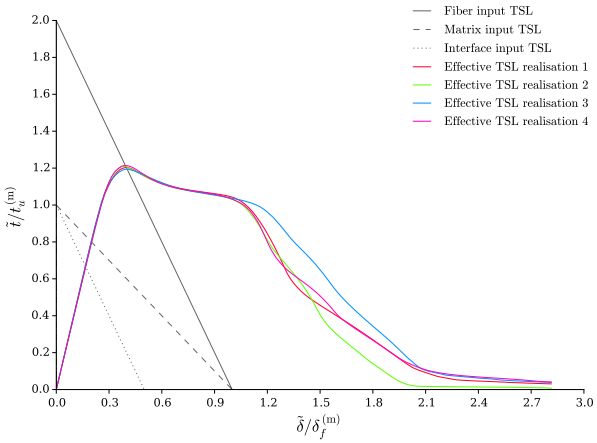

Figure B.4.9: LC3, $t_u^{(i)}/t_u^{(m)} = 1.0$: ETSLs.

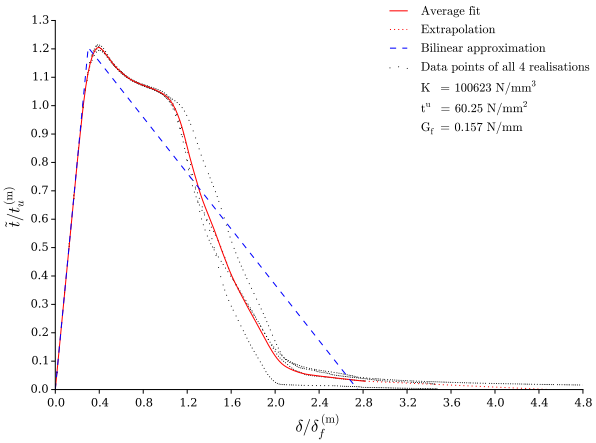

Figure B.4.10: LC3, $t_u^{(i)}/t_u^{(m)} = 1.0$: average fit.

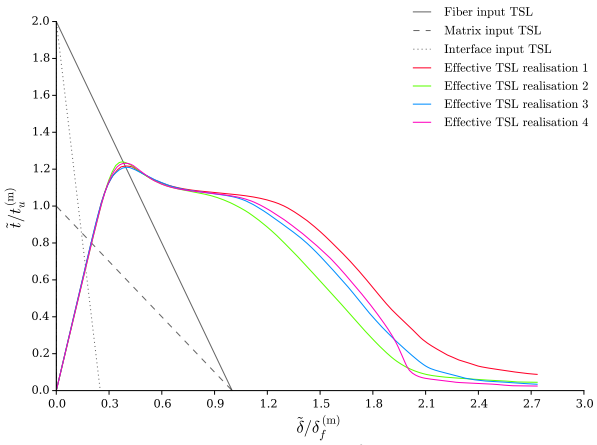

Figure B.4.11: LC3, $t_u^{(i)}/t_u^{(m)} = 2.0$: ETSLs.

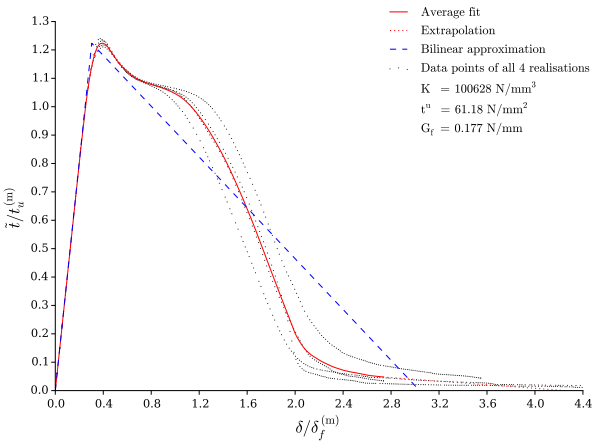

Figure B.4.12: LC3, $t_u^{(i)}/t_u^{(m)} = 2.0$: average fit.

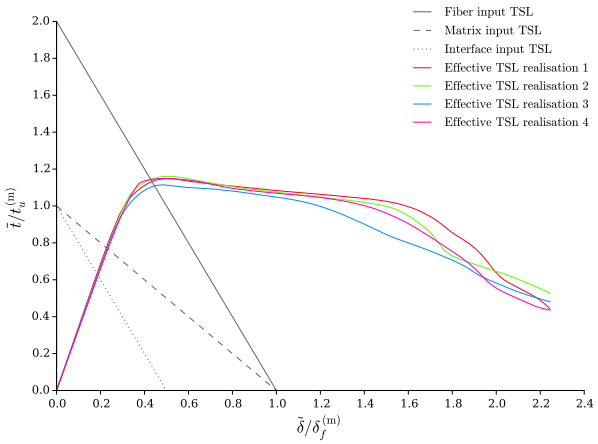

Figure B.4.13: LC4, $t_u^{(i)}/t_u^{(m)} = 1.0$: ETSLs.

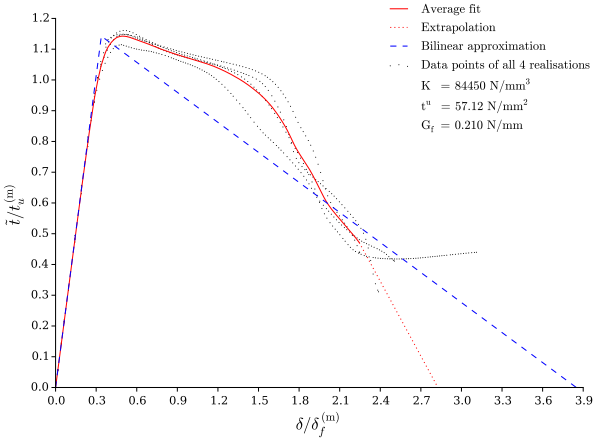

Figure B.4.14: LC4, $t_u^{(i)}/t_u^{(m)} = 1.0$: average fit.

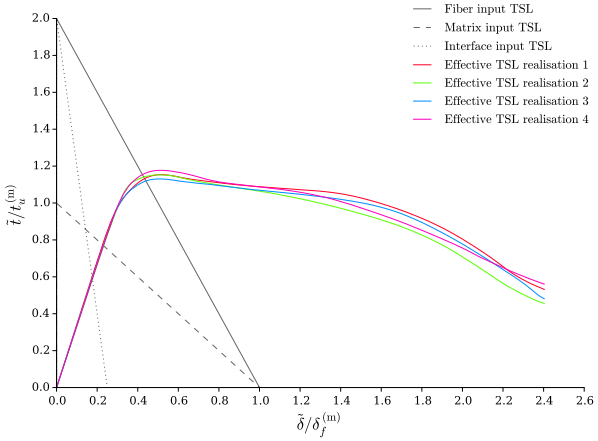

Figure B.4.15: LC4, $t_u^{(i)}/t_u^{(m)} = 2.0$: ETSLs.

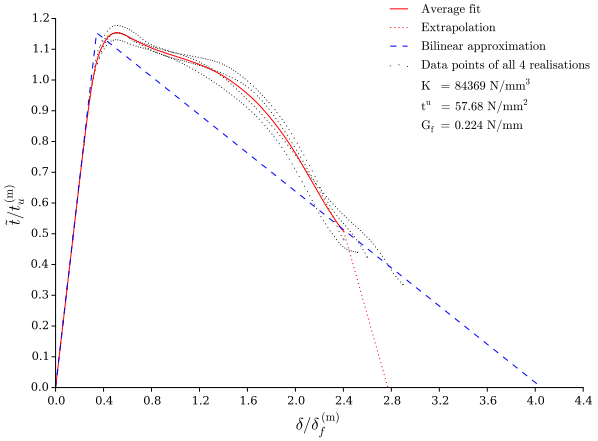

Figure B.4.16: LC4, $t_u^{(i)}/t_u^{(m)} = 2.0$: average fit.

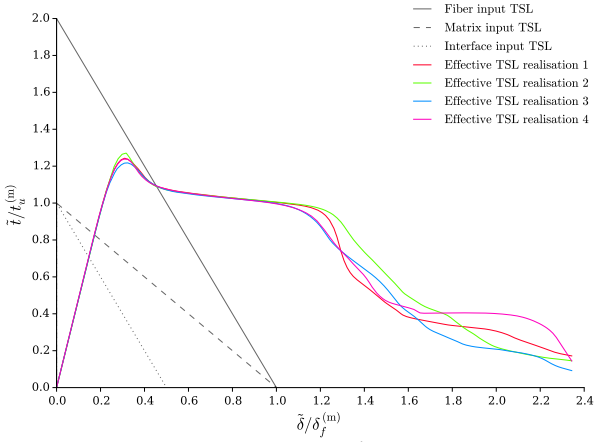

Figure B.4.17: LC5, $t_u^{(i)}/t_u^{(m)} = 1.0$: ETSLs.

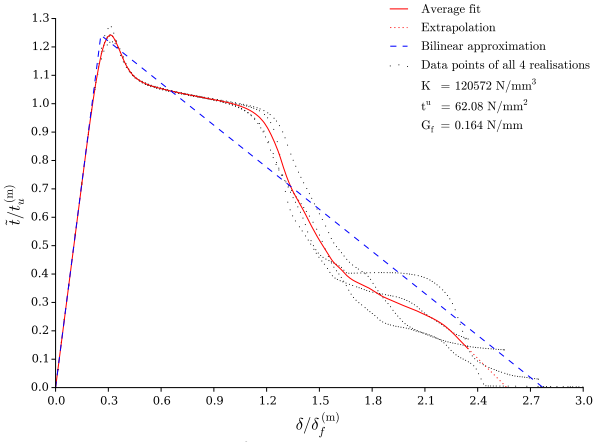

Figure B.4.18: LC5, $t_u^{(i)}/t_u^{(m)} = 1.0$: average fit.

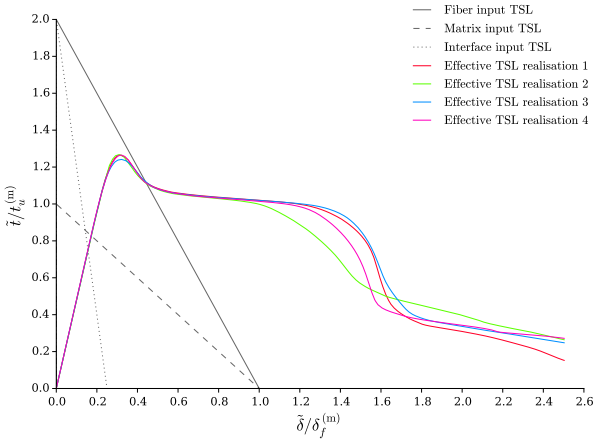

Figure B.4.19: LC5, $t_u^{(i)}/t_u^{(m)} = 2.0$: ETSLs.

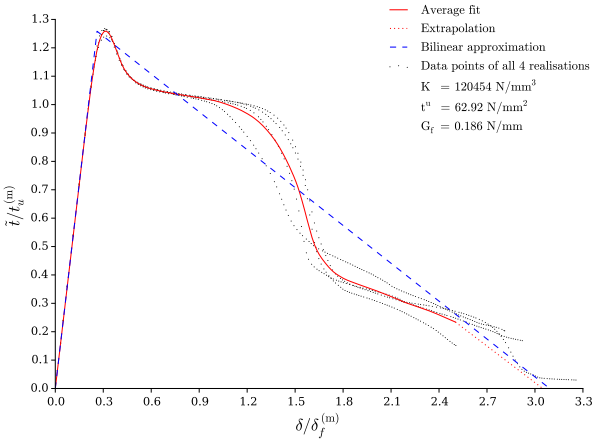

Figure B.4.20: LC5, $t_u^{(i)}/t_u^{(m)} = 2.0$: average fit.

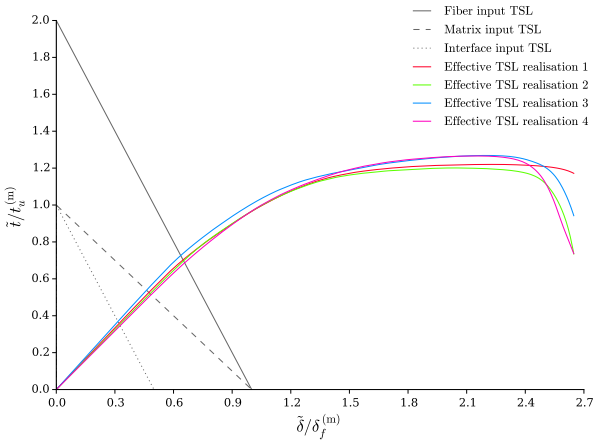

Figure B.4.21: LC6, $t_u^{(i)}/t_u^{(m)} = 1.0$: ETSLs.

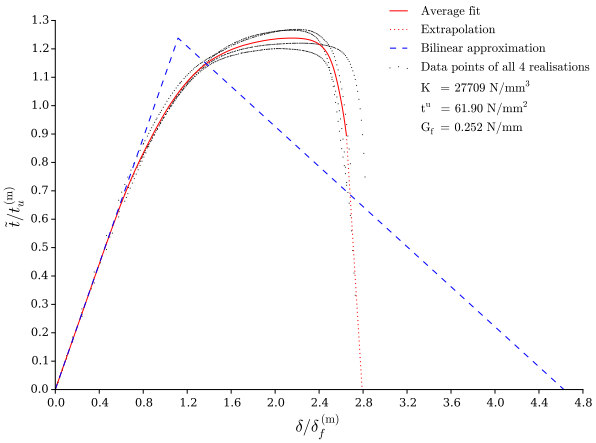

Figure B.4.22: LC6, $t_u^{(i)}/t_u^{(m)} = 1.0$: average fit.

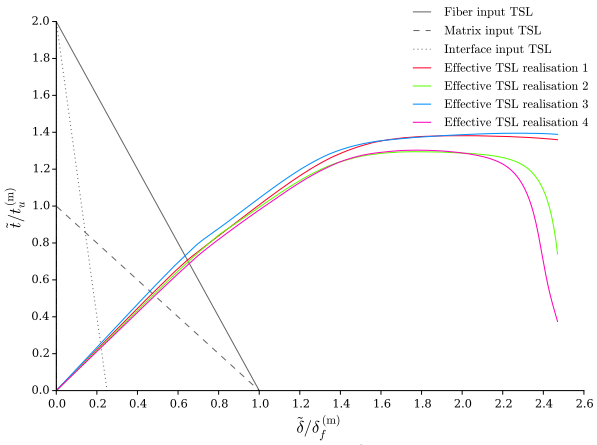

Figure B.4.23: LC6, $t_u^{(i)}/t_u^{(m)} = 2.0$: ETSLs.

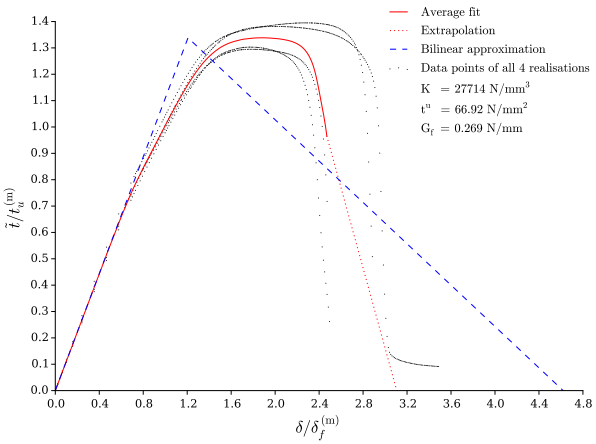

Figure B.4.24: LC6, $t_u^{(i)}/t_u^{(m)} = 2.0$: average fit.

B.5 Effect of Fibre Cohesive Strength

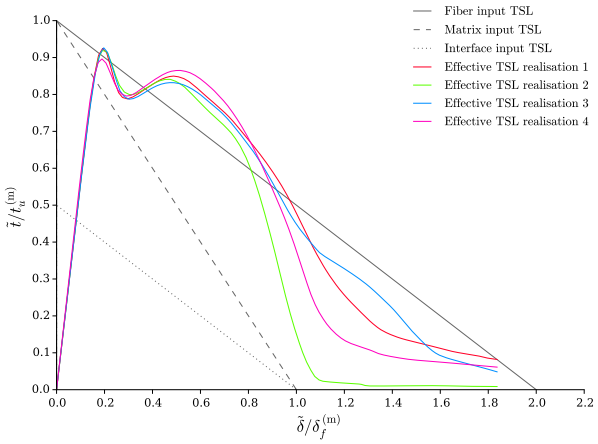

Figure B.5.1: LC1, $t_u^{(f)}/t_u^{(m)} = 1.0$: ETSLs.

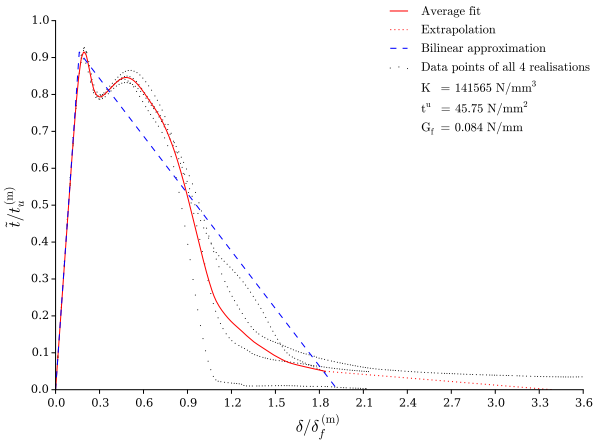

Figure B.5.2: LC1, $t_u^{(f)}/t_u^{(m)} = 1.0$: average fit.

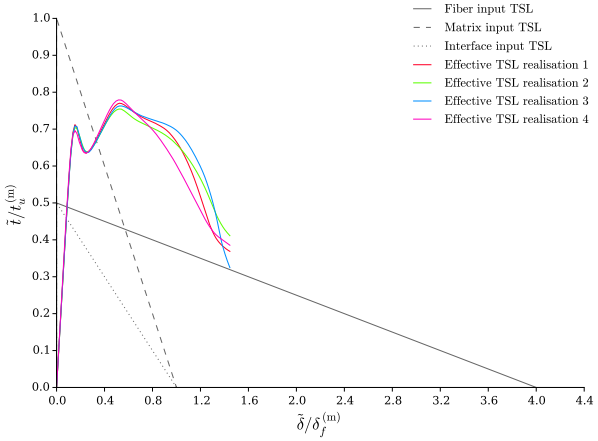

Figure B.5.3: LC1, $t_u^{(f)}/t_u^{(m)} = 0.5$: ETSLs.

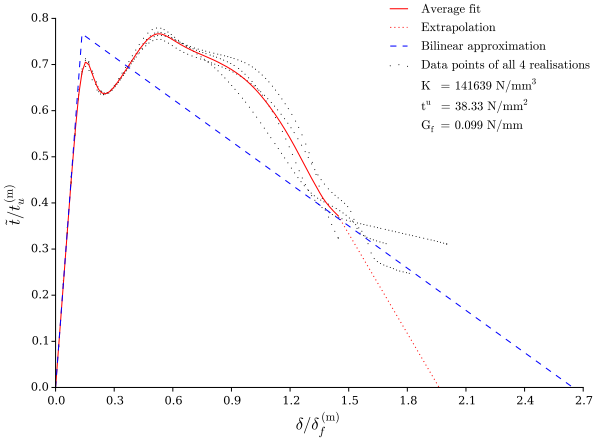

Figure B.5.4: LC1, $t_u^{(f)}/t_u^{(m)} = 0.5$: average fit.

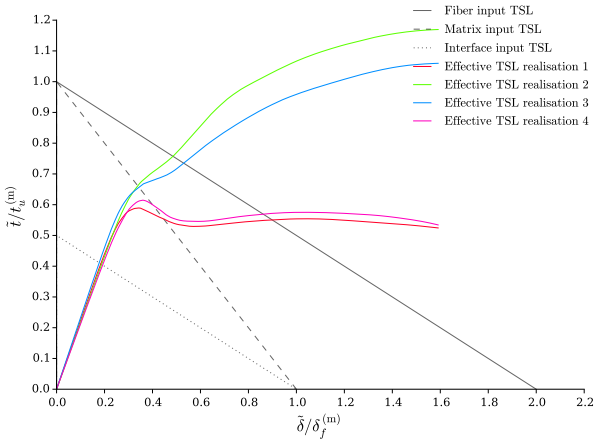

Figure B.5.5: LC2, $t_u^{(f)}/t_u^{(m)} = 1.0$: ETSLs.

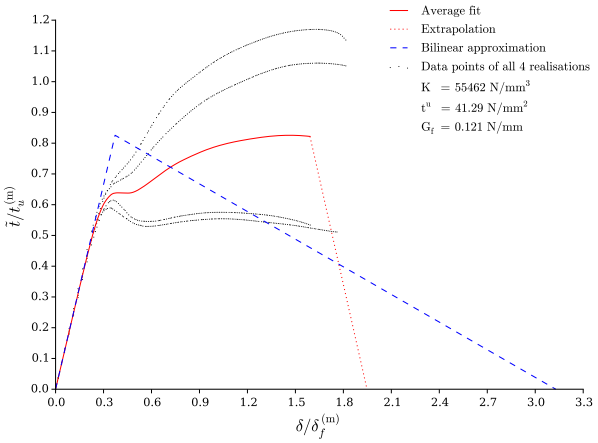

Figure B.5.6: LC2, $t_u^{(f)}/t_u^{(m)} = 1.0$: average fit.

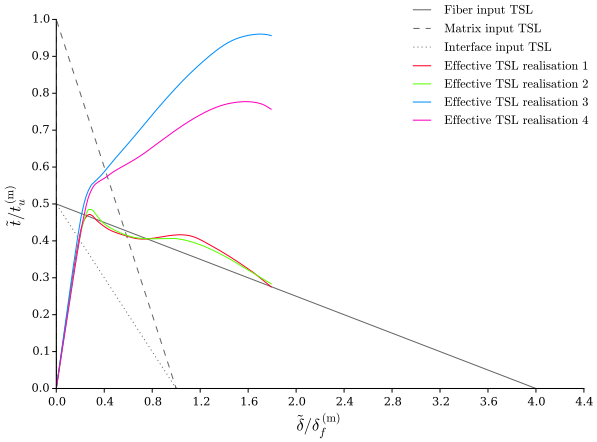

Figure B.5.7: LC2, $t_u^{(f)}/t_u^{(m)} = 0.5$: ETSLs.

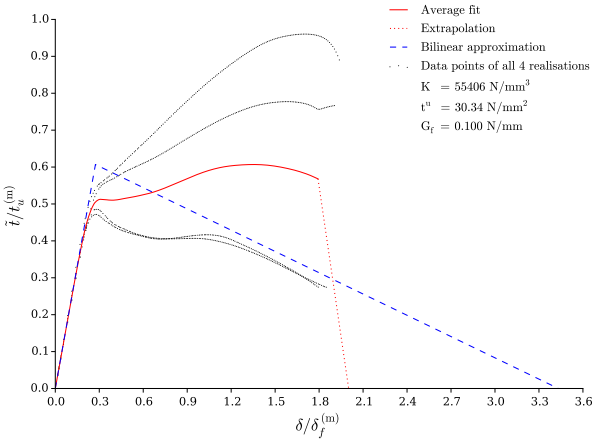

Figure B.5.8: LC2, $t_u^{(f)}/t_u^{(m)} = 0.5$: average fit.

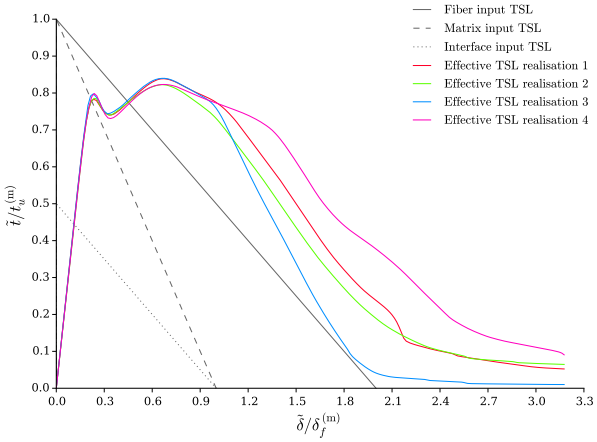

Figure B.5.9: LC3, $t_u^{(f)}/t_u^{(m)} = 1.0$: ETSLs.

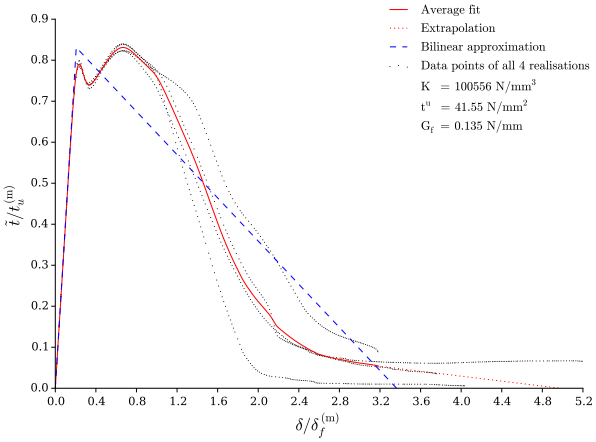

Figure B.5.10: LC3, $t_u^{(f)}/t_u^{(m)} = 1.0$: average fit.

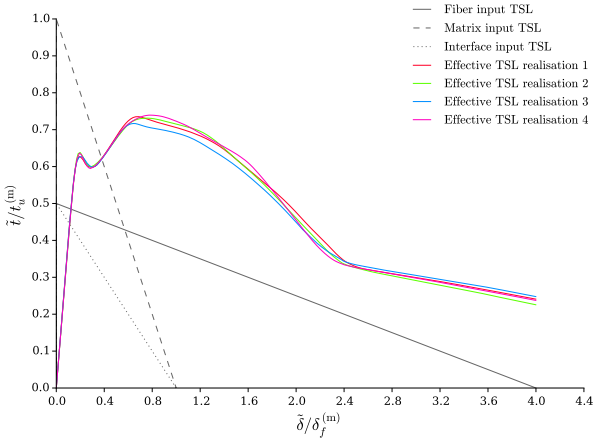

Figure B.5.11: LC3, $t_u^{(f)}/t_u^{(m)} = 0.5$: ETSLs.

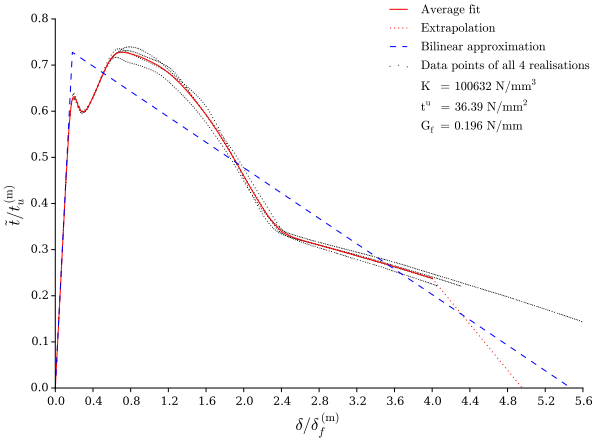

Figure B.5.12: LC3, $t_u^{(f)}/t_u^{(m)} = 0.5$: average fit.

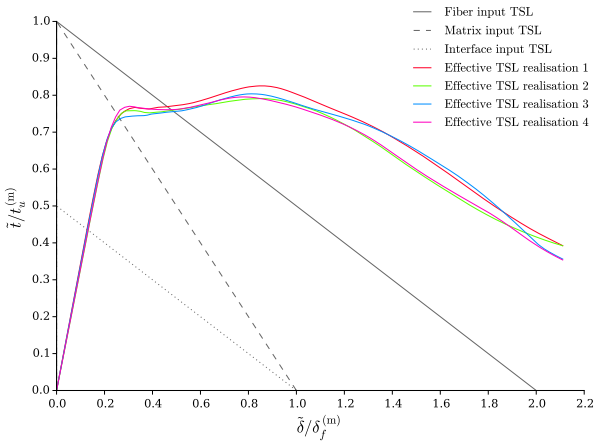

Figure B.5.13: LC4, $t_u^{(f)}/t_u^{(m)} = 1.0$: ETSLs.

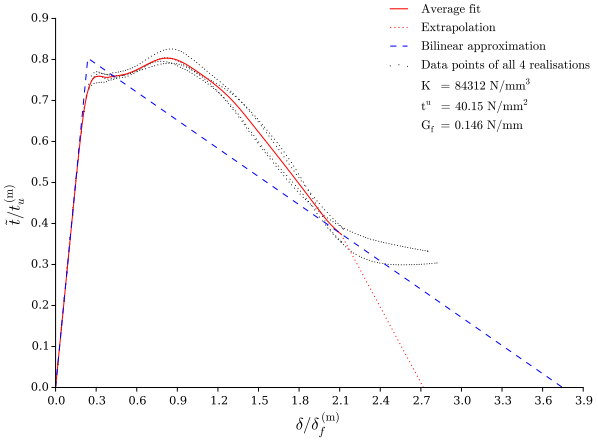

Figure B.5.14: LC4, $t_u^{(f)}/t_u^{(m)} = 1.0$: average fit.

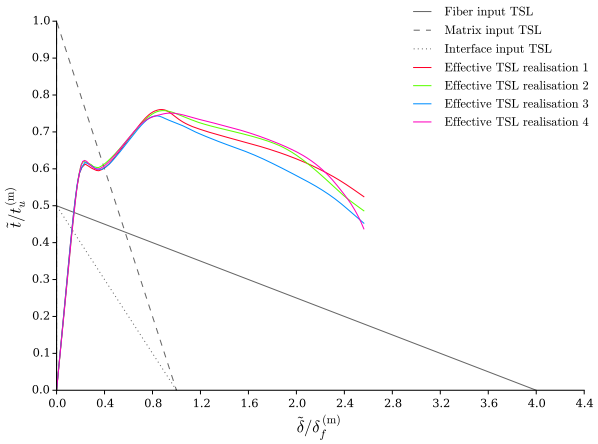

Figure B.5.15: LC4, $t_u^{(f)}/t_u^{(m)} = 0.5$: ETSLs.

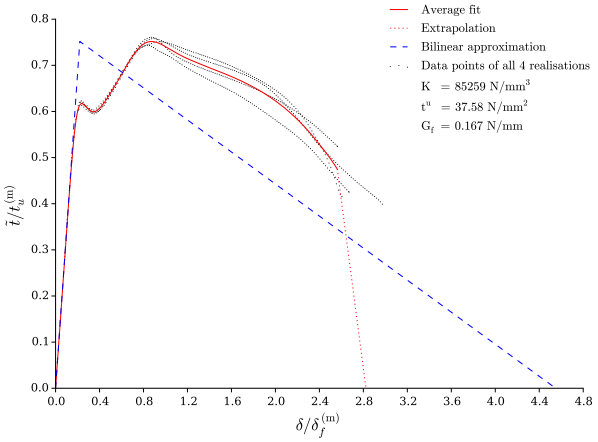

Figure B.5.16: LC4, $t_u^{(f)}/t_u^{(m)} = 0.5$: average fit.

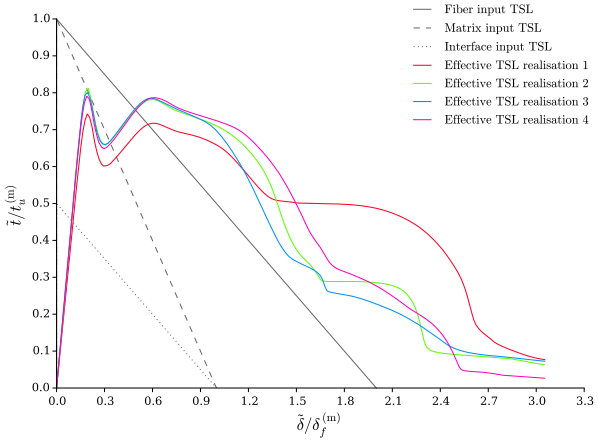

Figure B.5.17: LC5, $t_u^{(f)}/t_u^{(m)} = 1.0$: ETSLs.

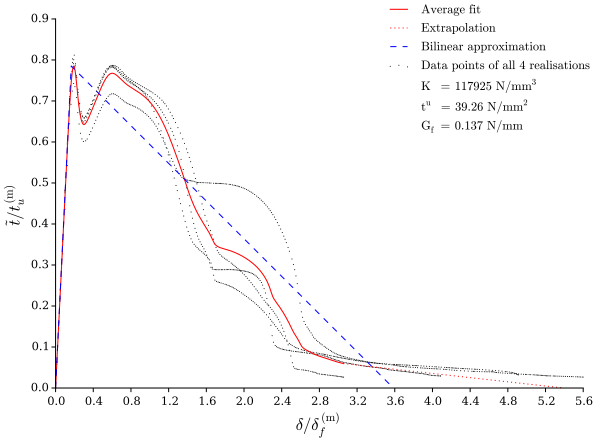

Figure B.5.18: LC5, $t_u^{(f)}/t_u^{(m)} = 1.0$: average fit.

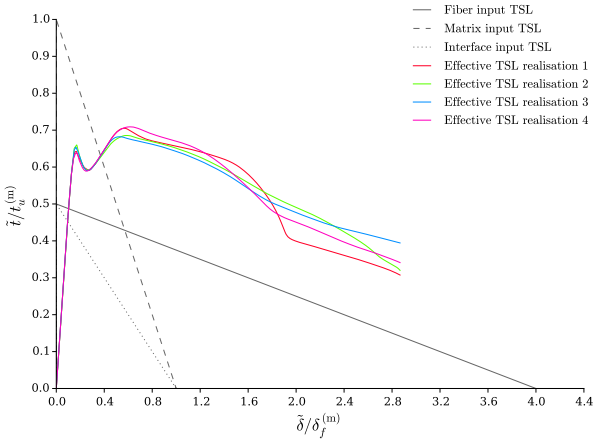

Figure B.5.19: LC5, $t_u^{(f)}/t_u^{(m)} = 0.5$: ETSLs.

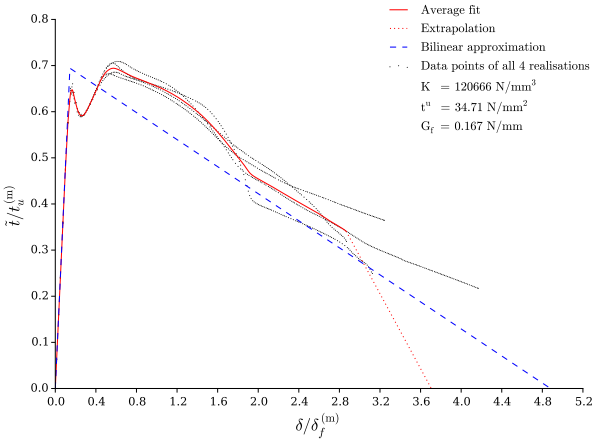

Figure B.5.20: LC5, $t_u^{(f)}/t_u^{(m)} = 0.5$: average fit.

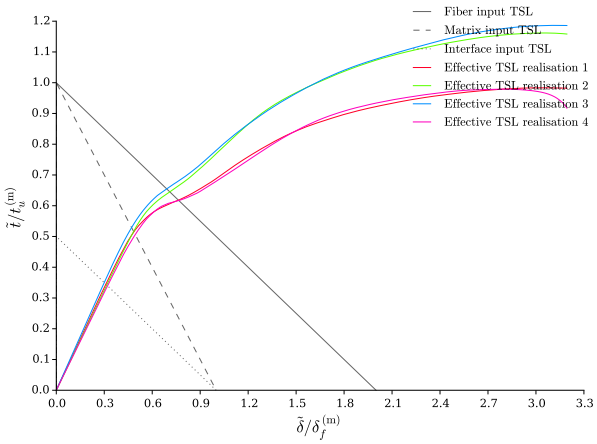

Figure B.5.21: LC6, $t_u^{(f)}/t_u^{(m)} = 1.0$: ETSLs.

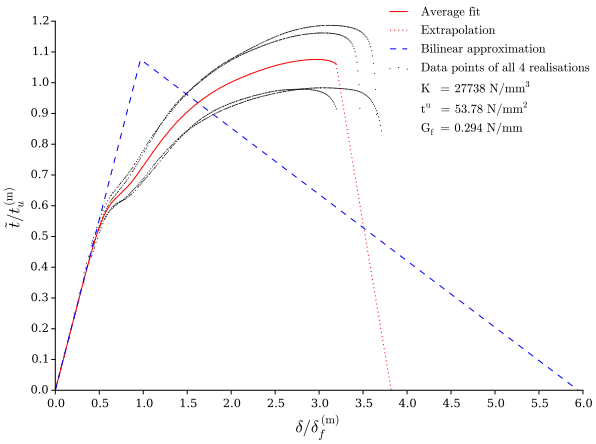

Figure B.5.22: LC6, $t_u^{(f)}/t_u^{(m)} = 1.0$: average fit.

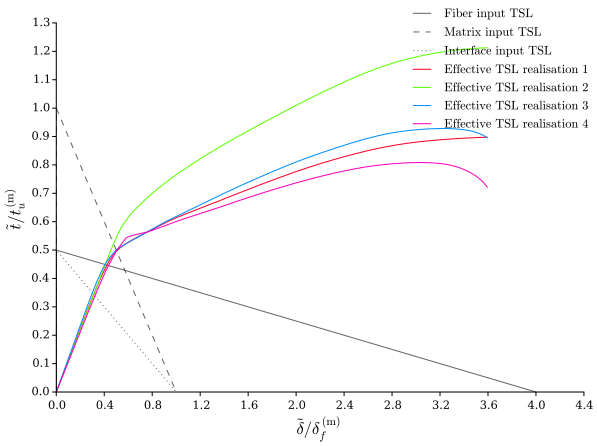

Figure B.5.23: LC6, $t_u^{(f)}/t_u^{(m)} = 0.5$: ETSLs.

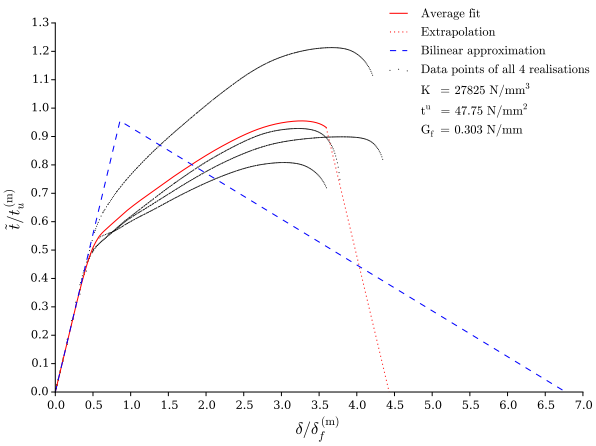

Figure B.5.24: LC6, $t_u^{(f)}/t_u^{(m)} = 0.5$: average fit.

B.6 Effect of Interface Fracture Energy

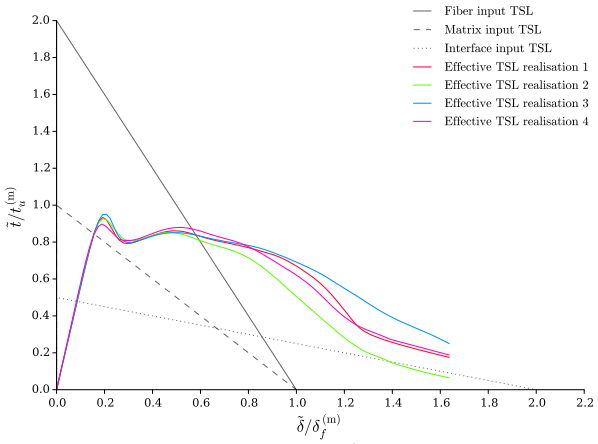

Figure B.6.1: LC1, $G_f^{(i)}/G_f^{(m)} = 1.0$: ETSLs.

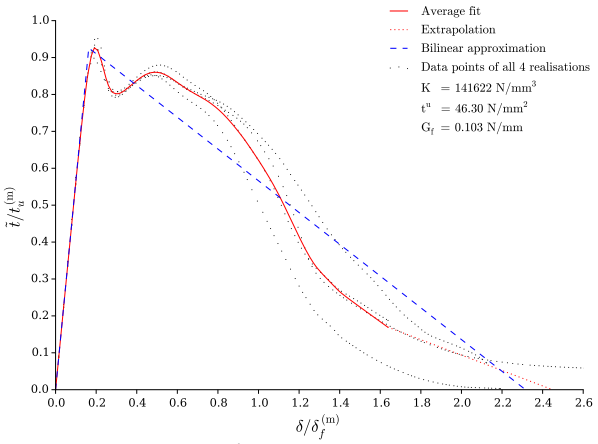

Figure B.6.2: LC1, $G_f^{(i)}/G_f^{(m)} = 1.0$: average fit.

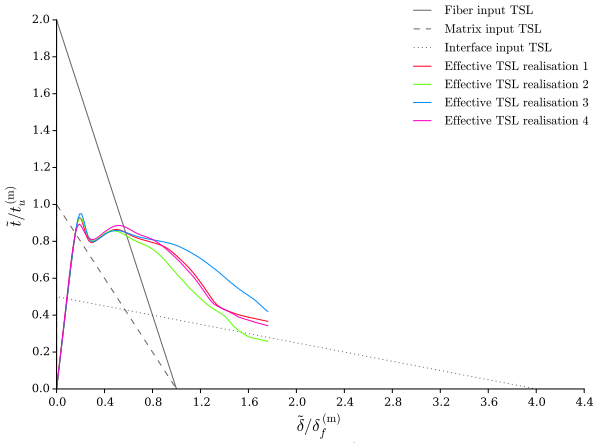

Figure B.6.3: LC1, $G_f^{(i)}/G_f^{(m)} = 2.0$: ETSLs.

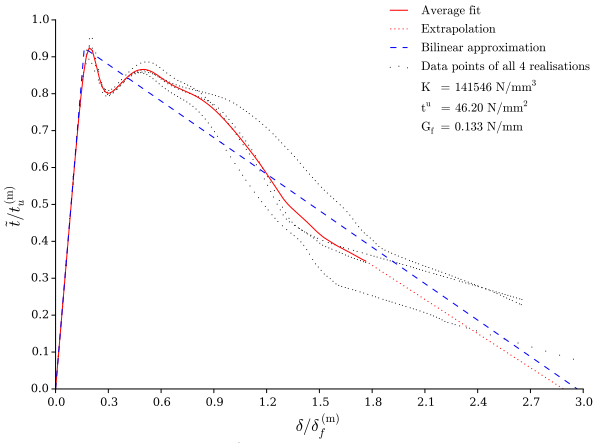

Figure B.6.4: LC1, $G_f^{(i)}/G_f^{(m)} = 2.0$: average fit.

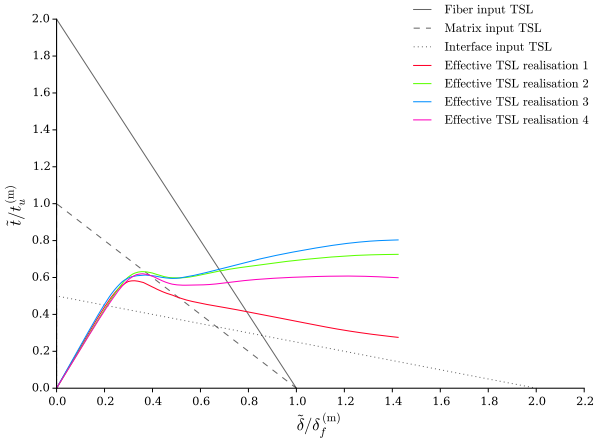

Figure B.6.5: LC2, $G_f^{(i)}/G_f^{(m)} = 1.0$: ETSLs.

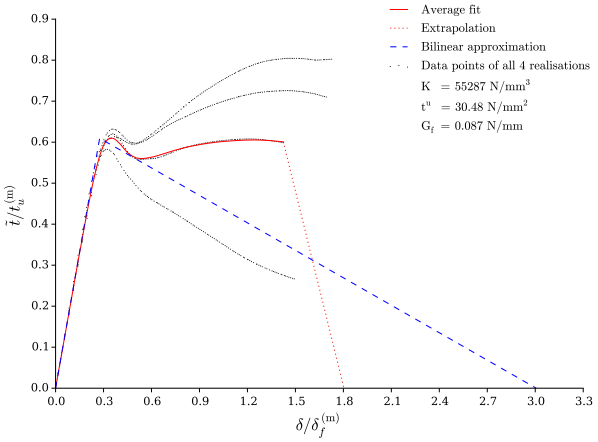

Figure B.6.6: LC2, $G_f^{(i)}/G_f^{(m)} = 1.0$: average fit.

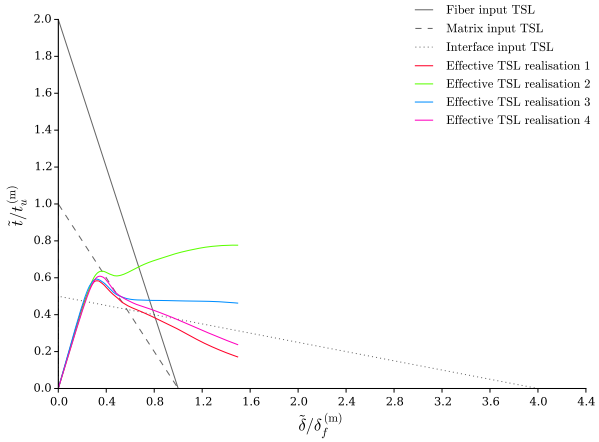

Figure B.6.7: LC2, $G_f^{(i)}/G_f^{(m)} = 2.0$: ETSLs.

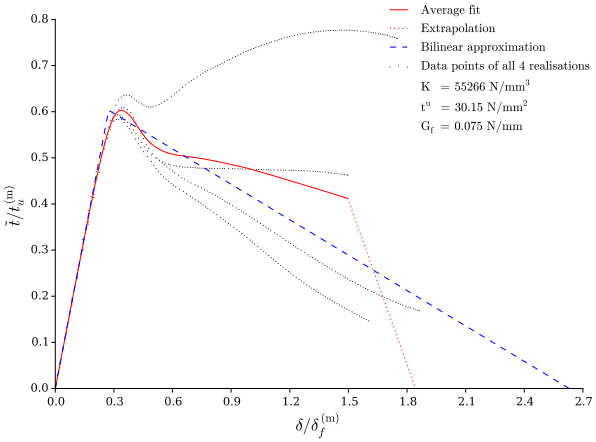

Figure B.6.8: LC2, $G_f^{(i)}/G_f^{(m)} = 2.0$: average fit.

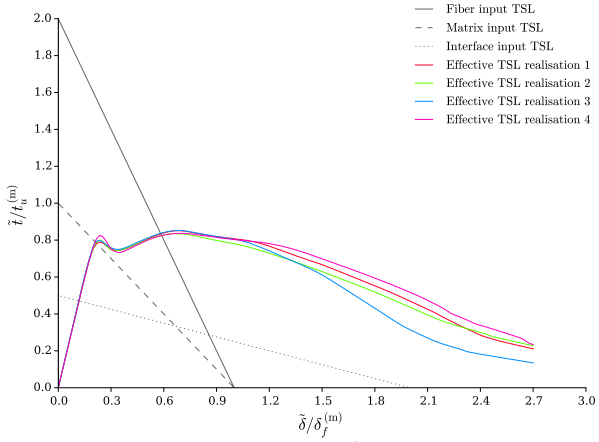

Figure B.6.9: LC3, $G_f^{(i)}/G_f^{(m)} = 1.0$: ETSLs.

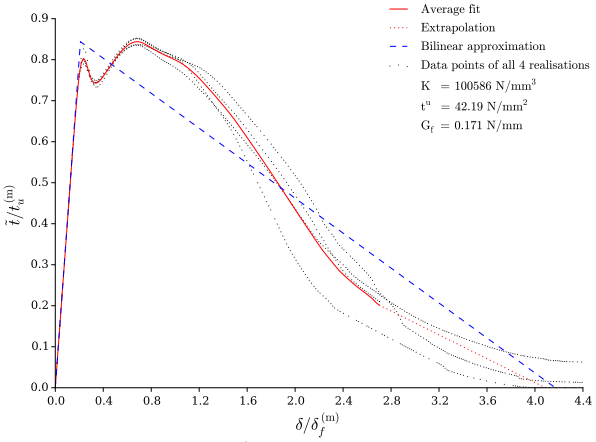

Figure B.6.10: LC3, $G_f^{(i)}/G_f^{(m)} = 1.0$: average fit.

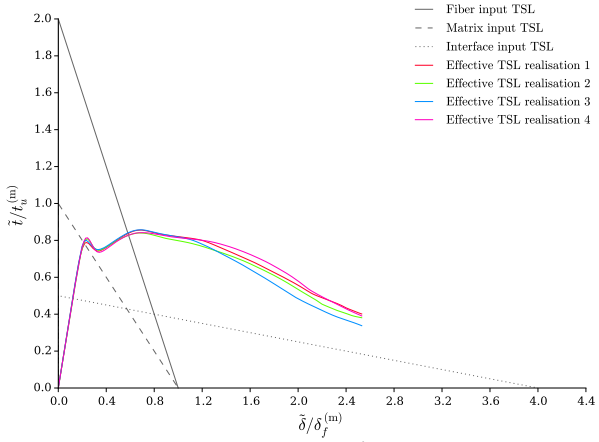

Figure B.6.11: LC3, $G_f^{(i)}/G_f^{(m)} = 2.0$: ETSLs.

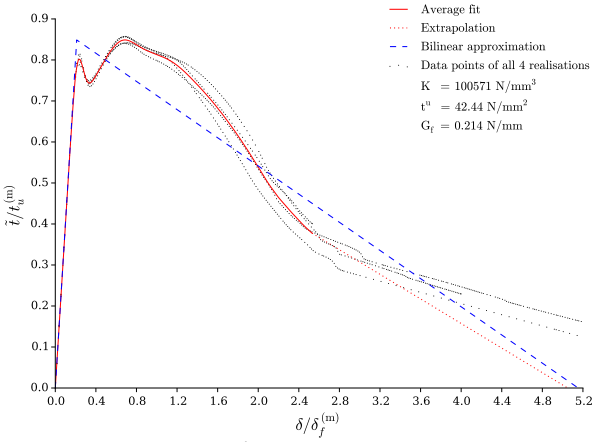

Figure B.6.12: LC3, $G_f^{(i)}/G_f^{(m)} = 2.0$: average fit.

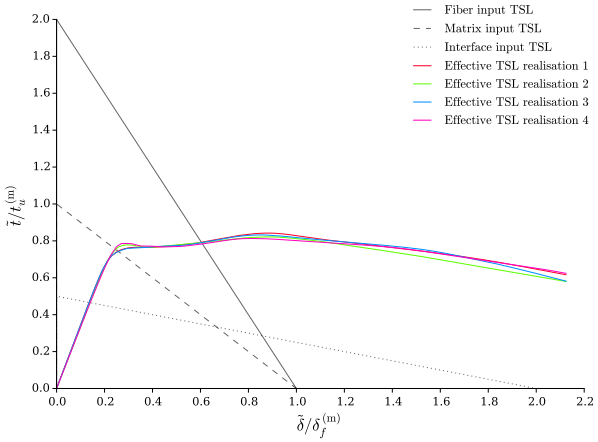

Figure B.6.13: LC4, $G_f^{(i)}/G_f^{(m)} = 1.0$: ETSLs.

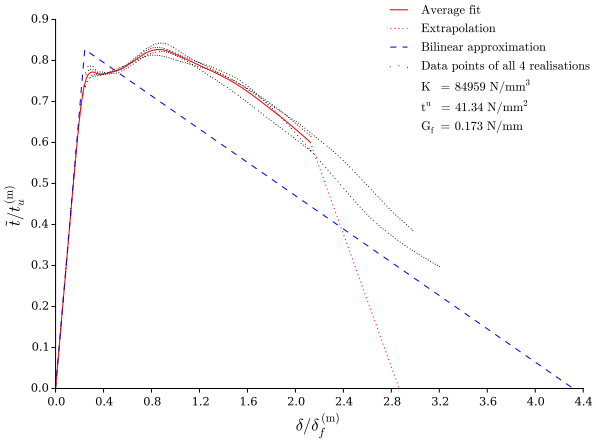

Figure B.6.14: LC4, $G_f^{(i)}/G_f^{(m)} = 1.0$: average fit.

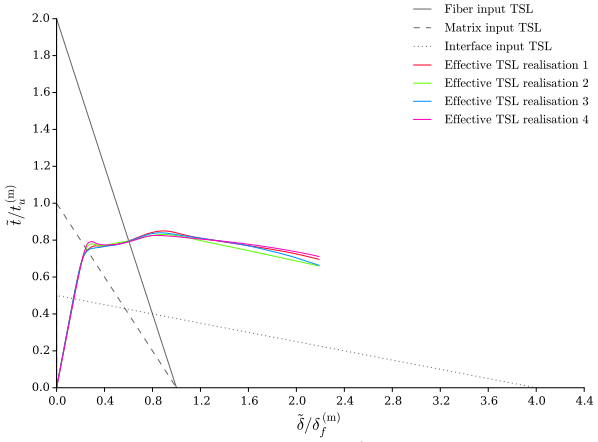

Figure B.6.15: LC4, $G_f^{(i)}/G_f^{(m)} = 2.0$: ETSLs.

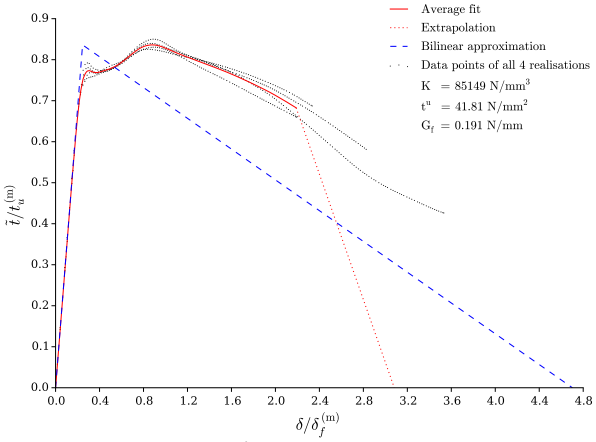

Figure B.6.16: LC4, $G_f^{(i)}/G_f^{(m)} = 2.0$: average fit.

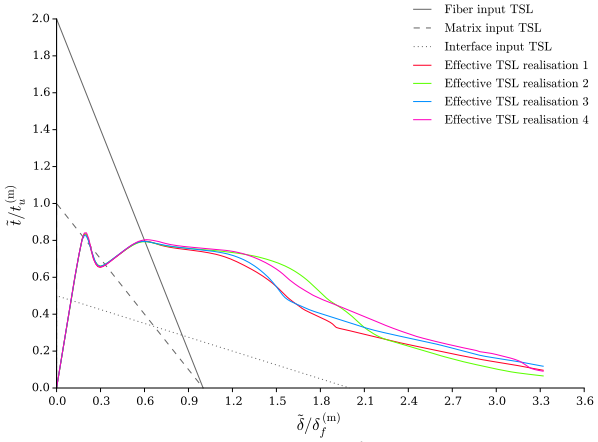

Figure B.6.17: LC5, $G_f^{(i)}/G_f^{(m)} = 1.0$: ETSLs.

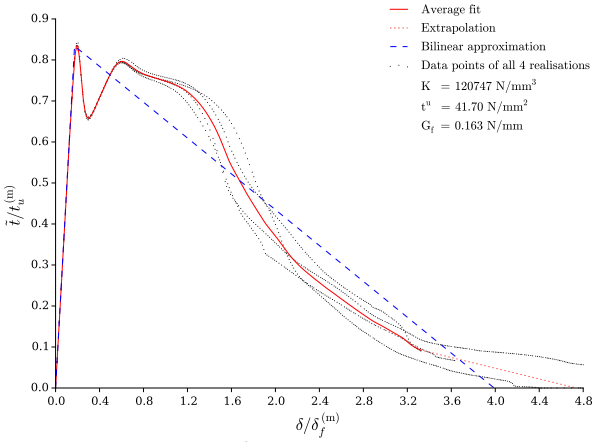

Figure B.6.18: LC5, $G_f^{(i)}/G_f^{(m)} = 1.0$: average fit.

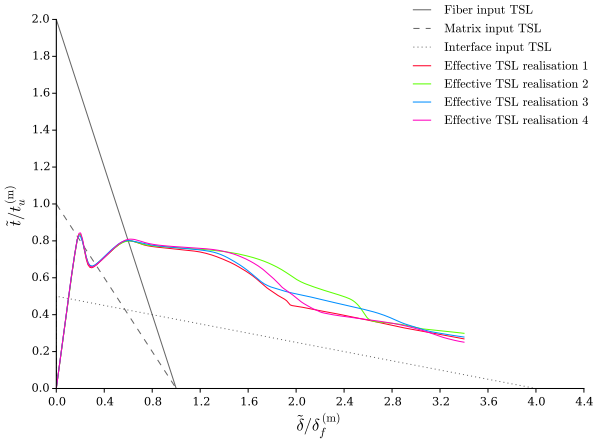

Figure B.6.19: LC5, $G_f^{(i)}/G_f^{(m)} = 2.0$: ETSLs.

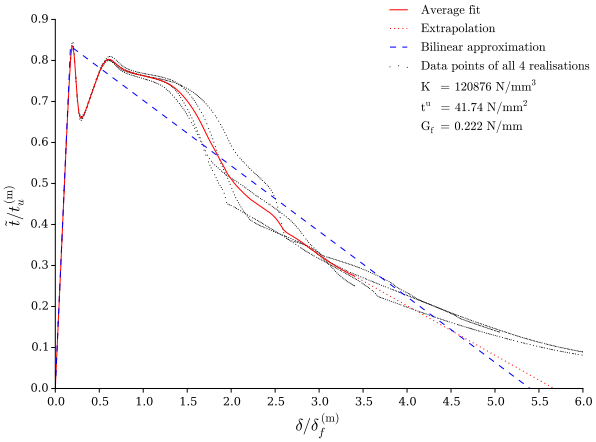

Figure B.6.20: LC5, $G_f^{(i)}/G_f^{(m)} = 2.0$: average fit.

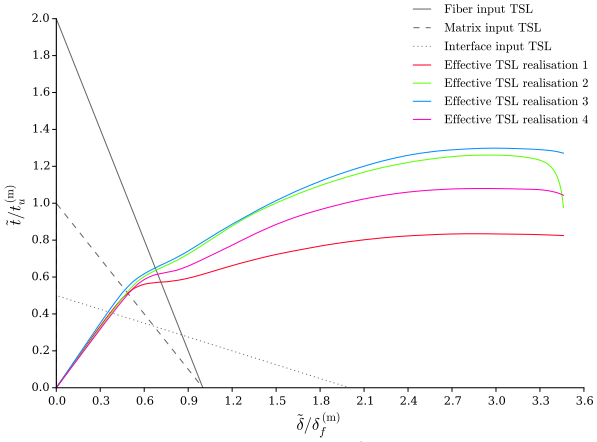

Figure B.6.21: LC6, $G_f^{(i)}/G_f^{(m)} = 1.0$: ETSLs.

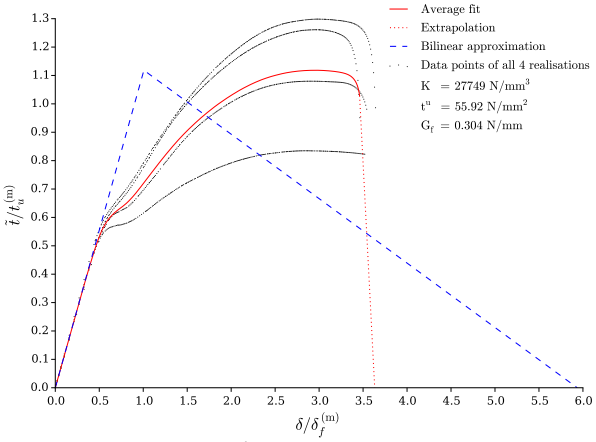

Figure B.6.22: LC6, $G_f^{(i)}/G_f^{(m)} = 1.0$: average fit.

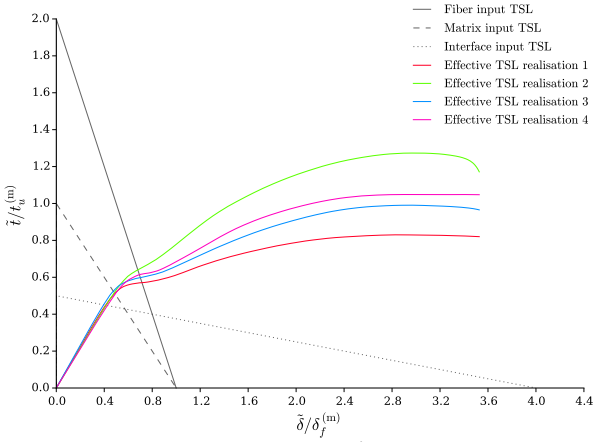

Figure B.6.23: LC6, $G_f^{(i)}/G_f^{(m)} = 2.0$: ETSLs.

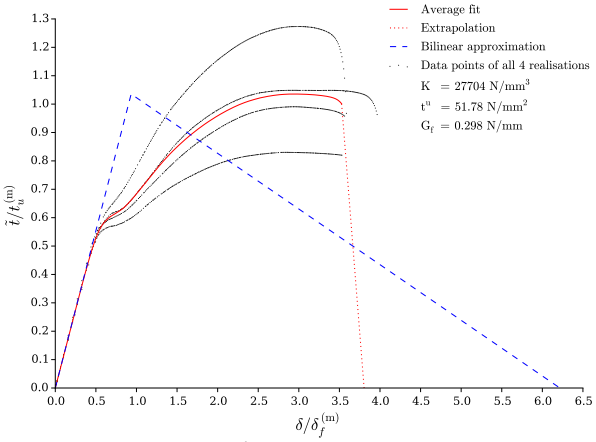

Figure B.6.24: LC6, $G_f^{(i)}/G_f^{(m)} = 2.0$: average fit.

B.7 Effect of Fibre Fracture Energy

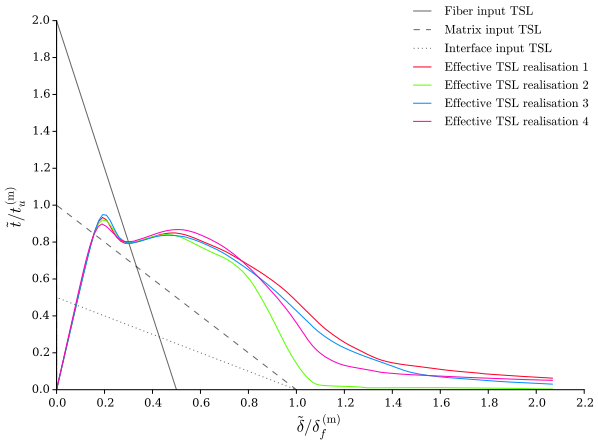

Figure B.7.1: LC1, $G_f^{(f)}/G_f^{(m)} = 1.0$: ETSLs.

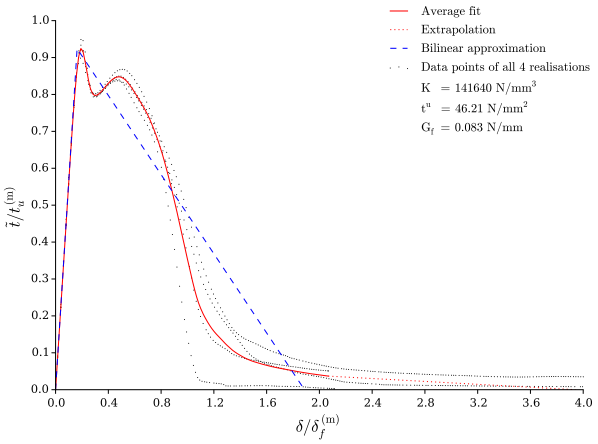

Figure B.7.2: LC1, $G_f^{(f)}/G_f^{(m)} = 1.0$: average fit.

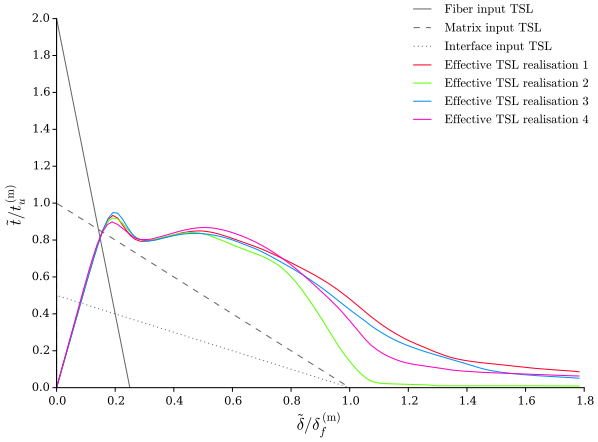

Figure B.7.3: LC1, $G_f^{(f)}/G_f^{(m)} = 0.5$: ETSLs.

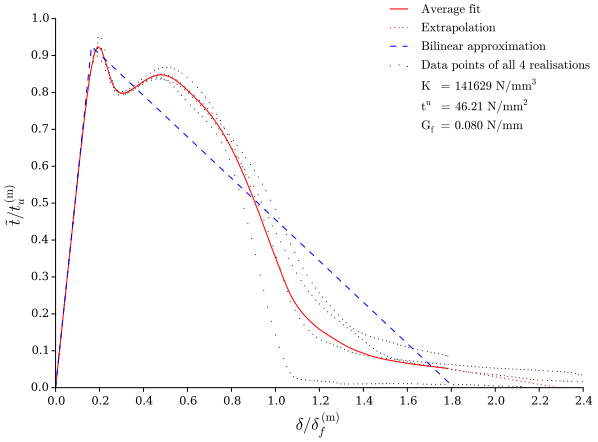

Figure B.7.4: LC1, $G_f^{(f)}/G_f^{(m)} = 0.5$: average fit.

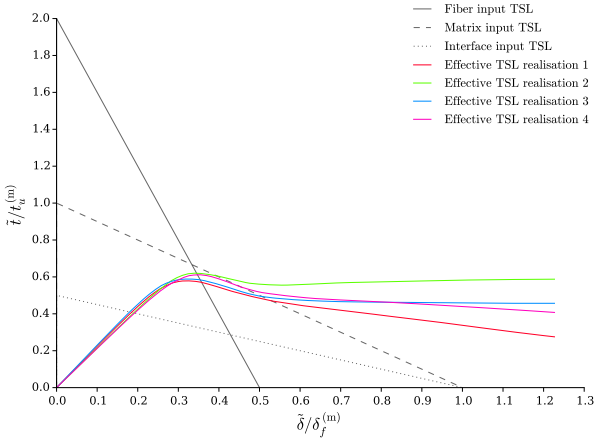

Figure B.7.5: LC2, $G_f^{(f)}/G_f^{(m)} = 1.0$: ETSLs.

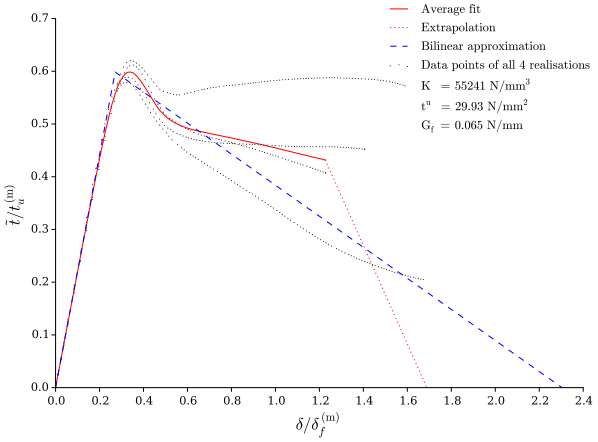

Figure B.7.6: LC2, $G_f^{(f)}/G_f^{(m)} = 1.0$: average fit.

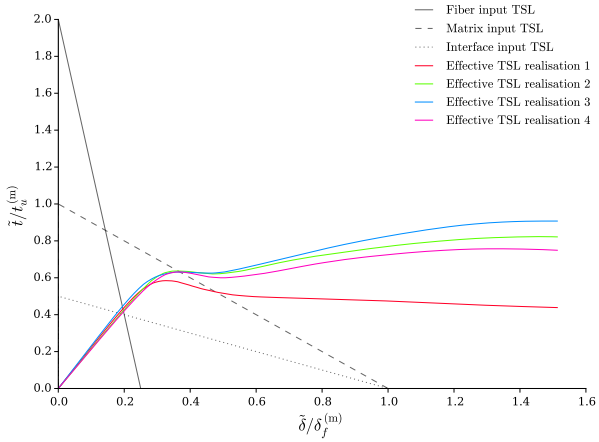

Figure B.7.7: LC2, $G_f^{(f)}/G_f^{(m)} = 0.5$: ETSLs.

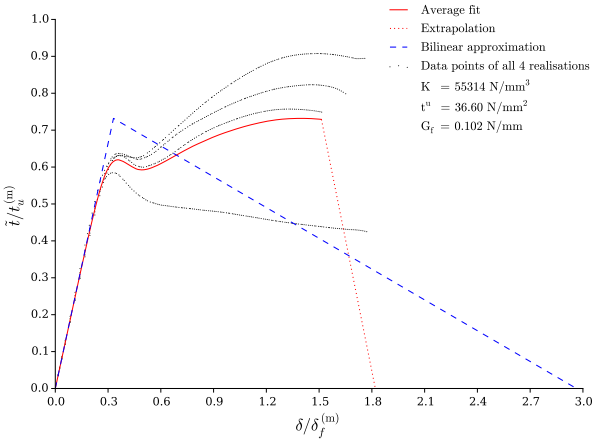

Figure B.7.8: LC2, $G_f^{(f)}/G_f^{(m)} = 0.5$: average fit.

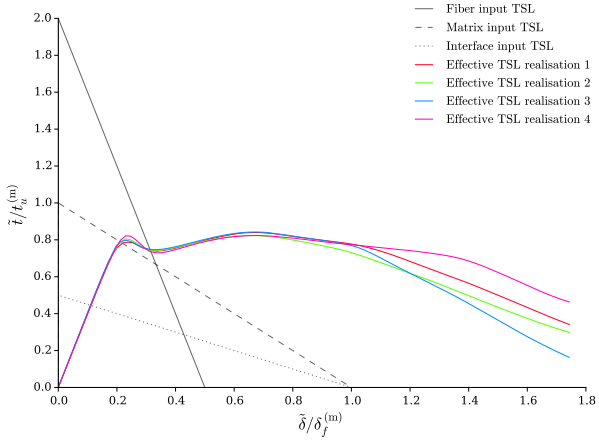

Figure B.7.9: LC3, $G_f^{(f)}/G_f^{(m)} = 1.0$: ETSLs.

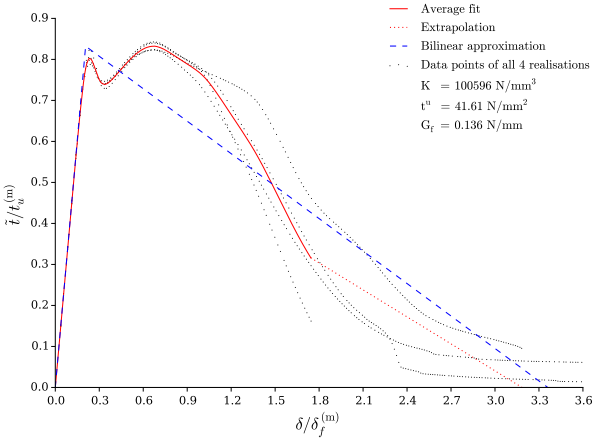

Figure B.7.10: LC3, $G_f^{(f)}/G_f^{(m)} = 1.0$: average fit.

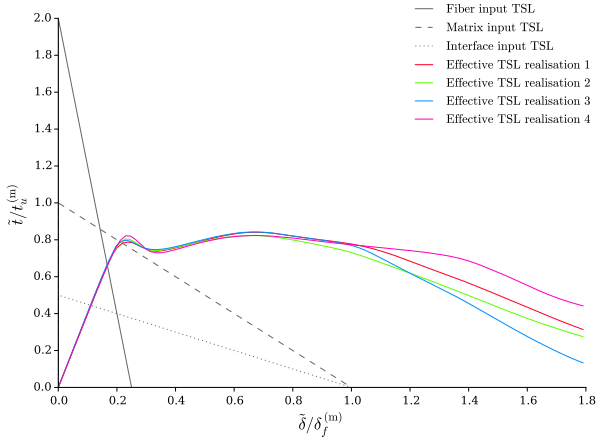

Figure B.7.11: LC3, $G_f^{(f)}/G_f^{(m)} = 0.5$: ETSLs.

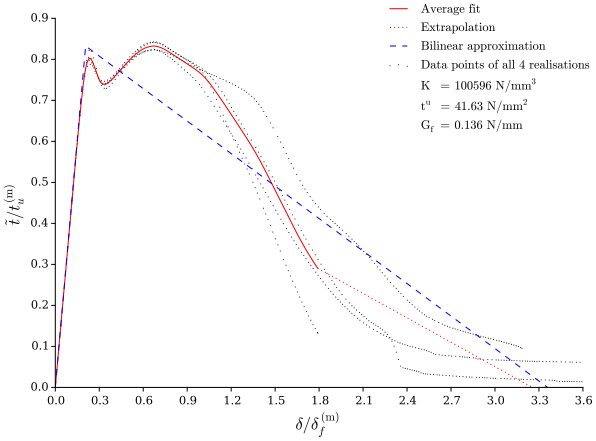

Figure B.7.12: LC3, $G_f^{(f)}/G_f^{(m)} = 0.5$: average fit.

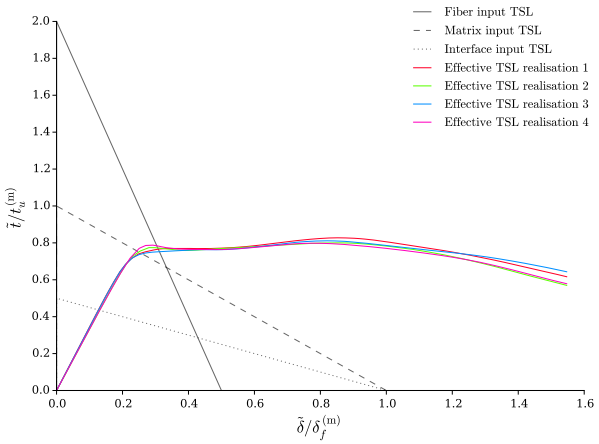

Figure B.7.13: LC4, $G_f^{(f)}/G_f^{(m)} = 1.0$: ETSLs.

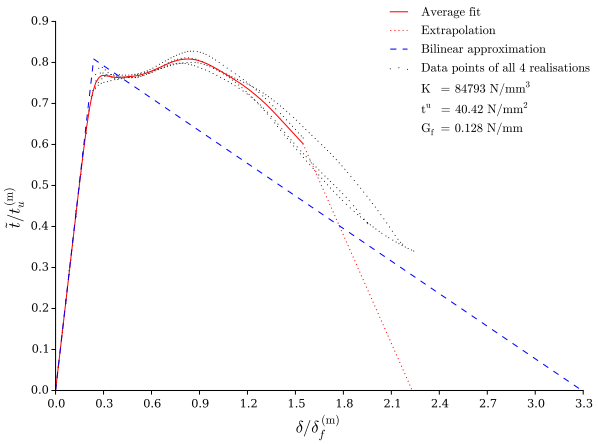

Figure B.7.14: LC4, $G_f^{(f)}/G_f^{(m)} = 1.0$: average fit.

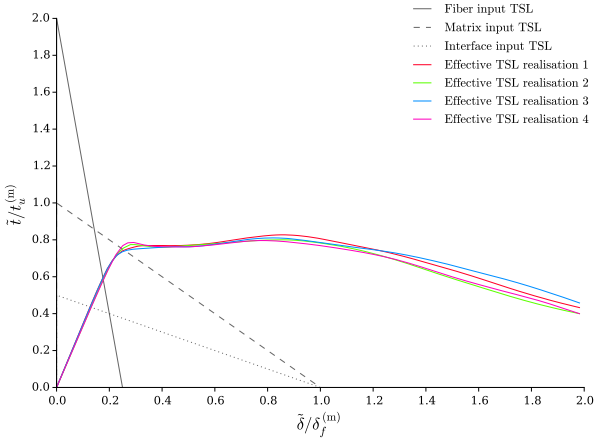

Figure B.7.15: LC4, $G_f^{(f)}/G_f^{(m)} = 0.5$: ETSLs.

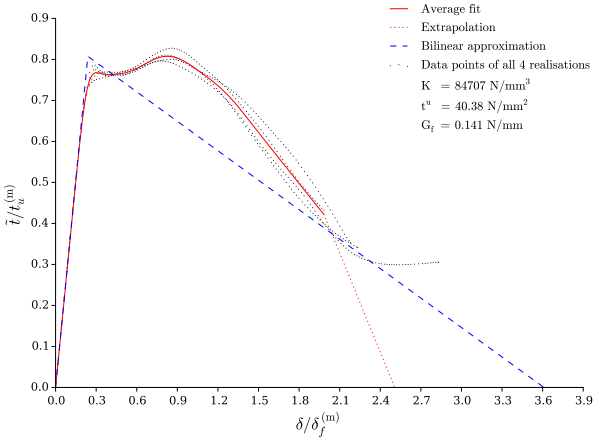

Figure B.7.16: LC4, $G_f^{(f)}/G_f^{(m)} = 0.5$: average fit.

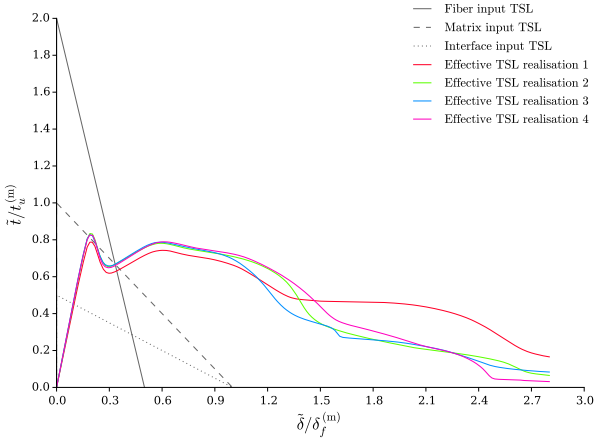

Figure B.7.17: LC5, $G_f^{(f)}/G_f^{(m)} = 1.0$: ETSLs.

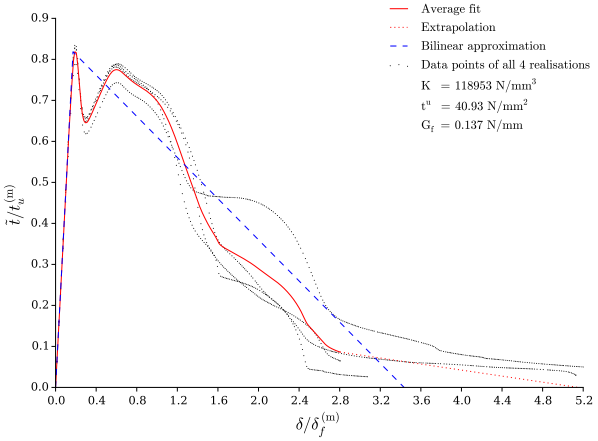

Figure B.7.18: LC5, $G_f^{(f)}/G_f^{(m)} = 1.0$: average fit.

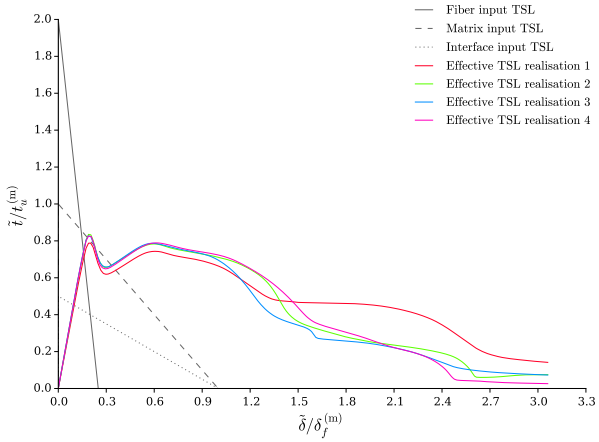

Figure B.7.19: LC5, $G_f^{(f)}/G_f^{(m)} = 0.5$: ETSLs.

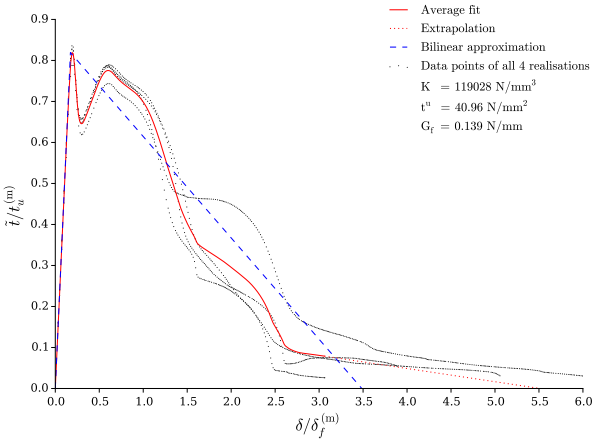

Figure B.7.20: LC5, $G_f^{(f)}/G_f^{(m)} = 0.5$: average fit.

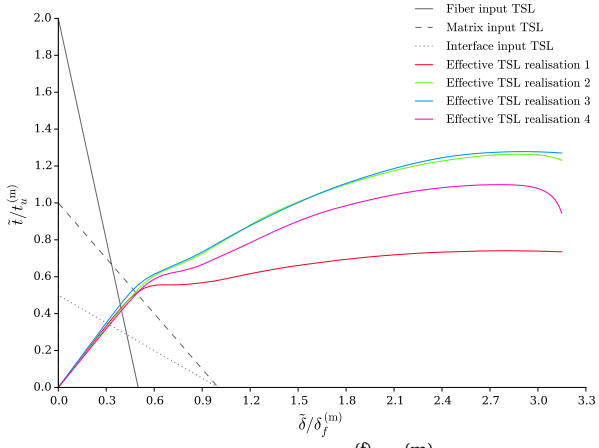

Figure B.7.21: LC6, $G_f^{(f)}/G_f^{(m)} = 1.0$: ETSLs.

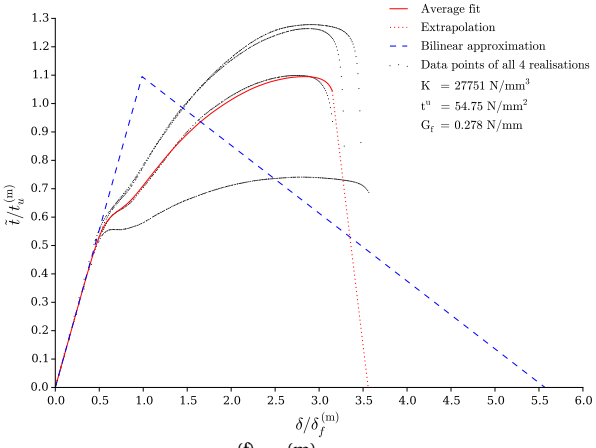

Figure B.7.22: LC6, $G_f^{(f)}/G_f^{(m)} = 1.0$: average fit.

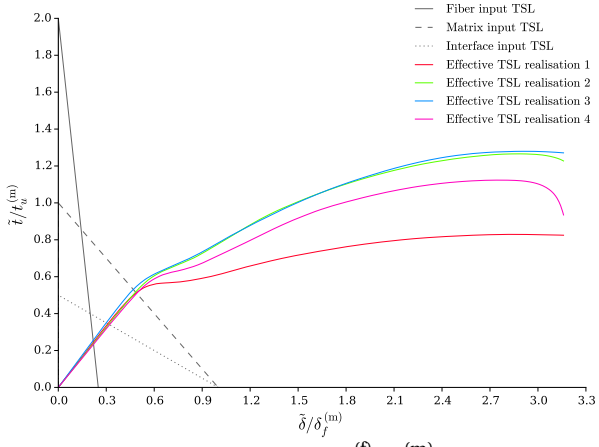

Figure B.7.23: LC6, $G_f^{(f)}/G_f^{(m)} = 0.5$: ETSLs.

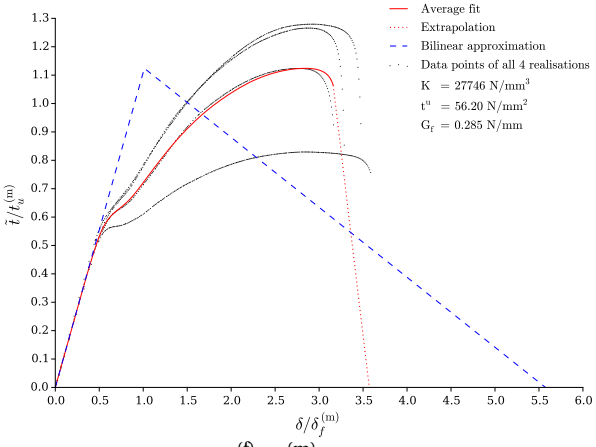

Figure B.7.24: LC6, $G_f^{(f)}/G_f^{(m)} = 0.5$: average fit.

B.8 Effect of Fibre Volume Fraction

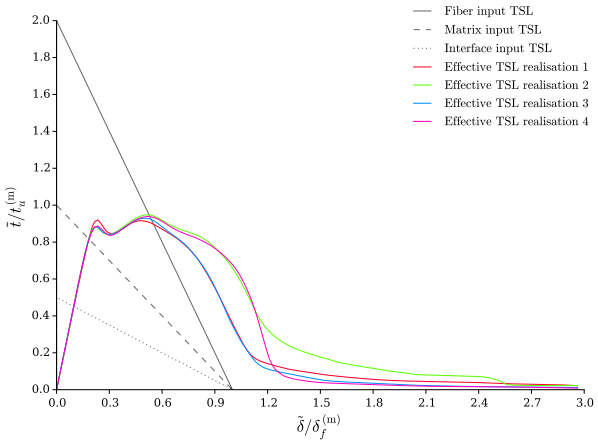

Figure B.8.1: LC1, $V_f = 30\%$: ETSLs.

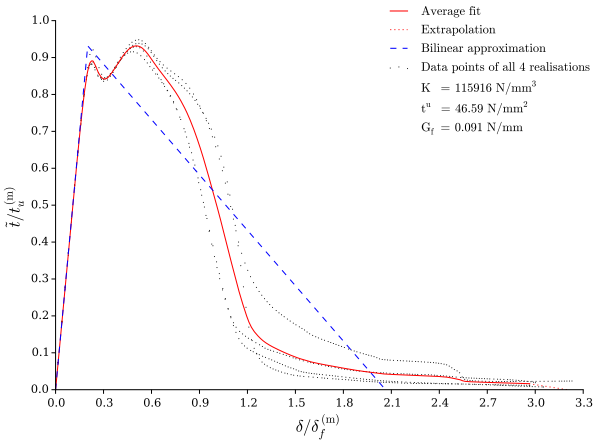

Figure B.8.2: LC1, $V_f = 30\%$: average fit.

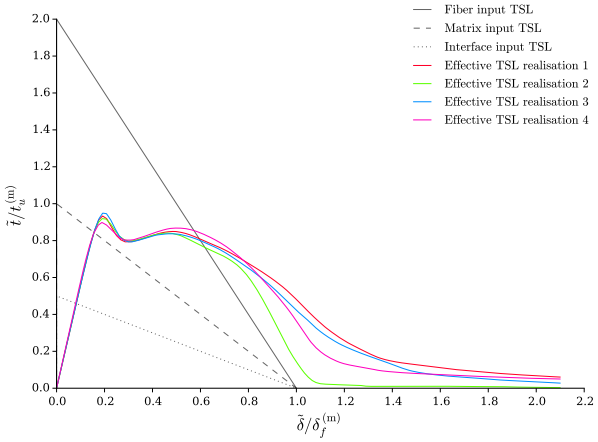

Figure B.8.3: LC1, $V_f = 40\%$: ETSLs.

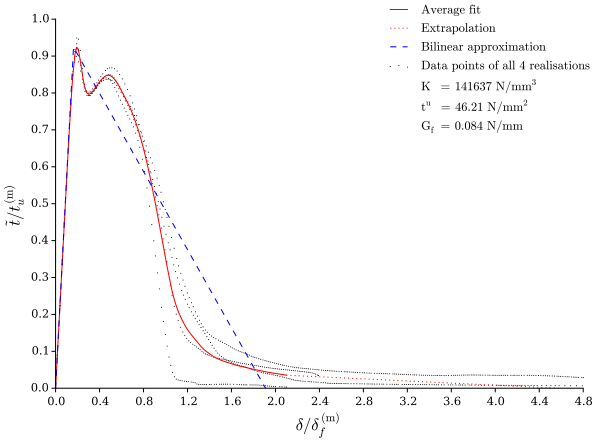

Figure B.8.4: LC1, $V_f = 40\%$: average fit.

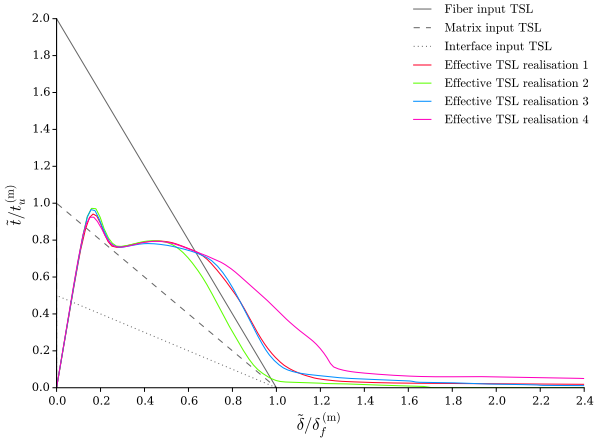

Figure B.8.5: LC1, $V_f = 50\%$: ETSLs.

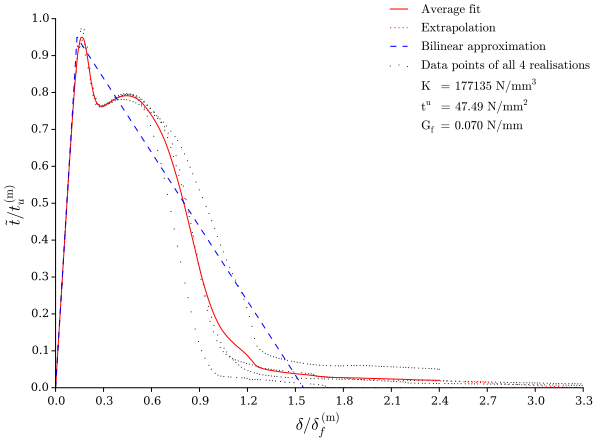

Figure B.8.6: LC1, $V_f = 50\%$: average fit.

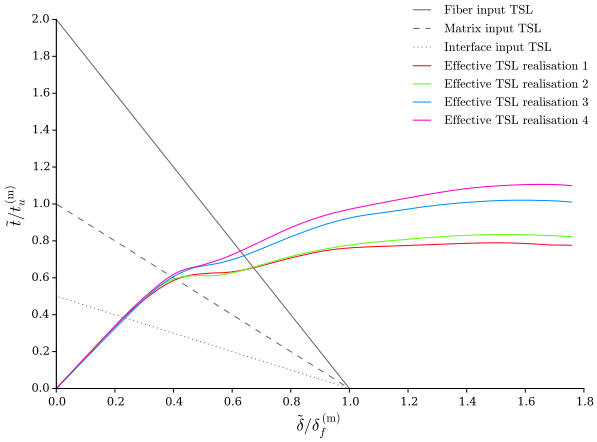

Figure B.8.7: LC2, $V_f = 30\%$: ETSLs.

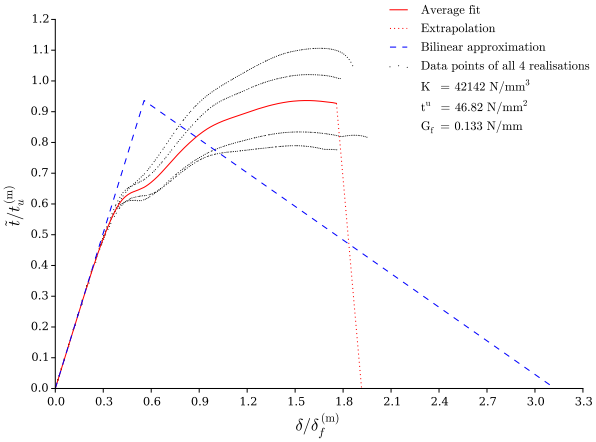

Figure B.8.8: LC2, $V_f = 30\%$: average fit.

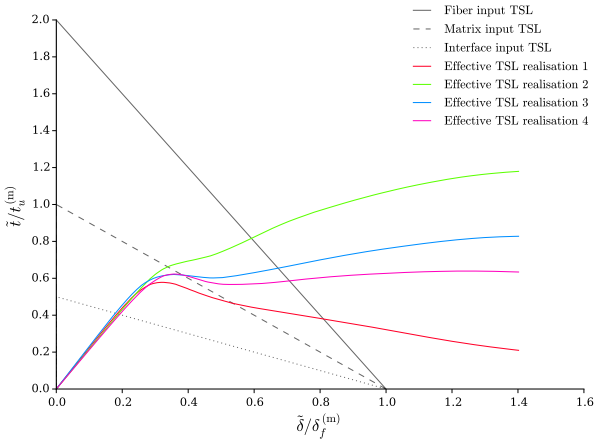

Figure B.8.9: LC2, $V_f = 40\%$: ETSLs.

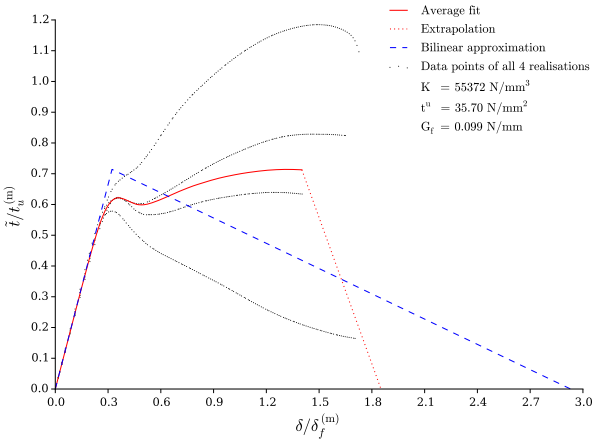

Figure B.8.10: LC2, $V_f = 40\%$: average fit.

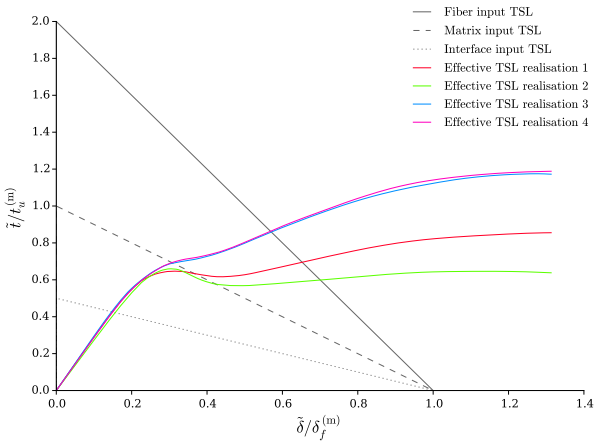

Figure B.8.11: LC2, $V_f = 50\%$: ETSLs.

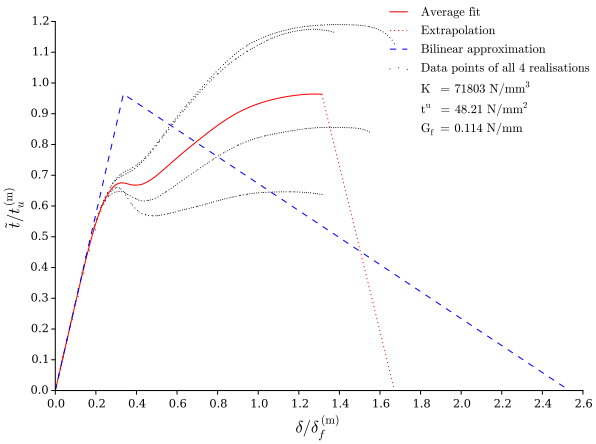

Figure B.8.12: LC2, $V_f = 50\%$: average fit.

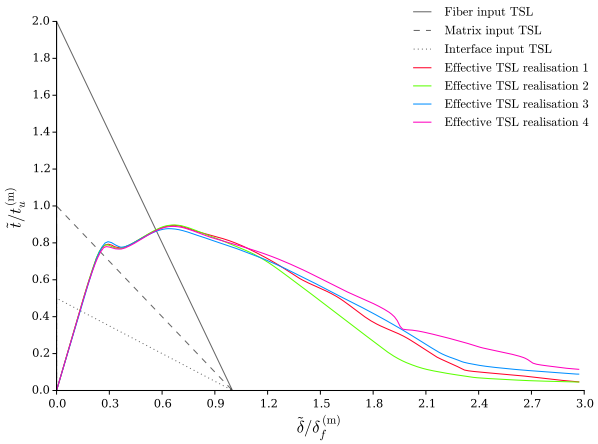

Figure B.8.13: LC3, $V_f = 30\%$: ETSLs.

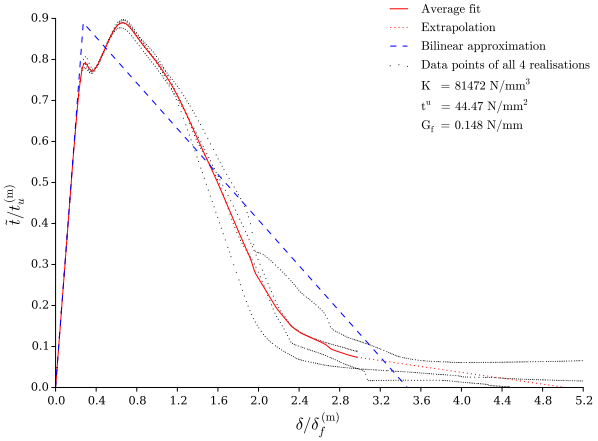

Figure B.8.14: LC3, $V_f = 30\%$: average fit.

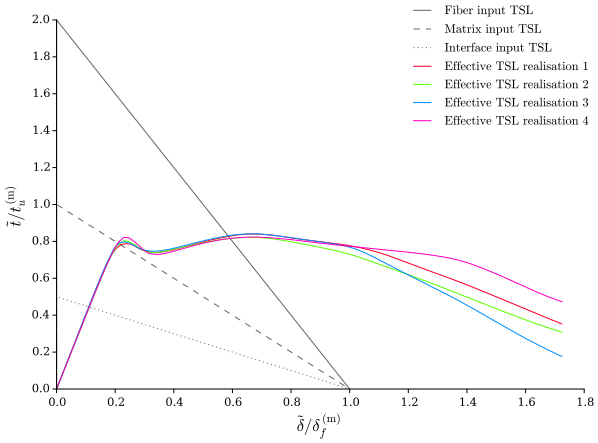

Figure B.8.15: LC3, $V_f = 40\%$: ETSLs.

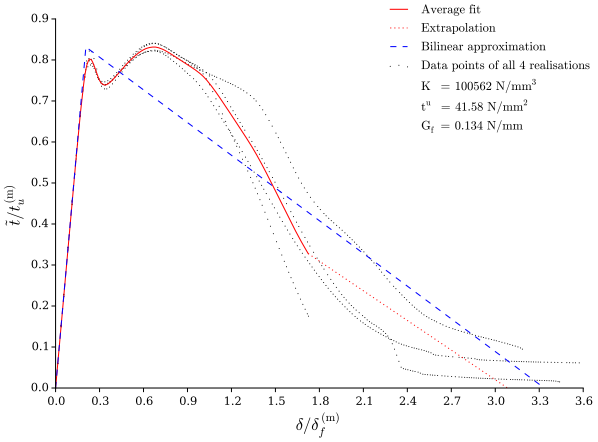

Figure B.8.16: LC3, $V_f = 40\%$: average fit.

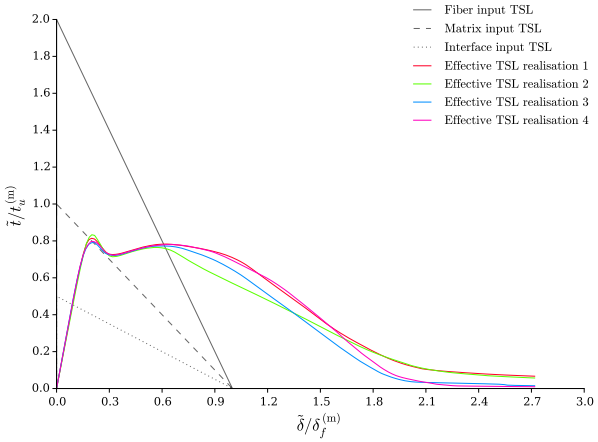

Figure B.8.17: LC3, $V_f = 50\%$: ETSLs.

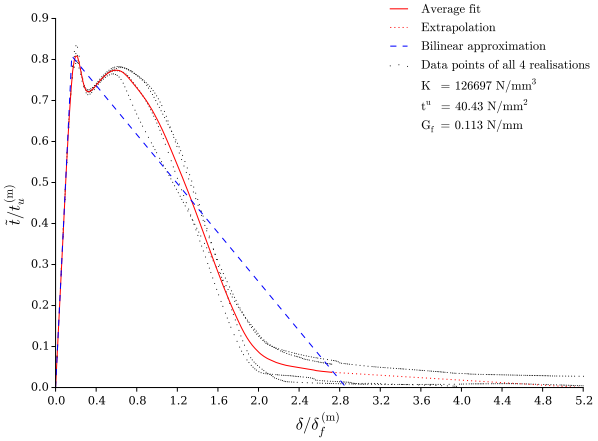

Figure B.8.18: LC3, $V_f = 50\%$: average fit.

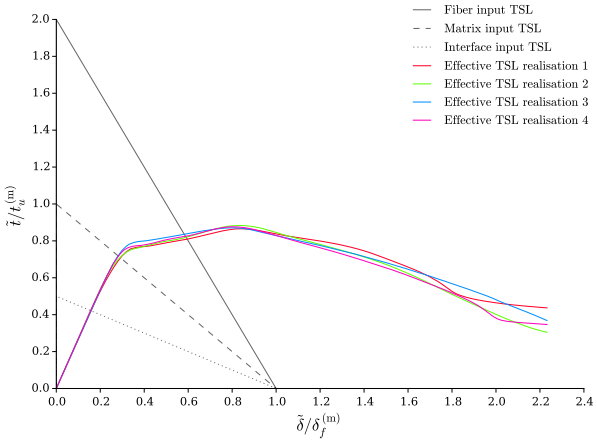

Figure B.8.19: LC4, $V_f = 30\%$: ETSLs.

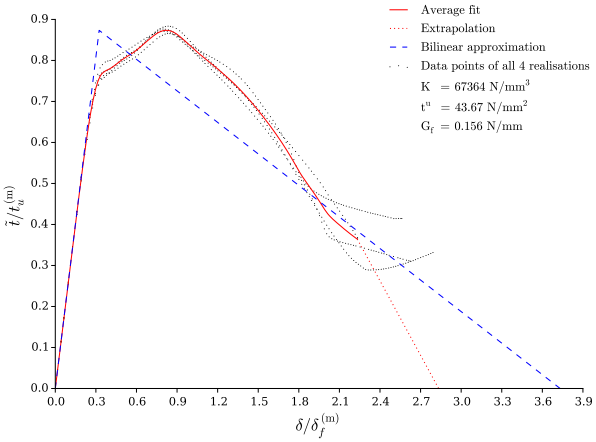

Figure B.8.20: LC4, $V_f = 30\%$: average fit.

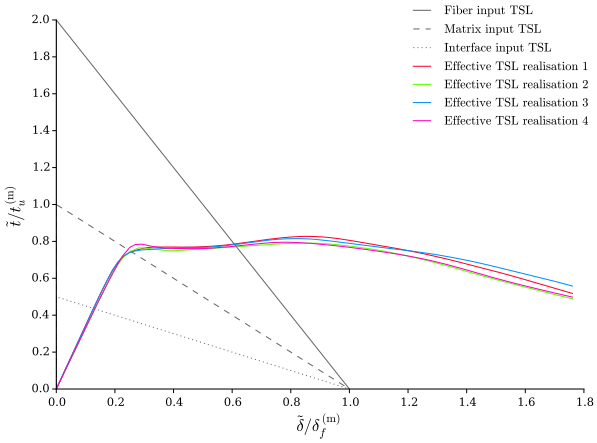

Figure B.8.21: LC4, $V_f = 40\%$: ETSLs.

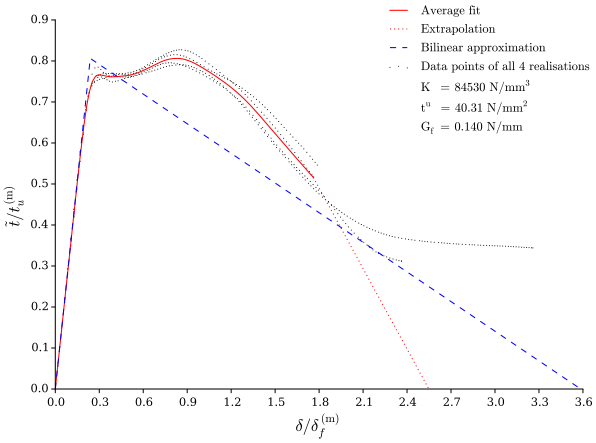

Figure B.8.22: LC4, $V_f = 40\%$: average fit.

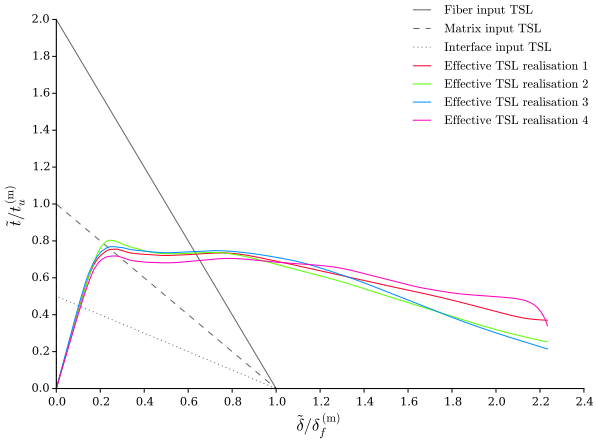

Figure B.8.23: LC4, $V_f = 50\%$: ETSLs.

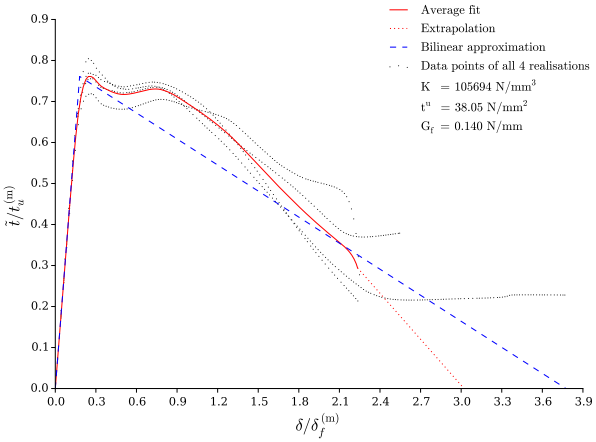

Figure B.8.24: LC4, $V_f = 50\%$: average fit.

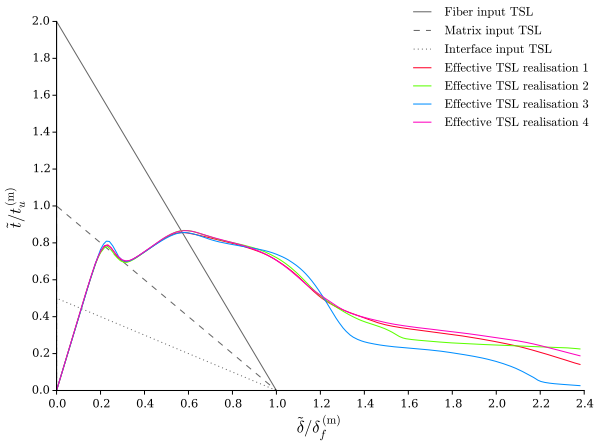

Figure B.8.25: LC5, $V_f = 30\%$: ETSLs.

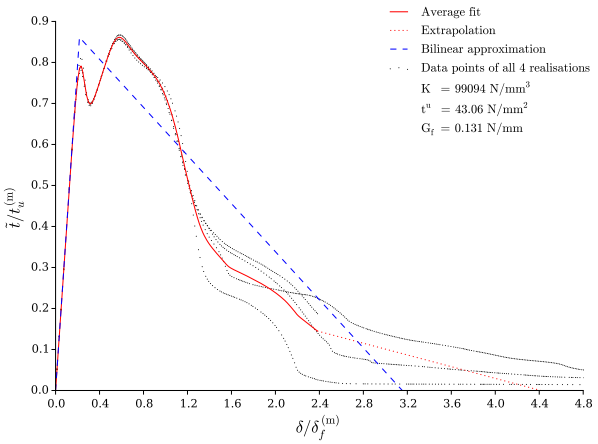

Figure B.8.26: LC5, $V_f = 30\%$: average fit.

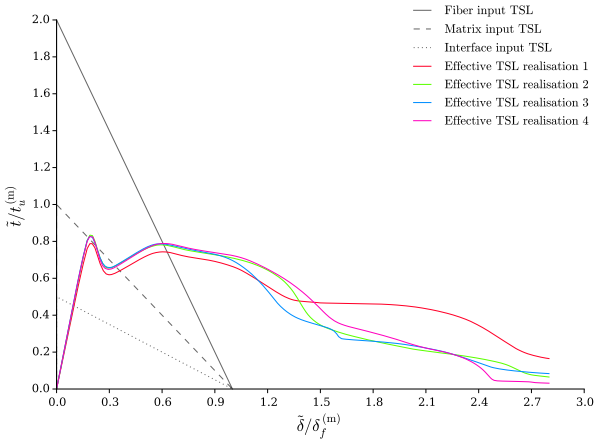

Figure B.8.27: LC5, $V_f = 40\%$: ETSLs.

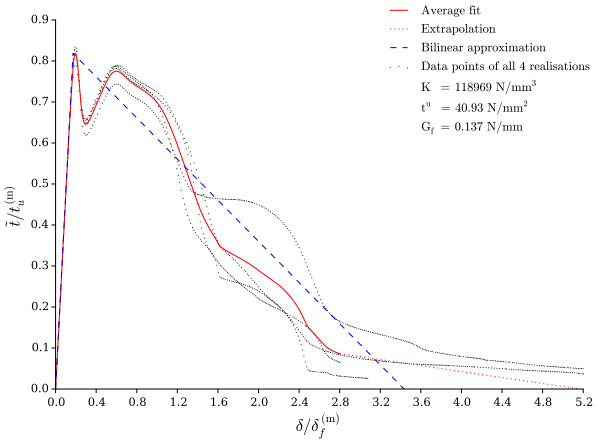

Figure B.8.28: LC5, $V_f = 40\%$: average fit.

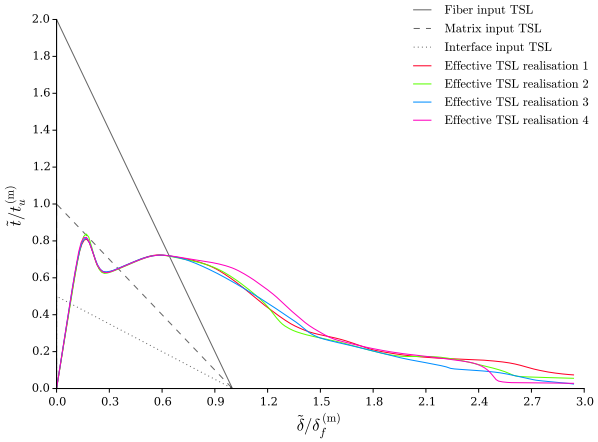

Figure B.8.29: LC5, $V_f = 50\%$: ETSLs.

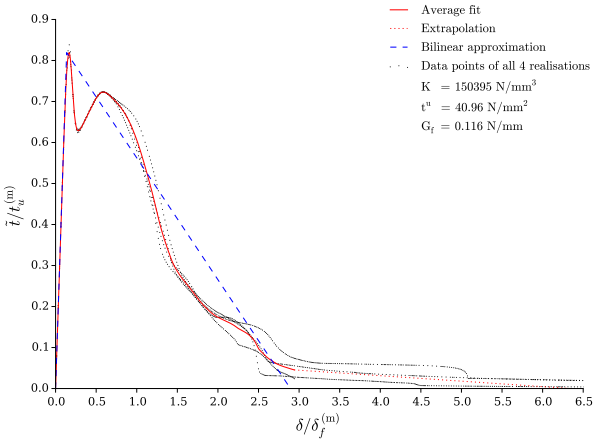

Figure B.8.30: LC5, $V_f = 50\%$: average fit.

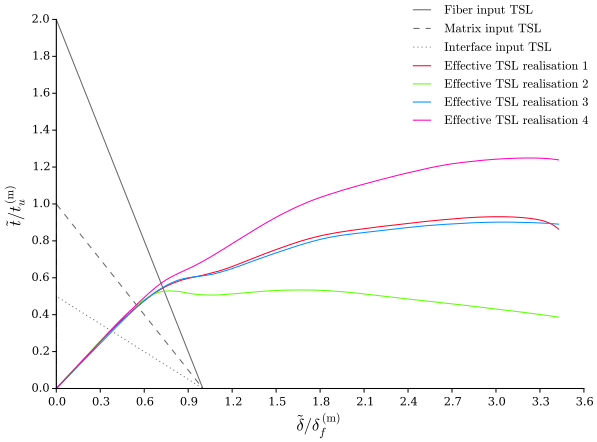

Figure B.8.31: LC6, $V_f = 30\%$: ETSLs.

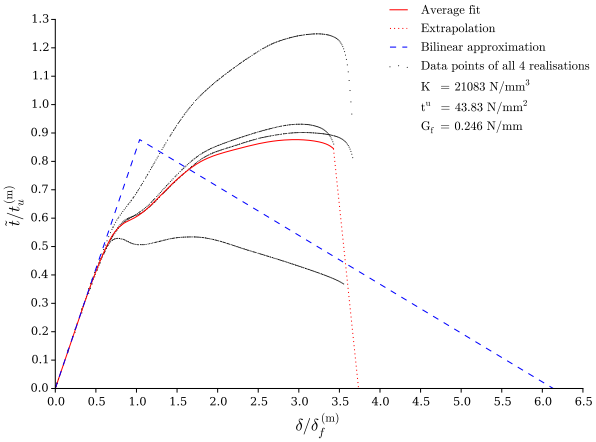

Figure B.8.32: LC6, $V_f = 30\%$: average fit.

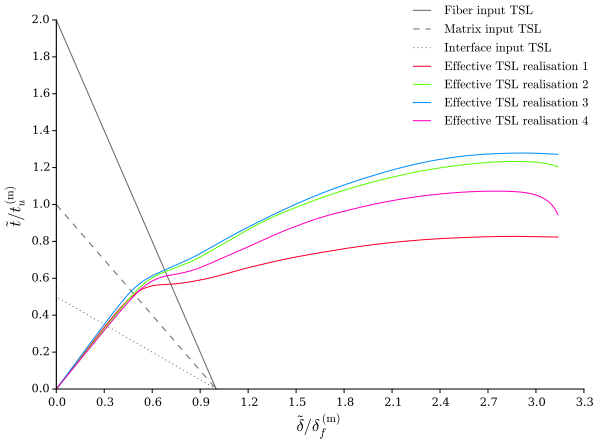

Figure B.8.33: LC6, $V_f = 40\%$: ETSLs.

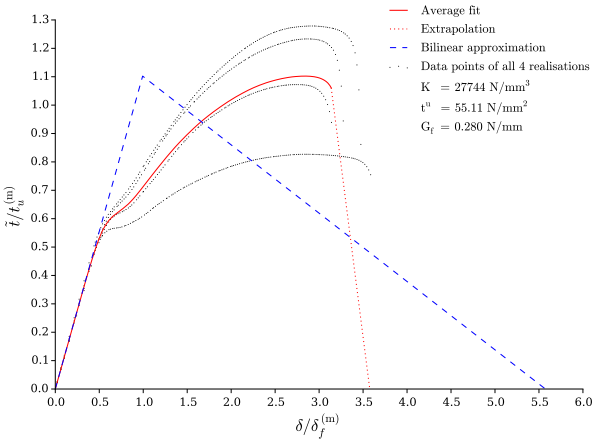

Figure B.8.34: LC6, $V_f = 40\%$: average fit.

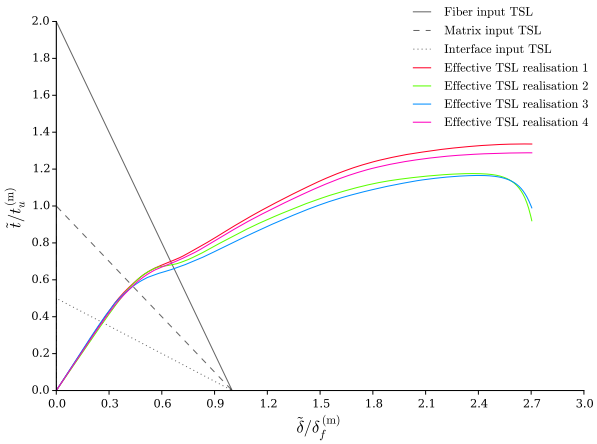

Figure B.8.35: LC6, $V_f = 50\%$: ETSLs.

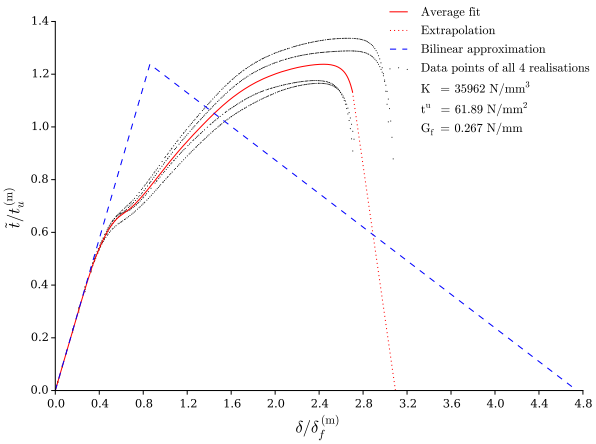

Figure B.8.36: LC6, $V_f = 50\%$: average fit.

Bibliography

[1] C. E. Inglis. Stress in a plate due to the presence of cracks and sharp corners. *Transactions of the Institute of Naval Architects*, 55:219–230, 1913.

[2] A. A. Griffith. The Phenomena of Rupture and Flow in Solids. *Philosophical Transactions of the Royal Society of London. Series A*, 221:163–198, 1921.

[3] G. R. Irwin. Onset of fast crack propagation in high strength steel and aluminum alloys. Technical report, Naval Research Laboratory, Washington D.C., 1956.

[4] J. R. Rice. Fracture mechanics. *Applied Mechanics Reviews*, 38(10):1271–1275, 1985.

[5] G. I. Barenblatt. The Mathematical Theory of Equilibrium Cracks in Brittle Fracture. *Advances in Applied Mechanics*, 7:55–129, 1962.

[6] T. L. Anderson. *Fracture Mechanics: Fundamentals and Applications*. CRC Press, third edition, 2005.

[7] S. W. Tsai and E. M. Wu. A General Theory of Strength for Anisotropic Materials. *Journal of Composite Materials*, 5(1):58–80, 1971.

[8] Z. Hashin and A. Rotem. A Fatigue Failure Criterion for Fiber Reinforced Materials. *Journal of Composite Materials*, 7:448–464, 1973.

[9] R. M. Christensen. Stress based yield/failure criteria for fiber composites. *International Journal of Solids and Structures*, 34(5):529–543, 1997.

[10] C. G. Dávila, N. Jaunky, and S. Goswami. Failure Criteria for FRP Laminates in Plane Stress. *Journal of Composite Materials*, 39(4):323–345, 2003.

[11] A. Needleman. A Continuum Model for Void Nucleation by Inclusion Debonding. *Journal of Applied Mechanics*, 54(3):525, 1987.

[12] X. P. Xu and A. Needleman. Numerical simulations of fast crack growth in brittle solids. *Journal of the Mechanics and Physics of Solids*, 42(9):1397–1434, 1994.

[13] V. Tvergaard. Effect of Fibre Debonding in a Whisker-reinforced Metal. *Materials Science and Engineering*, 125:203–213, 1990.

[14] V. Tvergaard and J. W. Hutchinson. The relation between crack growth resistance and

fracture process parameters in elastic-plastic solids. *Journal of the Mechanics and Physics of Solids*, 40(6):1377–1397, 1992.

[15] N. Moës, J. Dolbow, and T. Belytschko. A finite element method for crack growth without remeshing. *International Journal for Numerical Methods in Engineering*, 46(1):131–150, 1999.

[16] T. Belytschko and T. Black. Elastic Crack Growth in Finite Elements with Minimal Remeshing. *International Journal for Numerical Methods in Engineering*, 45:601–620, 1999.

[17] M. V. Cid Alfaro, A. S. J. Suiker, R. De Borst, and J. J. C. Remmers. Analysis of fracture and delamination in laminates using 3D numerical modelling. *Engineering Fracture Mechanics*, 76(6):761–780, 2009.

[18] M. V. Cid Alfaro, A. S. J. Suiker, and R. De Borst. Transverse failure behavior of fiber-epoxy systems. *Journal of Composite Materials*, 44(12):1493 – 1516, 2010.

[19] M. V. Cid Alfaro, A. S. J. Suiker, and R. De Borst. Multiscale Modelling of the Failure Behaviour of Fibre-Reinforced Laminates. *Multisale Methods in Computational Mechanics, Lecture Notes in Applied and Computational Mechanics*, 55:215–231, 2011.

[20] E. Orowan. Fracture and strength of solids. *Reports on Progress in Physics*, 12:185–232, 1949.

[21] T. Rabczuk. Computational Methods for Fracture in Brittle and Quasi-Brittle Solids: State-of-the-Art Review and Future Perspectives. *ISRN Applied Mathematics*, (849231), 2013.

[22] A. A. Wells. Unstable Crack Propagation in Metals: Cleavage and Fast Fracture. In *Proceedings of the Crack Propagation Symposium*, pages 210 – 230, Cranfield, UK, 1961.

[23] J. R. Rice. A Path Independent Integral and the Approximate Analysis of Strain Concentration by Notches and Cracks. *Journal of Applied Mechanics*, 35(2):379, 1968.

[24] S. Mohammadi. *XFEM Fracture Analysis of Composites*. John Wiley & Sons, Ltd, Teheran, Iran, 2012.

[25] J. Aboudi. Micromechanical analysis of the strength of unidirectional fiber composites. *Composites Science and Technology*, 33:79–96, 1988.

[26] C. Kassapoglou. *Design and Analysis of Composite Structures*. John Wiley & Sons, Ltd, 2010.

[27] R. Hill. *The Mathematical Theory of Plasticity*. Clarendon Press, Oxford, 1950.

[28] D. Xie and A. M. Waas. Discrete cohesive zone model for mixed-mode fracture using finite element analysis. *Engineering Fracture Mechanics*, 73(13):1783–1796, 2006.

[29] D. S. Dugdale. Yielding of steel sheets containing slits. *Journal of the Mechanics and Physics of Solids*, 8:100–104, 1960.

[30] A. Cornec, I. Scheider, and K. H. Schwalbe. On the practical application of the cohesive model. *Engineering Fracture Mechanics*, 70:1963–1987, 2003.

[31] K. Park and G. H. Paulino. Cohesive Zone Models: A Critical Review of Traction-Separation Relationships Across Fracture Surfaces. *Applied Mechanics Reviews*, 64(6), 2011.

[32] V. P. Nguyen. Discontinuous Galerkin/extrinsic cohesive zone modeling: Implementation caveats and applications in computational fracture mechanics. *Engineering Fracture Mechanics*, 128:37–68, 2014.

[33] J. J. Rimoli and J. J. Rojas. Meshing strategies for the alleviation of mesh-induced effects in cohesive element models. *International Journal of Fracture*, pages 29–42, 2015.

[34] V. Tvergaard and J. W. Hutchinson. The Influence of Plasticity on Mixed Mode Interface Toughness. *Journal of the Mechanics and Physics of Solids*, 41(6):1119–1135, 1993.

[35] P. H. Geubelle and J. S. Baylor. Impact-induced delamination of composites: a 2D simulation. *Composites Part B: Engineering*, 29(5):589–602, 1998.

[36] M. Ortiz and A. Pandolfi. Finite-deformation irreversible cohesive elements for three-dimensional crack-propagation analysis. *International Journal for Numerical Methods in Engineering*, 44:1267–1282, 1999.

[37] Z. J. Zhang, G. H. Paulino, and W. Celes. Extrinsic cohesive modelling of dynamic fracture and microbranching instability in brittle materials. *International Journal for Numerical Methods in Engineering*, 72(8):893–923, 2007.

[38] G. T. Camacho and M. Ortiz. Computational modelling of impact damage in brittle materials. *International Journal of Solids and Structures*, 33(20-22):2899–2938, 1996.

[39] K. Park, G. H. Paulino, W. Celes, and R. Espinha. Adaptive mesh refinement and coarsening for cohesive zone modeling of dynamic fracture. *International Journal for Numerical Methods in Engineering*, 92:1–35, 2012.

[40] W. Celes, G. H. Paulino, and R. Espinha. A compact adjacency-based topological data structure for finite element mesh representation. *International Journal for Numerical Methods in Engineering*, 64(11):1529–1556, 2005.

[41] R. Espinha, K. Park, G. H. Paulino, and W. Celes. Scalable parallel dynamic fracture simulation using an extrinsic cohesive zone model. *Computer Methods in Applied Mechanics and Engineering*, 266:144–161, 2013.

[42] D. Ashouri Vajari, B. N. Legarth, and C. F. Niordson. Micromechanical modeling of unidirectional composites with uneven interfacial strengths. *European Journal of Mechanics, A/Solids*, 42:241–250, 2013.

[43] S. Li, M. D. Thouless, A. M. Waas, J. A. Schroeder, and P. D. Zavattieri. Use of a cohesive-zone model to analyze the fracture of a fiber-reinforced polymer-matrix composite. *Composites Science and Technology*, 65(3-4):537–549, 2005.

[44] Z. H. Jin and C. T. Sun. Cohesive zone modeling of interface fracture in elastic bimaterials. *Engineering Fracture Mechanics*, 72(12):1905 – 1817, 2005.

[45] M. F. S. F. De Moura, J. P. M. Gonçalves, J. A. G. Chousal, and R. D. S. G. Campilho. Cohesive and continuum mixed-mode damage models applied to the simulation of the mechanical behaviour of bonded joints. *International Journal of Adhesion and Adhesives*, 28:419–426, 2008.

[46] I. Scheider and W. Brocks. Simulation of cup–cone fracture using the cohesive model. *Engineering Fracture Mechanics*, 70(14):1943–1961, 2003.

[47] Y. Freed and L. Banks-Sills. A new cohesive zone model for mixed mode interface fracture in bimaterials. *Engineering Fracture Mechanics*, 75(15):4583–4593, 2008.

[48] A. Needleman. An analysis of decohesion along an imperfect interface. *International Journal of Fracture*, 42(1):21–40, 1990.

[49] G. E. Beltz and J. R. Rice. Dislocation Nucleation Versus Cleavage Decohesion at Crack Tips. In T. C. Lowe, A. D. Rollett, P. S. Follansbee, and G. S. Daehn, editors, *Modeling the Deformation of Crystalline Solids: Physical Theory, Application, and Experimental Comparisons*, pages 457–480. Cambridge MA, 1991.

[50] X. P. Xu and A. Needleman. Void nucleation by inclusion debonding in a crystal matrix. *Modelling and Simulation in Materials Science and Engineering*, 1(2):111, 1993.

[51] K. Park, G. H. Paulino, and J. R. Roesler. A unified potential-based cohesive model of mixed-mode fracture. *Journal of the Mechanics and Physics of Solids*, 57(6):891–908, 2009.

[52] P. P. Camanho, C. G. Dávila, and M. F. S. F. De Moura. Numerical Simulation of Mixed-mode Progressive Delamination in Composite Materials. *Journal of Composite Materials*, 37(16):1415 – 1438, 2003.

[53] V. P. Nguyen. An open source program to generate zero-thickness cohesive interface elements. *Advances in Engineering Software*, 74:27–39, 2014.

[54] A. Turon, C. G. Dávila, P. P. Camanho, and J. Costa. An engineering solution for mesh size effects in the simulation of delamination using cohesive zone models. *Engineering Fracture Mechanics*, 74:1665–1682, 2007.

[55] F. Feyel and J. L. Chaboche. FE 2 multiscale approach for modelling the elastoviscoplastic behaviour of long fibre SiC/Ti composite materials. *Computer Methods in Applied Mechanics and Engineering*, 183(3-4):309–330, 2000.

[56] S. Loehnert and T. Belytschko. A multiscale projection method for macro/microcrack simulations. *International Journal for Numerical Methods in Engineering*, 71:1466–1482, 2007.

[57] T. Belytschko, S. Loehnert, and J. H. Song. Multiscale aggregating discontinuities: A method for circumventing loss of material stability. *International Journal for Numerical Methods in Engineering*, 73:869–894, 2008.

[58] V. Kouznetsova, M. G. D. Geers, and W. A. M. Brekelmans. Multi-scale constitutive modelling of heterogeneous materials with a gradient-enhanced computational homogenization scheme. *International Journal for Numerical Methods in Engineering*, 54(8):1235–1260, 2002.

[59] M. G. Kulkarni, P. H. Geubelle, and K. Matouš. Multi-scale modeling of heterogeneous adhesives: Effect of particle decohesion. *Mechanics of Materials*, 41:573–583, 2009.

[60] M. G. Kulkarni, K. Matouš, and P. H. Geubelle. Coupled multi-scale cohesive modeling of failure in heterogeneous adhesives. *International Journal for Numerical Methods in Engineering*, 84:916–946, 2010.

[61] V. P. Nguyen, M. Stroeven, and L. J. Sluys. An enhanced continuous-discontinuous multiscale method for modeling mode-I cohesive failure in random heterogeneous quasi-brittle materials. *Engineering Fracture Mechanics*, 79:78–102, 2012.

[62] E. W. C. Coenen, V. G. Kouznetsova, and M. G. D. Geers. Multi-scale continuous-discontinuous framework for computational- homogenization-localization. *Journal of the Mechanics and Physics of Solids*, 60(8):1486–1507, 2012.

[63] E. W. C. Coenen, V. G. Kouznetsova, E. Bosco, and M. G. D. Geers. A multi-scale approach to bridge microscale damage and macroscale failure: A nested computational homogenization-localization framework. *International Journal of Fracture*, 178(1-2):157–178, 2012.

[64] E. Bosco, V. G. Kouznetsova, E. W. C. Coenen, M. G. D. Geers, and A. Salvadori. A multiscale framework for localizing microstructures towards the onset of macroscopic discontinuity. *Computational Mechanics*, 54(2):299–319, 2014.

[65] E. B. Tadmor, M. Ortiz, and R. Phillips. Quasicontinuum analysis of defects in solids, 1996.

[66] F. F. Abraham, J. Q. Broughton, N. Bernstein, and E. Kaxiras. Spanning the length scales in dynamic simulation. *Computers in Physics*, 12(6):538–46, 1998.

[67] R. E. Miller and E. B. Tadmor. The Quasicontinuum Method: Overview, applications and current directions. *Journal of Computer-Aided Materials Design*, 9:203–239, 2002.

[68] M. Xu, R. Gracie, and T. Belytschko. Multiscale modeling with extended bridging domain method. In J. Fish, editor, *Bridging the Scales in Science and Engineering*. Oxford University Press, 2002.

[69] P. Aubertin, J. Réthoré, and R. De Borst. Energy conservation of atomistic/continuum coupling. *International Journal for Numerical Methods in Engineering*, 78:1365–1386, 2009.

[70] P. A. Guidault, O. Allix, L. Champaney, and C. Cornuault. A multiscale extended finite element method for crack propagation. *Computer Methods in Applied Mechanics and Engineering*, 197(5):381–399, 2008.

[71] R. Gracie and T. Belytschko. Concurrently coupled atomistic and XFEM models for dislocations and cracks. *International Journal for Numerical Methods in Engineering*, 78:354–378, 2009.

[72] C. V. Verhoosel, J. J. C. Remmers, M. A. Gutiérrez, and R. De Borst. Computational homogenization for adhesive and cohesive failure in quasi-brittle solids. *International Journal for Numerical Methods in Engineering*, 83(8-9):115–1179, 2010.

[73] V. Kouznetsova. *Computational homogenization for the multi-scale analysis of multi-phase materials*. Phd thesis, Netherlands Institute for Metals Research, 2002.

[74] V. P. Nguyen, O. Lloberas-Valls, M. Stroeven, and L. J. Sluys. Homogenization-based multiscale crack modelling: From micro-diffusive damage to macro-cracks. *Computer Methods in Applied Mechanics and Engineering*, 200:1220–1236, 2011.

[75] J. Fish and Z. Yuan. Multiscale enrichment based on partition of unity. *International Journal for Numerical Methods in Engineering*, 62:1341–1359, 2005.

[76] I. M. Gitman, H. Askes, and L. J. Sluys. Representative volume: Existence and size determination. *Engineering Fracture Mechanics*, 74:2518–2534, 2007.

[77] J. van Kan, G. Segal, and F. Vermolen. *Numerical Methods in Scientific Computing*. Delft Acedemic Press / VSSD, second edition, 2014.

[78] J. C. J. Schellekens and R. De Borst. On the Numerical Integration of Interface Elements. *International Journal for Numerical Methods in Engineering*, 36:43 – 66, 1993.

[79] N. Blal, L. Daridon, Y. Monerie, and S. Pagano. Criteria on the artificial compliance inherent to the intrinsic cohesive zone. *Comptes Rendus Mecanique*, 339:789–795, 2011.

[80] A. Turon, P. P. Camanho, J. Costa, and C. G. Dávila. A damage model for the simulation of delamination in advanced composites under variable-mode loading. *Mechanics of Materials*, 38(11):1072–1089, 2006.